

MODELING THE MORPHODYNAMICS OF SHOREFACE-CONNECTED SAND RIDGES

**HET MODELLEREN VAN DE MORFODYNAMICA
VAN KUSTAANGEHECHTE ZANDBANKEN**

(met een samenvatting in het Nederlands)

PROEFSCHRIFT

ter verkrijging van de graad van doctor aan de Universiteit Utrecht
op gezag van de rector magnificus, prof.dr. J.C. Stoof,
ingevolge het besluit van het college voor promoties
in het openbaar te verdedigen op

woensdag 26 november 2008 des middags te 2.30 uur

door

NICOLETTE CORINA VIS-STAR

geboren op 26 oktober 1979 te Rotterdam

PROMOTOR: PROF.DR. H.E. DE SWART

OPGEDRAGEN AAN

*mijn geliefde echtgenoot Christiaan
mijn geliefde zoon Benjamin
en mijn geliefde ouders*

Copyright © 2008 N.C. Vis-Star - All rights reserved

ISBN 978-90-393-4937-3

Cover Shoreface-connected sand ridges as obtained with a morphodynamic model (top-left). The background photograph illustrates two key elements in the growth process of these ridges: water and sand. Photograph by courtesy of Christiaan Vis - 2006.

Printed by PrintPartners Ipskamp, Enschede

This work is part of the research programme of the 'Stichting voor Fundamenteel Onderzoek der Materie (FOM)', which is financially supported by the 'Nederlandse Organisatie voor Wetenschappelijk Onderzoek (NWO)'.

CONTENTS

1	GENERAL INTRODUCTION	1
1.1	INTRODUCTION	1
1.2	THE COASTAL SYSTEM AND OBSERVED BEDFORMS	1
1.3	FOCUS AND MOTIVATION	3
1.4	THEORIES CONCERNING THE PRESENCE OF SFCR	5
1.5	MORPHODYNAMIC SELF-ORGANIZATION	5
1.6	GENERAL CONCEPTS OF SEDIMENT TRANSPORT	7
1.7	REVIEW OF PREVIOUS WORK	10
1.8	RESEARCH QUESTIONS AND APPROACH	12
2	INITIAL FORMATION OF SHOREFACE-CONNECTED SAND RIDGES: ROLE OF WAVES	15
2.1	INTRODUCTION	16
2.2	MODEL FORMULATION	16
2.2.1	SHelf GEOMETRY	16
2.2.2	GENERAL CONSIDERATIONS	17
2.2.3	HYDRODYNAMICS	17
2.2.4	BED EVOLUTION AND SEDIMENT TRANSPORT	20
2.2.5	ADDITIONAL ASSUMPTIONS	22
2.3	METHOD OF ANALYSIS	22
2.3.1	BASIC STATE	22
2.3.2	STABILITY ANALYSIS AND LINEARIZED MODEL	24
2.4	RESULTS	25
2.4.1	PARAMETER VALUES: DEFAULT CASE	25
2.4.2	BASIC STATE AND LINEAR STABILITY ANALYSIS: DEFAULT CASE	25
2.4.3	SENSITIVITY TO OFFSHORE ANGLE OF WAVE INCIDENCE AND INNER SHELF SLOPE	28
2.4.4	SENSITIVITY TO OFFSHORE WAVE HEIGHT AND INNER SHELF SLOPE	30
2.4.5	SENSITIVITY TO WAVE PERIOD AND INNER SHELF SLOPE	31
2.4.6	SENSITIVITY TO BED SLOPE PARAMETER FOR SUSPENDED SEDIMENT	32
2.5	DISCUSSION	33
2.5.1	PHYSICAL INTERPRETATION	33

2.5.2	MODEL LIMITATIONS	36
2.5.3	COMPARISON WITH FIELD OBSERVATIONS	37
2.6	CONCLUSIONS	39
APPENDICES		40
2.A	ANISOTROPY IN BED SHEAR-STRESS AND BEDLOAD TRANSPORT	40
2.B	EXPRESSIONS FOR OPERATORS \mathcal{S} AND \mathcal{L}	42
2.C	EXAMPLE OF ONE SPECIFIC EQUATION OF THE LINEAR SYSTEM	43
2.D	FLOW OVER TOPOGRAPHY PROBLEM	43
3	NONLINEAR DYNAMICS OF INNER SHELF SAND RIDGES: PATCH BEHAVIOR AND ROLE OF WAVES	45
3.1	INTRODUCTION	46
3.2	MODEL FORMULATION	47
3.3	METHOD OF ANALYSIS	49
3.3.1	BASIC STATE AND LINEAR STABILITY ANALYSIS	49
3.3.2	NONLINEAR MODEL: FINITE AMPLITUDE BEHAVIOR	50
3.3.3	ANALYSIS OF THE POTENTIAL ENERGY BALANCE OF THE BED-FORMS	51
3.4	RESULTS	52
3.4.1	PARAMETER VALUES: DEFAULT CASE	52
3.4.2	NONLINEAR ANALYSIS: DEFAULT CASE	53
3.4.3	SENSITIVITY TO OFFSHORE ANGLE OF WAVE INCIDENCE AND INNER SHELF SLOPE	57
3.4.4	SENSITIVITY TO OFFSHORE WAVE HEIGHT AND INNER SHELF SLOPE	58
3.4.5	SENSITIVITY TO WAVE PERIOD AND INNER SHELF SLOPE	59
3.4.6	SENSITIVITY TO NUMBER OF SUBHARMONIC MODES	59
3.5	DISCUSSION	68
3.5.1	PHYSICAL INTERPRETATION	68
3.5.2	MODEL LIMITATIONS	74
3.5.3	COMPARISON WITH FIELD OBSERVATIONS	75
3.6	CONCLUSIONS	75
APPENDIX		77
3.A	EXPRESSION FOR OPERATOR \mathcal{N}	77
4	EFFECT OF WAVE-TOPOGRAPHY INTERACTIONS ON THE FORMATION OF SAND RIDGES ON THE SHELF	79
4.1	INTRODUCTION	80
4.2	MODEL FORMULATION	82
4.2.1	SHELF GEOMETRY	82
4.2.2	HYDRODYNAMICS	83
4.2.3	BOTTOM EVOLUTION AND SEDIMENT TRANSPORT	86
4.2.4	ADDITIONAL ASSUMPTIONS	87
4.3	SOLUTION METHOD	87
4.3.1	BASIC STATE	88
4.3.2	LINEAR STABILITY ANALYSIS	89

4.4	RESULTS	91
4.4.1	PARAMETER VALUES: DEFAULT CASE	91
4.4.2	BASIC STATE AND LINEAR STABILITY ANALYSIS: DEFAULT CASE	92
4.4.3	SENSITIVITY TO THE WAVE-BEDFORM FEEDBACK MECHANISM	95
4.4.4	SENSITIVITY TO THE REFERENCE BOTTOM SLOPE	96
4.4.5	SENSITIVITY TO OTHER MODEL PARAMETERS	96
4.5	DISCUSSION	101
4.5.1	PHYSICAL INTERPRETATION	101
4.5.2	COMPARISON WITH OBSERVATIONS	104
4.5.3	MODEL SIMPLIFICATIONS	105
4.6	CONCLUSIONS	106
	APPENDIX	107
	4.A PERTURBED FLOW AND SEDIMENT TRANSPORT	107
5	EFFECT OF WAVE-BEDFORM FEEDBACKS ON THE FORMATION OF AND GRAIN SORTING OVER SHOREFACE-CONNECTED RIDGES	109
5.1	INTRODUCTION	110
5.2	MODEL FORMULATION	111
5.2.1	SHELF GEOMETRY	111
5.2.2	HYDRODYNAMICS	112
5.2.3	SEDIMENT CHARACTERISTICS	113
5.2.4	SEDIMENT DYNAMICS	113
5.3	SOLUTION METHOD	117
5.3.1	BASIC STATE	117
5.3.2	LINEAR STABILITY ANALYSIS	119
5.4	RESULTS	121
5.4.1	PARAMETER VALUES: DEFAULT CASE	121
5.4.2	BASIC STATE AND LINEAR STABILITY ANALYSIS: DEFAULT CASE	121
5.4.3	SENSITIVITY TO SEDIMENT CHARACTERISTICS	123
5.4.4	SENSITIVITY TO HIDING AND ROUGHNESS-INDUCED TURBULENCE	127
5.4.5	SENSITIVITY TO SETTLING LAG EFFECTS	129
5.4.6	SENSITIVITY TO OTHER MODEL PARAMETERS	129
5.5	DISCUSSION	130
5.5.1	PHYSICAL INTERPRETATION	130
5.5.2	COMPARISON WITH OBSERVATIONS	132
5.5.3	MODEL SIMPLIFICATIONS	133
5.6	CONCLUSIONS	134
	APPENDICES	136
	5.A SETTLING LAG IN THE CONCENTRATION EQUATION	136
	5.B PERTURBED FLOW AND SEDIMENT TRANSPORT	136

6	GENERAL DISCUSSION AND CONCLUSIONS	139
6.1	FORMATION OF SFCR: IMPROVED FORMULATION FOR STIRRING OF SED- IMENT BY WAVES	139
6.2	LONG-TERM EVOLUTION OF SFCR	140
6.2.1	IMPROVED FORMULATION FOR STIRRING OF SEDIMENT	140
6.2.2	ADDING SUBHARMONIC MODES	141
6.3	WAVE-BEDFORM INTERACTIONS	141
6.4	WAVE-BEDFORM FEEDBACKS AND GRAIN SORTING	142
6.5	SUGGESTIONS FOR FUTURE RESEARCH	142
	BIBLIOGRAPHY	145
	SAMENVATTING	151
	DANKWOORD	157
	CURRICULUM VITAE	157

CHAPTER 1

GENERAL INTRODUCTION

1.1 INTRODUCTION

A rich variety of bedforms is observed in coastal seas. Their generation requires an erodible seabed and forcing agents (e.g. currents, waves and tides), which are strong enough to mobilize sediment particles. In this thesis it is systematically explored, which physical processes are of importance for the formation and subsequent long-term evolution of one specific type of bottom pattern: the shoreface-connected sand ridges (hereafter abbreviated as sfc). This is done by using and extending existing idealized morphodynamic models and evaluating their performance by comparing the results with field data. As a starting point, in section 1.2 an overview is given of the different types of bedforms that are observed in coastal seas, including sfc. In section 1.3 the choice of the research topic is motivated and its relevance presented. Proposed hypotheses on the origin of sfc can be divided into two broad classes, which are discussed in section 1.4. At the basis of this thesis is the hypothesis of morphodynamic self-organization of which a conceptual explanation is given in section 1.5. In section 1.6 some general concepts of sediment and sediment transport are discussed. In section 1.7 a brief review is presented of previous modeling studies. Based on findings with and limitations of preceding work, the research questions are formulated (section 1.8). In this section the research approach is also discussed and an outline of the thesis is given.

1.2 THE COASTAL SYSTEM AND OBSERVED BEDFORMS

A coastal sea extends from the shoreline to the shelf break, where a steep slope in the seabed marks the transition from continental shelf to deep ocean (see Figure 1.1). The water motion in this region is forced in different ways (cf. *Wright and Short*, 1984). Many components with different length and time scales mutually interact. The wind blowing over the water surface generates wind waves (periods in the order of seconds and heights in the order of 1 – 2 m), wind-driven currents (velocities in the order of 0.5 m s^{-1}) and a set-up or set-down (dependent on the wind direction, in the order of 1 m) of water towards the shoreline. In shallow areas waves can force net currents (in the order of 1 m s^{-1}), a seaward-directed un-

ertow and rip currents. Furthermore, breaking of waves gives rise to turbulence and related vigorous mixing. The tides cause changes in the water level and current direction during the tidal period. In most coastal seas the semi-diurnal lunar (M_2) tide (period of 12 h 25 min) is the dominant tidal constituent. Typical values for the amplitude of the sea surface variation and of the tidal currents are ~ 1 m and ~ 1 m s^{-1} , respectively. Density-driven currents (in the order of 0.1 m s^{-1}) are induced by the outflow of fresh river water into the more saline sea. Sea level rise is estimated to be in the order of several decimeters per century.

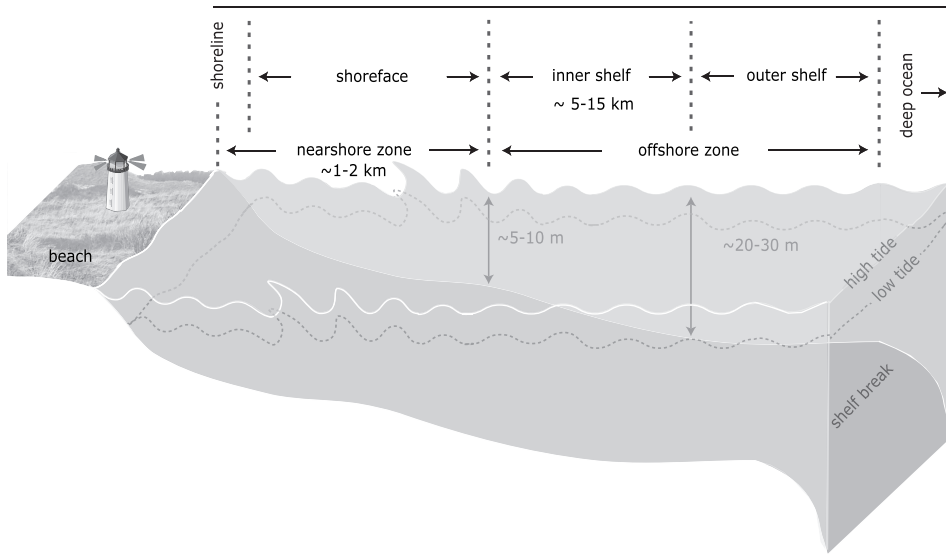


Figure 1.1: Sketch of the coastal region, where different subregions are indicated.

An essential aspect of the water motion is that it results in shear-stresses acting on the bottom and when these stresses exceed some critical value, sediment on the sea bottom is eroded and transported. The stronger the bottom shear-stresses, the more sediment can be transported. Spatial divergences in the sediment flux cause a change in bed level and result in the generation of different kinds of bedforms. The changes in the bottom morphology in turn affect the waves and currents due to changing water depths. The interactions between the water motion and the erodible bottom are often referred to as morphodynamic feedbacks.

In spite of the complexity of the processes, often relatively regular morphological patterns are observed in coastal seas. The specific forcing mechanisms, geometrical characteristics and sediment characteristics of the shelf region determine the time scale on which bedforms grow and disappear and also their spatial scale. Thus, different types of bedforms are found in the different subregions indicated in Figure 1.1. The nearshore zone is the area extending $\sim 1 - 2$ km seaward from the water line at high tide and comprises the swash zone (where waves dissipate through run-up), surf zone (where waves break) and shoaling zone (where wave height increases in shoreward direction). The section of the nearshore zone that

is permanently covered by water is defined as the shoreface. The nearshore zone has a steep cross-shore bottom slope (typically 1:100) and the water motion is dominated by shoaling, refraction and breaking of waves. Also tides play a role in determining the water level. The nearshore zone is a complex system, where bedforms such as ripples, beach cusps, swash bars, surf zone sand bars and megaripples (cf. *Short*, 1999) evolve on time scales of hours to years and spatial scales of centimeters to hundreds of meters. The offshore zone extends seaward from the nearshore zone up to the offshore end of the continental shelf (depths of 100 – 200 m). In this subregion waves become less dominant in forcing the water motion, whereas wind and tides become important. The cross-shore slope of the seabed is considerably smaller, being typically 1:1000 over the inner shelf and decreasing to almost constant depth on the outer shelf. The offshore zone is characterized by more elongated bedforms (length scale of several kilometers) compared to the ones in the nearshore zone. Moreover, they evolve on longer time scales (decades to centuries). These offshore bedforms include the tidal sand banks (e.g. *Pattiaratchi and Collins*, 1987; *Van de Meene*, 1994; *Liu et al.*, 1998), which are found on outer shelves in case that tidal currents are strong. The sorted bedforms, called rippled scour depressions by *Cacchione et al.* (1984), are found on inner continental shelves and are typically 100 – 200 m wide. They extend hundreds to thousands of meters in the cross-shore direction from the outer surf zone to the inner shelf and develop on time scales in the order of a month. Also sfcf are observed on inner shelves, in both tidal and nontidal environments, as will be discussed hereafter.

1.3 FOCUS AND MOTIVATION

In this thesis the emphasis is on sfcf, which are observed on sandy inner shelves (depths between 5 and 30 m). Early observations were reported on the most prominently present sfcf along the Atlantic shelf of North America by *Duane et al.* (1972), *Swift et al.* (1972) and *Swift and Field* (1981). In *Swift et al.* (1978) also sfcf occurring on European shelves were described. Moreover, sfcf were reported on the inner shelves of Brazil (*Figueiredo et al.*, 1982), Argentina (*Parker et al.*, 1982), Canada (*Hoogendoorn and Dalrymple*, 1986; *Amos et al.*, 1996), Belgium and the Netherlands (*Van de Meene and Van Rijn*, 2000), Germany (*Antia*, 1996a), Denmark (*Anthony and Leth*, 2002) and West Florida (*Twichell et al.*, 2003; *Edwards et al.*, 2003; *Harrison et al.*, 2003). Figure 1.2a shows sfcf located in the south-east part of the North Sea, along the German barrier island Spiekeroog.

Each of these coasts is characterized by a frequent passage of storms, which involve high waves and strong storm-driven currents. The tidal current amplitude varies significantly over the regions where these ridges occur. Generally, patches of 4 – 8 sfcf are observed, which have an oblique orientation with respect to the shoreline. More specifically, the seaward ends of the crests are located further up-current (i.e., in the direction opposite to that of the storm-driven flow) than their landward ends, thereby forming an angle of 10° – 50° with respect to the coastline. Individual sfcf are between 10 and 25 km long, their height ranges from 1 to 6 m and they have a width of 2 – 3 km. The alongshore distance between successive crests is between 2 and 6 km. The North American sfcf and some of the Argentine sfcf are asymmetric, with their seaward sides being steeper than their landward sides. Observations show that sfcf migrate in the direction of the storm-driven current with a characteristic speed

of $1 - 50 \text{ m yr}^{-1}$, depending on the measuring period. Also characteristic is a sorting of grain size over sfc. Most sfc in the Mid Atlantic Bight of the North American shelf reveal the coarsest (finest) sediments on the landward (seaward) flanks (grain size and topography variations are approximately 90° out of phase) (e.g. *Swift et al.*, 1972; *Schwab et al.*, 2000). Observed trends in mean grain size are similar for sfc on the inner shelf of Argentina (*Parker et al.*, 1982) and Germany (see Figure 1.2b).

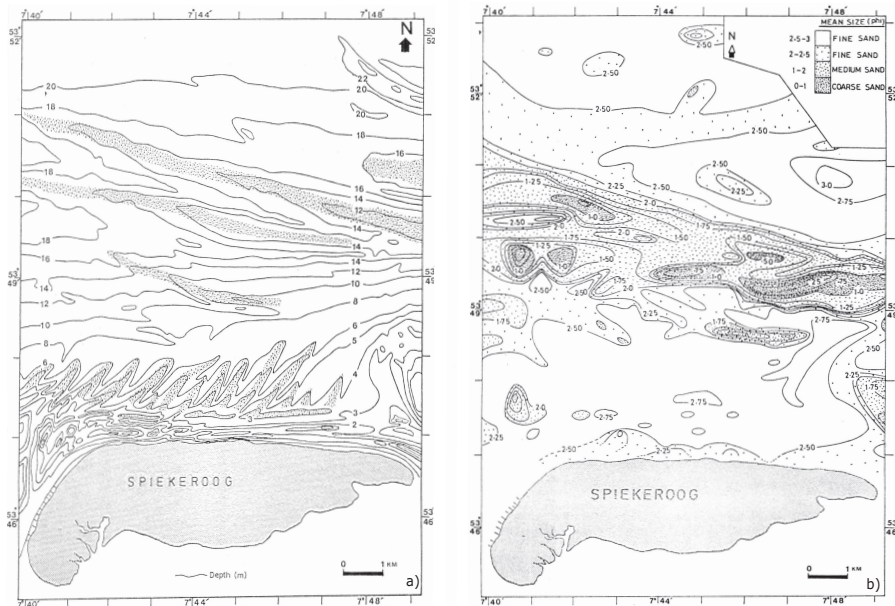


Figure 1.2: (a) Bathymetry (in meters) showing the topography of sfc on the Spiekeroog inner shelf. The mean longshore current is directed from west to east. (b) Distribution of sediment, characterized by the mean sedimentation diameter (phi-value), on the Spiekeroog inner shelf. Larger phi-values imply smaller grain sizes. Reprinted from *Antia* (1993).

Gaining more fundamental knowledge about the processes that control the morphodynamics of sfc is important for several reasons. Some of them are related to the movements of sfc, whereby they might affect the stability of pipelines, cables and oil rigs. Knowledge of the dynamical behavior of sfc is also crucial in regions where they intersect with shipping routes and anchor areas. Moreover, sfc are potential reservoirs for minerals and oil, because of their high preservation potential and good textural characteristics. The large volumes of sand stored in sfc are interesting for the construction industry and e.g. on the Dutch Zeeland ridges sand extractions have been taken place. Human interventions like the mining of sand and dredging of navigation channels, can have large consequences for the stability of coasts (sand may be transported away from the beach) and therefore require careful studies.

The same holds for the impact of other interferences like sea level rise. A crucial question is whether sfcR will recover from interventions, i.e., whether they constitute a self-restoring system. Finally, sfcR along the central Dutch coast seem to play an important role in the protection of the shoreline against wave action and in this way contribute to coastal stability (Van de Meene *et al.*, 1996). The investigation of sfcR is also a way of gaining insight into the fundamental physics that may dominate the coupling between the water motion and the bottom.

1.4 THEORIES CONCERNING THE PRESENCE OF SFCR

Long time scales (order of centuries) are involved in the development of sfcR. Therefore, observations are not sufficient to provide good understanding about their dynamics. Proposed hypotheses on the origin of sfcR can be divided into two broad classes. The first is that sfcR are relict features from before the Holocene transgression (McClennen and McMaster, 1971; Swift *et al.*, 1972) and originated during a period of sea level rise. The second is that they emerge due to inherent dynamic interactions between the water motion and the sandy bed (called morphodynamic self-organization). Although some features appear to be largely relict, observations by cf. Swift *et al.* (1978) and Twichell *et al.* (2003) show that sediment transport in sfcR areas is significant, especially under stormy conditions. So, even when sfcR have a relict origin, they are often subject to sediment reworking by modern shelf processes. McBride and Moslow (1991) argue that ebb-tidal deltas provided the initial sand source for the development of many sfcR and shelf processes act as modifying agents in the evolution during and after ebb-tidal delta deposition.

1.5 MORPHODYNAMIC SELF-ORGANIZATION

The second hypothesis mentioned in the previous section, i.e., the hypothesis of morphodynamic self-organization, forms the basis of the research presented in this thesis. The inherent coupling between the water motion and the bottom topography (through the transport of sediment) in some cases results in a positive feedback, due to which small perturbations in the bottom start to grow and morphological features are formed. A positive feedback results when convergence (divergence) of sediment transport occurs above a crest (trough) and sediment will be deposited (eroded) on the crest (from the trough). In contrast, small perturbations in the bottom will decay when convergence of sediment transport takes place in the troughs and divergence of sediment transport above the crests. In case that neither a positive nor a negative feedback occurs, the system is in morphodynamic equilibrium. Note also that if the maximum convergence of sediment flux occurs upstream or downstream of the crest, the bed-forms will migrate. A schematic view of the morphodynamic self-organization mechanism is given in Figure 1.3.

Whether the self-organization mechanism results in the formation of sfcR can be investigated with the use of process-based morphodynamic models. The latter are based on physical laws for the water motion, erosion, deposition and transport of sediment and bottom change. Figure 1.4 gives a schematic representation of such a model.

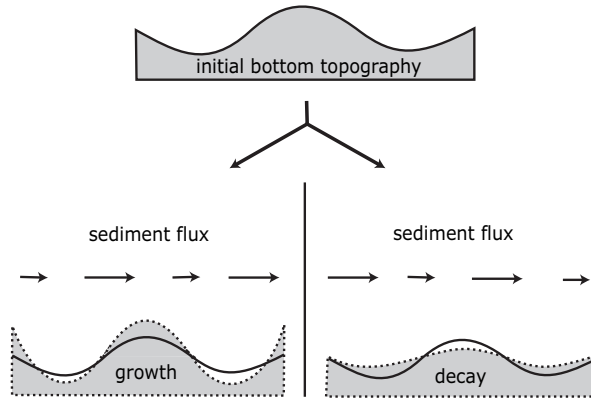


Figure 1.3: Illustration of the morphodynamic self-organization mechanism, which can explain the formation of sfcf. Interactions between the water motion and the erodible seabed (through the transport of sediment) cause perturbations in the bottom to grow or decay.

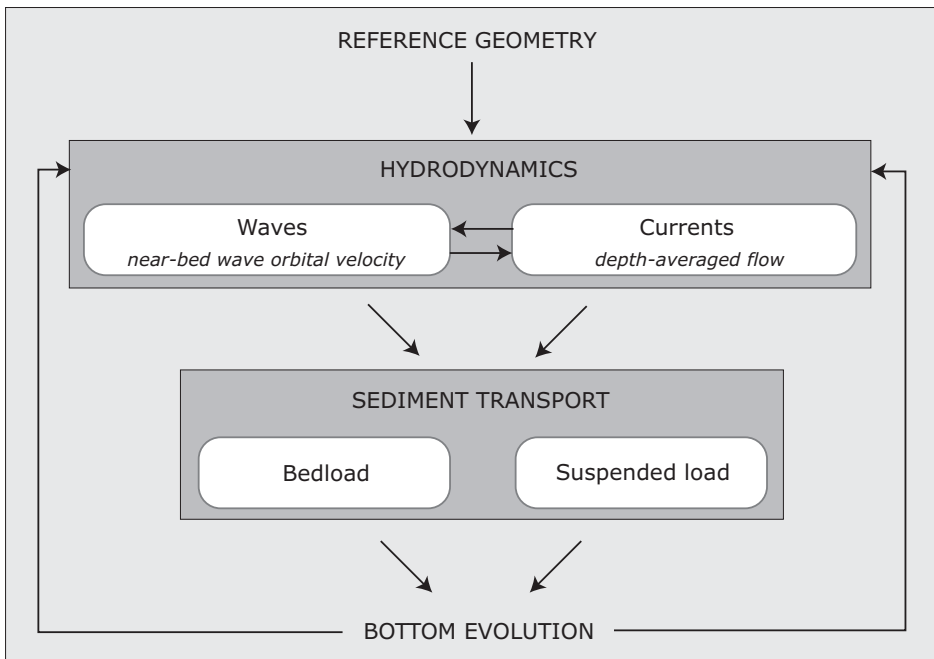


Figure 1.4: Schematic representation of the morphodynamic model based on the hypothesis that sfcf form as a consequence of inherent dynamic interactions. For more details see the text.

The starting point of a morphodynamic model is an initial reference geometry (the basic state), which is alongshore uniform and no bedforms are present yet. The water motion, consisting of contributions of both waves and currents, interacts with this bottom and is capable of eroding and transporting sediment. The stronger the water motion, the more sediment is transported. Due to mass conservation of sediment, spatial differences in this sediment transport cause bottom changes. Since the water motion is affected by the changing bottom, the morphodynamic loop has to be repeated. A linear stability analysis is used to study the initial growth of small perturbations, with an arbitrary spatial structure, evolving on the basic state. As the perturbations are small, the system of equations is linearized and the linear system constitutes an eigenvalue problem, which can be solved. The result is a set of linear eigenmodes of which the growth rates and migration speeds are given by the eigenvalues. An initial perturbation will evolve in case of a positive growth rate (positive morphodynamic feedback). The perturbation having the largest growth rate is called the initially fastest growing or most preferred mode. The basic idea of a linear stability analysis is that, starting from some random perturbation (which contains all modes), the initially fastest growing mode will dominate the solution after some time. The long-term evolution of bottom perturbations is investigated with a fully nonlinear morphodynamic spectral model (including nonlinear processes when perturbations attain a considerable amplitude). The nonlinear model describes the time evolution of amplitudes of known eigenmodes of the linear system. With a nonlinear model it is possible to investigate the finite-amplitude behavior of sfc, i.e., whether the characteristics of sfc (like height, migration speed and longshore spacing) tend to a constant value and do not change in time anymore.

Idealized process-based models, as described above, have been applied successfully in coastal morphodynamics. They have been used to explain the formation of many types of bedforms as a result of morphodynamic self-organization. These phenomena include e.g. sea ripples (*Vittori and Blondeaux, 1992; Blondeaux et al., 2000*), nearshore bars (*Falqués et al., 1996; Vittori et al., 1999; Falqués et al., 2000; Ribas et al., 2003; Calvete et al., 2005; Garnier et al., 2006*), tidal sand banks and sand waves (*Huthnance, 1982; Gerkema, 2000; Roos et al., 2004; Besio et al., 2006*).

1.6 GENERAL CONCEPTS OF SEDIMENT TRANSPORT

In this section basic concepts are discussed of sediment and sediment transport. Just a short summary will be given of processes and definitions that will be used in this thesis. For more detailed information is referred to *Fredsøe and Deigaard (1992), Soulsby (1997)* and *Gyr and Hoyer (2006)*.

SEDIMENT PROPERTIES

The sediment on the inner shelf is found to be nonuniform coarse-sized to medium-sized sand with diameters in the order of 0.5 mm. This material is noncohesive, therefore processes like flocculation are not important. Natural sediments always contain particles of different sizes. The grain size distribution is log-normal, i.e., plotting the weight percentage against the logarithm of the diameter of a grain yields a normal distribution. Therefore, it is convenient to

use a logarithmic scale for the grain diameter, the phi-scale, on which the grain diameter in ϕ -units is $-\log_2$ of the grain diameter in mm. The phi-values are normally distributed, where the mean grain diameter is defined in such a way that 50% of the grains have a smaller (larger) diameter than the mean. The standard deviation of the distribution gives a measure of the sorting. A relatively uniform sand mixture is characterized by a small value for the sorting. On the other hand a poorly sorted sediment mixture has a large standard deviation.

The shape of individual grains causes a volume of sediment to consist of a fraction of empty space. The packing fraction of sediment is defined as the ratio of the space occupied by the grains and the total space. The porosity of a sediment volume is defined as the ratio of empty space and total space, thus is equal to 1 minus the packing fraction. The porosity of natural noncohesive sediment mixtures is typically 0.4.

The angle of repose is defined as the maximum angle of a stable slope build by a collection of sediment particles. It is the angle between this maximum slope and the horizontal surface. The angle of repose is e.g. determined by shape and size of the grains, friction between the grains and packing fraction. Grains that are piled on each other above this critical angle, will avalanche down the slope until the angle of repose is reached. Natural noncohesive sediment mixtures have an angle of repose of approximately 30° .

SEDIMENT MOVEMENT

Sediment will only be transported if the bottom shear-stress τ (which is proportional to the squared velocity) exceeds a critical value, τ_c . Instead of τ_c , often the critical friction velocity u_{*c} is used, which is defined as $u_{*c} = (\tau_c/\rho)^{1/2}$, where ρ is the density of water. The threshold curve for sediment movement is given in Figure 1.5 as a function of grain size and friction velocity (also called shear velocity). The settling velocity w_s is related to the grain size and is defined as the rate at which a sediment particle settles in a still fluid. The settling velocity is determined by the balance between the net gravitational and frictional force and is dependent on the shape and size of a sediment particle.

Figure 1.5 illustrates that u_{*c} for coarse sediment is large and when $u_* > u_{*c}$ the sediment will start to move as bedload. In case of bedload transport sediment grains move in more or less continuous contact with the bed, by rolling, sliding or saltation. For larger friction velocities a transition will take place from bedload to suspended load sediment transport. The latter occurs when sediment is entrained into the interior of the fluid. For $u_* > u_{*c}$, the fine sediment comes into suspension very easily and is transported as suspended load (hardly as bedload). Sediment on a sloping bed experiences an additional force due to gravity, which can result in downslope transport of sediment. An illustration of bedload and suspended load sediment transport is given in Figure 1.6.

In contrast to bedload transport, suspended load transport is generally not determined by local flow conditions. This is because sediment in suspension needs time to settle to the bed. Thus, in case of inhomogeneous and/or nonstationary conditions, the sediment concentration will lag behind the local flow. This is referred to as settling lag.

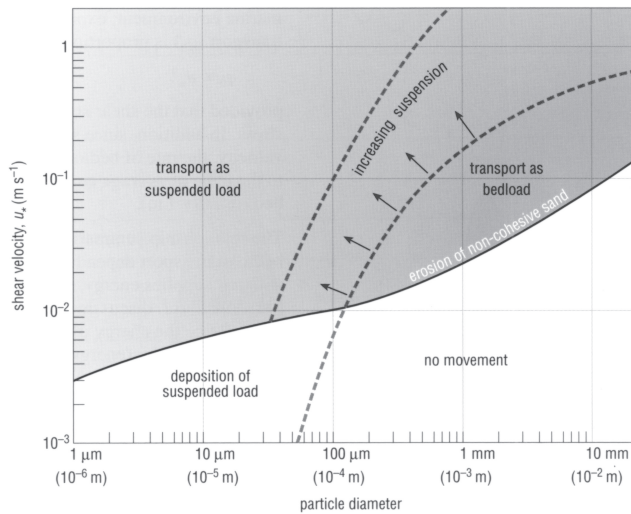


Figure 1.5: Empirically determined diagram showing the threshold curve for noncohesive sediment movement and the curve at which a transition from bedload to suspended load transport takes place as a function of friction velocity and grain size. Broken lines represent gradational boundaries. Scales are logarithmic. Reprinted from *Open University* (2001).

The way grains are arranged in the sediment surface layer at the bottom also affects the sediment transport. It is more difficult to entrain sediment grains from a densely packed surface layer with small porosity than from a loosely packed surface. Additionally, when the surface layer consists of sediment particles of different sizes, smaller grains can hide between the coarser grains. Hence, they experience less fluid drag and the bedload transport for finer grains in a sediment mixture is reduced with respect to that for a uniform bed (a process called dynamic hiding). If the critical friction velocity for a sediment mixture is different from u_{*c} for uniform sediment it is called static hiding (*Seminara, 1995*). In a sediment mixture, the phenomenon of hiding also affects the entrainment of sediment into the fluid interior (*Garcia and Parker, 1991*) and hence suspended load transport.

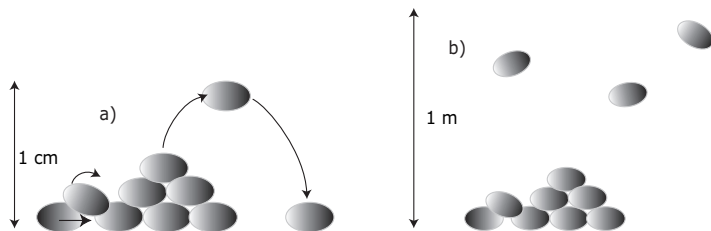


Figure 1.6: An illustration of (a) bedload and (b) suspended load sediment transport.

FORMULATIONS FOR NONCOHESIVE SEDIMENT TRANSPORT

Many formulations for sediment transport are given in the literature (cf. *Soulsby, 1997; Gyr and Hoyer, 2006*, for an overview). Important pioneering work was done by *Bagnold (1963)*. The choice of a specific formula depends on sediment properties and flow conditions (waves and currents). In this thesis the formulation of *Bailard (1981)* for bedload transport is used, which is derived for uniform and noncohesive sediment. According to the latter formulation the bedload sediment transport depends nonlinearly on the local friction velocity and its magnitude and direction are corrected for bed slopes. Suspended load sediment transport generally requires solving a concentration equation with imposed formulations for turbulent diffusion of sediment and entrainment of sediment at the bed. In this thesis the formulation for sediment entrainment is that proposed by *Van Rijn (1993)*. If sediment is nonuniform, the transport of sediment with diameter d_i is related to the sediment transport corresponding to grains having the mean size d_m . Subsequently, corrections are made for e.g. the probabilities of occurrence of grains of a specific diameter and hiding. In this thesis the formulation for bedload transport of a sediment mixture is similar as in *Seminara (1995)*. Furthermore, the *Garcia and Parker (1991)* formulation for entrainment of sediment is used in the suspended load transport for a sediment mixture.

1.7 REVIEW OF PREVIOUS WORK

Trowbridge (1995) was the first who demonstrated, using a process-based model, that sfcf can form due to morphodynamic self-organization. He investigated the stability properties of a storm-driven alongshore flow, with a cross-shore gradient, on a sandy shelf bounded by a straight coast and with a transverse bottom slope. His model consists of the depth-averaged shallow water equations, ignoring Coriolis and bottom friction terms, and a bottom evolution equation. The sediment transport due to bedload processes is linearly related to the mean flow and involves a constant, which represents stirring of sediment by waves. *Trowbridge (1995)* applied the quasi-steady assumption, i.e., the flow responds instantly to the changing bottom, as the characteristic hydrodynamic time scale (order of days) is much smaller than the morphodynamic time scale (order of decades to centuries for sfcf). This model simulates the initial growth and down-current migration of up-current oriented ridges having similar shape as the observed sfcf in the field (see Figure 1.7). The latter is the consequence of a positive coupling between small topographic perturbations superimposed on the mean alongshore uniform equilibrium state and the induced small hydrodynamic perturbations such that sand transport is convergent over sfcf. Essential for the growth of up-current rotated sfcf is the presence of a transversely sloping reference bottom and an offshore deflection of the current over sfcf. A drawback of the model is that it yields no preferred alongshore wavenumber of sfcf, as is illustrated in Figure 1.7a. Also, the growth rate is quite small.

The model of *Trowbridge (1995)* was extended by *Falqués et al. (1999)* to include Coriolis terms and bottom shear-stresses in the momentum equations. Thus, sources for the production of vorticity were introduced. Additionally, sediment transport due to bottom slopes was accounted for. They concluded that vorticity dynamics does not play a dominant role in the formation of sfcf. However, the effect of bed slopes is crucial to obtain a preferred mode

of which the spacing agrees with field observations. *Restrepo* (2001) included the effect of wave-induced Stokes drift in the model and found that it tempered the growth mechanism.

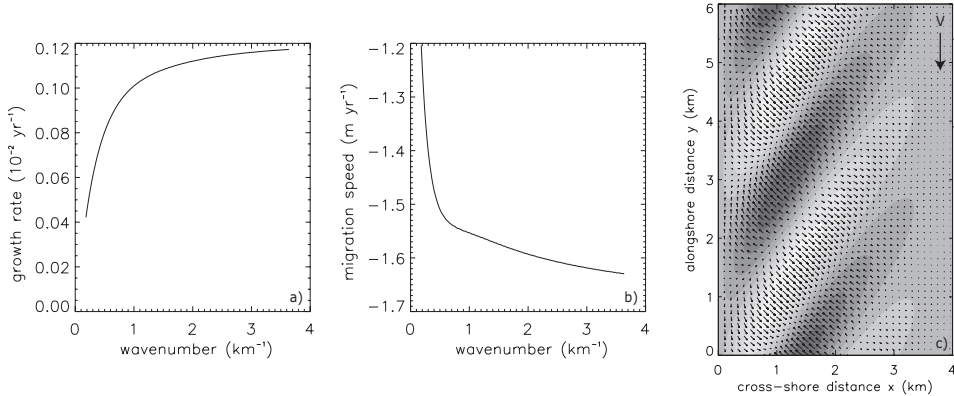


Figure 1.7: Growth rates (a) and migration speeds (b) as a function of the longshore wavenumber as obtained with the model of *Trowbridge* (1995). (c) Bottom pattern (grayscale; light: crests, dark: troughs) and perturbations (small arrows) in basic longshore velocity field (in the direction of the thick arrow) for a longshore wavenumber $k = 1.8 \text{ km}^{-1}$.

The influence of tides on the formation of sfcf was investigated by *Calvete et al.* (2001b). In contrast to e.g. the micro-tidal American shelf, along the Dutch and German coasts strong tidal currents occur. As a consequence, even during fair weather conditions bottom stresses are sufficiently strong to erode and transport sediment particles. It was demonstrated that depending on the actual tidal conditions, the intensity of the storm-driven current and the fraction of time during which storms prevail either sfcf, tidal sand ridges or a combination of these features are formed.

One drawback of the studies mentioned so far is that the ratio of time scales related to growth and migration of the bedforms is not in accordance with field data. This is e.g. visible in Figure 1.7, where the migration speed has the right order of magnitude, but the growth rate is very small. Another drawback is the sensitivity of the instability mechanism to the cross-shore profile of the storm-driven current. Realistic sfcf are only obtained for a pressure-driven longshore flow. Field data (*Lentz et al.*, 1999) however indicate that the forcing of currents by a longshore wind stress is of more importance.

Calvete et al. (2001a) argued that these artefacts were due to the neglect of suspended load transport and spatial variations in stirring of sediment by waves. In their model suspended load sediment transport is calculated by solving the concentration equation including formulations for entrainment and settling of sediment. Furthermore, the profile of the storm-driven flow follows from a balance between forces due to the longshore pressure gradient, wind stress and bottom friction. The results of their model, which accounts for the processes mentioned above, compare favorably well with field data (concerning both growth and migration

of the ridges). Moreover, the results are only weakly sensitive to the profile of the storm-driven flow. Their model indicates that growth of sfcr is mainly controlled by suspended load transport, whilst sfcr migrate predominantly due to bedload transport.

In *Walgreen et al. (2002)* it was investigated under what conditions sfcr and tidal sand ridges occur simultaneously, as is the case in the southern North Sea. They showed that the dynamics during storms and fair weather differs strongly and different types of bedforms develop. Both types of bedforms can emerge when both steady and tidal currents are present (with a strong steady component during storms) and storms occur during $\sim 2 - 8\%$ of the time. In the North Sea these conditions prevail.

Calvete et al. (2002) and *Calvete and De Swart (2003)* investigated the long-term dynamics of sfcr by expanding the flow and bottom perturbations in a truncated series of eigenmodes. The result is a set of equations describing the time evolution of the amplitudes. *Calvete and De Swart (2003)* showed that after the initial growth stage ridge profiles become asymmetric and reach a finite height. Their results also indicated that adding subharmonic modes (i.e., eigenmodes with wavelengths being larger than that of the most preferred mode) strongly influences the transient behavior of sfcr. Furthermore, subharmonic modes are excited in such a way that the dominant mode in the saturated state has a larger wavelength than that of the initially fastest growing mode.

As was already mentioned in section 1.3, field data of sfcr show a persistent spatial variation of mean grain size over the bedforms. *Walgreen et al. (2003)* developed and analyzed a model to investigate the physical mechanisms, which cause the observed grain size distribution and the effect of sediment sorting on the initial growth of sfcr. The study was done for a bimodal sediment mixture. Results indicate that the bimodal character of the sediment causes the growth rate of the most preferred mode to decrease and its spacing and migration speed to increase. The model also shows that the coarse (fine) sediment is found on the up-current (down-current) flank, which is in reasonable agreement with observations.

1.8 RESEARCH QUESTIONS AND APPROACH

Although all models that were discussed in the previous section have led to considerable insight in the dynamics of sfcr, they suffer from a serious drawback: they all use a strongly simplified description of waves in calculating sediment stirring. In the model of *Trowbridge (1995)* sediment stirring is assumed to be a constant. In all the other models sediment stirring is only dependent on the undisturbed longshore-averaged water depth such that stirring of sediment by waves increases into shallow water (inversely proportional to the water depth).

In all chapters of this thesis wave variables are explicitly calculated by using linear wave theory. Thus, processes like shoaling and refraction are explicitly accounted for. Stirring of sediment by waves is related to the amplitude of the near-bed wave orbital velocity in the basic state. New is that the sensitivity of results with respect to the period, height and direction of the waves can be investigated. An extra new aspect in chapter 3 is the research into the patch behavior of sfcr. In chapters 2 and 3 stirring of sediment by waves is not affected

by the presence of bedforms. In a recent study by *Calvete et al.* (2005) a sophisticated wave transformation model, based on phase-averaged equations for wave frequency, wavevector and wave height, was used to study the initial formation of sand bars in the surf zone under normal wave incidence. They showed that explicit modeling of wave-bedform interactions is crucial for obtaining good agreement between model results and field data. Therefore, in chapters 4 and 5 stirring of sediment due to wave orbital motions induced by bedforms is also taken into account. Moreover, in chapter 5 the effect of a bimodal sediment mixture on the growth and migration of sfcf together with the distribution of the mean grain size over sfcf is studied. In previous work on sfcf gradients in the mean grain size in the basic state were not considered, whereas in general, going seaward, the mean grain size becomes finer. According to a study by *Murray and Thieler* (2004) on sorted bedforms, it is important to include the dependency of sediment entrainment on bottom roughness. The above-mentioned two subjects, together with settling lag effects in the concentration equation, are also investigated in chapter 5. The specific research questions are:

1. What is the influence of replacing a crude by a more physics-based formulation for stirring of sediment by waves (which accounts for shoaling and refraction processes) on the initial growth, migration and shape of sfcf? And which physical mechanisms are responsible for the growth and migration of sfcf?
2. What is the influence of replacing a crude by a more physics-based formulation for stirring of sediment by waves on the long-term evolution of sfcf? Which physical processes control the migration, saturation behavior and spatial pattern of the bedforms? And what is the sensitivity of the results to the amount of modes considered, including modes that have a larger wavelength than that of the initially most preferred mode?
3. How do waves interact with bedforms growing on the seabed and what is the influence of wave-bedform interactions on the initial growth rate, migration speed and spatial characteristics of sfcf? Furthermore, which physical mechanisms are responsible for the growth and migration of sfcf in this case?
4. To what extent do wave-bedform interactions, settling lag effects, a spatially nonuniform mean grain size and dependence of sediment entrainment on bottom roughness determine the initial growth rate, migration speed and shape of sfcf together with the grain size sorting over sfcf? And what is the effect of sediment sorting on the growth and migration of sfcf?

To find answers to the research questions given above, idealized process-based models are used and applied to the micro-tidal shelf of Long Island (USA). The Long Island shelf is chosen since complicating tidal currents are only of minor importance at this location. Furthermore, a large amount of field data is available for this shelf. Idealized models are characterized by a simplified geometry and only processes are retained that are expected to be crucial for the phenomenon studied. These kind of models are used, because they allow for a systematic mathematical and physical analysis. The actual mechanisms that are crucial for the morphodynamic behavior of sfcf can thus be unraveled. Complex models on the other hand are able to deal with more realistic settings, but have to be solved numerically and their results are more difficult to interpret.

Chapter 2 deals with the first research question by studying the stability properties of an erodible inner shelf, which is forced by a longshore storm-driven current and shoaling and refracting waves. The model used is an extension of the model by *Calvete et al.* (2001b) in that wave variables and in particular the near-bed wave orbital motion (which determines stirring of sediment from the bed) are calculated with a shoaling-refraction model instead of using a parameterization. A linear stability analysis is applied to investigate the initial growth of eigenmodes (representing sfcf), which result from inherent feedbacks between the erodible bed and the water motion.

Chapter 3 is a nonlinear extension to the work discussed in chapter 2 and deals with the second research question. The full system of nonlinear equations is solved to study the evolution of sfcf in time and their saturated state. Eigenmodes of the linear system (chapter 2) are used as expansion modes in the nonlinear analysis. Specific emphasis is placed on the role of subharmonic modes (modes that have longer wavelength than the initially most preferred mode). Physical processes are analyzed by using an analysis of the potential energy balance of the bedforms: considering production terms and dissipation terms. The analysis is similar to the one used by *Garnier et al.* (2006). A new variable that is considered here is the instantaneous global longshore migration speed.

In chapter 4, which deals with the third research question, stirring of sediment by waves depends on the actual depth, rather than on the longshore-averaged depth. The latter introduces processes like bedform-induced wave shoaling and refraction. Also the effect of critical shear-stresses for erosion of sediment is investigated in the context of this model. A thorough analysis is performed of physical mechanisms, which determine initial temporal and spatial characteristics of sfcf.

The last research question is addressed in chapter 5. There, a coupling is made between the models of *Walgreen et al.* (2003) and the model used in chapter 4, i.e., the effects of wave-bedform interactions and grain sorting can be investigated simultaneously. At the end, in chapter 6 a summary is given of the results in this thesis. A discussion on these results is also presented, together with suggestions for further research.

CHAPTER 2

INITIAL FORMATION OF SHOREFACE-CONNECTED SAND RIDGES: ROLE OF WAVES

ABSTRACT

The initial evolution of shoreface-connected sand ridges (hereafter abbreviated as sfc_r) is investigated with a morphodynamic model, which governs the behavior of waves, currents, sediment transport and the bed level on the inner shelf. The currents are described by the depth-averaged shallow water equations and forced by wind. Transport of sediment is the result of the joint action of stirring of sediment by waves and its subsequent transport by currents. New is that wave variables are calculated with a shoaling-refraction model instead of using a parameterization. A linear stability analysis is applied to investigate the initial growth of eigenmodes (representing ridges), which result from inherent feedbacks between the erodible bed and the water motion. Model simulations show that a necessary condition for growth of sfc_r is that the transverse bottom slope of the inner shelf exceeds a critical value. This critical bottom slope is larger for larger offshore angles of wave incidence, for higher waves and for low-frequency waves. Once the critical bed slope is exceeded, bedforms will evolve of which the characteristic length scale, growth time and migration speed depend on the offshore wave conditions. The alongshore spacing of the most preferred mode increases if either the offshore angle of wave incidence (measured with respect to the shore-normal), the wave height or wave period become larger. The growth rate of sfc_r is smallest for high-angle, high-amplitude and low-frequency waves. The migration speed of sfc_r hardly changes if the offshore angle of wave incidence is varied. But it exhibits a maximum for an offshore wave height of about 1.8 m and is largest for low-frequency waves. The model results are explained in terms of physical mechanisms. *

*Parts of the results in this chapter were published in the paper entitled *Finite amplitude dynamics of shoreface-connected ridges: role of waves*, by N.C. Vis-Star, H.E. de Swart and D. Calvete (2008), Proc. of the 5th IAHR symposium on River, Coastal and Estuarine Morphodynamics (eds. C. M. Dohmen-Janssen & S. J. M. H. Hulscher), vol. 2, pp. 691-698, Taylor & Francis.

2.1 INTRODUCTION

Field data collected at various storm-dominated inner shelves of coastal seas (depths between 5 – 30 m) reveal the presence of patches of large-scale sfc (Swift and Field, 1981; Harrison *et al.*, 2003, and references herein). Typically, a patch consists of 4 – 8 sfc, where the latter have heights of several meters and are spaced several kilometers apart. Sfc have an oblique orientation such that their seaward ends are shifted in the dominant direction of the storm-driven flow. Another characteristic is the downstream migration of sfc with several meters per year. As sfc seem to affect the stability of the beach (Van de Meene and Van Rijn, 2000), gaining more fundamental understanding about their dynamics is relevant for coastal zone management purposes.

Several studies focused on gaining fundamental understanding about the initial growth of sfc (see chapter 1 for a more extensive review). Trowbridge (1995) demonstrated that sfc can grow due to feedbacks between the waves (which stir sediment from the bottom), the storm-driven current (which transports the sediment) and the sandy bottom. Falqués *et al.* (1999) and Calvete *et al.* (2001a) extended his model by including Coriolis terms, bottom shear-stresses, sediment transport due to bottom slopes, suspended load sediment transport and spatial variations in stirring of sediment by waves. Improvements with respect to the Trowbridge model were 1) the occurrence of a preferred mode and 2) the results are hardly sensitive to the cross-shore profile of the storm-driven current. Furthermore, in the study by Calvete *et al.* (2001a) both growth rate and migration speed are in agreement with field data.

In this chapter a new linear model will be discussed in which wave properties follow from applying physical principles. Thus, processes like shoaling and refraction are explicitly accounted for. The objective of the present work is to analyze the initial behavior of sfc in dependence of offshore wave characteristics and the transverse bottom slope of the inner shelf. The model also provides essential information for a subsequent model, discussed in chapter 3, that focuses on the long-term behavior of sfc.

This chapter is organized as follows. The model formulation is presented in section 2.2. The method of analysis follows in section 2.3 and continues in section 2.4 with a presentation of the results. In section 2.5 results are interpreted in terms of physical mechanisms, followed by a discussion on model limitations and a comparison with field observations. Finally, the conclusions are given in section 2.6.

2.2 MODEL FORMULATION

2.2.1 SHELF GEOMETRY

The reference geometry (see Figure 2.1) is similar as that used in previous studies. It represents an inner shelf, which is, in the cross-shore direction x , bounded by the shoreface at its shallow side ($x = 0$) and by the outer shelf at its deeper part ($x = L_s$). The inner shelf is unbounded in the longshore direction y . The z -axis is directed vertically upward and $z = 0$

represents the still water level. The longshore- and time-averaged bottom depths at $x = 0$ and $x = L_s$ are H_0 and H_s , respectively. The inner shelf has a linear transverse bottom slope $\beta = (H_s - H_0)/L_s$ and the outer shelf is represented by a horizontal bottom. In the absence of bedforms, the bottom profile is longshore uniform. For example, typical values for the Long Island inner shelf are $H_0 \sim 14$ m, $H_s \sim 20$ m and $L_s \sim 5.5$ km.

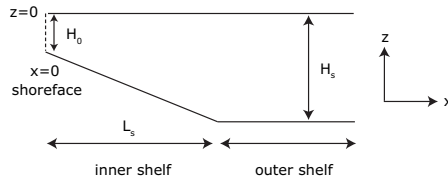


Figure 2.1: Side view of a typical longshore- and time-averaged bottom topography of the continental shelf, representing the inner and outer shelf, in the shore-normal direction. Symbols are explained in the text.

2.2.2 GENERAL CONSIDERATIONS

The ridges we are interested in mainly develop during storms. Strong winds generate large waves, which stir the sediment from the bottom. Subsequently, the sediment particles are transported by the storm-induced longshore current. Under fair weather conditions it is assumed that the bottom shear-stress is smaller than the critical stress for erosion of sediment particles from the seabed. Hence, the model used is representative for stormy conditions, which prevail during a certain time fraction (about 5%).

The water motion comprises waves (time scale ~ 10 s) and currents (time scale \sim days). The time scale on which the morphology evolves is much longer: in the order of decades to centuries.

2.2.3 HYDRODYNAMICS

WAVES

The wave transformation model is based on linear wave theory. This holds if waves have a small steepness and amplitudes, which are much smaller than the water depth. For waves (wind and swell) and water depths (inner shelf region) we are considering, this will generally be the case.

Wind-generated waves usually show randomly varying wave heights, periods and directions. *Longuet-Higgins* (1952) discussed the statistical properties of waves characterized by a narrow band of frequencies and orientations. The narrow spectrum is centered around a peak frequency, wavenumber and wave orientation. Locally, a realization of the free surface elevation ζ (measured with respect to the mean water level $z = z_s$) is described by

$$\zeta = \frac{\mathcal{H}}{2} \cos \Phi, \quad \Phi = \kappa_x x + \kappa_y y - \omega t. \quad (2.1)$$

Here, Φ is the wave phase, whilst the wave height \mathcal{H} is random and described by a Rayleigh distribution. Furthermore, $\kappa_x = -\kappa \cos \theta$ and $\kappa_y = \kappa \sin \theta$ are the x - and y -component of the wavevector $\vec{\kappa}$ and κ is the wavenumber. The peak frequency associated with the random wave field is ω and θ is the angle of wave incidence measured with respect to the shore-normal (clockwise deviation with respect to the shore-normal means positive θ and vice versa, see Figure 2.2). Finally, t is time.

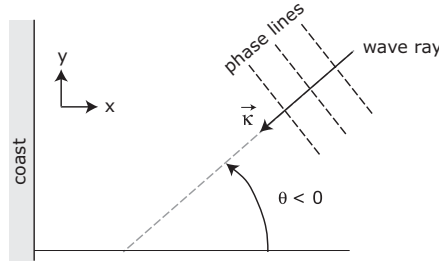


Figure 2.2: Definition of the angle of wave incidence θ . It is measured with respect to the shore-normal. Clockwise (anti-clockwise) deviation with respect to the shore-normal means positive (negative) θ .

The probability density distribution of values \mathcal{H}' attained by the wave height reads

$$P(\mathcal{H}') = \frac{2\mathcal{H}'}{\mathcal{H}_{rms}^2} e^{-(\mathcal{H}'/\mathcal{H}_{rms})^2}, \quad (2.2)$$

with \mathcal{H}_{rms} the root-mean-square wave height. The wave energy density \mathcal{E} (per surface area) of a random wave field is defined as

$$\mathcal{E} = \rho g \langle \zeta^2 \rangle = \frac{1}{8} \rho g \mathcal{H}_{rms}^2. \quad (2.3)$$

Here, ρ is the water density, g is the gravitational acceleration and the brackets $\langle \rangle$ denote a time average over several wave periods and integration over all possible wave heights. Below, equations are discussed that govern the behavior of κ , θ , ω and \mathcal{E} , which are allowed to vary slowly in space and time. Considering the definition for the wave phase Φ in equation (2.1), the latter implies that locally

$$\vec{\kappa} = (\kappa_x, \kappa_y) = \left(\frac{\partial \Phi}{\partial x}, \frac{\partial \Phi}{\partial y} \right), \quad \omega = -\frac{\partial \Phi}{\partial t}. \quad (2.4)$$

From this follows the law of conservation of wave crests:

$$\frac{\partial \vec{\kappa}}{\partial t} + \vec{\nabla} \omega = 0, \quad (2.5)$$

which shows that the change in the number of wave crests in a certain domain is determined by the difference between incoming and outgoing waves through the boundaries. Here, $\vec{\nabla}$

is the two-dimensional (horizontal) nabla vector with components $\frac{\partial}{\partial x}$ and $\frac{\partial}{\partial y}$ in the x - and y -direction, respectively. The frequency of gravity waves is related to wavenumber κ by the dispersion relation

$$\omega^2 = g\kappa \tanh(\kappa D). \quad (2.6)$$

The wavenumber is the length of the wavevector, $\kappa = (\kappa_x^2 + \kappa_y^2)^{1/2}$, and D is the water depth (averaged over many waves). Refraction of waves by currents, causing a Doppler shift in frequency, is neglected here. This can be justified by assuming that the typical phase speed of the waves is much larger than the current velocity. The angle of wave incidence is governed by the wavenumber identity relation:

$$\frac{\partial}{\partial y} (\kappa \cos \theta) + \frac{\partial}{\partial x} (\kappa \sin \theta) = 0. \quad (2.7)$$

Finally, the wave energy density is governed by the wave energy balance:

$$\frac{\partial \mathcal{E}}{\partial t} + \vec{\nabla} \cdot (\vec{c}_g \mathcal{E}) = \mathcal{F} - \mathcal{D}. \quad (2.8)$$

As in relation (2.6), refraction of waves by currents is neglected. Also, wave diffraction is not considered. The group velocity vector of the waves \vec{c}_g has amplitude c_g and components $c_{gx} = -c_g \cos \theta$ and $c_{gy} = c_g \sin \theta$. Its magnitude c_g is

$$c_g = \frac{\partial \omega}{\partial \kappa} = \frac{\omega}{2\kappa} \left(1 + \frac{2\kappa D}{\sinh(2\kappa D)} \right). \quad (2.9)$$

The two terms on the right-hand side of equation (2.8) are the source of energy provided by wind forcing \mathcal{F} and the energy dissipation \mathcal{D} , respectively. Dissipation can be the consequence of different processes, e.g. bottom friction, whitecapping and wave breaking. In the inner shelf region the dissipation is dominated by bottom friction. The formulation for the dissipation of wave energy used in this study is (adopted from *Komen et al.*, 1994):

$$\mathcal{D} = \frac{2c_f \kappa u_{rms} \mathcal{E}}{\sinh(2\kappa D)}. \quad (2.10)$$

Here, c_f is the bottom drag coefficient and

$$u_{rms} = \frac{\omega \mathcal{H}_{rms}}{2 \sinh(\kappa D)} \text{ (hereafter written as } u_w), \quad (2.11)$$

is the root-mean-square amplitude of the near-bed wave orbital velocity (hereafter called wave orbital velocity). It is assumed that dissipation and generation of wave energy cancel on the outer shelf, hence $\mathcal{F} = \mathcal{D}|_{x=L_s}$. This implies that wave properties do not change on the outer shelf.

As boundary conditions the offshore root-mean-square wave height, wave period ($T = 2\pi/\omega$) and offshore angle of wave incidence are imposed. The transformation of wave properties across the inner shelf domain is determined by equations (2.5)-(2.11).

CURRENTS

Let \vec{v} denote the depth- and wave-averaged flow velocity with components u and v in the x - and y -direction, respectively. The depth- and wave-averaged shallow water equations (representative for stormy conditions) are assumed to govern the large-scale currents and read

$$\frac{\partial \vec{v}}{\partial t} + (\vec{v} \cdot \vec{\nabla}) \vec{v} + f \vec{e}_z \times \vec{v} = -g \vec{\nabla} z_s + \frac{\vec{\tau}_s - \vec{\tau}_b}{\rho D}, \quad (2.12)$$

$$\frac{\partial D}{\partial t} + \vec{\nabla} \cdot (D \vec{v}) = 0. \quad (2.13)$$

Here, f is the Coriolis parameter, \vec{e}_z is a unit vector in the vertical direction, $D = z_s - z_b$ is the water depth and $\vec{\tau}_s$ and $\vec{\tau}_b$ represent the wind stress and bed shear-stress. In the definition for the water depth, z_s and z_b are the free surface elevation and the bottom depth, both measured with respect to the undisturbed water level $z = 0$. The effects of waves on currents through the transfer of net mass (wave-asymmetry) and net momentum (wave-induced radiation stresses) are neglected here, as is tidal forcing of currents. The model simplifications are further discussed in section 2.5.2.

The mean alongshore wind stress τ_{sy} , which is assumed to be constant, drives a longshore flow. An expression for the mean bed shear-stress $\vec{\tau}_b$ is derived from the law, which states that the instantaneous bed shear-stress depends quadratically on the instantaneous velocity (which comprises waves and currents). During storms the amplitude of the wave orbital velocity is much larger than the magnitude of the storm-induced current. Assuming waves and currents to be near-parallel, it follows that the mean bed shear-stress becomes linear in the current:

$$\vec{\tau}_b = \rho r u_w \vec{v}, \quad (2.14)$$

where r is a dimensionless friction coefficient computed for random waves. The latter is a factor $\sqrt{\pi}/2$ smaller compared to the case of monochromatic waves and is defined in appendix 2.A. Note the difference with the friction coefficient of *Calvete et al.* (2001a): their $r_c = r u_w$. Moreover, in equation (2.14), u_w is the wave orbital velocity as defined in the first part of this section. A more sophisticated formulation for the bed shear-stress, which accounts for the possibility of a net bed shear-stress to act in a different direction than the net current, is also discussed in appendix 2.A and will be considered later on.

The boundary conditions are that the cross-shore flow component u vanishes at $x = 0$ and far offshore. The bed level z_b has a fixed level at these two locations.

2.2.4 BED EVOLUTION AND SEDIMENT TRANSPORT

Conservation of sediment mass yields the bed evolution equation

$$(1 - p) \frac{\partial z_b}{\partial t} + \vec{\nabla} \cdot \vec{q}_b + \vec{\nabla} \cdot \vec{q}_s = 0, \quad (2.15)$$

where p is the porosity of the bed and \vec{q}_b and \vec{q}_s denote the wave-averaged volumetric sediment transport per unit width as bedload and suspended load, respectively. Here, it is assumed

that the seabed consists of noncohesive sediment with a uniform size. In case of bedload transport sediment grains move in more or less continuous contact with the bed, by rolling, sliding or saltation. When particles are small and the bed shear-stress is large, part of the sediment goes into suspension. The interaction between individual grains is lost and the particles are transported without having any contact with the bed (suspended load transport). Field observations analyzed by *Green et al. (1995)* revealed that during storms large amounts of sand are transported as suspended load. *Calvete et al. (2001a)* argued that both types of transport must be included in the sediment transport formulation to correctly describe the growth and migration of sfc. Therefore, in this chapter both bedload and suspended load transport are considered. Formulations for these transports are given below.

BEDLOAD

The formulation of *Bailard (1981)* is used to derive an expression for the bedload transport of sediment. Under stormy conditions and for waves and the storm-driven current being almost parallel, it becomes:

$$\vec{q}_b = \frac{3}{2} \nu_b u_w^2 \left(\vec{v} - \lambda_b u_w \vec{\nabla} z_b \right). \quad (2.16)$$

The coefficient ν_b depends on sediment properties and λ_b is the bed slope parameter, which is related to the angle of repose of the sediment. A more general formulation for equation (2.16), which accounts for the possibility of a net bedload sediment transport that is in a different direction than the net longshore current, is discussed in appendix 2.A. Note that effects of critical shear-stresses for erosion are ignored, i.e., it is assumed that grains will start to move as soon as a shear-stress is exerted. Coefficient λ_b is a factor $3\sqrt{\pi}/4$ larger compared to the case of monochromatic waves. The first contribution to \vec{q}_b represents the net sediment transport due to a stirring of sediment by waves and the subsequent transport by the net current. The second contribution accounts for gravitational effects on sediment grains in the bedload layer. Hereafter, the first contribution is called the current-induced sediment transport (denoted as $\vec{q}_{b,a}$) and the second the bed slope-induced sediment transport (denoted as $\vec{q}_{b,d}$).

SUSPENDED LOAD

The wave-averaged suspended load sediment transport is a modified version of the formulation proposed by *Bailard (1981)* and reads

$$\vec{q}_s = C \vec{v} - \lambda_s u_w^5 \vec{\nabla} z_b. \quad (2.17)$$

Here, C is the depth-integrated volumetric concentration of sediment and λ_s is the bed slope parameter for suspended sediment. The latter is a factor $15\sqrt{\pi}/8$ larger compared to the case of monochromatic waves. Also \vec{q}_s consists of a current-induced contribution $\vec{q}_{s,a} = C \vec{v}$ and a bed slope-induced contribution $\vec{q}_{s,d} = -\lambda_s u_w^5 \vec{\nabla} z_b$. To compute the current-induced flux of suspended sediment a concentration equation is used, which describes the depth-integrated concentration of sediment C ,

$$\frac{\partial C}{\partial t} + \vec{\nabla} \cdot (C \vec{v}) = \alpha u_w^3 - \gamma \frac{C}{D}. \quad (2.18)$$

The second term on the left-hand side accounts for settling lag effects, i.e., it takes time for sediment to reach the bottom when the decreasing current cannot maintain it in suspension. Thus, settling occurs at some distance from the location where sediment has been entrained. The first term on the right-hand side describes erosion of sand and the second term sediment deposition. Here, α and γ are known coefficients and α is a factor $3\sqrt{\pi}/4$ larger compared to the case of monochromatic waves. The corresponding boundary condition is that the concentration vanishes far from the coast.

2.2.5 ADDITIONAL ASSUMPTIONS

The model formulation can be further simplified. As sfc evolve on a time scale (decades to centuries), which is long compared to that of hydrodynamic processes (seconds to weeks), the quasi-steady hypothesis is used: time derivatives in equations (2.5), (2.8), (2.12)-(2.13) and (2.18) are neglected. Physically, this means that the water motion adjusts instantly to a new bed level. Application of the quasi-steady approach to equation (2.5) implies that the wave frequency ω is a constant (given by the boundary condition). Furthermore, the rigid-lid approximation is used, which is justified by the fact that the velocity of water particles is small with respect to the phase speed of gravity waves (small Froude number). As the free surface elevation is much smaller than the undisturbed water depth in this case, the local depth can be approximated by $D \simeq \tilde{D} = -z_b$ in all equations.

2.3 METHOD OF ANALYSIS

Following *Trowbridge* (1995) and others it is assumed that sfc develop as free instabilities of a steady longshore uniform basic state. The latter describes incoming waves and a storm-driven current on an inner shelf with a plane slope and a sandy bottom (sfc are not yet present). The initial growth of morphodynamic features is investigated by performing a linear stability analysis of the basic state. As the focus is on the initial growth of bed features, the governing equations are linearized, which means that only terms that are proportional to the amplitude of the perturbations are retained. The linearization procedure is outlined in section 2.3.2. The result is an eigenvalue problem, which is solved numerically using a spectral collocation method. The solution for a fixed bed level yields the perturbed wave and velocity fields, which in turn are used to calculate changes in the bed level. From here on we denote solutions of primary wave variables by $\mathcal{X} = (\kappa, \theta, \mathcal{E})$ and those of other dependent variables by $\Psi = (u, v, z_s, C, z_b)$.

2.3.1 BASIC STATE

It turns out that in case $H = H(x)$, the model allows for a basic state that is steady and alongshore uniform. Hence, $\mathcal{X} = \mathcal{X}_b(x)$ and $\Psi = \Psi_b(x)$, where we write $\mathcal{X}_b = (K, \Theta, E)$ and $\Psi_b = (U, V, \xi, C, -H)$. Thus, K , Θ and E represent the basic state wavenumber, angle of wave incidence and wave energy, respectively. Likewise, U , V , ξ , C and H represent the basic state cross-shore and longshore velocity component, free surface elevation, depth-integrated volume concentration of sediment and bottom elevation, respectively.

Now substitute $\mathcal{X} = \mathcal{X}_b$ in equations (2.6)-(2.11). It follows, as ω is constant, that equation (2.6) relates the basic state wavenumber $K(x)$ to water depth $H(x)$. This relation is transcendental in K and can be solved using a root-finding procedure. Next, equation (2.7) reduces to $K \sin \Theta = \text{constant}$, which is Snell's law. For a given angle of wave incidence $\Theta = \Theta_s$ on the outer shelf, it follows

$$\sin \Theta = \frac{K_s \sin \Theta_s}{K}. \quad (2.19)$$

Here, K_s is the wavenumber at $x = L_s$, which is known from the dispersion relation. As it is assumed that dissipation and generation of wave energy cancel on the outer shelf, wave properties do not change on the outer shelf and $K_s = K_\infty$. The basic state wave energy $E(x)$ is governed by

$$\frac{d}{dx} (-E C_g \cos \Theta) = \mathcal{F}_b - \mathcal{D}_b, \quad (2.20)$$

where C_g , \mathcal{F}_b and \mathcal{D}_b are obtained from equations (2.9)-(2.11) by substitution of basic state variables. As boundary condition the wave energy $E = E_s$ (or equivalently, $H_{rms,s}$) on the outer shelf is prescribed. In fact, E_s is equal to the wave energy far offshore, as wave properties do not change on the outer shelf in the model. The basic state wave orbital velocity $U_w(x)$ is important for calculating the basic state flow and sediment transport.

The basic state current only has a longshore component with a cross-shore gradient, i.e., $U = 0$ and $\vec{v} = (0, V(x))$. The latter follows from the continuity equation (2.13) in the basic state. Substitution in equation (2.12) yields the momentum balance of the basic state:

$$fV = g \frac{d\xi}{dx}, \quad 0 = \frac{\tau_{sy} - \tau_{by}}{\rho H}. \quad (2.21)$$

The first equation determines the cross-shore set-up or set-down of the water level due to Coriolis effects. The second equation and the linear friction law (2.14) determine the basic state alongshore velocity profile:

$$V = \frac{\tau_{sy}}{\rho r U_w}. \quad (2.22)$$

Note that the formulation for the alongshore velocity is only valid under wave-dominated conditions. The corresponding basic state depth-integrated relative volume concentration $C(x)$, follows from substitution of the basic state variables into equation (2.18) and boils down to a balance between the erosion and deposition flux near the bed,

$$C = \frac{\alpha}{\gamma} H U_w^3. \quad (2.23)$$

It follows from equations (2.16)-(2.18) that the total sediment transport in the basic state has a longshore component, which is independent of y , but a nonconstant offshore component (due to the transverse bottom slope). The latter implies that the sediment mass balance is not identically satisfied. However, the change in bed level due to divergence of this transport is much slower ($\sim 10^{-5} \text{ m yr}^{-1}$) than the change in bed level of sfcf ($\sim 10^{-2} \text{ m yr}^{-1}$), hence this effect can be neglected. Thus, to a good approximation, the basic state defines a morphodynamic equilibrium.

2.3.2 STABILITY ANALYSIS AND LINEARIZED MODEL

The stability properties of the basic state are considered by studying the dynamics of small perturbations evolving on this basic state. Hence, $\Psi = \Psi_b + \Psi'$ is substituted in equations (2.12)-(2.18). In principle, also perturbations in the wave variables have to be considered: $\mathcal{X} = \mathcal{X}_b + \mathcal{X}'$. However, similar as in previous studies, we assume $\mathcal{X}' = 0$. Physically, this means that wave-topography interactions, i.e., wave refraction and shoaling and dissipation of wave energy due to the presence of bedforms, are neglected. In chapters 4 and 5 the effect of including wave-topography interactions will be investigated.

Both \mathcal{X}_b and Ψ_b are defined in section 2.3.1. Furthermore, $\Psi'(x, y, t) = (u', v', \eta', c', h')$ denote the perturbed variables, which are assumed to have small values with respect to their basic state values. As the morphodynamic patterns, which are investigated, are naturally confined to the inner shelf, appropriate offshore boundary conditions are $\Psi' \rightarrow 0$ for $x \rightarrow \infty$. At the shoreface ($x = 0$) the boundary conditions are a vanishing cross-shore flow component ($u' = 0$) and a bottom elevation, which is fixed to its basic state value ($h' = 0$). Linearizing the equations with respect to the small perturbed variables, results in a system of linear differential equations of the type

$$\mathcal{S} \frac{\partial \Psi'}{\partial t} = \mathcal{L} \Psi', \quad (2.24)$$

where \mathcal{S} is a 5×5 matrix (containing the temporal information of the perturbations) and \mathcal{L} is a matrix operator, which are both defined in appendix 2.B. Here, it suffices to state that \mathcal{L} involves derivatives with respect to x and y and that its coefficients only depend on x . Note that use of the quasi-steady approximation implies that time derivatives of hydrodynamical variables are excluded, thus only element $\mathcal{S}(5, 5)$ of matrix \mathcal{S} is nonzero. The linearized system sustains wave-like solutions, which travel in the y -direction and of which the amplitude can grow (or decay) exponentially in time:

$$\Psi' = \Re \left\{ \hat{\psi}(x) e^{iky + \sigma t} \right\}. \quad (2.25)$$

Here, \Re denotes the real part of the solution, k the longshore wavenumber (which can be assigned any value), the hat denotes the as yet unknown cross-shore structure of the solution and σ the complex frequency. Substituting expressions (2.25) into the equations for the small perturbations yields the perturbed flow and sediment transport equations. As an example, the linearized equation for the perturbed cross-shore velocity component \hat{u} is given in appendix 2.C. The equations for the small perturbations resemble those obtained by *Calvete et al.* (2001a), except that their parameterization (2.5) for u_w is not used.

The equations, together with the specified boundary conditions, define an eigenvalue problem

$$\sigma \mathcal{S} \hat{\psi} = \mathcal{L}_k \hat{\psi}, \quad (2.26)$$

where σ are the complex eigenvalues and $\hat{\psi}$ are the eigenfunctions. The latter ones give the cross-shore structure of the perturbations. Finally, the linear matrix operator \mathcal{L}_k follows from operator \mathcal{L} , defined in equation (2.24), by replacing $\partial/\partial y$ by ik .

The growth rate and migration speed of the bottom perturbations follow from the complex frequency ($\sigma = \sigma_r + i\sigma_i$). The real part σ_r is the growth rate and the migration speed is given by $V_m = -\sigma_i/k$. If, for specific choices of the model parameters, the growth rates of all perturbations (i.e., for all k) are negative, they all decay and the basic state is stable. Conversely, if there are perturbations with positive growth rates the basic state is unstable and exponentially growing modes exist. In the latter case, the perturbation with the largest growth rate, which is attained for a specific $k = k_p$, is called the most preferred eigenmode. The basic idea of a linear stability analysis is that, starting from some random perturbation (which contains all Fourier modes), the fastest growing mode will dominate the solution after some time. The inverse of the growth rate σ_r gives a characteristic time scale for the formation in nature (called the e -folding growth time T_g). Solutions of the eigenvalue problem are obtained numerically by applying a collocation method using Chebyshev polynomials as base functions (Canuto *et al.*, 1988). Chebyshev polynomials have been successfully used in previous morphodynamic model studies (e.g. Falqués *et al.*, 1996; Ribas *et al.*, 2003; Van der Vegt *et al.*, 2007).

2.4 RESULTS

2.4.1 PARAMETER VALUES: DEFAULT CASE

Runs were performed with parameter values that are representative for the micro-tidal inner shelf of Long Island, which is located at a latitude of $\sim 40^\circ$ N. At this location the depth varies from $H_0 = 14$ m to $H_s = 20$ m over an inner shelf width of $L_s = 5.5$ km ($\beta = 1.1 \times 10^{-3}$). However, the default experiment is performed for an inner shelf slope, which is approximately 60% of its observed value. The latter is done in order to enable comparison with results concerning the saturation behavior of sfcrl as presented in chapter 3, which is only possible up to this value of β . The wind stress $\tau_{sy} = -0.4$ N m $^{-2}$, the offshore root-mean-square wave height $H_{rms,s} = 1.5$ m, the wave period $T = 11$ s and the offshore angle of wave incidence $\Theta_s = -20^\circ$. Values of the other parameters are: $r = 2.0 \times 10^{-3}$, $c_f = 3.5 \times 10^{-3}$, $\nu_b = 5.6 \times 10^{-5}$ s 2 m $^{-1}$, $\lambda_b = 0.65$, $\lambda_s = 7.5 \times 10^{-4}$ s 4 m $^{-3}$, $\alpha/\gamma = 9.5 \times 10^{-5}$ s 3 m $^{-3}$ and $p = 0.4$. These parameter values are different from the ones used by Calvete *et al.* (2001a), see section 2.5 for a discussion on this.

In section 2.4.2 results of the basic state and linear analysis are presented for the default case just described. The sensitivity of the results to offshore wave characteristics (angle of wave incidence Θ_s , wave height $H_{rms,s}$ and wave period T) and transverse bottom slope β are indicated in section 2.4.3, 2.4.4 and 2.4.5. Finally, an additional sensitivity study is performed in section 2.4.6, where the influence of the bed slope parameter for suspended load transport is investigated.

2.4.2 BASIC STATE AND LINEAR STABILITY ANALYSIS: DEFAULT CASE

In this section results are presented for the default parameter values given in the previous section. The cross-shore profiles for the basic state wave variables are shown in Figure 2.3.

A decrease in water depth causes a shortening and refraction of the waves. Wave height increases towards the shore due to decreasing group velocity. As a result, the wave orbital velocity also increases with decreasing depths and reaches an amplitude of $\sim 0.54 \text{ m s}^{-1}$ at the shoreface. The onshore increase of U_w plays an important role in the growth process of sfc (see section 2.5).

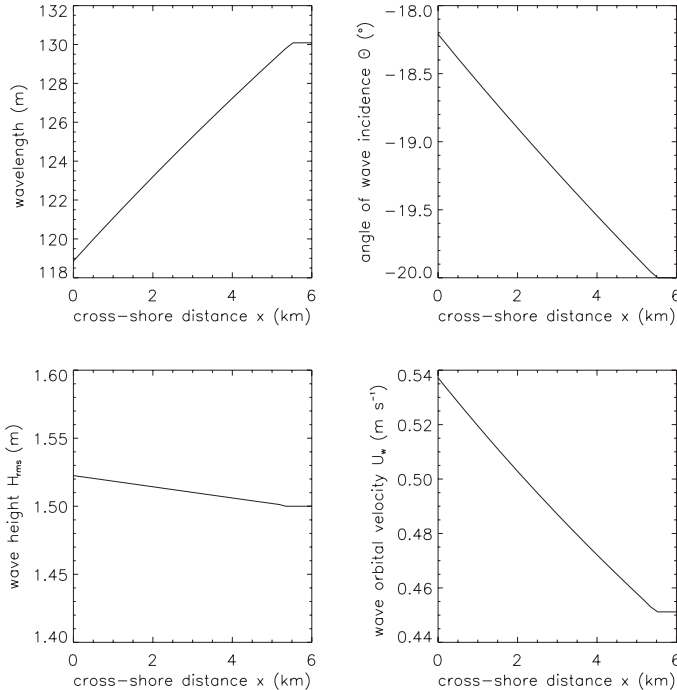


Figure 2.3: Basic state; cross-shore profiles of wavelength, angle of wave incidence, root-mean-square wave height and wave orbital velocity. Default case.

Figure 2.4 shows the cross-shore profiles of the amplitude of the longshore current and of the depth-integrated sediment concentration, which correspond to the basic state. The magnitude of the longshore current is inversely proportional to the wave orbital velocity and hence has its smallest value (of about 0.37 m s^{-1}) at the shoreface. The current is directed southward (minus sign). The depth-integrated concentration of sediment increases towards the shoreface, as the larger wave orbital motion stirs more sediment into suspension.

Figure 2.5 shows the growth rates and migration velocities of one growing mode and four decaying cross-shore modes as a function of the longshore wavenumber. The computed growth rates and migration speeds are calculated for continuous storm conditions. In reality storms only occur during a certain time fraction. For a typical 5% time fraction of storm weather, the growth rates and migration speeds would be a factor 20 smaller. For the default model set-up, a maximum growth rate is found for $k = k_p \sim 0.8 \text{ km}^{-1}$, which corresponds to a longshore

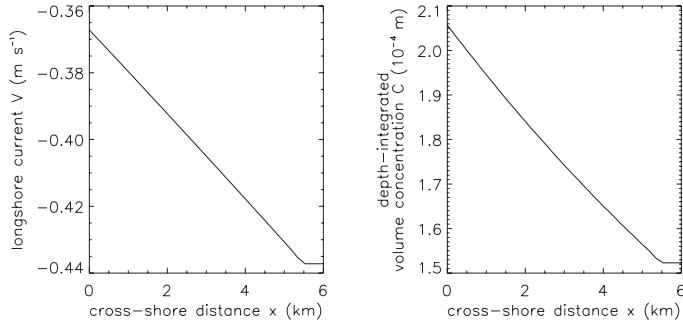


Figure 2.4: Basic state; cross-shore profiles of longshore current and depth-integrated volume concentration of sediment. Default case.

wavelength of the bedforms of $\lambda_p = 2\pi k_p^{-1} \sim 8$ km. The e -folding time $T_g = \sigma_r^{-1}$ of the growth process is approximately 165 yr. The bottom pattern of the most preferred mode is shown in Figure 2.6a and it clearly resembles up-current rotated sfc, which cover the entire width of the inner shelf. The angle between crest axis and coastline (from here on denoted as φ) is about 30° . The perturbed flow (small arrows) is deflected offshore (onshore) over the crests (troughs). It will be demonstrated later on that this deflection is an important element in the mechanism that causes growth of sfc. Sfc migrate southward in the direction of the current (indicated by the thick arrow) with a speed of 23 m yr^{-1} . Following one specific ridge, denoted by I, it will be at the position shown in Figure 2.6b after about 1 century and at the position in Figure 2.6c after approximately 2 centuries.

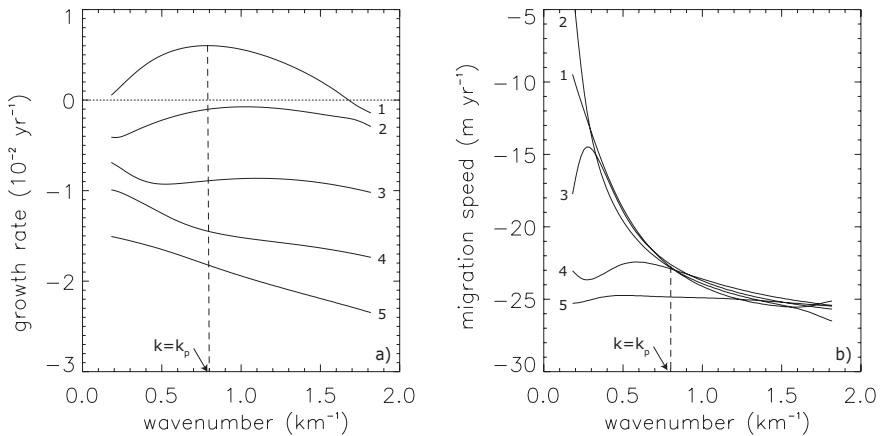


Figure 2.5: Growth rates (a) and migration velocities (b) for the first five cross-shore modes as a function of the longshore wavenumber. The most preferred mode (with wavenumber $k = k_p$) is indicated by the dashed line.

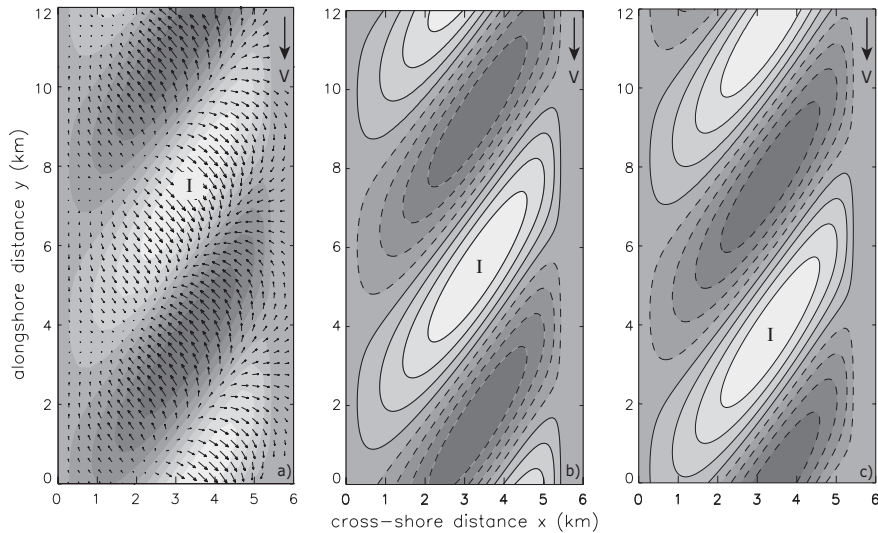


Figure 2.6: (a) Bottom pattern (grayscale; light: crests, dark: troughs) and perturbations (small arrows) in basic longshore velocity field (in the direction of the thick arrow) for the initially most preferred mode. Following one specific crest, denoted by I, migration of the bottom pattern with almost 2 km and 4 km is visible in panel (b) and (c), respectively. The time interval between the different plots is approximately 100 yr.

2.4.3 SENSITIVITY TO OFFSHORE ANGLE OF WAVE INCIDENCE AND INNER SHELF SLOPE

Sensitivity of the model results with respect to the offshore angle of wave incidence Θ_s and the transverse bottom slope of the inner shelf β are investigated in this section. Results are presented for situations ranging from an inner shelf with no slope to an inner shelf with a realistic value for the transverse slope. Here, a variation in β corresponds to a variation in H_s . All other parameters have their default values.

The cross-shore profile for the basic state wave orbital velocity U_w is shown in Figure 2.7a for different values of the transverse bottom slope of the inner shelf. It shows that for a flat inner shelf the wave orbital velocity remains constant at a value of 0.53 m s^{-1} . For a realistic transverse bottom slope, the offshore wave orbital velocity is smaller due to a larger offshore water depth. However, the onshore increase in the wave orbital velocity is quite strong due to wave shoaling. The latter process causes the wave orbital velocity to be larger than 0.53 m s^{-1} at the shoreface. Cross-shelf profiles of U_w for different offshore angles of wave incidence are shown in Figure 2.7b. The offshore wave orbital velocity is about 0.45 m s^{-1} and independent of the offshore angle of wave incidence. The increase in amplitude towards shallower depths is tempered by wave refraction, which is stronger if incident waves become more oblique. Later on it will be demonstrated that the behavior of dU_w/dx is important to understand the sensitivity of bedform growth to a change in wave characteristics.

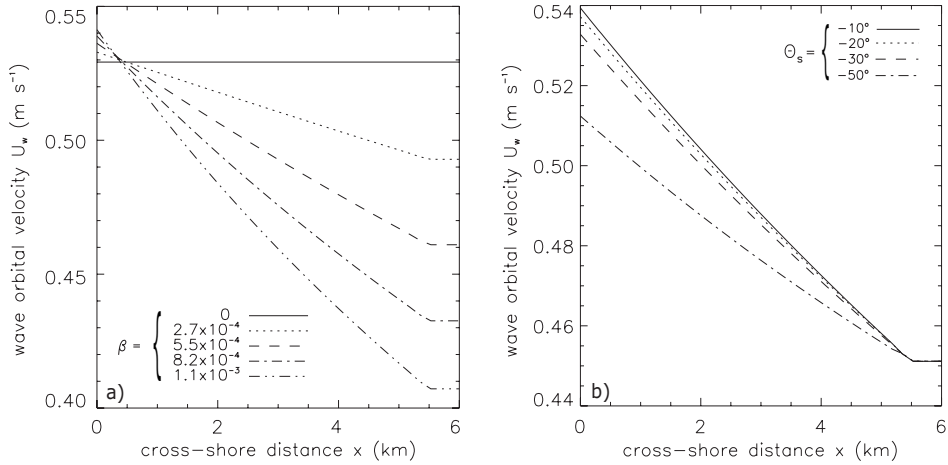


Figure 2.7: Cross-shore profiles of the wave orbital velocity in the basic state for (a) different values of the transverse bottom slope of the inner shelf and (b) different offshore angles of wave incidence.

Contour plots of the longshore spacing, growth rate and migration speed of the initially most preferred mode as a function of the transverse bottom slope of the inner shelf and the offshore angle of wave incidence are given in Figure 2.8. The results indicate that a necessary condition for growth of sfcr is that the transverse bottom slope β exceeds a critical value β_c . This critical bottom slope β_c depends on the offshore angle of wave incidence. An increase from $\Theta_s = -2^\circ$ to $\Theta_s = -50^\circ$ results in an increase in β_c from 1.8×10^{-4} to 2.7×10^{-4} , respectively. Once bedforms start to form, increasing the slope of the inner shelf leads to a decrease in the alongshore spacing of the most preferred mode. The same trend is visible for a decrease in the offshore angle of wave incidence. The growth rate of the most preferred mode

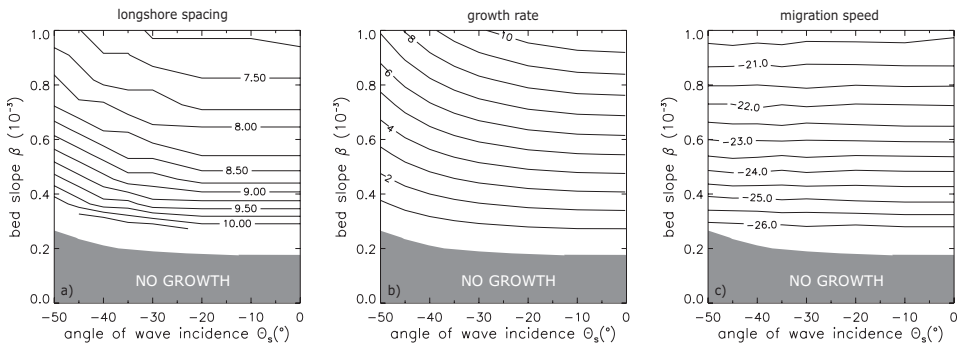


Figure 2.8: Contour plots of equal (a) longshore spacing (km), (b) growth rate (10^{-3} yr^{-1}) and (c) migration speed (m yr^{-1}) of the initially most preferred mode in the $\Theta_s - \beta$ plane.

increases with increasing β and with decreasing Θ_s . Furthermore, migration speeds slightly decrease with increasing bottom slope, while they hardly change if the offshore angle of wave incidence is varied. The sensitivity of the migration speed to the transverse bottom slope β can be approximated by $V_m/V_* = -1.0 + 330(\beta - \beta_c)$, where $\beta_c = 0.3 \times 10^{-3}$ and $V_* = 26 \text{ m yr}^{-1}$. For realistic values of the inner shelf slope and offshore angle of wave incidence the growth rate is in the order of $1.1 \times 10^{-2} \text{ yr}^{-1}$, the migration speed is about 20 m yr^{-1} and the distance between successive crests of the initially most preferred mode is about 7 km. The up-current orientation of sfcr and their cross-shore span of 5.5 km is independent of the offshore angle of wave incidence and inner shelf slope. The angle between crest axis and coastline is similar for different values of Θ_s and β .

2.4.4 SENSITIVITY TO OFFSHORE WAVE HEIGHT AND INNER SHELF SLOPE

In Figure 2.9a cross-shore profiles of U_w are shown for different offshore root-mean-square wave heights. The larger the offshore root-mean-square wave height, the larger the offshore wave orbital velocity. The onshore increase in the wave orbital velocity is stronger for higher waves due to a more intense shoaling.

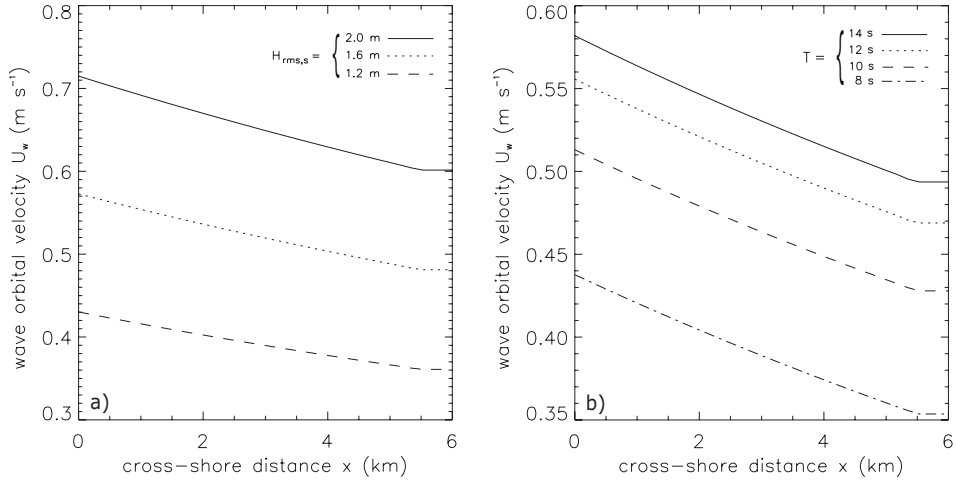


Figure 2.9: Cross-shore profiles of the wave orbital velocity in the basic state for (a) different offshore root-mean-square wave heights and (b) different wave periods.

In Figure 2.10 contour plots of longshore spacing, growth rate and migration speed of the most preferred mode in the $H_{rms,s} - \beta$ plane are shown. Note that for offshore wave heights smaller than 1.2 m, the model assumption that the wave orbital velocity is larger than the current amplitude is no longer satisfied. The longshore spacing of the most preferred mode is smaller for steeper transverse bottom slopes. The longshore spacing increases with an increase in the offshore root-mean-square wave height. The critical transverse bottom slope

increases from 1.0×10^{-4} to 4.3×10^{-4} when the offshore root-mean-square wave height is increased from 1.2 m to 2.0 m, respectively. As long as the critical inner shelf slope is exceeded, the growth rate of the bedforms increases and the migration speed decreases with increasing transverse bottom slope of the inner shelf.

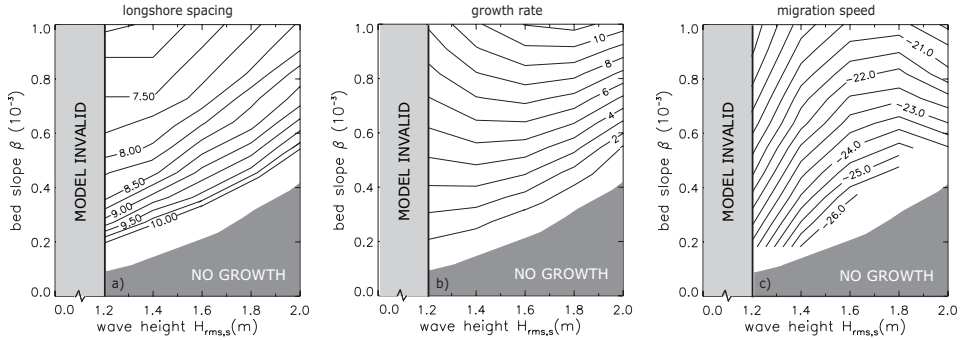


Figure 2.10: As Figure 2.8, but in the $H_{rms,s} - \beta$ plane.

The dependence of these variables on the offshore wave height is more complicated. In general, the growth rate decreases with an increase in offshore wave height. However, for offshore wave heights between 1.2 m and 1.6 m and large bed slopes an opposite trend is visible. Furthermore, it appears that for an offshore wave height of about 1.8 m the migration speed exhibits a maximum: the migration is slower for both smaller and larger offshore waves. The orientation of the bottom pattern with respect to the shoreline does not depend on the offshore wave height.

2.4.5 SENSITIVITY TO WAVE PERIOD AND INNER SHELF SLOPE

In Figure 2.9b cross-shore profiles of U_w are shown for different wave periods. These profiles illustrate that the wave orbital velocity is larger for low-frequency waves. The onshore increase in the wave orbital velocity is of the same order for low-frequency and high-frequency waves.

The dependence of the longshore spacing, growth rate and migration speed on the transverse bottom slope β and the wave period T are shown in Figure 2.11. For a wave period smaller than 8 s, the model assumption that a weak current limit is considered is no longer satisfied. The longshore spacing varies between about 7 km and 10 km and is larger for smaller transverse bottom slopes and low-frequency waves. In general, the initially most preferred mode evolves slower and migrates faster when the wave period is increased. Again, a critical bed slope has to be exceeded before growing bedforms are obtained. The bedforms cover the entire width of the inner shelf under all conditions and are up-current oriented. The angle between crest axis and coastline is $\varphi \sim 30^\circ$ for both low- and high-frequency waves.

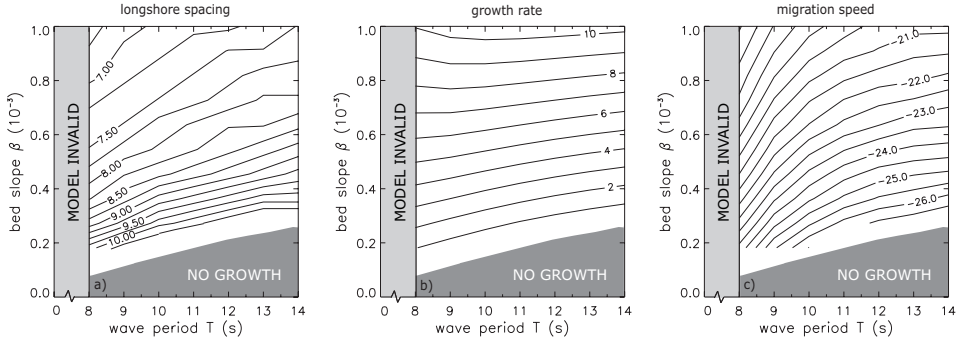


Figure 2.11: As Figure 2.8, but in the $T - \beta$ plane.

2.4.6 SENSITIVITY TO BED SLOPE PARAMETER FOR SUSPENDED SEDIMENT

Sensitivity of model results to changes in the bed slope parameter for suspended sediment λ_s is investigated (see Figure 2.12). The reason for this is the higher value used for λ_s in this study compared to former studies (see section 2.5 for a discussion on this). For a bed slope parameter, which is a factor 10 smaller than the default value, the most preferred mode obtained by the model has a smaller longshore wavelength: $\lambda \sim 6.5$ km. The e -folding time $T_g = \sigma_r^{-1}$ of the growth process decreases to become ~ 115 yr (full-storm years). The sfcr migrate southward with a slightly larger speed of 25 m yr^{-1} . Performing a run with the

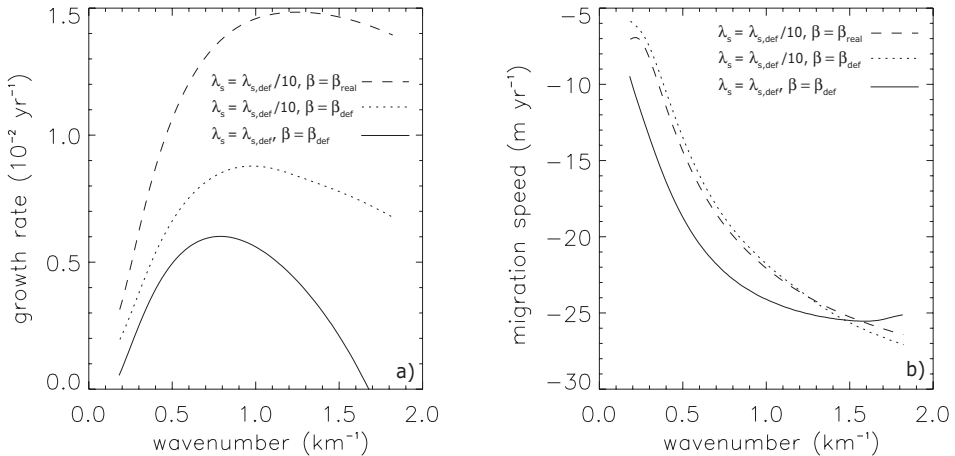


Figure 2.12: Growth rates (a) and migration velocities (b) of the most preferred mode as a function of the longshore wavenumber for the default case, a case with the bed slope parameter for suspended sediment, which is a factor 10 smaller and all other parameters default and a case with a ten times smaller λ_s and realistic inner shelf bed slope and all other parameters default.

smaller λ_s , but for the measured value of the Long Island inner shelf bottom slope results in sfcr with a spacing of 5 km, an e -folding growth time of ~ 65 yr and a migration speed of 24 m yr^{-1} . After correction for a typical 5% time fraction of stormy weather, these values are $T_g \sim 1300 \text{ yr}$ and $V_m \sim 1.2 \text{ m yr}^{-1}$.

2.5 DISCUSSION

In this section a physical interpretation is given of the results in the previous sections. The sensitivity of the evolution of sfcr to offshore wave properties and the inner shelf slope is explained, using concepts for the formation of sfcr as discussed by *Trowbridge* (1995) and by *Calvete et al.* (2001a). In addition, various model limitations are discussed and results are compared with field observations.

2.5.1 PHYSICAL INTERPRETATION

The equation governing the evolution of the bed perturbations is derived from the linearized version of the bed evolution equation (2.15), the linearized continuity equation (i.e., the third equation of system (2.B-1) in appendix 2.B, which is used to eliminate the perturbed longshore velocity v') and the linearized formulations for \vec{q}_b and \vec{q}_s in (2.16) and (2.17), respectively. In case that settling lag effects are neglected, the result is

$$\begin{aligned} \overbrace{(1-p) \frac{\partial h'}{\partial t}}^{T0} + \overbrace{\frac{3}{2} \nu_b U_w^2 V \frac{\partial h'}{\partial y}}^{T1} - \overbrace{\vec{\nabla} \cdot (\lambda_{bs} \vec{\nabla} h')}^{T2} = \\ - \overbrace{\frac{d}{dx} \left(\frac{3}{2} \nu_b \frac{U_w^2}{H} \right) H u'}^{T3} - \overbrace{\frac{d}{dx} \left(\frac{C}{H} \right) H u'}^{T4}, \end{aligned} \quad (2.27)$$

where $\lambda_{bs} = (3/2)\nu_b\lambda_b U_w^3 + \lambda_s U_w^5$. In the bed evolution equation (2.27), term T0 represents the growth or decay of bedforms. Bedforms grow (decay) if $\partial h'/\partial t > 0$ ($\partial h'/\partial t < 0$) above the crests. Term T1 describes the alongshore migration of the bed perturbations due to bedload transport of sediment, whereas term T2 is a consequence of the downslope sediment transport and causes diffusion of bedforms.

The different sources of instability are given by the two terms on the right-hand side of the bed evolution equation. First consider term T3 in the specific case of $(3/2)\nu_b U_w^2 \rightarrow K_{stir} = \text{constant}$, which is the case discussed by *Trowbridge* (1995). Clearly, this term $\neq 0$ if the transverse bottom slope $dH/dx = \beta \neq 0$. For $\beta > 0$ sfcr grow if u' and h' are positively correlated, i.e., the current should exhibit an offshore deflection over the crests. As u' decreases seaward, due to the increase in water depth, the current is convergent. As here sediment transport is linearly related to the current, deposition of sediment occurs on top of the crests and sfcr will grow. An obliquely oriented ridge can induce a deflection of the longshore current as a consequence of water mass continuity, which causes an increase in the cross-bank component of the flow over the crest. Only for up-current oriented sfcr the deflection

in the current is directed offshore above its crest, thus only up-current rotated sfcr will grow. The offshore current deflection over sfcr is obtained with the model and visible in Figure 2.6a.

A more general case is considered by *Calvete et al.* (2001a), who consider term T3 and T4 in equation (2.27), where U_w now depends explicitly on H and $C \sim HU_w^3$ (see equation (2.23)). They argue that stirring of sediment by waves increases towards the coast, which is an additional source of sediment deposition over the crests and thus growth is enhanced. More generally, sfcr grow if the cross-shore gradient of the depth-averaged volumetric sediment concentration in the basic state is negative. The latter quantity is defined as $\frac{d(C/H)}{dx}$, thus U_w^3 should decrease with increasing distance from the coast. It appears that term T4 is dominant over term T3. A sketch of the Trowbridge and Calvete mechanisms is given in Figure 2.13. The offshore deflection of the longshore current over an up-current oriented ridge is illustrated in the top view in Figure 2.13a. The cross-section through the ridge in Figure 2.13b shows (1) a convergence of the flow as it enters deeper water and (2) a decrease in the wave orbital velocity into deeper water. As a consequence, sediment transport converges and sediment is deposited on the crests. The convergence is most effective on the downstream side of the ridge, again due to flow convergence, which explains the downstream migration of the bedforms.

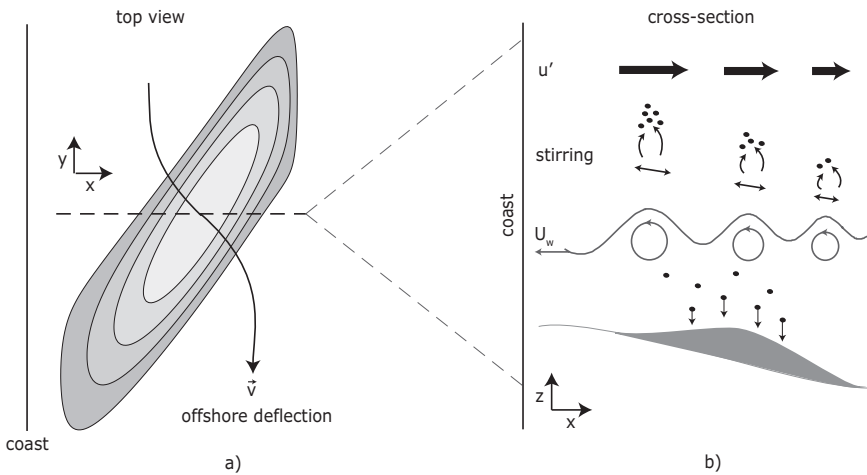


Figure 2.13: Schematic view of the Trowbridge and Calvete mechanisms. (a) An up-current rotated ridge causes an offshore deflection of the current. (b) Flow converges when it enters deeper water, which causes sediment convergence over the ridge. This effect is enhanced by nonuniform wave stirring: stirring of sediment by waves is stronger in shallow water compared to deep water and thus also causes convergence of sediment over the ridge.

Sensitivity of the model results (longshore spacing, growth rate and migration speed) to offshore wave characteristics can be understood by considering the magnitude of the different terms in equation (2.27). Whether bedforms have the tendency to grow or decay, depends on

the competition between advective terms (T3 and T4, of which T4 is dominant) and the diffusion term (T2), which render unstable and stable bottom perturbations, respectively. If the advective terms are larger than the diffusion term bedforms can grow, otherwise they decay. Variation in parameter values leads to changes in the growth rate if the absolute change in the magnitude of the advective terms is different from that of the diffusive term. Furthermore, changes in the longshore spacing of bedforms occur if there is a change in the magnitude of the ratio of advective and diffusive terms. Term T2 is proportional to U_w^5 , whereas term T4 is proportional to $\frac{d}{dx} \left(\frac{C}{H} \right) \frac{u'}{H} \sim \frac{d}{dx} \left(\frac{C}{H} \right) \frac{V}{H^2} h'$. The latter estimate follows from water mass continuity. Note that V itself is inversely proportional to U_w due to frictional effects. The magnitude of the bedform migration is determined by term T1, which is proportional to $U_w^2 V/H \sim U_w/H$.

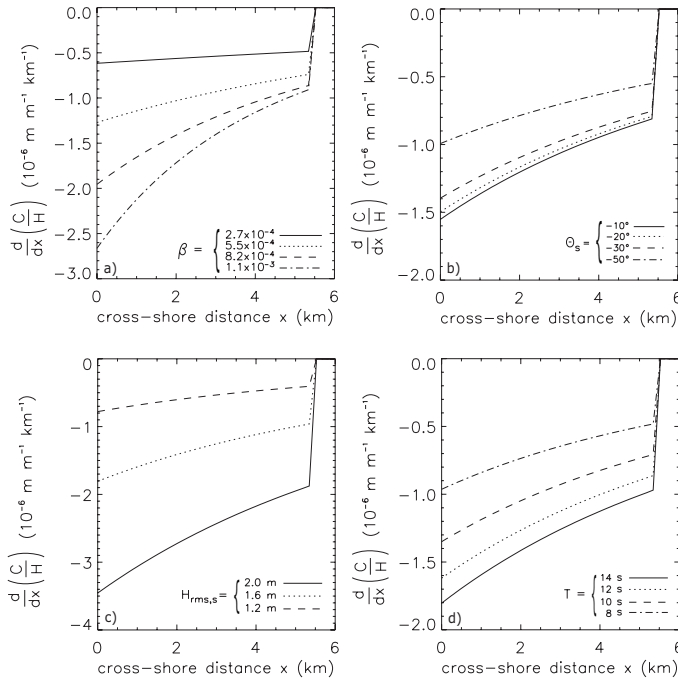


Figure 2.14: Cross-shore profiles of the cross-shore gradient in the depth-averaged volume concentration in the basic state for (a) different values for the transverse bottom slope of the inner shelf, (b) different offshore angles of wave incidence, (c) different offshore root-mean-square wave heights and (d) different wave periods. Other parameters have their default values.

Let us now consider the case of increasing the bed slope β . Here, an increase in β corresponds with an increase in H_s and thus a larger water depth at the outer shelf. Across the major part of the inner shelf, an increase in β results in a smaller wave orbital velocity (see Figure 2.7a) and thus $T2 \sim U_w^5$ decreases. On the other hand, considering Figure 2.14a, the cross-shore gradient in the depth-averaged sediment concentration increases for a larger slope. Together with an increase in the magnitude of V , due to a reduced friction, term T4 clearly increases.

Hence, the growth rate of bedforms becomes larger for larger β . The relative increase of T4/T2 with increasing β results in a preferred wavelength, which is smaller on steeper inner shelf slopes. As the migration is determined by $T1 \sim U_w/H$, it explains the decrease in migration speed with increasing β .

In a similar way the dependence of growth rate, migration speed and longshore spacing of bedforms on the magnitude of the offshore wave height can be understood. The wave orbital velocity is proportional to $H_{rms,s}$ and therefore T2 is larger for higher offshore waves. The dominant advection term T4 also increases (see Figure 2.14c), but not as fast as T2. The absolute increase in T2 is so large compared to the absolute increase in T4 that bedforms grow slower in case of larger offshore wave heights. As the ratio T4/T2 also increases, bedforms have longer spacings for higher offshore waves. In general, bedform migration increases with the presence of higher offshore waves, which corresponds with the increase in the magnitude of U_w . Note that under conditions that term T3 and T4 become large (e.g. for high offshore waves), their imaginary parts will no longer be small compared to term T1 and will therefore also contribute to the migration speed. This might explain the decrease in migration speed when waves become very high (see Figure 2.10). The sensitivity of model results to a variation in the offshore angle of wave incidence and wave period can be explained using similar arguments. A summary is given in Table 2.1.

Table 2.1: Sensitivity of model results to the transverse bottom slope and offshore wave characteristics. For an explanation see the main text.

	$T1 \sim \frac{U_w^2 V}{H}$	$T2 \sim U_w^5$	$T4 \sim \frac{d}{dx} \left(\frac{C}{H} \right) \frac{V}{H^2}$	σ_r	λ_p	V_m
$\beta \uparrow$	\downarrow	\downarrow	\uparrow	\uparrow	\downarrow	\downarrow
$H_{rms,s} \uparrow$	\uparrow	$\uparrow\uparrow$	\uparrow	\downarrow	\uparrow	\uparrow
$ \Theta_s \uparrow$	\simeq	\downarrow	$\downarrow\downarrow$	\downarrow	\uparrow	\simeq
$T \uparrow$	\uparrow	$\uparrow\uparrow$	\uparrow	\downarrow	\uparrow	\uparrow

2.5.2 MODEL LIMITATIONS

The model used in this study is highly idealized and describes only specific aspects of sfcf. Below, a few of its limitations are discussed. First, the linear stability analysis employed, describes the initial growth of bedforms and therefore yields no information about their finite amplitude. The long-term evolution of sfcf will be investigated in detail in chapter 3. Second, the results presented in this chapter were obtained with a version of the model in which feedbacks between waves and growing bedforms were ignored. However, bedforms will affect wave refraction and shoaling and thereby the wave orbital motion and sediment transport. The effect of wave-bedform interactions on the formation of sfcf is investigated in chapters 4 and 5. Also considered in chapter 5 is nonuniform sand. In this chapter a single grain size is used, but data show clear variations in grain size over sfcf. Sediment with different grain sizes causes selective transport and grain size sorting, as is observed in nature.

Furthermore, in the present model radiation stresses exerted by the waves and refraction of waves due to the longshore current are ignored. The use of linear wave theory assumes symmetrical waves that only cause stirring of sediment and no net sediment transport due to wave-asymmetry. By using a depth-averaged model, the role of the vertical structure of the currents is neglected. However, field data (e.g. *Niedoroda et al.*, 1984) reveal the presence of vertical circulation cells perpendicular to the coast. Also, the suspended sediment concentration exhibits a pronounced vertical structure (cf. *Green et al.*, 1995). This suggests that taking into account 3D processes in the current and sediment transport model might be important.

In the present study we consider the micro-tidal American shelf, for which it is justifiable to consider only storm-driven currents and neglect the relatively weak tidal flows. However, near e.g. the Dutch and German coasts strong tidal currents occur and bottom stresses are sufficiently strong to erode and transport sediment even during fair weather. *Calvete et al.* (2001b) demonstrated that, depending on the weather climate and the geometrical characteristics of the shelf, a variety of large-scale bedforms are formed (including tidal sand banks and sfcf). According to *Walgreen et al.* (2002) overtides can have a large effect on migration speeds of sfcf, but not on their growth rates. It would be interesting to explore the effect of tidal flow in the context of the present model. The evolution of sfcf is only considered for storm conditions. The formulations used for the bed shear-stress and sediment transport during storms are based on several assumptions. Under storm conditions, when the wave orbital velocity is large compared to the storm-induced longshore current, the bed shear-stress and advective sediment transport can be linearized, thus $\vec{\tau}_b \sim \mathcal{A}_\tau \cdot \vec{v}$ and $\vec{q}_{b,a} \sim \mathcal{A}_q \cdot \vec{v}$, respectively. In the present chapter it is assumed that the waves are directed parallel to the current, which implies that \mathcal{A}_τ and \mathcal{A}_q are isotropic (scalar \times unity tensor). However, often there will be an angle between the direction of the waves and the net current and in that case \mathcal{A}_τ and \mathcal{A}_q are anisotropic tensors (see for explicit expressions appendix 2.A). Tensor \mathcal{A}_τ represents the possibility of a net bed shear-stress that acts in a different direction than the net current and tensor \mathcal{A}_q represents the possibility that the net bedload transport and net current have different directions (called anisotropy). Additional experiments performed for the default case, indicate that the effects of anisotropy are small, i.e., anisotropy leads to a small decrease in growth rate and migration speed and a small increase in longshore spacing of the bedforms. Interesting is the additional onshore contribution to the sediment flux in case of anisotropic conditions. A similar study as in the present chapter in which different weather conditions are considered, e.g. alternative forcing by severe, mild or weak storms, will affect the bed shear-stress and sediment transport and could also give a better view on the growth time scale and migration speed of sfcf.

2.5.3 COMPARISON WITH FIELD OBSERVATIONS

The model results have been compared with data of sfcf from different inner shelves. Particular attention has been paid to the alongshore spacing between successive crests, the angle between crestlines and coastline, the cross-shelf extent of sfcf, their growth time and their migration speed.

Model results for the measured slope of the Long Island inner shelf and realistic wave conditions, taking into account that storms and fair weather alternate, indicate that the most preferred mode has a longshore spacing $\lambda \sim 7$ km. This is larger than the observed spacing at this shelf (*Niedoroda and Swift*, 1981; *Schwab et al.*, 2000). Generally, observed spacings of sfcr range from 2 – 6 km. Note that sensitivity experiments indicate that the spacing predicted by the model decreases when smaller values of the wave height, wave period or angle of wave incidence at the outer shelf are taken. As explained in section 2.5.1, the longshore spacing of bedforms is determined by the ratio of the magnitudes of the advective and diffusive sediment transport, $\lambda \sim \lambda_p [\vec{q}_{s,a}]/[\vec{q}_{s,d}]$, where λ_p is the wavelength of the initially most preferred mode. The fact that the model overestimates the longshore spacing of the bedforms is due to a small $[\vec{q}_{s,a}]$ in this chapter. In chapter 4 it will be argued that a (new) physical mechanism for ridge growth exists for which $[\vec{q}_{s,a}]$ is considerably larger. Hence, the longshore spacing predicted by the model will decrease and yield better comparison with data.

The angle between coastline and crest axis obtained with the model for a variation in offshore wave properties and inner shelf bottom slope is $\varphi \sim 30^\circ$. Positive values of φ indicate that the ridges are up-current oriented, i.e., their offshore ends are shifted up-current with respect to their attachments at the shoreface. The value of this angle for sfcr that occur at Long Island inner shelf is $\varphi \sim 30 - 40^\circ$ (*Schwab et al.*, 2000). Thus, the model predicts the correct orientation of the crests. *Duane et al.* (1972) analyzed data of sfcr at different shelves and concluded that most sfcr have angles φ between 10° and 50° . Almost all sfcr have positive angles, so they are up-current oriented. This is also predicted by the model.

As with previous models (*Trowbridge*, 1995; *Calvete et al.*, 2001a), sfcr obtained with the present model cover the entire width of the inner shelf. The observed sfcr at Long Island shelf extend about 2.5 km over the shelf, i.e., a coverage of about 50%. Inspection of patterns of sfcr at other shelves, as presented in *Swift et al.* (1978) and *Van de Meene and Van Rijn* (2000), reveals that most sfcr stretch over half of the width of the inner shelf. In chapter 4 it will be shown that a new physical mechanism will cause the bedforms to become more trapped to the coast such that comparison with observations improves.

Finally, we consider the growth time scale T_g and migration speed V_m of sfcr. Considering the results for the measured slope of the Long Island inner shelf we obtain $T_g \sim 1800$ yr and $V_m \sim 1$ m yr⁻¹, after correction for the time fraction that storms occur. There are no direct field data of T_g , but the evolution time scale of sfcr is estimated to be in the order of decades to centuries. As explained, the growth rate predicted by the model $\sigma_r \sim ([\vec{q}_{s,a}] + [\vec{q}_{s,d}]) k_p/H_0$, where k_p is the wavenumber of the initially most preferred mode and H_0 the depth at the toe of the shoreface. The growth time ($1/\sigma_r$) is somewhat high due to the small value for $[\vec{q}_{s,a}]$ in this chapter. Again, due to the new physical mechanism which will be discussed in chapter 4, $[\vec{q}_{s,a}]$ will be larger and growth time scales reduce. With regard to the migration speed, observed values range from 1 – 50 m yr⁻¹, depending on the measuring period (e.g. *Duane et al.*, 1972; *Van de Meene and Van Rijn*, 2000). All sfcr migrate in the downstream direction, as is also predicted by the model. In all observational studies it is stressed that storms are highly episodic events and that during a single, severe storm sfcr can migrate over longer distances than in an entire year without such a storm. Also, the modeled values are subject

to high uncertainties. They scale linearly with the time fraction during which storms prevail (here 5% is assumed) and the thickness of the suspended load layer. Furthermore, the magnitude of suspended load transport is determined by α/γ in the concentration equation (2.18), for which it is difficult to obtain an accurate value from field data. As a consequence, a difference in the modeled values of a factor of order 5 – 10 seems quite plausible.

2.6 CONCLUSIONS

In this chapter a model was developed and analyzed, which describes the initial formation of sfcf on micro-tidal inner shelves due to the interaction between waves, a storm-driven long-shore current and the sandy bottom. The most distinct difference between the present model and those of *Trowbridge* (1995) and *Calvete et al.* (2001a) is that here wave variables are calculated with a shoaling-refraction model instead of using a parameterization.

The objective of this study was to investigate the influence of changes in offshore wave characteristics on the growth of sfcf. For a model setting that resembles the situation at Long Island inner shelf, it was found that the fastest growing mode resembles sfcf of which the offshore ends are shifted up-current with respect to their attachments to the shoreface. Typical alongshore distances between successive crests are several kilometers and sfcf migrate several meters per year downstream. A typical growth rate is in the order of several centuries.

A physical analysis has revealed that in this model sfcf grow due to two different mechanisms. The first is the one described by *Trowbridge* (1995), which involves the offshore deflection of the current over sfcf over a transversely sloping bottom. The second is described by *Calvete et al.* (2001a) and involves the joint action of cross-shore gradients in the depth-averaged sediment concentration of the reference state (i.e., the state in which bedforms are absent) and the offshore deflection of the current over sfcf. A variation in offshore wave characteristics affects the wave transformation across the inner shelf. Therefore, the cross-shore profile of U_w (the wave orbital velocity in the basic state) will alter and as a result, the advective sediment transport due to suspended load processes $[\vec{q}_{s,a}]$ and due to bedload processes $[\vec{q}_{b,a}]$, as well as the diffusive sediment transports $[\vec{q}_{s,d}]$ and $[\vec{q}_{b,d}]$ will change. Therefore, the growth rate ($\sim ([\vec{q}_{s,a}] + [\vec{q}_{s,d}]) k_p / H_0$, where k_p is the wavenumber of the initially fastest growing mode and H_0 the depth at the toe of the shoreface), the longshore spacing ($\sim \lambda_p [\vec{q}_{s,a}] / [\vec{q}_{s,d}]$, where $\lambda_p = 2\pi / k_p$) and the migration speed ($\sim k_p [\vec{q}_{b,a}]$) vary for a change in offshore wave characteristics. The initial growth of bedforms is fastest for high inner shelf bed slopes, small angles of wave incidence, small offshore wave heights and high-frequency waves. The longshore spacing of sfcf increases with an increase in the offshore wave height, wave period or $|\Theta_s|$, whereas it decreases with an increase in β . The migration speed is independent of the offshore angle of wave incidence and it is smallest for large transverse bed slopes and small offshore root-mean-square wave heights or wave periods. Comparison with field data reveals that the model overestimates the growth time scale and longshore spacing of the bedforms. It is possible to tune the model by means of parameter λ_s . That path is not followed here, as a new physical mechanism (see chapter 4) will turn out to be responsible for a growth time scale and longshore spacing, which are in better agreement with data.

APPENDICES

2.A ANISOTROPY IN BED SHEAR-STRESS AND BEDLOAD TRANSPORT

The frictional force between the bed and the flow is important in the hydrodynamics and due to the bed shear-stress (see section 2.2.3). The instantaneous bed shear-stress $\vec{\tau}_{b,t}$ for a certain realization of the wave field is defined as:

$$\vec{\tau}_{b,t} = \rho c_f |\vec{v}_t| \vec{v}_t. \quad (2.A-1)$$

Here, ρ is the water density and \vec{v}_t is the instantaneous near-bed flow for a certain realization \mathcal{H}' of the wave height \mathcal{H} . Furthermore, c_f is a wave friction factor, which is considered to be a constant (also considered by *Mei*, 1989, p. 480-481). In general, c_f depends on the magnitude of the current, the amplitude of the wave orbital motion and the angle between waves and currents (cf. *Grant and Madsen*, 1979; *Soulsby*, 1997). We split the instantaneous near-bed flow into two components,

$$\vec{v}_t = \vec{v}_{nb} + \vec{v}_w, \quad (2.A-2)$$

where the near-bed flow velocity $\vec{v}_{nb} = \gamma_v \vec{v}$ and \vec{v}_w is the wave-induced orbital velocity close to the bed. Furthermore, \vec{v} is the depth- and wave-averaged velocity and coefficient γ_v accounts for the vertical structure of the flow. For example, if the flow has a logarithmic distribution, the thickness of the wave boundary layer is δ_w (~ 0.1 m), the roughness length is z_0 (~ 0.01 m) and the depth at the toe of the shoreface is H_0 (~ 14 m), it follows

$$\gamma_v = \frac{\ln(\delta_w/z_0)}{\ln(H_0/z_0) - 1} \sim 0.35. \quad (2.A-3)$$

According to linear wave theory the near-bed wave orbital velocity is given by

$$\vec{v}_w = u_o \cos(\omega t) \hat{v}_w, \quad u_o = \frac{\omega \mathcal{H}}{2 \sinh(\kappa D)}. \quad (2.A-4)$$

Here, u_o is the amplitude of the near-bed wave orbital velocity, ω is the wave frequency and \hat{v}_w is the unit vector in the direction of wave propagation. With respect to the coordinate system that is used in this chapter $\hat{v}_w = (-\cos \theta, \sin \theta)$, with θ the angle between wave direction and the x -axis. Furthermore, t is time, κ is the wavenumber and D the mean water depth. During storms large waves are present and cause the amplitude of the wave-induced velocity to be much larger than the current amplitude. In that case $\vec{\tau}_{b,t}$ can be developed as

$$\vec{\tau}_{b,t} = \rho c_f |\vec{v}_w| \left[1 + \frac{\vec{v}_{nb} \cdot \vec{v}_w}{|\vec{v}_w|^2} + \dots \right] (\vec{v}_{nb} + \vec{v}_w). \quad (2.A-5)$$

So

$$\vec{\tau}_b \equiv \langle \vec{\tau}_{b,t} \rangle = \rho c_f \langle |\vec{v}_w| \rangle \vec{v}_{nb} + \rho c_f \langle (\vec{v}_{nb} \cdot \vec{v}_w) \frac{\vec{v}_w}{|\vec{v}_w|} \rangle, \quad (2.A-6)$$

where the brackets $\langle \rangle$ denote a time average over several wave periods and integration over all possible wave heights of the random wave field (which are Rayleigh distributed, see equation (2.2)). Performing the averaging and integration, we get e.g.

$$\langle |\vec{v}_w| \rangle = \int_0^\infty \frac{\omega \mathcal{H}'}{2 \sinh(\kappa D)} P(\mathcal{H}') d\mathcal{H}' |\overline{\cos(\omega t)}| = \frac{1}{2} \sqrt{\pi} u_{rms} \frac{2}{\pi}, \quad (2.A-7)$$

where the overbar denotes the time average over several wave periods and $u_{rms} = \frac{\omega \mathcal{H}_{rms}}{2 \sinh(\kappa D)}$ is the wave orbital velocity. The latter is denoted as u_w below. So

$$\vec{\tau}_b = \rho \frac{c_f \gamma_v}{\sqrt{\pi}} u_w \mathcal{A}_\tau \cdot \vec{v}, \quad \mathcal{A}_\tau = \underline{\underline{\delta}} + \hat{v}_w \hat{v}_w. \quad (2.A-8)$$

Here, $\underline{\underline{\delta}}$ denotes the unit tensor and tensor \mathcal{A}_τ appears as a result of the nonlinear interaction between the current and waves. The latter accounts for the possibility that the net bed shear-stress acts in a different direction than the net current. With respect to the coordinate system used in this chapter \mathcal{A}_τ is written as

$$\mathcal{A}_\tau = \begin{pmatrix} 1 + \cos^2 \theta & -\cos \theta \sin \theta \\ -\cos \theta \sin \theta & 1 + \sin^2 \theta \end{pmatrix}. \quad (2.A-9)$$

From equation (2.A-6) it follows that under the assumption that waves and currents are parallel that

$$\vec{\tau}_b = \rho r u_w \vec{v}, \quad (2.A-10)$$

where $r = 2c_f \gamma_v / \sqrt{\pi}$ is a dimensionless friction coefficient. In this case tensor \mathcal{A}_τ is isotropic, i.e., the net bed shear-stress acts in the direction of the net current \vec{v} .

The linearized expression for the bedload sediment transport (see section 2.2.4) is derived in a similar way. The *Bailard* (1981) formulation gives

$$\vec{q}_{b,t} = \hat{\nu}_b \left(|\vec{v}_t|^2 \vec{v}_t - \hat{\lambda}_b |\vec{v}_t|^3 \vec{\nabla} z_b \right). \quad (2.A-11)$$

Here, coefficient $\hat{\nu}_b$ depends on sediment properties and $\hat{\lambda}_b$ is the bed slope parameter, where both are defined for the case of monochromatic waves. Furthermore, z_b is the bottom depth measured with respect to the undisturbed water level. Substituting equation (2.A-2) and considering wave-dominated conditions, $\vec{q}_{b,t}$ can be developed as

$$\vec{q}_{b,t} = \hat{\nu}_b |\vec{v}_w|^2 \left[1 + \frac{2(\vec{v}_{nb} \cdot \vec{v}_w)}{|\vec{v}_w|^2} + \dots \right] (\vec{v}_{nb} + \vec{v}_w) - \hat{\nu}_b \hat{\lambda}_b |\vec{v}_w|^3 [1 + \dots] \vec{\nabla} z_b. \quad (2.A-12)$$

Subsequently, it follows

$$\vec{q}_b \equiv \langle \vec{q}_{b,t} \rangle = \hat{\nu}_b \langle |\vec{v}_w|^2 \rangle \vec{v}_{nb} + 2\hat{\nu}_b \langle (\vec{v}_{nb} \cdot \vec{v}_w) \rangle \vec{v}_w - \hat{\nu}_b \hat{\lambda}_b \langle |\vec{v}_w|^3 \rangle \vec{\nabla} z_b. \quad (2.A-13)$$

Performing the time averaging over several wave periods and integration over all possible wave heights of the random wave field, we obtain

$$\vec{q}_b = \frac{1}{2} \hat{\nu}_b \gamma_v u_w^2 \mathcal{A}_q \cdot \vec{v} - \frac{1}{\sqrt{\pi}} \hat{\nu}_b \hat{\lambda}_b u_w^3 \vec{\nabla} z_b, \quad \mathcal{A}_q = \underline{\underline{\delta}} + 2\hat{v}_w \hat{v}_w. \quad (2.A-14)$$

Here, \mathcal{A}_q is a tensor, which represents the possibility of a bedload sediment transport that is in a different direction than the net longshore current. Under the assumption that waves and currents are near-parallel, \mathcal{A}_q becomes isotropic and the net sediment transport as bedload is in the same direction as the net current. Using $\nu_b = \hat{\nu}_b \gamma_v$ and $\lambda_b = \frac{2\hat{\lambda}_b}{3\sqrt{\pi}\gamma_v}$, it follows

$$\langle \vec{q}_b \rangle = \frac{3}{2} \nu_b u_w^2 \left(\vec{v} - \lambda_b u_w \vec{\nabla} z_b \right). \quad (2.A-15)$$

The model simulations in section 2.4 are performed with an isotropic bed shear-stress and an isotropic bedload sediment transport. In section 2.5 also results are discussed for anisotropic conditions.

2.B EXPRESSIONS FOR OPERATORS \mathcal{S} AND \mathcal{L}

The linear system of partial differential equations describing the evolution of the flow, mass, concentration and bottom can be symbolically written as

$$\mathcal{S} \frac{\partial \Psi'}{\partial t} = \mathcal{L} \Psi', \quad (2.B-1)$$

where Ψ' and matrix \mathcal{S} (containing all the temporal information of the perturbations) are given by

$$\mathcal{S} = \begin{pmatrix} 0 & 0 & 0 & 0 & 0 \\ 0 & 0 & 0 & 0 & 0 \\ 0 & 0 & 0 & 0 & 0 \\ 0 & 0 & 0 & 0 & 0 \\ 0 & 0 & 0 & 0 & 1-p \end{pmatrix}, \quad \Psi' = \begin{pmatrix} u' \\ v' \\ \eta' \\ c' \\ h' \end{pmatrix}.$$

The linear operator \mathcal{L} involves spatial derivatives and its coefficients only depend on x :

$$\mathcal{L} = \begin{pmatrix} V \frac{\partial}{\partial y} + \frac{rU_w}{H} & -f & g \frac{\partial}{\partial x} & 0 & 0 \\ \frac{dV}{dx} + f & V \frac{\partial}{\partial y} + \frac{rU_w}{H} & g \frac{\partial}{\partial y} & 0 & 0 \\ \frac{dH}{dx} + H \frac{\partial}{\partial x} & H \frac{\partial}{\partial y} & 0 & 0 & -V \frac{\partial}{\partial y} \\ \frac{dC}{dx} + C \frac{\partial}{\partial x} & C \frac{\partial}{\partial y} & 0 & V \frac{\partial}{\partial y} + \frac{\gamma}{H} & \frac{\gamma C}{H^2} \\ \mathcal{L}_{51} & -\frac{3}{2} \nu_b U_w^2 \frac{\partial}{\partial y} - C \frac{\partial}{\partial y} & 0 & -V \frac{\partial}{\partial y} & \mathcal{L}_{55} \end{pmatrix}.$$

The elements \mathcal{L}_{51} and \mathcal{L}_{55} of operator \mathcal{L} are

$$\begin{aligned} \mathcal{L}_{51} &= -\frac{3}{2} \nu_b U_w^2 \frac{\partial}{\partial x} - 3 \nu_b U_w \frac{dU_w}{dx} - \frac{dC}{dx} - C \frac{\partial}{\partial x}, \\ \mathcal{L}_{55} &= \frac{3}{2} \nu_b \lambda_b \left(3U_w^2 \frac{dU_w}{dx} \frac{\partial}{\partial x} + U_w^3 \frac{\partial^2}{\partial x^2} + U_w^3 \frac{\partial^2}{\partial y^2} \right) \\ &\quad + \lambda_s \left(U_w^5 \frac{\partial^2}{\partial x^2} + 5U_w^4 \frac{dU_w}{dx} \frac{\partial}{\partial x} + U_w^5 \frac{\partial^2}{\partial y^2} \right). \end{aligned}$$

The operator \mathcal{L}_k in equation (2.26) follows from \mathcal{L} by replacing $\frac{\partial}{\partial y}$ by ik .

2.C EXAMPLE OF ONE SPECIFIC EQUATION OF THE LINEAR SYSTEM

The procedure of the linear stability analysis, as described in section 2.3.2, is illustrated for the cross-shore momentum equation. The first step is to split the model variables in a basic state contribution and a perturbation on this basic state: $(u, v, z_s, \mathcal{C}, z_b) = (U, V, \xi, C, -H) + (u', v', \eta', c', h')$. Substitution of the latter into the cross-shore momentum balance (see equation (2.12)) and assuming the amplitude of the perturbations to be small, a linear differential equation is obtained:

$$V \frac{\partial u'}{\partial y} - f v' = -g \frac{\partial \eta'}{\partial x} - \frac{r U_w}{H} u'. \quad (2.C-1)$$

The linear cross-shore momentum equation allows for solutions, which are alongshore-periodic and of which the amplitude can grow (or decay) exponentially in time:

$$(u', v', \eta', c', h') = \Re \left\{ \left(\hat{u}(x), \hat{v}(x), \hat{\eta}(x), \hat{c}(x), \hat{h}(x) \right) e^{iky + \sigma t} \right\}. \quad (2.C-2)$$

Substituting expressions (2.C-2) into the equation for the perturbed cross-shore velocity component (2.C-1) yields

$$ikV \hat{u} - f \hat{v} = -g \frac{d\hat{\eta}}{dx} - \frac{r U_w}{H} \hat{u}. \quad (2.C-3)$$

Derivation of the perturbed alongshore momentum balance, mass conservation equation, concentration equation and sediment mass balance is done in a similar way. The fully linearized system of differential equations is given in appendix 2.B.

2.D FLOW OVER TOPOGRAPHY PROBLEM

In appendix 2.B the full linearized system of differential equations, as considered in this chapter, is given. This system is solved in two steps. The first step is to solve the equations for u' , v' , η' and c' for a given bottom perturbation h' , which is called the flow over topography problem. The latter is done by cross-differentiating the linearized momentum equations (elimination of η') and substituting the solutions (2.25) for u' and v' . The result is a Fourier-transformed vorticity equation. From the linearized and Fourier-transformed continuity equation an expression is obtained, which relates \hat{v} to \hat{h} and \hat{u} ,

$$\hat{v} = \frac{V}{H} \hat{h} + \frac{i}{k} \frac{d\hat{u}}{dx} + \frac{i}{kH} \frac{dH}{dx} \hat{u}. \quad (2.D-1)$$

Substitution of expression (2.D-1) into the Fourier-transformed vorticity equation yields a single equation for the cross-shore velocity amplitude \hat{u} as a function of the bottom perturbation \hat{h} :

$$\mathcal{U}_{02} \frac{d^2 \hat{u}}{dx^2} + \mathcal{U}_{01} \frac{d\hat{u}}{dx} + \mathcal{U}_{00} \hat{u} = \mathcal{H}_1 \frac{d\hat{h}}{dx} + \mathcal{H}_0 \hat{h}, \quad (2.D-2)$$

where the coefficients are given by

$$\begin{aligned}
 \mathcal{U}_{02} &= ikV + \frac{rU_w}{H}, \\
 \mathcal{U}_{01} &= \frac{ikV}{H} \frac{dH}{dx} + \frac{r}{H} \frac{dU_w}{dx}, \\
 \mathcal{U}_{00} &= r \left(-\frac{k^2 U_w}{H} + \frac{1}{H^2} \frac{dH}{dx} \frac{dU_w}{dx} - \frac{2U_w}{H^3} \left(\frac{dH}{dx} \right)^2 + \frac{U_w}{H^2} \frac{d^2 H}{dx^2} \right) \\
 &\quad - ik \left(k^2 V - \frac{f}{H} \frac{dH}{dx} + \frac{d^2 V}{dx^2} - \frac{1}{H} \frac{dV}{dx} \frac{dH}{dx} - \frac{V}{H} \frac{d^2 H}{dx^2} + \frac{V}{H^2} \left(\frac{dH}{dx} \right)^2 \right), \\
 \mathcal{H}_1 &= -\frac{k^2 V^2}{H} + \frac{ikrU_w V}{H^2}, \\
 \mathcal{H}_0 &= k^2 \left(-\frac{fV}{H} - \frac{2V}{H} \frac{dV}{dx} + \frac{V^2}{H^2} \frac{dH}{dx} \right) \\
 &\quad + ikr \left(\frac{V}{H^2} \frac{dU_w}{dx} - \frac{2U_w V}{H^3} \frac{dH}{dx} + \frac{U_w}{H^2} \frac{dV}{dx} \right).
 \end{aligned}$$

Now that both flow components are known for a given bottom perturbation, the second step is to calculate the wave-averaged sediment transport. The evolution of the bottom is determined by convergences and divergences of the sediment transport according to the bed evolution equation (2.15). Substitution of the solutions (2.25) for h' and u' results in a Fourier-transformed bed evolution equation, which is solved for the bottom perturbations and the system is closed.

CHAPTER 3

NONLINEAR DYNAMICS OF INNER SHELF SAND RIDGES: PATCH BEHAVIOR AND ROLE OF WAVES

ABSTRACT

The long-term evolution of shoreface-connected sand ridges (hereafter abbreviated as sfc) is investigated with a nonlinear morphodynamic model, which governs the dynamics of waves, currents, sediment transport and the bed level on the inner shelf. Wave variables are calculated with a shoaling-refraction model instead of using a parameterization. The spectral model describes the time evolution of amplitudes of known eigenmodes of the linearized system (chapter 2). Bottom pattern formation occurs if the transverse bed slope of the inner shelf β exceeds a critical value β_{c1} . For $\beta > \beta_{c2}$ the model exhibits explosive behavior. Here, β_{c1} and β_{c2} are functions of the model parameters. Experiments show that the critical bed slope β_{c1} increases for larger offshore angles of wave incidence, larger offshore wave heights and longer wave periods and that the corresponding maximum height of sfc decreases whilst the saturation time increases. Also, the sensitivity of the properties of modeled sfc to changes in the number ($N - 1$) of resolved subharmonics (of the initially fastest growing mode) is investigated. For any N the model shows the growth and subsequent saturation of the height of sfc. The saturation time is several thousands of years, which suggests that observed sfc have not reached their saturated state yet. The migration speed of and average longshore spacing between sfc in the saturated state differ from those in the initial state. Analysis of the potential energy balance of sfc reveals that bed slope-induced sediment transport is crucial for the saturation process. In the transient stage sfc occur in patches. The overall characteristics of the bedforms (saturation time, final maximum height, average longshore spacing and migration speed) hardly vary with N . However, individual time series of modal amplitudes and bottom patterns strongly depend on N . As N is not well-known, the detailed evolution of sfc can only be predicted over a limited time interval. *

*Parts of the results in this chapter were published in Proceedings of the 5th IAHR symposium: *Finite amplitude dynamics of shoreface-connected ridges: role of waves*, by N.C. Vis-Star, H.E. de Swart and D. Calvete (2008).

3.1 INTRODUCTION

Patches of sfcrr are found on storm-dominated inner shelves, with a characteristic spacing between successive crests of several kilometers (*Swift and Field, 1981; Van de Meene and Van Rijn, 2000; Antia, 1996a*). Typically, a patch consists of 4 – 8 ridges. Sfcrr migrate in the direction of the storm-driven current, with a velocity of several meters per year. The estimated lifetime of sfcrr is several thousands of years. The crests can reach up to one-third of the water depth in the shallowest areas, and troughs are excavated by the same amount below the mean seabed level (*Dyer and Huntley, 1999*). Sfcrr have asymmetrical bottom profiles, with gentle slopes on the landward (upstream) sides and steep slopes on the seaward (downstream) sides.

As was demonstrated in the previous chapter, the initial growth of sfcrr can be modeled using an idealized process-based model. The results indicate that sfcrr can originate as free morphodynamic instabilities of a coupled water-erodible bottom system. It was shown that the wavelength, characteristic e -folding time scale and migration speed of the bedforms depend on the specific offshore wave characteristics. The model is able to reproduce many characteristics of observed sfcrr. However, this model is only valid for bedforms having small amplitudes compared to the water depth, because it employs a linear stability analysis. According to field data, sfcrr can reach amplitudes of several meters, thereby indicating the importance of nonlinear processes for their generation. The validity of results with the linear analysis for the nonlinear regime is investigated with a model that is based on a nonlinear stability analysis.

Calvete et al. (2002) and *Calvete and De Swart (2003)* investigated the long-term dynamics of sfcrr by expanding the flow and bottom perturbations in a truncated series of eigenmodes. The result is a set of equations describing the time evolution of the amplitudes. *Roos et al. (2004)* used a similar technique in a morphodynamic study for tidal sand banks. The model of *Calvete and De Swart (2003)* is also applied by *De Swart and Calvete (2003)* and by *Hommes et al. (2007)* to study the response of sfcrr to large-scale sand extraction. The results of the nonlinear model for sfcrr showed that after the initial growth stage ridge profiles become asymmetric and reach a finite height. *Calvete and De Swart* also found that adding subharmonic modes (i.e., eigenmodes with wavelengths being larger than that of the initially most preferred mode) strongly influences the transient behavior of sfcrr. Furthermore, subharmonic modes are excited in such a way that in the saturated state they dominate over the initially most preferred mode of the linear analysis. However, their results do not explain the patchy behavior of sfcrr.

In the present chapter a new nonlinear model will be discussed in which wave properties follow from applying physical principles. Thus, processes like shoaling and refraction are explicitly accounted for. Recent studies on the nonlinear dynamics of bars in the surf zone using a finite difference model by e.g. *Caballeria et al. (2002)* and *Garnier et al. (2006)* showed that these processes play a significant role. The objectives of the present work are twofold. The first is to analyze the long-term behavior of sfcrr in dependence of offshore wave characteristics and the transverse bottom slope of the inner shelf. Specific emphasis is put on the role of subharmonics in generating patches of sfcrr. This is because adding subharmonics

implies that modes become more closely spaced in the spectral domain, thereby potentially allowing for the occurrence of group (or modulation) behavior. The second objective is to identify physical processes that control the migration and saturation behavior by analyzing the potential energy balance of the bedforms: considering production terms and dissipation terms. The analysis extends the one used by *Garnier et al. (2006)* in the sense that also the instantaneous global longshore migration speed is investigated.

This chapter is organized as follows. The model formulation is presented in section 3.2. The method of analysis follows in section 3.3 and continues in section 3.4 with a presentation of the results. The chapter ends with a discussion and conclusions in section 3.5 and 3.6, respectively.

3.2 MODEL FORMULATION

We adopt the model formulation of chapter 2. The coupled dynamics of waves, storm-driven currents and the sandy bed is considered on an idealized inner shelf (see Figure 3.1). The latter is bounded on the landward side ($x = 0$) by the transition to the shoreface (depth H_0) and on the seaward side ($x = L_s$) by the outer shelf (depth H_s). The mean transverse bottom slope is $\beta = (H_s - H_0) / L_s$.

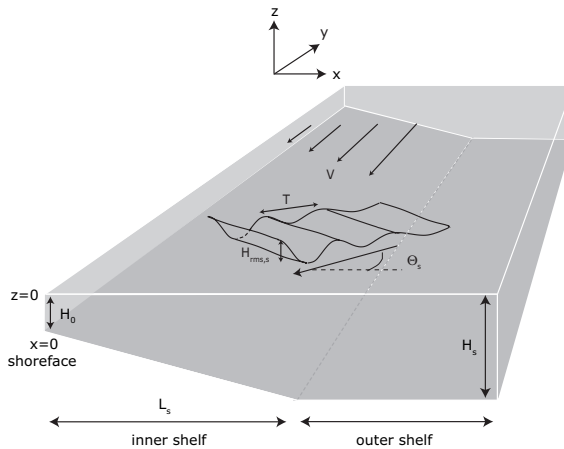


Figure 3.1: Schematic representation of a typical time-averaged bottom topography of the continental shelf, representing the inner and outer shelf. Forcing of the water motion is due to (obliquely) incident waves and a storm-driven current. Symbols are explained in the text.

The water motion is forced by imposed wave conditions at the outer shelf (offshore angle of wave incidence, offshore root-mean-square wave height and wave period) and a wind stress that forces a net current. Sand is only transported during severe weather conditions (which occur about 5% of the time) and is the result of the joint action of waves (stirring sand from the bottom) and a longshore storm-driven flow (causing net sand transport). Hence, the model is representative for storms. After application of the rigid-lid approximation (sea

surface elevation \ll mean depth) and the quasi-steady approach (hydrodynamics adjusts instantaneously to a new bed level), the wave equations are:

$$\omega^2 = g\kappa \tanh(\kappa\tilde{D}), \quad (3.1)$$

$$\frac{\partial}{\partial y} (\kappa \cos \theta) + \frac{\partial}{\partial x} (\kappa \sin \theta) = 0, \quad (3.2)$$

$$\vec{\nabla} \cdot (\vec{c}_g \mathcal{E}) = \mathcal{F} - \mathcal{D}, \quad \mathcal{E} = \frac{1}{8} \rho g \mathcal{H}_{rms}^2, \quad (3.3)$$

$$u_w = \frac{\omega \mathcal{H}_{rms}}{2 \sinh(\kappa\tilde{D})}. \quad (3.4)$$

Here, ω , g , κ and $\tilde{D} = -z_b$ are the wave frequency, acceleration due to gravity, wavenumber and water depth, respectively. The bottom depth z_b is measured with respect to the undisturbed water level $z = 0$. The angle of wave incidence (measured with respect to the shore-normal) is θ . The wave energy density \mathcal{E} is governed by the energy balance (3.3), where the horizontal nabla operator $\vec{\nabla}$ has components $\partial/\partial x$ and $\partial/\partial y$ in the x - and y -direction, respectively. Furthermore, \vec{c}_g is the group velocity vector of the waves with amplitude c_g and components $c_{gx} = -c_g \cos \theta$ and $c_{gy} = c_g \sin \theta$. The source of energy is \mathcal{F} and \mathcal{D} denotes the energy dissipation by bottom friction (formulations are given in section 2.2.3 of chapter 2). In the definition for the wave energy, ρ is the water density and \mathcal{H}_{rms} is the root-mean-square wave height. Finally, the root-mean-square amplitude of the near-bed wave orbital motion u_w (hereafter called wave orbital velocity) depends on the other variables and is input in the modules for the current and the sediment transport.

The currents are described by the quasi-steady depth-averaged shallow water equations

$$(\vec{v} \cdot \vec{\nabla})\vec{v} + f \vec{e}_z \times \vec{v} = -g\vec{\nabla}z_s + \frac{\vec{\tau}_s - \vec{\tau}_b}{\rho\tilde{D}}, \quad (3.5)$$

$$\vec{\nabla} \cdot (\tilde{D}\vec{v}) = 0, \quad (3.6)$$

$$\vec{\tau}_s = (0, \tau_{sy}), \quad \vec{\tau}_b = \rho r u_w \vec{v}. \quad (3.7)$$

Here, \vec{v} denotes the depth- and wave-averaged flow velocity with components u and v in the x - and y -direction, respectively, and $z = z_s$ is the level of the mean sea surface. Furthermore, f is the Coriolis parameter and \vec{e}_z is a unit vector in the vertical direction. It is assumed that the wind stress vector $\vec{\tau}_s$ only has a nonzero y -component τ_{sy} . The mean bed shear-stress $\vec{\tau}_b$ depends linearly on the current, as waves are strong compared to currents during stormy weather. Furthermore, waves and currents are assumed to be near-parallel. In the definition for the bed shear-stress, r is a friction coefficient computed for narrow-banded random waves.

The bed evolution equation (3.8) and the formulations for the sediment transport (3.9)-(3.11) read

$$(1-p) \frac{\partial z_b}{\partial t} + \vec{\nabla} \cdot \vec{q}_b + \vec{\nabla} \cdot \vec{q}_s = 0, \quad (3.8)$$

$$\vec{q}_b = \frac{3}{2} \nu_b u_w^2 \left(\vec{v} - \lambda_b u_w \vec{\nabla} z_b \right) = \vec{q}_{b,a} + \vec{q}_{b,d}, \quad (3.9)$$

$$\vec{q}_s = \mathcal{C} \vec{v} - \lambda_s u_w^5 \vec{\nabla} z_b = \vec{q}_{s,a} + \vec{q}_{s,d}, \quad (3.10)$$

$$\vec{\nabla} \cdot (\mathcal{C} \vec{v}) = \alpha u_w^3 - \gamma \frac{\mathcal{C}}{D}. \quad (3.11)$$

In the bed evolution equation t is time, p is the porosity of the bed and \vec{q}_b and \vec{q}_s denote the wave-averaged sediment transport as bedload and suspended load, respectively. The latter two are divided into a current-induced part $\vec{q}_{\cdot,a}$ and a bed slope-induced part $\vec{q}_{\cdot,d}$. In the expressions for bedload and suspended load transport, ν_b , α and γ are known coefficients, \mathcal{C} is the depth-integrated volumetric concentration of sediment and λ_b and λ_s are the bed slope parameters for bedload and suspended load, respectively.

As boundary conditions offshore wave properties (root-mean-square wave height, period and angle of wave incidence) are imposed. Furthermore, the cross-shore flow component u vanishes at $x = 0$ and far offshore, the bed level z_b is kept fixed at these two positions and the sediment concentration vanishes far from the coast.

3.3 METHOD OF ANALYSIS

3.3.1 BASIC STATE AND LINEAR STABILITY ANALYSIS

In the previous chapter it was shown that sfer can form as free morphodynamic instabilities of a basic state. From here on primary wave variables are denoted by $\mathcal{X} = (\kappa, \theta, \mathcal{E})$ and other dependent variables by $\Psi = (u, v, z_s, \mathcal{C}, z_b)$. The basic state is steady and along-shore uniform. It is characterized by a shelf topography $H(x)$, an incoming wave field with wavenumber $K(x)$, angle of wave incidence $\Theta(x)$ and wave energy $E(x)$ (or equivalently, root-mean-square wave height $H_{rms}(x)$), a storm-driven current $\vec{v} = (U(x), V(x))$, a free surface elevation $\xi(x)$ and a depth-integrated volumetric concentration of sediment $C(x)$. Hence, $\mathcal{X} = \mathcal{X}_b(x) = (K, \Theta, E)$ and $\Psi = \Psi_b(x) = (U, V, \xi, C, -H)$. Both \mathcal{X}_b and Ψ_b are defined in chapter 2, section 2.3.1. It describes shoaling and refracting waves and a storm-driven flow along the coast (hence $U = 0$).

The stability properties of the basic state are considered by studying the dynamics of small perturbations evolving on this basic state. Hence,

$$\Psi = \Psi_b + \Psi' \quad (3.12)$$

and $\Psi'(x, y, t) = (u', v', \eta', c', h')$ denote the perturbed variables, which are assumed to have small values with respect to their basic state values. In principal, also perturbations in the wave variables have to be considered: $\mathcal{X} = \mathcal{X}_b + \mathcal{X}'$. However, similar as in previous studies and the previous chapter, we assume $\mathcal{X}' = 0$. Physically, this means that wave-topography interactions, i.e., wave refraction and shoaling and dissipation of wave energy due to the presence of bedforms are neglected. In chapters 4 and 5 the effect of including wave-topography interactions will be investigated for a linear model.

3.3.2 NONLINEAR MODEL: FINITE AMPLITUDE BEHAVIOR

Substitution of equations (3.12) into the equations of motion of section 3.2 yields the system

$$\mathcal{S} \frac{\partial \Psi'}{\partial t} = \mathcal{L} \Psi' + \mathcal{N}(\Psi'). \quad (3.13)$$

Here, the 5×5 matrix \mathcal{S} contains the temporal information of the perturbations and has one nonzero element: $\mathcal{S}(5, 5) = 1 - p$. The linear matrix operator \mathcal{L} contains all the linear terms and $\mathcal{N}(\Psi')$ is the nonlinear vector operator, which includes all nonlinear terms in the equations of motion for the perturbations. Note that the nonlinear vector operator \mathcal{N} was not present in the previous chapter, which is a consequence of the fact that there it was assumed that the perturbations have infinitesimal amplitudes and therefore nonlinear interactions can be neglected. In order to investigate the long-term evolution of sfcr the full set of nonlinear equations (3.13) has to be considered. The expressions for operators \mathcal{S} and \mathcal{L} are the same as in chapter 2 and can be found in appendix 2.B. The expression for the new nonlinear vector operator \mathcal{N} is given in appendix 3.A.

Following *Calvete and De Swart* (2003) the perturbations are written as

$$\Psi'(x, y, t) = \Psi_0(x, t) + \psi(x, y, t), \quad (3.14)$$

where the unknown contributions Ψ_0 have a longshore uniform structure and the contributions ψ are expanded into a truncated series of (known) eigenmodes of the linear system:

$$\psi = \Re \left\{ \sum_{j=1}^J \sum_{n_j=1}^{N_j} \check{\psi}_{jn_j}(t) \tilde{\psi}_{jn_j}(x) e^{ik_j y} \right\}. \quad (3.15)$$

Here, for each alongshore wavenumber k_j , n_j refers to the cross-shore modenumber, $\check{\psi}_{jn_j}(t)$ are the unknown modal amplitudes and $\tilde{\psi}_{jn_j}(x)$ the known cross-shore structures of the eigenfunctions of the linear problem. Expansions (3.14) and (3.15) are substituted in the nonlinear equations of motion. After averaging over the alongshore direction, equations are obtained for the longshore uniform flow modes and bottom mode, which are subsequently subtracted from the original equations. The results are projected onto the adjoint linear eigenmodes. This procedure yields a set of nonlinear algebraic equations for the flow amplitudes \check{u}_{jn_j} , \check{v}_{jn_j} , $\check{\eta}_{jn_j}$ and \check{c}_{jn_j} and a set of nonlinear differential equations for the amplitudes of the bottom modes \check{h}_{jn_j} . A third-order time integration scheme is used to solve the resulting system of equations (see *Karniadakis et al.*, 1991). *Calvete* (1999) describes in more detail the solution procedure for a similar system of equations.

Here, the choice is to include the most preferred mode with wavenumber k_p (largest initial growth rate) in the nonlinear expansion, as we are interested whether it is still the dominant mode in the bottom pattern on the long term. Furthermore, several superharmonics and generally some subharmonics are used, such that a total number J of different longshore wavenumbers k_j is included. Thus, if only superharmonics are included, the system is solved on a domain with longshore length $L_y = 2\pi/k_p$. By including $(N - 1)$ subharmonic modes the domain becomes longer: $L_y = 2\pi N/k_p$. In both cases periodic boundary

conditions in the longshore direction are applied. Wavenumbers that fit in the domain are $k_j = 2\pi j/L_y = \frac{j}{N}k_p$ ($j = 1, 2, 3, \dots$), as is illustrated in Figure 3.2. An individual mode is denoted by $(j/N, n_j)$.

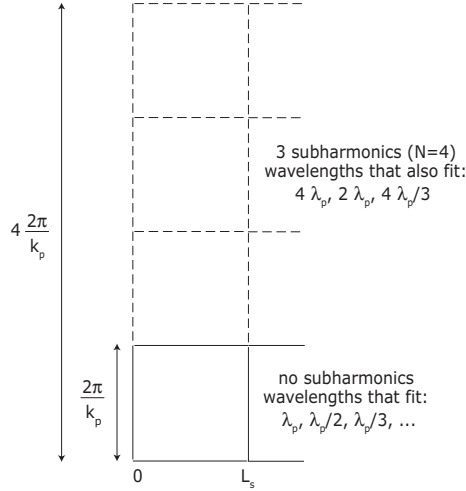


Figure 3.2: Illustration of the length of the alongshore domain for which solutions of the nonlinear system are considered. A case without subharmonic modes and a case including 3 subharmonic modes are shown.

3.3.3 ANALYSIS OF THE POTENTIAL ENERGY BALANCE OF THE BEDFORMS

In order to investigate the saturation behavior of bedforms *Garnier et al.* (2006) developed a method to study the global properties of the bedforms on the whole domain. It boils down to deriving a potential energy balance of bottom perturbations by multiplying the linearized version of the bed evolution equation (3.8) with the bed elevation h' and integrating over the whole domain. It reads

$$(1 - p) \frac{\partial}{\partial t} \left(\frac{1}{2} |h|^2 \right) = P + \Delta, \quad (3.16)$$

where

$$|h| = (\overline{h'^2})^{\frac{1}{2}}, \quad (3.17)$$

$$P = -\overline{h' \left(\vec{\nabla} \cdot \vec{q}_{b,a} + \vec{\nabla} \cdot \vec{q}_{s,a} \right)} = \overline{(\vec{q}_{b,a} + \vec{q}_{s,a}) \cdot \vec{\nabla} h'}, \quad (3.18)$$

$$\Delta = -\overline{h' \left(\vec{\nabla} \cdot \vec{q}_{b,d} + \vec{\nabla} \cdot \vec{q}_{s,d} \right)} = -\overline{\left(\frac{3}{2} \nu_b \lambda_b u_w^3 + \lambda_s u_w^5 \right) |\vec{\nabla} h'|^2}. \quad (3.19)$$

Note that $\frac{1}{2}|h|^2$ measures (apart from a factor $\rho_s(1-p)g$, with ρ_s the density of the sediment) the potential energy density of the bedforms and the overbar indicates the average over the domain. In the last step of equation (3.19) the theorem of Green and the definitions for $\bar{q}_{b,d}$ and $\bar{q}_{s,d}$ (see equations (3.9) and (3.10)) have been applied. Term P , which describes the generation of potential energy due to the advective bedload and suspended load transport, is positive if the advective sediment transport and bed slopes are positively correlated. Furthermore, term Δ describes the loss of potential energy due to bed slope-induced sediment transport. This term is always negative, because $\bar{q}_{b,d}$ and $\bar{q}_{s,d}$ are diffusive transports.

An instantaneous global growth rate of sfc $\tilde{\sigma}_r$ is defined as

$$\tilde{\sigma}_r \equiv \frac{1}{\overline{|h|^2}} \frac{\partial}{\partial t} \left(\frac{1}{2} \overline{|h|^2} \right). \quad (3.20)$$

The definition is such that if the bed pattern is represented by a single wave

$$h' = \Re \left\{ \hat{h}(x) e^{iky + \sigma t} \right\}, \quad (3.21)$$

then $\tilde{\sigma}_r \rightarrow \sigma_r$, i.e., the initial growth rate. A new variable that is considered in this study is the instantaneous global longshore migration speed \tilde{V}_m , defined as

$$\tilde{V}_m = - \frac{1}{\left(\frac{\partial h'}{\partial y} \right)^2} \frac{\overline{\partial h' / \partial t}}{\partial y \partial t}. \quad (3.22)$$

Again, this definition is such that for a single wave $\tilde{V}_m \rightarrow V_m$, i.e., the initial migration speed. Also, for any h' that is a function of x and $(y - V_m t)$ it follows that $\tilde{V}_m = V_m$.

3.4 RESULTS

3.4.1 PARAMETER VALUES: DEFAULT CASE

Runs were performed with parameter values that are representative for the micro-tidal inner shelf of Long Island, located at a latitude of $\sim 40^\circ$ N. The depth varies from $H_0 = 14$ m to $H_s = 20$ m over an inner shelf width of $L_s = 5.5$ km ($\beta = 1.1 \times 10^{-3}$). However, the default experiment is performed for an inner shelf slope which is approximately 60% of its observed value. The latter is a consequence of the fact that analysis of the saturation behavior of sfc is only possible up to this value of β . This aspect will be further discussed in section 3.5. The alongshore wind stress $\tau_{sy} = -0.4$ N m $^{-2}$, the offshore root-mean-square wave height $H_{rms,s} = 1.5$ m, the wave period $T = 11$ s and the offshore angle of wave incidence $\Theta_s = -20^\circ$. Values of the other parameters are: $r = 2.0 \times 10^{-3}$, $c_f = 3.5 \times 10^{-3}$, $\nu_b = 5.6 \times 10^{-5}$ s 2 m $^{-1}$, $\lambda_b = 0.65$, $\lambda_s = 7.5 \times 10^{-4}$ s 4 m $^{-3}$, $\alpha/\gamma = 9.5 \times 10^{-5}$ s 3 m $^{-3}$ and $p = 0.4$. The motivation for this choice has been discussed in the previous chapter. Growth rates and migration speeds are calculated for continuous storm conditions. In reality storms only occur during a certain time fraction (about 5%) and numbers would be a factor 20 smaller.

The nonlinear evolution for the default case was truncated at $J = 64$ and $N_j = 10$ (a total amount of 640 modes) and no subharmonics were included ($N = 1$). In the time integration a time step of about 1 full-storm year was used. For these values of the spectral parameters and time step computational stability was reached for bottom slopes up to 60% of realistic values. Both adding more modes and decreasing the time step did not change the solutions.

In section 3.4.2 the evolution of sfcf is analyzed for the default parameter values given. The sensitivity of the results to offshore wave characteristics (angle of wave incidence, root-mean-square wave height and wave period) and transverse bottom slope are presented in sections 3.4.3-3.4.5. Finally, in section 3.4.6 the effect of including subharmonics in the nonlinear analysis is investigated.

3.4.2 NONLINEAR ANALYSIS: DEFAULT CASE

The growth rates and migration speeds obtained with the linear model of chapter 2 were already presented in Figure 2.5. The run performed with the nonlinear model for the default setting ($N = 1$) used $k = k_p \sim 0.8 \text{ km}^{-1}$ of the initially most preferred mode as the smallest wavenumber in the spectral expansions. In total $J = 64$ longshore and $N_j = 10$ cross-shore eigenmodes are used. An individual mode is denoted by $(j/N, n_j)$, where $j = 1, 2, \dots, J$ and $n_j = 1, 2, \dots, N_j$. These modes are indicated by the dots in Figure 3.3.

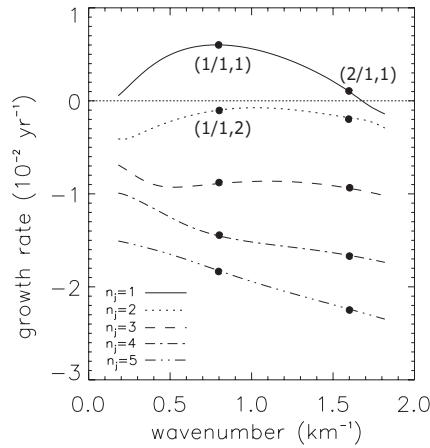


Figure 3.3: Linear growth rates for cross-shore mode n_j as a function of the longshore wavenumber. The most preferred mode is indicated by $(1/1, 1)$. The dots indicate modes that are included in the nonlinear analysis for $N = 1$. Note that the growth rate curves are identical to those in Figure 2.5.

The bottom pattern of the most preferred mode, the first superharmonic mode with $k = 2k_p$ and the second cross-shore mode with $k = k_p$ are shown in Figures 3.4a, 3.4b and 3.4c, respectively. These are three of the 640 bottom modes included in the nonlinear analysis. The total system which is solved, contains 4×640 algebraic equations, 640 differential equations and 5 equations for the longshore uniform variables ($k = 0$ mode).

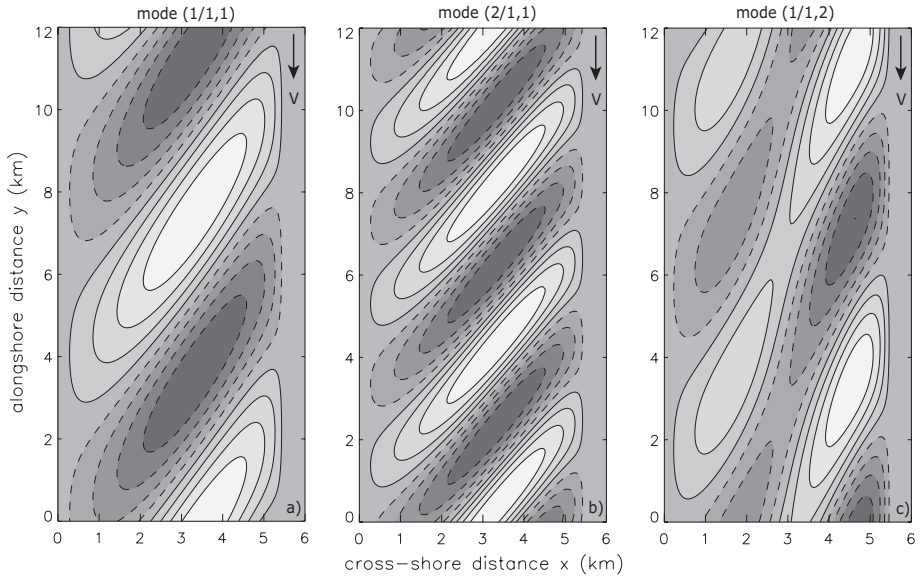


Figure 3.4: Bottom pattern (grayscale; light: crests, dark: troughs) for (a) mode $(1/1, 1)$, (b) mode $(2/1, 1)$ and (c) mode $(1/1, 2)$. The arrow indicates the direction of the basic state longshore velocity.

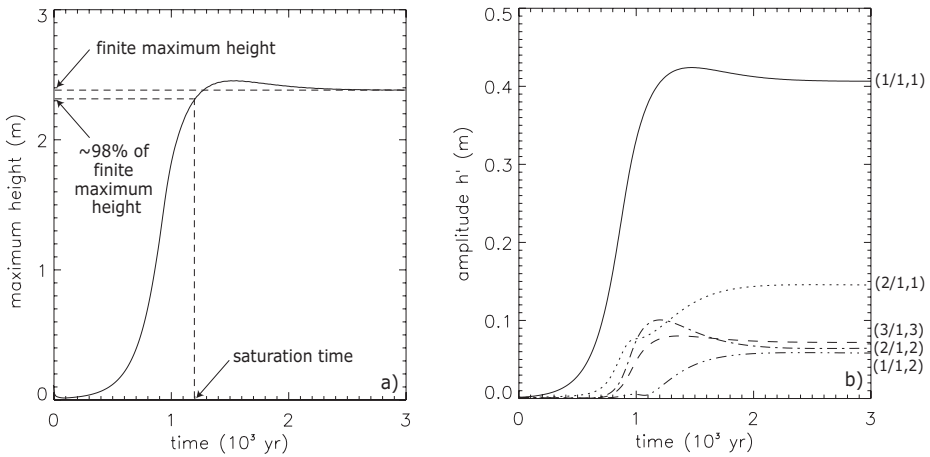


Figure 3.5: (a) Time evolution of the maximum height of the bedforms for the default case. The finite maximum height and saturation time are indicated by the dashed lines. (b) Time evolution of the amplitude of the five bottom modes, which have the largest amplitude at $t = 3 \times 10^3$ yr. Modes are denoted as $(j/N, n_j)$, where j is the longshore modenumber, $(N - 1)$ the amount of subharmonic modes included and n_j the cross-shore modenumber, respectively.

Figure 3.5a shows the time evolution of the maximum height (crest to trough) of the bedforms for the default case. All bottom modes included in the simulation have small (in the order of 1 mm) amplitudes at $t = 0$. In the initial stage the height of the bedforms increases exponentially, which is in accordance with linear theory. A deviation of this behavior for $t \rightarrow 0$ is due to the selection process (only after some time the most preferred mode will prevail). Next, a stage occurs where the bedform height grows more slowly, which is a consequence of nonlinear interactions. An interesting overshoot in bedform height is visible just before the saturated state is reached and the maximum height of the bedforms tends to a constant finite value of about 2.4 m. The saturation time is defined as the time needed to attain a height, which is 98% of the finite maximum height. In this case the saturation time is about 1200 years. In addition, Figure 3.5b shows the time evolution of the amplitude of the five bottom modes that are largest at the final time of the simulation ($t = 3 \times 10^3$ yr). It clearly demonstrates that e.g. the linearly damped modes (3/1,3), (2/1,2) and (1/1,2) become excited, which is due to the competition between different modes in the nonlinear stage of the evolution. Nonlinear competition is most apparent in the crossing of amplitudes of modes halfway the simulation. Note that the initially most preferred mode (1/1,1) is still the dominant one in the saturated state. Both the observed overshoot in bedform height and the crossing of modes were not present in the simulations by *Calvete and De Swart* (2003) for $N = 1$. This difference will be explained in section 3.5.

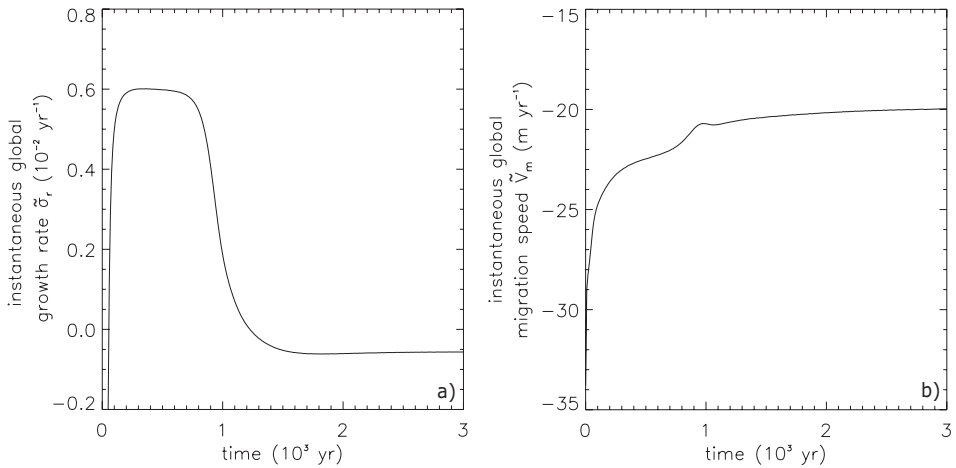


Figure 3.6: Time evolution of the instantaneous global (a) growth rate $\tilde{\sigma}_r$ and (b) migration speed \tilde{V}_m . Default case.

Figure 3.6 shows the temporal evolution of the instantaneous global growth rate and migration speed of sfc. The results indicate that initially the growth rate is negative, which can be understood from the linear analysis. The latter indicates that on the short term only mode (1/1,1) and (2/1,1) have positive growth rates, whereas all the other modes included will decay. It takes about 50 yr before the growth rate becomes positive and another 150 yr before self-organization has resulted in dominance of the initially fastest growing mode. In

the initial stage of the evolution, during a period of about 500 yr, growth corresponds to that predicted by the linear stability analysis and the height of the bedforms increases exponentially in time. After that nonlinear processes become important and cause a fast reduction in growth rate. In the finite stage sfcr exhibit no net growth and their migration has stabilized at about 20 m yr^{-1} , which is smaller than during the linear evolution. At the moment that the ordering of modes changes, the instantaneous global growth rate also changes and a jump occurs in the curve of the migration speed.

The bottom patterns for the default case at different stages in the long-term evolution are shown in Figure 3.7. After 50 yr sfcr start to emerge. After about 500 yr nonlinear processes become important and the bottom pattern becomes more asymmetrical, i.e., the seaward (downstream) flank becomes much steeper than the landward (upstream) flank. The sfcr migrate in the negative y -direction (in the direction of the mean storm-driven flow indicated by the arrow), during the initial evolution slightly faster than in the saturated state. Both the above-mentioned steepening of the lee sides and migration of sfcr are visible in the longshore profiles of depth at two times during the evolution (see Figure 3.8). The alongshore spacing of sfcr in the saturated state equals that of the initially most preferred mode.

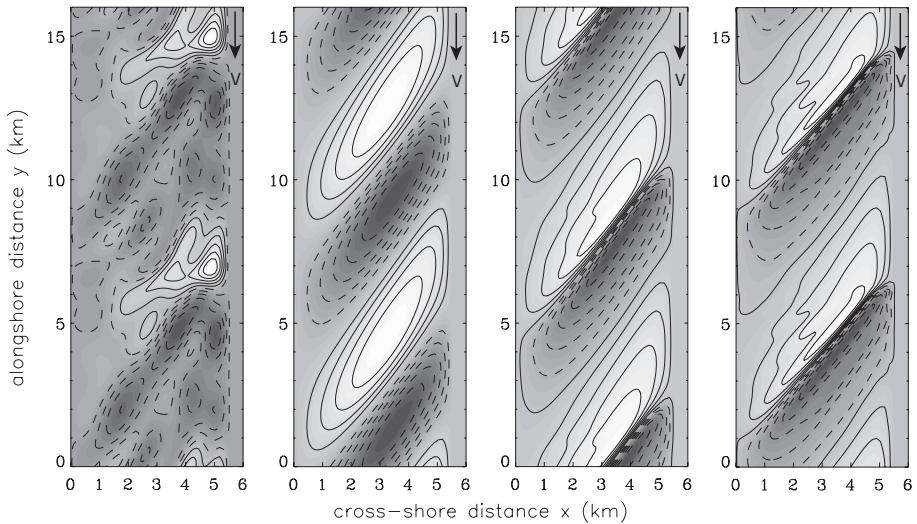


Figure 3.7: Bottom pattern (grayscale; light: crests, dark: troughs) at $t \sim 50, 500, 1000$ and 2000 yr. The arrow indicates the direction of the basic state longshore velocity. Default case.

The longshore uniform $k = 0$ mode plays a minor role in the dynamics, since its amplitude is only about 5% of that of the nonuniform perturbations. The longshore-averaged bottom profile (not shown) is slightly deeper near the shoreface and slightly shallower near the transition to the outer shelf (in the order of millimeters). Thus, hardly no sediment is transported to or away from the inner shelf. The incorporation of the $k = 0$ mode leads to a reduction in the longshore current velocity, but the effect is very small (less than 1%).

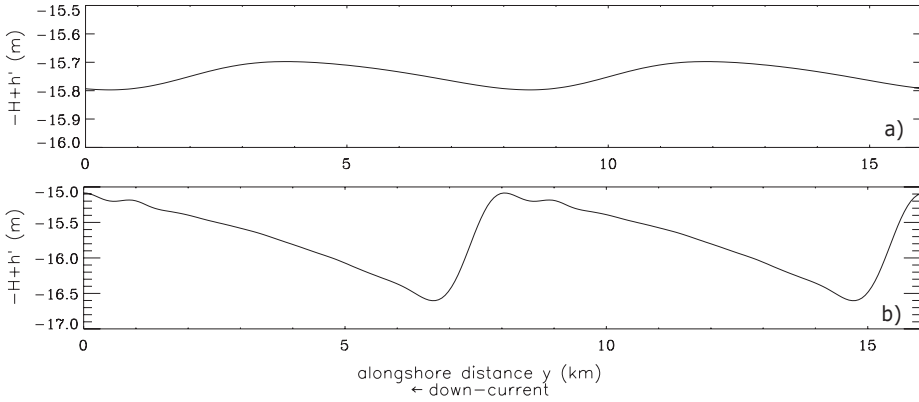


Figure 3.8: Longshore profiles of depth $-H + h'$ at a cross-shore location halfway the inner shelf. The profiles are taken at (a) $t \sim 500$ yr and (b) $t \sim 1000$ yr. Note the difference in vertical scale. Bedforms travel in the negative y -direction, from right to left. Default case.

3.4.3 SENSITIVITY TO OFFSHORE ANGLE OF WAVE INCIDENCE AND INNER SHELF SLOPE

Sensitivity of the default model results to Θ_s and β are investigated in this section. The angle is measured with respect to the shore-normal, where positive (negative) Θ_s indicate a clockwise (anti-clockwise) deviation (see Figure 2.2). A range of wave angles was examined, which covers the range of conditions observed. Furthermore, results are presented for $0 < \beta \lesssim 1 \times 10^{-3}$ (realistic value). Here, a variation in β (for definition see section 3.2) corresponds to a variation in H_s . All other parameters have their default values.

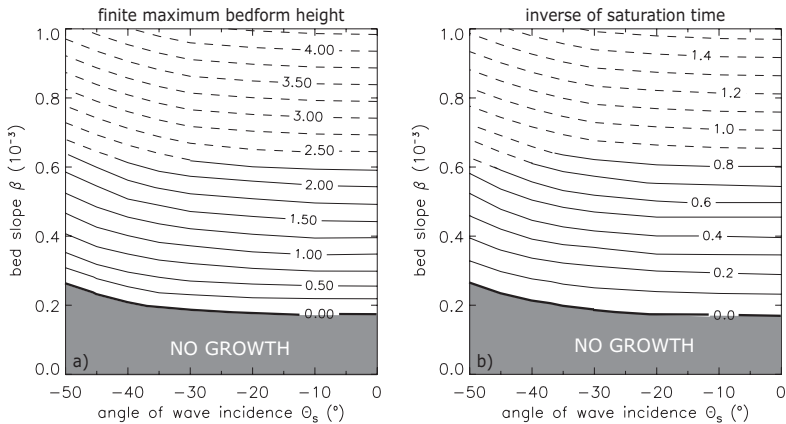


Figure 3.9: Contour plot of equal (a) finite maximum height (m) of sfcf and (b) inverse of saturation time (10^{-3} yr^{-1}) in the $\Theta_s - \beta$ plane. Solid lines: obtained with nonlinear model, dotted lines: extrapolated.

Simulations for a variation in Θ_s and β show that a critical transverse bottom slope β_{c1} has to be exceeded before sfcr start to develop. The time evolution of the maximum height of the bedforms for $\beta > \beta_{c1}$ is generally characterized by growth, reduction in growth and saturation. For values of β larger than β_{c2} the model blows up due to numerical instabilities. Here, β_{c1} and β_{c2} are functions of the model parameter values. Contour plots of the finite maximum bedform height and inverse of saturation time in the $\Theta_s - \beta$ plane are given in Figure 3.9a and Figure 3.9b, respectively. As in Figure 2.8, the critical transverse bottom slope β_{c1} increases from 1.8×10^{-4} to 2.7×10^{-4} for $\Theta_s = -2^\circ$ to $\Theta_s = -50^\circ$, respectively. Numerically stable solutions are obtained up to about 60% of realistic values of the inner shelf slope (solid lines) and are extrapolated into the regime of realistic bed slopes (dotted lines). Larger bottom slopes cause the growth to become faster and bedforms to attain a larger finite maximum height. For normally incident waves, evolving bedforms grow faster and they become higher than those formed under obliquely incident waves. Extrapolating to realistic values of the inner shelf slope and offshore angle of wave incidence, sfcr would reach a finite height somewhat larger than 4 m and their saturation would occur in about 700 yr. The overshoot in bedform height seen in Figure 3.5a is only present for waves, which approach the coast under a relatively small angle.

3.4.4 SENSITIVITY TO OFFSHORE WAVE HEIGHT AND INNER SHELF SLOPE

The finite maximum bedform height and inverse of saturation time in dependence of the inner shelf slope and offshore root-mean-square wave height are given in Figure 3.10.

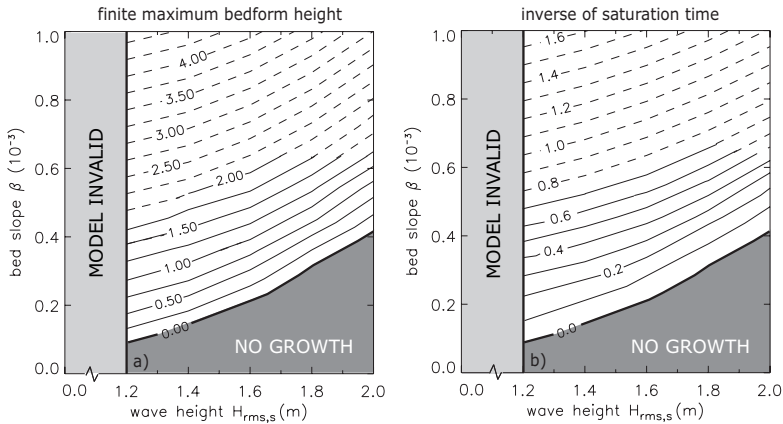


Figure 3.10: As Figure 3.9, but in the $H_{rms,s} - \beta$ plane.

A necessary condition for growth of sfcr is that a critical transverse bottom slope β_{c1} has to be exceeded. An increase in β_{c1} from 1.0×10^{-4} to 4.3×10^{-4} is obtained for an increase in root-mean-square wave height from 1.2 m to 2.0 m. For a slope which exceeds the critical value, evolving bedforms grow faster and become higher for smaller offshore wave heights. The dependence of the final height and the saturation time on the offshore wave height is

quite strong. In case of e.g. $H_{rms,s} = 1.2$ m and $\beta = 4.0 \times 10^{-3}$ sfcf attain a finite height of about 1.75 m, whereas for $H_{rms,s} = 2.0$ m and the same bed slope the critical bed slope is not exceeded and no bedforms will develop.

3.4.5 SENSITIVITY TO WAVE PERIOD AND INNER SHELF SLOPE

In Figure 3.11 contour plots are shown of the finite maximum bedform height and inverse of saturation time in the $T - \beta$ plane. As in Figure 2.11, the critical transverse bed slope β_{c1} increases from 1.0×10^{-4} to 2.7×10^{-4} for an increase in wave period from 8 s to 14 s. For larger bed slopes sfcf evolve and it appears that the shorter the wave period, the higher bedforms become and the faster they evolve. Sensitivity of results to changes in the wave period are moderate.

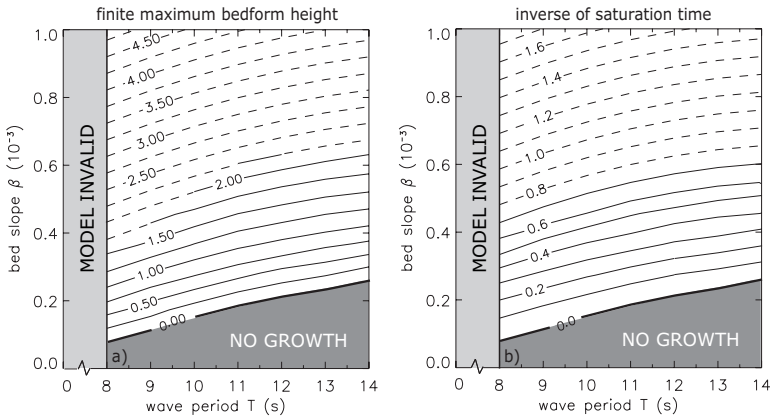


Figure 3.11: As Figure 3.9, but in the $T - \beta$ plane.

3.4.6 SENSITIVITY TO NUMBER OF SUBHARMONIC MODES

In the results presented so far, only the initially most preferred mode and its superharmonics were included in the truncated series of eigenmodes. It is likely however that also subharmonic modes, which have a longer wavelength than the initially most preferred mode, will influence the saturation behavior of sfcf. Therefore, model runs were performed including subharmonic modes. In order to reduce computational time, the runs were done for a smaller transverse bottom slope of the inner shelf than was used for the default case in section 3.4.2, i.e., $\beta = 2.7 \times 10^{-4}$ (about 25% of the realistic value). Values for the other parameters are as in the default experiment. For the small transverse bottom slope chosen, only a few modes are needed in the spectral analysis in case of $N = 1$ (no subharmonics): $J = 8$ and $N_j = 5$ (in total 40 modes). Note that the total system which is solved, contains 4×40 algebraic equations, 40 differential equations and 5 equations for the longshore uniform variables ($k = 0$ mode).

The initially most preferred mode for the chosen slope has an alongshore spacing of $\lambda_p \sim 10$ km, an e -folding time scale $T_g \sim 1100$ yr and a migration speed $V_m \sim -26$ m yr $^{-1}$. Saturation of the bedform height takes place after a period of ~ 9000 yr at a value of 0.57 m. The sensitivity of the saturation process to changes in the number of modeled subharmonic modes is investigated. The initially most preferred mode for runs including subharmonics is the $(N/N,1)$ mode. The spectral range $[0, 8k_p]$ is kept constant and thus with increasing N the spectral resolution changes such that $J = 8N$ (see Figure 3.12).

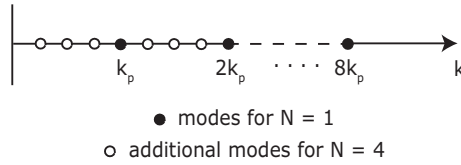


Figure 3.12: The spectrum of modes included in the nonlinear model. Closed circles include the fastest growing mode and superharmonics, open circles include $(N-1)$ subharmonics. In this example $N = 4$.

The temporal evolution of the maximum height of the bedforms is shown in Figure 3.13 for different N . Curves for $8 < N < 16$ are all located in between the curves for $N = 8$ and $N = 16$. Initially, sfcr grow exponentially in time, which is followed by saturation. The most important effect of adding subharmonic modes is an increase in the finite maximum height attained by the bedforms, which is now 0.66 m instead of 0.57 m. The saturation time becomes slightly longer. However, both the increase in the finite bedform height and saturation time are almost independent of the choice of number N .

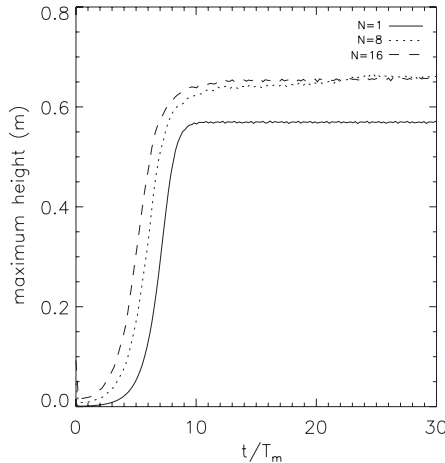


Figure 3.13: Maximum height of the bedforms versus t/T_m for model runs in which $(N-1)$ subharmonic modes are included. For the present bottom slope $T_m \sim 1000$ yr, whereas for the realistic slope $T_m \sim 100$ yr. Here, $\beta = 2.7 \times 10^{-4}$.

The time evolution of the amplitude of the individual modes resolved yields information about their mutual interactions. Figure 3.14 shows for $N = 10$ the time evolution of the five largest bottom modes at $t/T_m \sim 8$, $t/T_m \sim 15$, $t/T_m \sim 50$ and $t/T_m \sim 100$. For the present bottom slope ($\beta = 2.7 \times 10^{-4}$) the morphodynamic time scale $T_m \sim 1000$ yr, whereas for the realistic slope $T_m \sim 100$ yr.

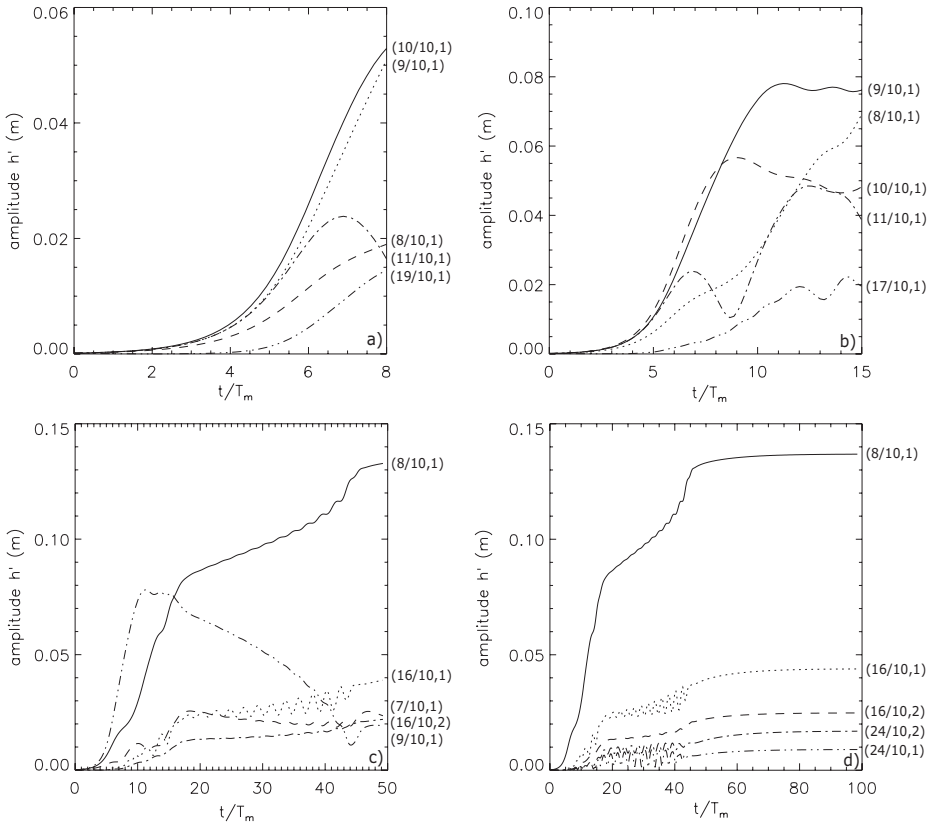


Figure 3.14: Time evolution of the amplitude of the five bottom modes, which have the largest amplitude at (a) $t/T_m \sim 8$, (b) $t/T_m \sim 15$, (c) $t/T_m \sim 50$ and (d) $t/T_m \sim 100$. For the present bottom slope $T_m \sim 1000$ yr, whereas for the realistic slope $T_m \sim 100$ yr. Modes are denoted as $(j/N, n_j)$, where j is the longshore modenummer, $(N - 1)$ the amount of subharmonic modes included and n_j the cross-shore modenummer, respectively. Here, $N = 10$ and $\beta = 2.7 \times 10^{-4}$.

During the first stage, up to about $t/T_m \sim 8$, the initially most preferred $(10/10, 1)$ mode has the largest amplitude and the growth is predominantly exponential. In the course of time non-linear processes become important and subharmonic modes, i.e., the $(9/10, 1)$ and $(8/10, 1)$ mode, become more dominant than the initially most preferred mode. Note that, although the bedform height is saturated for $t/T_m \gtrsim 8$, the amplitudes of the individual modes are not and thus the length scale and shape of the bedforms are still changing. Slightly after $t/T_m = 15$,

the $(9/10, 1)$ mode rapidly decreases in amplitude, whereas the $(8/10, 1)$ mode increases in amplitude and becomes dominant. Just before $t/T_m \sim 50$ the initially most preferred mode disappears from the graph and is no longer one of the five largest bottom modes. It takes a very long time before the amplitudes of the individual modes are more or less saturated. The wavelength of the saturated bedforms is dominated by the $(8/10, 1)$ mode and is approximately $\frac{10}{8} * 10 = 12.5$ km (see Figure 3.15). Furthermore, a difference in the height of individual crests and depths of individual troughs can be observed.

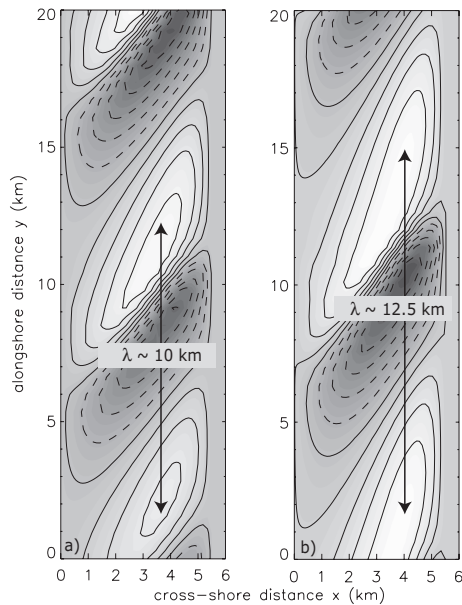


Figure 3.15: Bottom pattern (grayscale; light: crests, dark: troughs) at (a) $t/T_m \sim 8$ and (b) $t/T_m \sim 100$. For the present bottom slope $T_m \sim 1000$ yr, whereas for the realistic slope $T_m \sim 100$ yr. Here, $N = 10$. Note the difference in heights of individual crests and depths of individual troughs.

Information about the temporal evolution of the instantaneous global growth rate and migration speed in case $N = 1$ is given in Figure 3.16. The behavior is similar to Figure 3.6, only growth rates are smaller and saturation times longer due to the smaller transverse bottom slope of the inner shelf. The model has an initialization period, which is visible in the peak in the instantaneous global growth rate curve for small t .

Figure 3.17 shows the temporal evolution of the instantaneous global growth rate and migration speed for a case including subharmonic modes: $N = 10$. The shaded areas mark specific time periods during which a sudden change in growth rate and migration speed is visible. These changes are linked to a re-ordering of modes and will be discussed in section 3.5. Both the instantaneous global growth rate and migration speed seem to stabilize on the long term, where the latter is smaller than during the linear evolution.

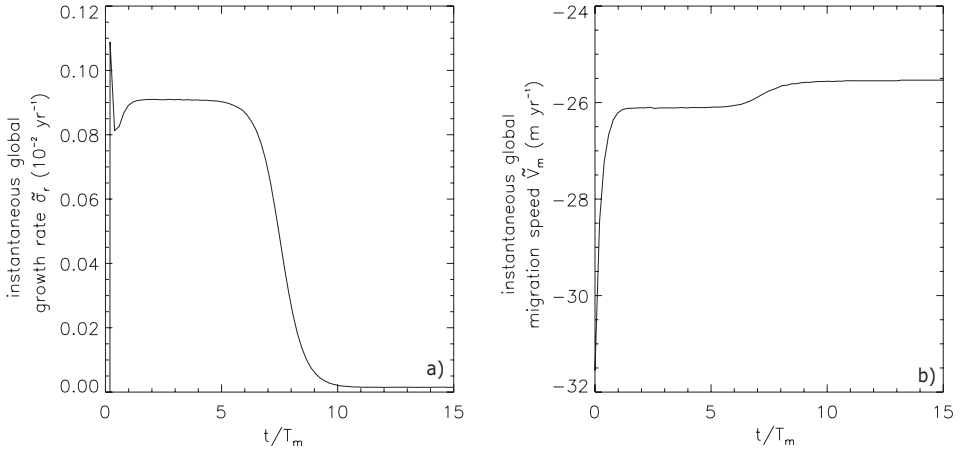


Figure 3.16: Time evolution of the instantaneous global (a) growth rate $\tilde{\sigma}_r$ and (b) migration speed \tilde{V}_m . Here, $N = 1$ and $\beta = 2.7 \times 10^{-4}$.

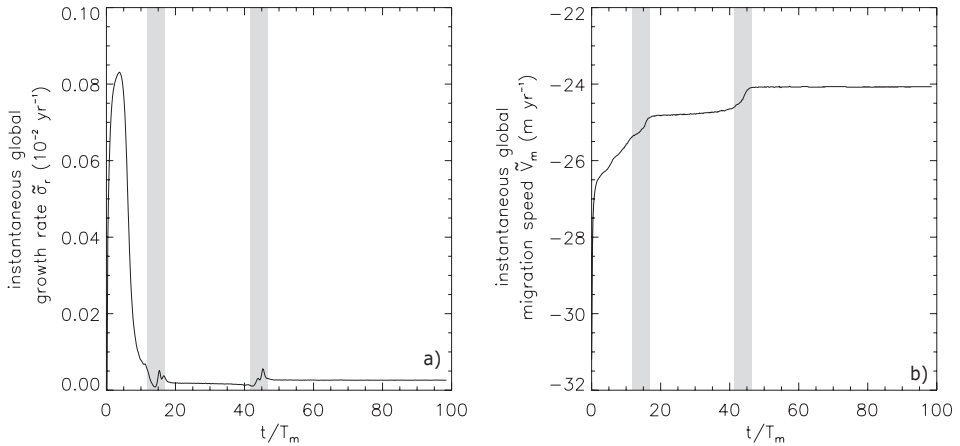


Figure 3.17: Time evolution of the instantaneous global (a) growth rate $\tilde{\sigma}_r$ and (b) migration speed \tilde{V}_m . Shaded areas indicate time periods during which jumps occur in the curves for $\tilde{\sigma}_r$ and \tilde{V}_m . Here, $N = 10$ and $\beta = 2.7 \times 10^{-4}$.

It appears that the time evolution of the amplitude of the five fastest growing modes depends strongly on the amount of subharmonics included in the calculations. As is visible in Figure 3.18, in case of $N = 8$, $N = 12$ or $N = 16$, a period of $t/T_m \sim 60$ is not sufficient to reach saturation of the amplitudes of individual modes, whereas for $N = 10$ amplitudes were saturated after that period. This sensitivity to N is surprising, as Figure 3.13 indicates that the saturation time scale for the bedform height shows only a very weak dependence on N .

In case $N = 8$, Figure 3.18d shows that on a time scale of $\sim 100T_m$ saturation of the amplitudes of the individual modes occurs. The five fastest growing modes do no longer cross and the $(7/8, 1)$ mode is by far the dominant one, which indicates a wavelength of the final bedforms of approximately $\frac{8}{7} * 10 = 11.4$ km.

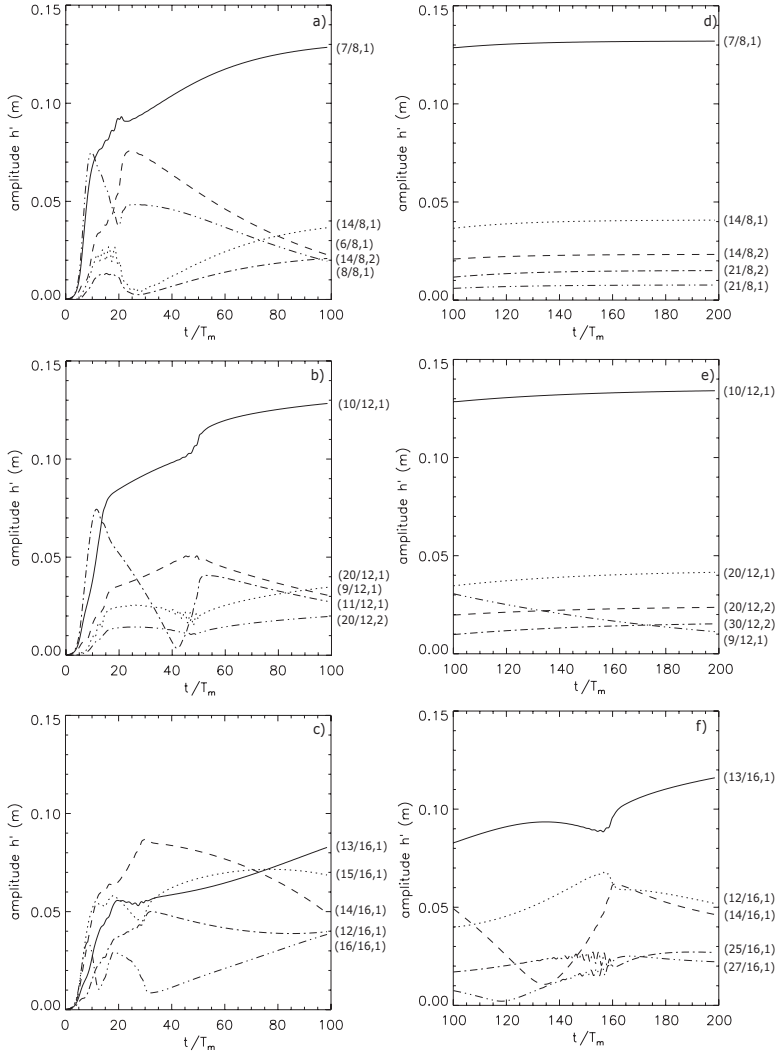


Figure 3.18: Time evolution of the amplitude of the five bottom modes, which have the largest amplitude (Left) at $t/T_m \sim 100$ for (a) $N = 8$, (b) $N = 12$ and (c) $N = 16$ and (Right) at $t/T_m \sim 200$ for (d) $N = 8$, (e) $N = 12$ and (f) $N = 16$. For the present bottom slope $T_m \sim 1000$ yr, whereas for the realistic slope $T_m \sim 100$ yr. Modes are denoted as $(j/N, n_j)$, where j is the longshore modenumber, $(N - 1)$ the amount of subharmonic modes included and n_j the cross-shore modenumber, respectively. Here, $\beta = 2.7 \times 10^{-4}$.

In case $N = 12$, a total period of $t/T_m \sim 200$ is sufficient to lead to the appearance of individual modes with saturated amplitudes. The significance of the $(9/12, 1)$ mode continuously decreases for $t/T_m \gtrsim 50$. The $(10/12, 1)$ mode is dominant in the final stage and indicates a wavelength of the final bedforms of approximately $\frac{12}{10} * 10 = 12.0$ km.

Figure 3.18f shows that if $N = 16$, even a time period of $t/T_m \sim 200$ is not enough to reach saturation of the amplitudes of the individual modes. Another period of $t/T_m \sim 100$ (see Figure 3.19) is necessary to reduce the nonlinear interactions between the modes, such that the dominant ones appear and the others disappear. Dominance of the $(13/16, 1)$ mode indicates a wavelength of the final bedforms of approximately $\frac{16}{13} * 10 = 12.3$ km. Summarizing, results obtained for different N indicate that the wavelength of bedforms in the saturated state is in the range of 11.5 – 12.5 km, which denotes a mild lengthening of bedforms in time.

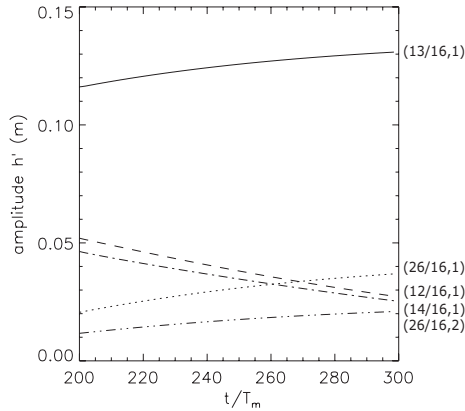


Figure 3.19: Time evolution of the amplitude of the five bottom modes, which have the largest amplitude at $t/T_m \sim 300$ for $N = 16$. For the present bottom slope $T_m \sim 1000$ yr, whereas for the realistic slope $T_m \sim 100$ yr. Modes are denoted as $(j/N, n_j)$, where j is the longshore modenummer, $(N - 1)$ the amount of subharmonic modes included and n_j the cross-shore modenummer, respectively.

A common trend in the experiments discussed above is that in the saturated state the second mode in amplitude has a longshore wavelength, which is half that of the dominant one. For the third mode in amplitude both the alongshore and cross-shore wavelength are twice as small as the dominant wavelength in the expansion. Apparently, the modes which are of significance in the final state, have length scales which are integer multiples of the dominant one.

A new and interesting phenomenon captured by the nonlinear model for runs including subharmonics, is the patchiness of sfcf during their stage towards saturation. Sfcf are also observed in patches. Stretches of the inner shelf where several sfcf are present are alternated with stretches where no sfcf occur. This was never obtained with previous models. A clear illustration is given in Figure 3.20, where the bottom patterns at $t/T_m \sim 8$ are given along a significant coastal stretch for runs including a different number of subharmonics.

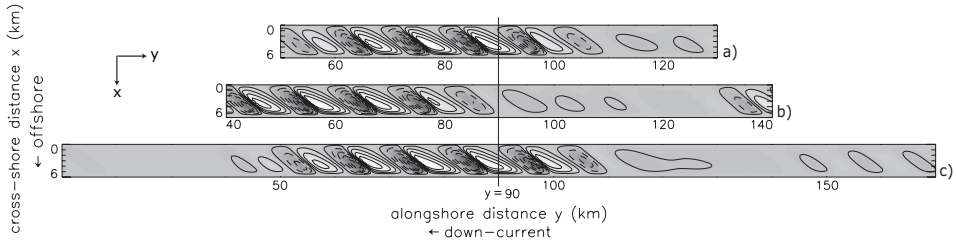


Figure 3.20: Bottom pattern (grayscale; light: crests, dark: troughs) at $t/T_m \sim 8$ for (a) $N = 8$, (b) $N = 10$ and (c) $N = 16$. For the present bottom slope $T_m \sim 1000$ yr, whereas for the realistic slope $T_m \sim 100$ yr. The shoreface is at the top and left is downstream. Here, the longshore extent of the domain is $\sim N\lambda_p$ and $\beta = 2.7 \times 10^{-4}$.

The figure illustrates that the patchiness itself is independent of the number of subharmonic modes included in the analysis. However, the precise coastal stretches where patches of sfcr occur are definitely different and depend strongly on the choice for N and time t . Parameter N is not clear from field data and thus the model results suggest that the detailed evolution of sfcr is only predictable for a finite amount of time. Figure 3.20 also illustrates that the height and orientation of individual sfcr vary within a patch of sfcr. The patchiness of sfcr is almost absent at a later stage in the evolution, e.g. $t/T_m \sim 20$, as shown in Figure 3.21. The longshore profiles of depth at two different times during the evolution and for different N (Figure 3.22), visualize in another way the variation in patchiness and bedform height.

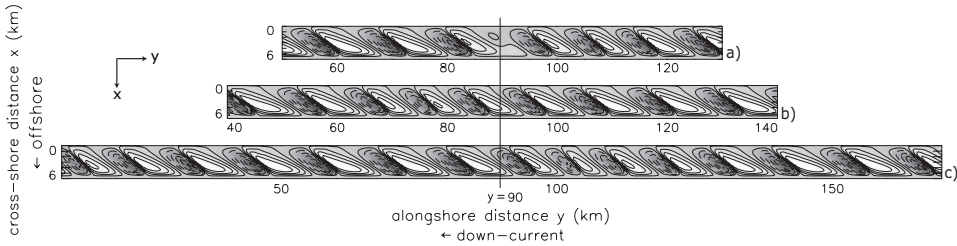


Figure 3.21: Bottom pattern (grayscale; light: crests, dark: troughs) at $t/T_m \sim 20$ for (a) $N = 8$, (b) $N = 10$ and (c) $N = 16$. For the present bottom slope $T_m \sim 1000$ yr, whereas for the realistic slope $T_m \sim 100$ yr. The shoreface is at the top and left is downstream. Here, the longshore extent of the domain is $\sim N\lambda_p$ and $\beta = 2.7 \times 10^{-4}$.

Whether sfcr occur in patches or not is strongly related to the interactions between different modes included in the nonlinear analysis. Modulation behavior will occur when (1) the spectrum of growing modes is sufficiently narrow and (2) modes that have significant amplitudes also have comparable wavelengths and amplitudes. The narrowness of the spectrum appears to be sufficient for all the performed experiments including subharmonic modes. The second requisite is obeyed during the transient stage of the evolution, for an example see Figure 3.14 in case that $N = 10$. Here, after a period of $t/T_m \sim 8$ the $(10/10, 1)$ mode and $(9/10, 1)$ mode (thus modes with comparable wavelengths) have comparable amplitudes. However, at

a later stage in the evolution (e.g. $t/T_m \sim 20$), the amplitudes of modes with successive modenumbers are not that close. In fact, obtained patterns are a superposition of the dominant mode and its superharmonics and these imply ridge activity everywhere on the inner shelf.

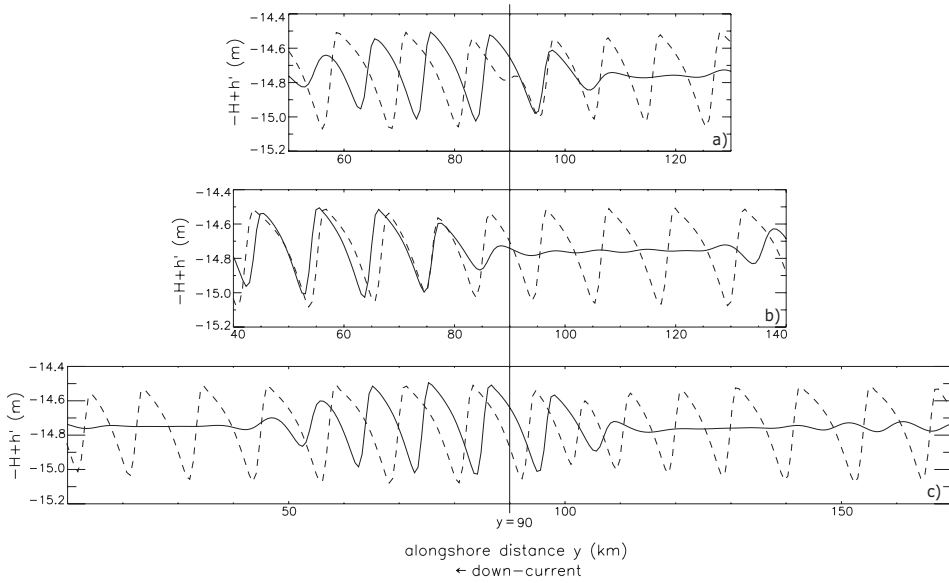


Figure 3.22: Longshore profiles of depth $-H + h'$ at a cross-shore location halfway the inner shelf. The profiles are taken at $t/T_m \sim 8$ (straight lines) and $t/T_m \sim 20$ (dashed lines) and given for (a) $N = 8$, (b) $N = 10$ and (c) $N = 16$. Bedforms travel in the negative y -direction, from right to left. Here, the longshore extent of the domain is $\sim N\lambda_p$ and $\beta = 2.7 \times 10^{-4}$.

The bedforms behave as anormal dispersive waves, which means that shorter waves migrate faster. This was already illustrated in Figure 2.5b, where the absolute value of the migration speed increases for an increase in wavenumber. Another consequence of the anormal dispersion of sfcf is that their group velocity is larger than their phase velocity. For the most preferred mode the migration speed (which is the phase velocity of the bedforms) was given as $\sim 26 \text{ m yr}^{-1}$ in the down-current direction, whereas the group velocity appears to be $\sim 31 \text{ m yr}^{-1}$ downstream. Modulation behavior is the result, which is illustrated in Figure 3.23, where the bottom patterns at different times are shown for $N = 10$. The bedforms (which occur in patches) migrate in time and the difference in group and phase velocity is visible in changes in the appearance of the patch in time. More specifically, the height of an individual crest (denoted as I) changes in time, which is due to the fact that it moves from left to right with respect to the group. The decrease in migration speed with an increase in bedform height, as e.g. visualized in Figure 3.13 together with Figure 3.17, is also typical for anormal dispersive waves.

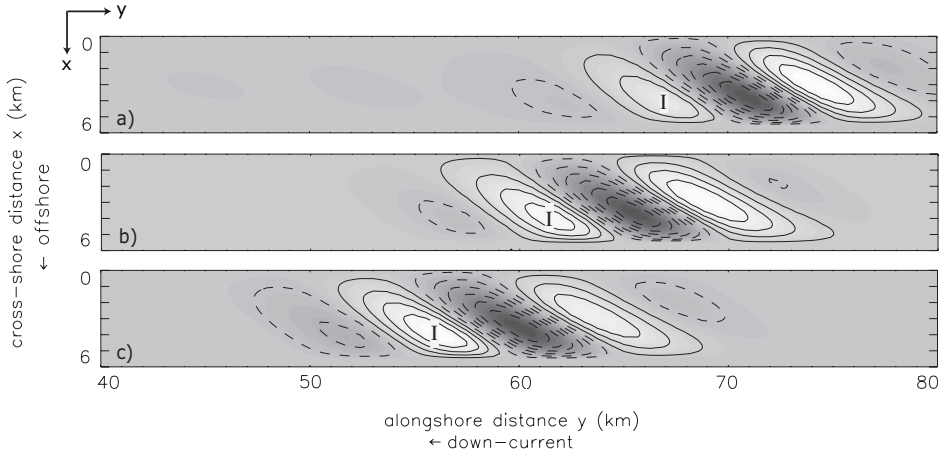


Figure 3.23: Bottom pattern (grayscale; light: crests, dark: troughs) at (a) $t/T_m \sim 1.0$, (b) $t/T_m \sim 1.2$ and (c) $t/T_m \sim 1.4$. The shoreface is at the top and left is downstream. One wave group is shown, which travels downstream with group velocity $\sim 31 \text{ m yr}^{-1}$. Also an individual crest, as denoted by I, migrates downstream, with phase velocity $\sim 26 \text{ m yr}^{-1}$, which is smaller than the group velocity. Anormal dispersion behavior is observed: individual crests/troughs enter the wave group on the left-hand side, pass through the group to leave again on the right-hand side. This is illustrated by the change in height of crest I in time. Here, $N = 10$ and $\beta = 2.7 \times 10^{-4}$.

3.5 DISCUSSION

In the previous chapter a physical interpretation has been given of results obtained with a linear morphodynamic model, which models the initial development of sfc. In this model wave characteristics are calculated with a shoaling-refraction model. The sensitivity of the initial evolution of sfc to offshore wave characteristics and the transverse bottom slope of the inner shelf was discussed. In the present chapter the simulations are extended into the nonlinear regime, which yields information about the finite amplitude behavior of sfc. Therefore, here a physical interpretation is given of the ridge saturation process and the sensitivity of the latter to a change in offshore wave properties and the inner shelf slope. The analysis of the potential energy balance of the bedforms, as described in section 3.3.3, is a helpful tool for this and is performed for $\beta = 2.7 \times 10^{-4}$, $J = 8$ and $N_j = 5$. All other parameters have their default values. The potential energy balance analysis is also used to interpret the results obtained with different numbers of subharmonic modes. In addition, various model limitations are discussed and results are compared to field observations.

3.5.1 PHYSICAL INTERPRETATION

NO SUBHARMONIC MODES

Simulations without subharmonic modes show that, starting from an initial bottom without bedforms, morphodynamic self-organization results in the formation of migrating sfc. Due

to nonlinear effects, the initial exponential growth of the height of sfcf (see chapter 2) reduces, such that their height tends to a constant value. Sfcf grow (decay) when the instantaneous global growth rate, as defined in equation (3.20), is positive (negative). In the initial stage of evolution the production P of potential energy due to the transport of sediment is larger than the loss of potential energy Δ . As bedform amplitudes grow, P and Δ change in such a way that saturation will occur when $\tilde{\sigma}_r = 0$, i.e., the generation of potential energy is equal to the loss of potential energy. In Figure 3.24a both P and Δ , distinguished by their bedload and suspended load part (subscripts b and s , respectively), are plotted as a function of time for the default case without subharmonics ($N = 1$). Also the sum $P + \Delta$ is shown.

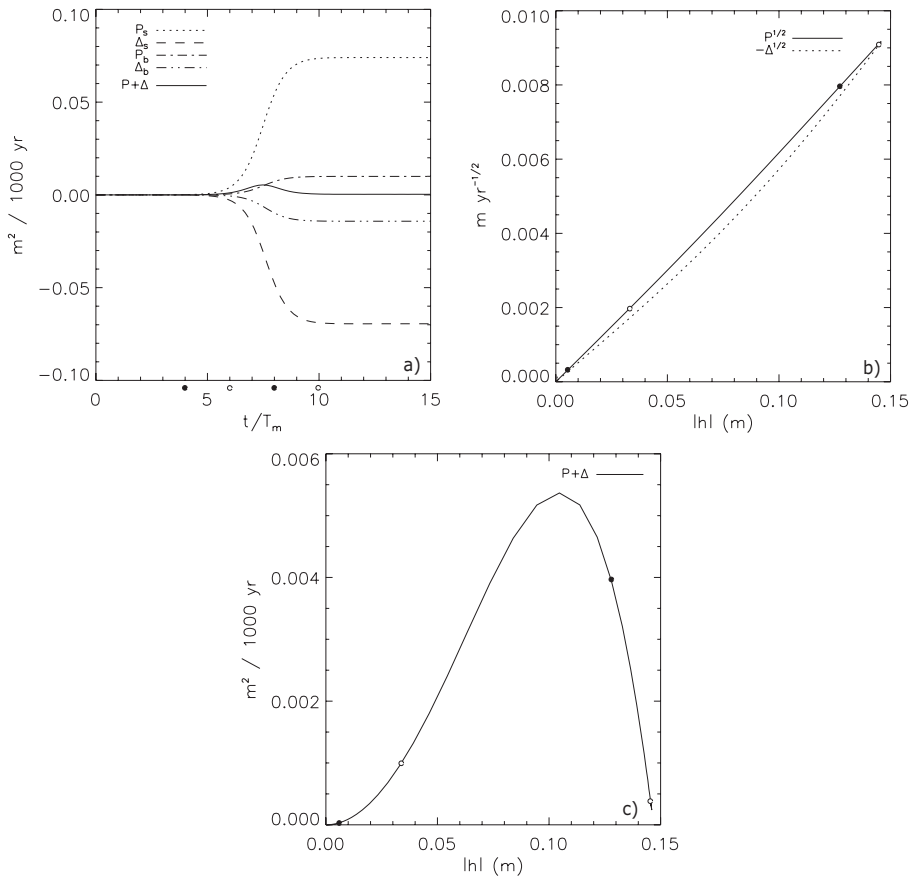


Figure 3.24: (a) Time evolution of production and dissipation terms due to suspended load and bedload sediment transport and their sum. The alternative closed and open circles below the time axis are positioned at $t/T_m \sim 4$, $t/T_m \sim 6$, $t/T_m \sim 8$ and $t/T_m \sim 10$. These times are also indicated in the two other subplots. For the present bottom slope $T_m \sim 1000$ yr, whereas for the realistic slope $T_m \sim 100$ yr. (b) Square root of the production and dissipation terms as a function of $|h|$. (c) The sum ($P + \Delta$) as a function of $|h|$. Here, $N = 1$ and $\beta = 2.7 \times 10^{-4}$.

During the linear stage of the evolution the separate production and dissipation terms are small and only slowly increase. In order to have growth, $P + \Delta > 0$. The gap between total production and total dissipation is largest during the stage of the evolution in which strong nonlinear interactions occur and the growth rate rapidly decreases. Saturation occurs when production and dissipation terms exactly balance, i.e., $\tilde{\sigma}_r = 0$. Full saturation takes longer than the time period shown in the graph, as the growth rate is slowly approaching zero. Interesting to notice is that in the saturated state $|P_s| > |\Delta_s|$, but $|P_b| < |\Delta_b|$, implying that suspended load transport terms still induce net production of potential energy, while bedload transport terms cause a net loss of potential energy. Furthermore, the loss of potential energy due to bed slope-induced sediment transports is necessary to compensate for the production of potential energy by advective suspended load transport. Figure 3.24b shows $P^{1/2}$ and $-\Delta^{1/2}$ as a function of $|h|$. Note that the time that the system needs to pass through the part of the curve for relative small bar amplitude is short compared to the time needed to approach the end of the curve. The alternative closed and open circles below the time axis in Figure 3.24a represent four specific time values, which are also plotted in Figure 3.24b,c. Initially, P is larger than $-\Delta$ and significant bar growth occurs. On the longer term both curves approach each other and cross for $|h| \sim 0.15$ m. Here, bar growth ceases and the final balance between P and Δ is reached. The latter is clear from Figure 3.24c in which the sum $P + \Delta$ is plotted as a function of $|h|$. The sum increases to reach a maximum at $|h| \sim 0.10$ m, subsequently decreasing to become almost zero at $|h| \sim 0.15$ m.

Experiments were carried out for different values of the transverse bottom slope of the inner shelf and offshore wave properties (all other parameters have their default values). All results indicate an almost linear relation between the final height of sfcR and the transverse slope β . Moreover, the saturation time decreases for a higher transverse slope, i.e., the saturation time $\sim \beta^{-1}$. The same trend was found with the model in which wave properties were governed by a parameterization. Sensitivity experiments show longer saturation times and lower finite bedform heights if the offshore wave height is increased. This can be understood by considering the magnitude of the production and dissipation of potential energy. The maximum ridge height in the saturated state and the saturation time depend on the competition between production (P_s and P_b , of which P_s is dominant) and dissipation ($|\Delta_s|$ and $|\Delta_b|$, of which $|\Delta_s|$ is dominant). Term P_s is proportional to $U_w^3 V$, term $|\Delta_s|$ to U_w^5 . Note that V is inversely proportional to U_w due to frictional effects. For an increase in the offshore wave height, U_w increases, as it is proportional to $H_{rms,s}$. Both P_s and $|\Delta_s|$ increase, but the ratio $P_s/|\Delta_s|$ decreases, causing a smaller finite bedform height and longer saturation time in case of larger $H_{rms,s}$. Note that in the model of *Garnier et al.* (2006) for nearshore sand bars the opposite behavior occurs, i.e., the ratio $P_s/|\Delta_s|$ increases with increasing $H_{rms,s}$. This is attributed to the fact that in their model the longshore current V , which is an important factor for P_s , is driven by wave-induced radiation stresses, rather than by wind. The consequence of this forcing mechanism is that V increases (faster than linear) with $H_{rms,s}$. Therefore, in case of larger offshore wave heights, nearshore sand bars reach larger finite heights and saturate faster. Model results indicate that an increase in the height of sfcR causes a decrease in their migration, which is a consequence of the fact that sfcR show anomalous dispersion behavior. For such waves, e.g. capillary waves (*Crapper*, 1984) and alternate bars in rivers (*Schielen et al.*, 1993), it is known that the phase speed decreases with increasing wave height.

ROLE OF SUBHARMONIC MODES

Results for model simulations including subharmonic modes show a significant effect on the dynamics of sfcr. In Figure 3.17 sudden changes in the instantaneous global growth rate and migration speed of sfcr were observed (shaded areas) in case of $N = 10$. To further understand these jumps and the behavior of the bedforms, their potential energy balance is analyzed. Results are shown in Figure 3.25.

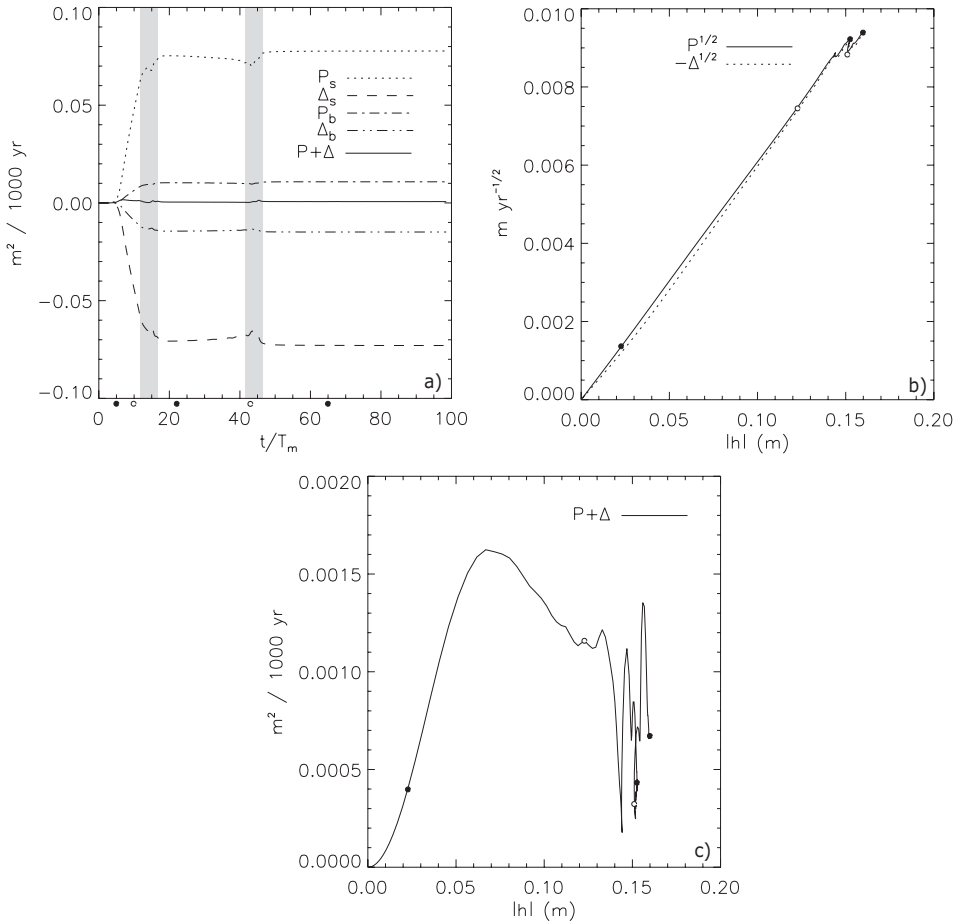


Figure 3.25: (a) Time evolution of production and dissipation terms due to suspended load and bedload sediment transport and their sum. Shaded areas indicate time periods during which jumps occur in all the curves. The alternative closed en open circles below the time axis are positioned at $t/T_m \sim 5$, $t/T_m \sim 10$, $t/T_m \sim 22$, $t/T_m \sim 43$ and $t/T_m \sim 65$ (after $t/T_m \sim 65$ no changes occur). These times are also indicated in the two other subplots. For the present bottom slope $T_m \sim 1000$ yr, whereas for the realistic slope $T_m \sim 100$ yr. (b) Square root of the production and dissipation terms as a function of $|h|$. (c) The sum $(P + \Delta)$ as a function of $|h|$. Here, $N = 10$ and $\beta = 2.7 \times 10^{-4}$.

In Figure 3.25a time series are shown of the gain and loss of potential energy due to bed-load and suspended load sediment transport, respectively. The time periods during which jumps occur are marked. These jumps represent significant changes in competitive behavior of individual bottom modes included in the nonlinear analysis, as is clear from Figure 3.14. In Figure 3.25b the jumps are also visible in the curves around $|h| = 0.15$ m. Note that the time that the system needs to pass through the part of the curve for relative small bar amplitude is short compared to the time needed to approach the end of the curve. The alternative open and closed circles below the time axis in Figure 3.25a represent five specific time values, which are also plotted in Figure 3.25b,c. Around saturation time the increase in $|h|$ is rather gradual. From Figure 3.25c it seems that a balance between production and dissipation is not reached. This, however is due to numerical accuracy, as the absolute error in the computation of both the production and dissipation term is about $3 \times 10^{-7} \text{ m}^2 \text{ yr}^{-1}$. Performing the potential energy analysis for runs including different amount of subharmonic modes (results not shown) all show the same behavior. The gross characteristics of sfc, e.g. instantaneous global growth rate, instantaneous global migration speed, alongshore spacing and finite amplitude, are a robust model result, independent of the amount of subharmonic modes included. However, changes in the competition between individual modes are quite unpredictable and also very dependent on the amount of subharmonic modes. As the bottom evolution is strongly dependent on parameter N , the evolution of sfc can only be predicted for a finite amount of time.

The lengthening of patterns in the course of time is consistent with that found in other nonlinear morphodynamic models, e.g. that of *Calvete and De Swart* (2003) for sfc, that of *Coco et al.* (2004) for beach cusps, that of *Murray and Thieler* (2004) for sorted bedforms, that of *Ashton and Murray* (2006) for shoreline sand waves and the model of *Garnier et al.* (2006) for nearshore sand bars. The shift in length scale is similar as in *Coco et al.* (2004), but in the other studies the lengthening is larger.

NUMERICAL RESOLUTION PROBLEMS

As stated before, the model runs are performed for an inner shelf bottom slope, which is smaller than the observed one. This is the consequence of the occurrence of numerical instabilities for large bottom slopes of the inner shelf. Sometimes numerical instabilities can be overcome by taking into account more longshore or cross-shore modes or by decreasing the time step in the nonlinear calculations.

For a bottom slope of the inner shelf $\beta = 5.5 \times 10^{-4}$, taking into account $J = 8$ alongshore modes is not sufficient to prevent the occurrence of unbounded solutions. However, increasing the amount of alongshore modes to $J = 16$ yields saturation behavior, as can be seen in Figure 3.26a. The time evolution of the five bottom modes, which have the largest amplitude at $t/T_m \sim 1.5$, is shown in Figure 3.26b for $J = 8$. Similarly, Figure 3.26c shows for $J = 16$ the time evolution of the five largest bottom modes at $t/T_m \sim 2.0$. Once the smallest length scale, i.e., mode $(8/1, 5)$, starts to grow very rapidly, instability behavior occurs for $J = 8$. Clearly, in case that $J = 16$, normal saturation behavior occurs.

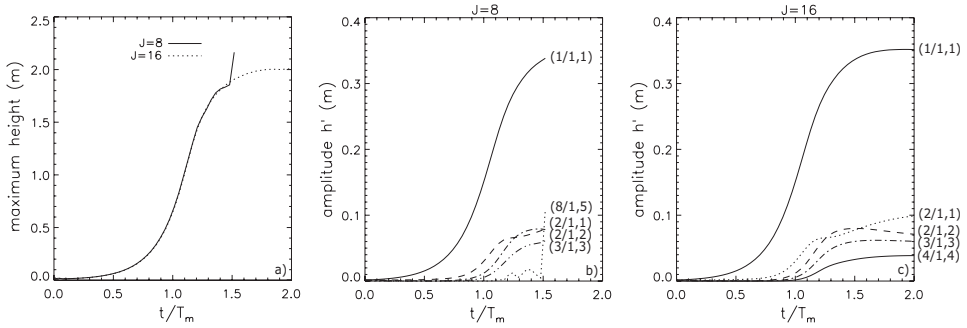


Figure 3.26: (a) Time evolution of the maximum height of the bedforms for $J = 8$ and $J = 16$, $N_j = 5$, $N = 1$ and $\beta = 5.5 \times 10^{-4}$. Time evolution of the amplitude of the five bottom modes, which have the largest amplitude at (b) $t/T_m \sim 1.5$ for $J = 8$ and at (c) $t/T_m \sim 2.0$ for $J = 16$. Modes are denoted as $(j/N, n_j)$, where j is the longshore modenummer, $(N - 1)$ the amount of subharmonic modes included and n_j the cross-shore modenummer, respectively. For the present bottom slope $T_m \sim 1000$ yr, whereas for the realistic slope $T_m \sim 100$ yr.

The bottom patterns at $t/T_m \sim 1.5$ ($J = 8$) and $t/T_m \sim 2.0$ ($J = 20$) are shown in Figure 3.27 and this figure affirms the dominance of the smallest length scale in the exploding case.

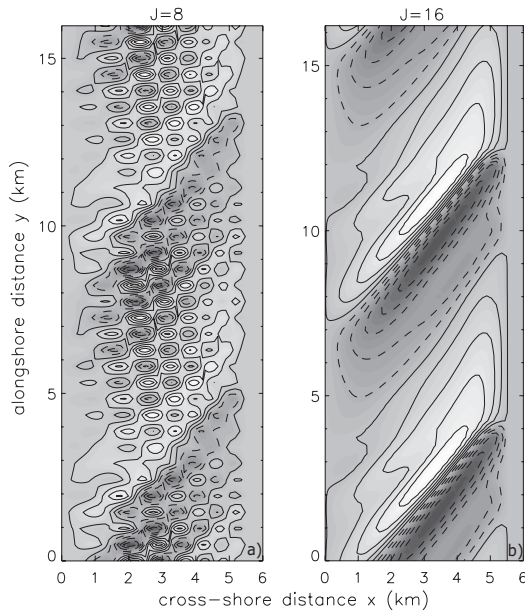


Figure 3.27: Bottom pattern (grayscale; light: crests, dark: troughs) for (a) $J = 8$ and (b) $J = 16$ at $t/T_m \sim 1.5$. Here, $N_j = 5$, $N = 1$ and $\beta = 5.5 \times 10^{-4}$.

3.5.2 MODEL LIMITATIONS

In chapter 2 several model limitations have been mentioned. All of these also apply to the present study, except for the fact that here a nonlinear stability analysis is performed, which also describes the long-term evolution of sfc. Several additional limitations, related to the nonlinear part of the model, are discussed in this section.

Using a measured value of the transverse bed slope, solutions become unbounded before the saturated state is reached. The results presented in this chapter were obtained with a version of the model in which interactions between waves and growing bedforms were ignored. The latter will be considered in the next chapter. Nonlinear experiments including wave-bedform feedbacks revealed spurious modes in the linear analysis, which have to be filtered. When incorporated in the nonlinear model, sfc continue to grow on the long term and numerical instabilities arise before the saturated state is reached. An explanation for the latter is that stirring of sediment by waves increases with increasing ridge height. This tendency will be counteracted by e.g. wave breaking, a process which is not yet implemented in the model.

The spectral method itself is also subject to limitations. The solutions of the linear system, which are used as expansion modes, are dependent on the specific parameter values used. Simulations in which strong, mild and weak storms alternate, as will be the case in reality, are feasible, but require different eigenmodes for the different realizations. Thus, several transformations between the spectral domain and the physical space have to be performed.

Note that the present model assumes a constant mean sea level, whereas in several studies (cf. *Swift and Field, 1981; McBride and Moslow, 1991*) it is argued that sea level changes during the Holocene play an important role in the evolution of sfc. To assess the sensitivity of model results to different sea level stands, runs were performed using different cross-shore bottom profiles. The latter were constructed by generalizing the 'Bruun rule' (*Bruun, 1954, 1962*), following concepts discussed in *Masetti et al. (2008)*. Starting from a given profile, a sea level rise Δ_s will cause the new depth of the outer shelf to become $H_s + \Delta_s$ (Figure 3.28).

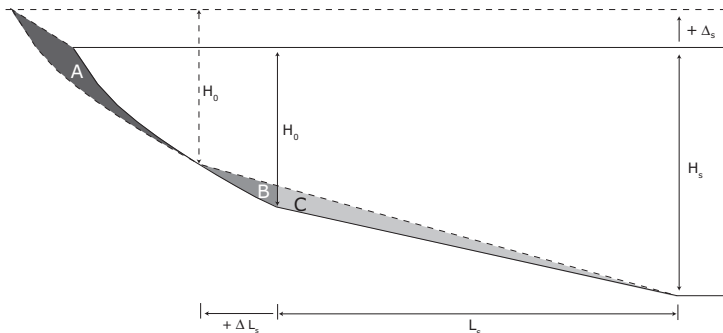


Figure 3.28: Sketch of the evolution of the shelf geometry under sea level rise. In case of *Bruun (1954)*: $A = B$. In case of *Masetti et al. (2008)*: $A = B + C$.

Second, the depth at the transition from shoreface to inner shelf remains unchanged (value H_0), but its location shifts landward (distance ΔL_s). Third, the depth profile between coastline and inner shelf maintains its equilibrium shape and it is shifted upward and landward. The distance ΔL_s is calculated by imposing that the total volume of sand per unit width between coast and outer shelf remains unchanged. This results in a new transverse bottom slope β of the inner shelf (larger for positive Δ_s). Experiments for different values of Δ_s were performed, starting from the default situation with subharmonics ($N = 10$). It was found that the overall behavior of the model does not change if Δ_s is varied. The main quantitative changes are that the height of the ridges increases (from 0.65 m to 2.2 m if $\Delta_s = +1$ m) and the saturation time scale decreases. This is mainly caused by the increase of β .

The reconstruction method we applied is highly idealized, but nevertheless yields a first idea of how sfcf might respond to changes in mean sea level. The numerical model of *Masetti et al.* (2008) is more advanced: it calculates the explicit time dependence of bottom profiles under the influence of sea level rise and also accounts for the underlying stratigraphy. Furthermore, the 'Bruun rule' often yields results that do not comply with observations, because it ignores three-dimensional and site-specific aspects (*Cooper and Pilkey*, 2004). Ultimately, profile reconstructions should be tested against data. Such information however is not available for the Long Island shelf.

3.5.3 COMPARISON WITH FIELD OBSERVATIONS

Field data on both the morphological evolution and the hydrodynamics are rather scarce. Comparison between model results and field data is therefore limited. Generally, observations show patches of 4 – 8 sfcf. In the present study we were able to reproduce the patchiness of sfcf, which was never done before. The number of sfcf per patch is in quite good agreement with the field data. The spatial patterns of the finite-amplitude sfcf exhibit typical asymmetric profiles with steep slopes at the downstream sides. Extrapolating default model results to the realistic inner shelf bottom slope yields bedforms with a finite height of ~ 4 m and a saturation time scale of ~ 700 yr. These values have the correct order of magnitude if compared with field data (e.g. *Duane et al.*, 1972).

3.6 CONCLUSIONS

In this chapter the long-term evolution of sfcf has been investigated and the sensitivity of model results to offshore wave properties and the inner shelf bed slope has been explored. For any forcing conditions (wind, waves) a critical transverse bed slope has to be exceeded before sfcf will grow. Once this critical bed slope is exceeded, sfcf initially form as free morphodynamic instabilities and their height increases exponentially in time. On the long term sfcf attain a finite height which becomes constant and they exhibit asymmetric profiles with steep lee sides. Numerical stable solutions could be obtained up to about 60% of the observed bed slope (in case of no subharmonics). For larger values of β solutions become singular at some point during the evolution. Instability behavior is related to a rapid growth of the smallest length scale included in the nonlinear analysis. Analysis of the potential energy balance of sfcf shows that bed slope-induced sediment transports are crucial for the saturation process.

If subharmonic modes are included, sfc_r also show saturation and the finite height increases with about 15% compared to simulations without subharmonics. However, the initially most preferred mode is no longer dominant in the saturated state. It even yields no significant contribution to the saturated bedforms. Due to nonlinear interactions subharmonic modes dominate and cause a 20% increase in the distance between successive sfc_r in time. Furthermore, the saturation time of the amplitudes of individual modes is much longer than the time scale on which the ridge height saturates. Considering the age of sfc_r, time scales of order $10 T_m$ are realistic, which suggests that observed sfc_r have not reached their final stage of development yet. In the transient stage sfc_r occur in patches and the number of ridges per patch is in the observed range of 4 – 8. Results indicate that the detailed evolution of sfc_r is only predictable over a finite time interval, whereas the overall characteristics (e.g. instantaneous global growth rate, instantaneous global migration speed, finite bedform height and alongshore spacing) are also predictable for long time scales. Model results and observations are in fairly good agreement.

APPENDIX

3.A EXPRESSION FOR OPERATOR \mathcal{N}

The partial differential equations describing the evolution of the flow, mass, concentration and bottom can be symbolically written as

$$\mathcal{S} \frac{\partial \Psi'}{\partial t} = \mathcal{L} \Psi' + \mathcal{N}(\Psi') \quad (3.A-1)$$

The expressions for operators \mathcal{S} and \mathcal{L} are the same as in chapter 2 and given in appendix 2.B. New are the nonlinear contributions of the vector $\mathcal{N} = (\mathcal{N}_1, \mathcal{N}_2, \mathcal{N}_3, \mathcal{N}_4, \mathcal{N}_5)$:

$$\begin{aligned} \mathcal{N}_1 &= u' \frac{\partial u'}{\partial x} + v' \frac{\partial u'}{\partial y} + \frac{rU_w u'}{H - h'} - \frac{rU_w u'}{H}, \\ \mathcal{N}_2 &= u' \frac{\partial v'}{\partial x} + v' \frac{\partial v'}{\partial y} + \frac{rU_w (V + v')}{H - h'} - \frac{rU_w V}{H - h'} - \frac{rU_w v'}{H}, \\ \mathcal{N}_3 &= -u' \frac{\partial h'}{\partial x} - h' \frac{\partial u'}{\partial x} - v' \frac{\partial h'}{\partial y} - h' \frac{\partial v'}{\partial y}, \\ \mathcal{N}_4 &= c' \frac{\partial u'}{\partial x} + u' \frac{\partial c'}{\partial x} + c' \frac{\partial v'}{\partial y} + v' \frac{\partial c'}{\partial y} + \frac{\gamma c' h'}{H^2}, \\ \mathcal{N}_5 &= -\left(\vec{\nabla} \cdot \vec{q}' - \mathcal{L}(\vec{\nabla} \cdot \vec{q}') \right). \end{aligned}$$

Here, the perturbed total volumetric transport of sediment \vec{q}' consists of a bedload and suspended load contribution, $\vec{q}' = \vec{q}'_b + \vec{q}'_s$, and $\mathcal{L}(\vec{\nabla} \cdot \vec{q}')$ is the linearized part of $\vec{\nabla} \cdot \vec{q}'$.

CHAPTER 4

EFFECT OF WAVE-TOPOGRAPHY INTERACTIONS ON THE FORMATION OF SAND RIDGES ON THE SHELF

ABSTRACT

The role of wave-topography interactions in the formation of shoreface-connected sand ridges (hereafter abbreviated as sfc) on micro-tidal inner shelves is investigated with an idealized morphodynamic model. The latter uses the two-dimensional shallow water equations to describe a storm-driven flow on an inner shelf with an erodible bottom and a transverse slope. Both bedload and suspended load sediment transport are included. New are the incorporation of a wave module based on physical principles and a critical shear-stress for erosion. A linear stability analysis is used to study the initial growth of bedforms, by analyzing the initial growth of small perturbations evolving on an alongshore uniform basic state, which describes a storm-driven flow on a micro-tidal inner shelf. Model simulations show that wave-topography interactions cause sfc to become more trapped to the coast. Both growth and migration of sfc are controlled by suspended load transport. The physical mechanism responsible for ridge growth is related to transport by the storm-driven current of sediment that is entrained due to wave orbital motions induced by bedforms. This new mechanism even acts in absence of a transverse bottom slope. The orientation, spacing and shape of the modeled sfc agree well with field observations from different shelves. *

*This chapter is based on the paper entitled *Effect of wave-topography interactions on the formation of sand ridges on the shelf*, by N. C. Vis-Star, H. E. de Swart and D. Calvete, published in *J. Geophys. Res.*, 112, C06012, doi: 10.1029/2006JC003844.

4.1 INTRODUCTION

A rich variety of sand ridges is observed in coastal and shelf seas. In *Dyer and Huntley* (1999) a classification scheme is presented based on the long-term evolution of the ridges in relation with the present-day hydrodynamic setting. The bedforms that will be considered in this chapter are type 2B(ii) in this scheme: sfc, which are characterized by crests oriented obliquely with respect to the shoreline. They evolve on inner shelves (depths between 5 and 30 m) where storms occur frequently. Early observations were reported on the most prominently present sfc along the Atlantic shelf of North America by *Duane et al.* (1972), *Swift et al.* (1972) and *Swift and Field* (1981). In *Swift et al.* (1978) sfc that occur on European shelves were described. Sfc were also observed on the Brazilian shelf (*Figueiredo et al.*, 1982), the Argentinean shelf (*Parker et al.*, 1982), the Canadian shelf (*Hoogendoorn and Dalrymple*, 1986; *Amos et al.*, 1996), the Belgian and central Dutch coast (*Van de Meene and Van Rijn*, 2000), the German shelf (*Antia*, 1996a), the Danish shelf (*Anthony and Leth*, 2002) and the West Florida shelf (*Twichell et al.*, 2003; *Edwards et al.*, 2003; *Harrison et al.*, 2003).

A noticeable characteristic of sfc is their rhythmic structure with a typical alongshore spacing between successive crests of 2–6 km. Lengths of individual crests are between 10 and 25 km and heights range from 1 to 6 m. Both observations (*Swift et al.*, 1978; *Antia*, 1996a; *Van de Meene and Van Rijn*, 2000) and model studies (*Trowbridge*, 1995; *Calvete et al.*, 2001a) indicate that the growth of sfc takes place during storms. Stormy weather is characterized by high waves (wave heights of 2–4 m) and a mean storm-driven flow of up to 0.5 m s^{-1} . The orientation of sfc is related to the dominant direction of the storm-driven flow. The seaward ends of the crests are shifted up-current with respect to their attachments to the shoreface, thereby making an angle of $10 - 50^\circ$ with respect to the coastline. Exceptions to this are sfc found on the central part of the Danish west coast, which have angles of about 60° and sfc on the west-central Florida shelf, which are oriented at angles of $58 - 75^\circ$. All sfc show a migration in the direction of the storm-driven current with a magnitude of $1 - 50 \text{ m yr}^{-1}$ (depending on the measuring period) and they evolve on a time scale of decades to centuries.

Proposed hypotheses on the origin of sfc can be divided into two broad classes. The first is that sfc are relict features from before the Holocene transgression (*McClennen and McMaster*, 1971; *Swift et al.*, 1972). The second is that they emerge due to inherent dynamic interactions between the water motion and the sandy bed (called morphodynamic self-organization). Although some features appear to be largely relict, observations by cf. *Swift et al.* (1978) and *Twichell et al.* (2003) show that sediment transport in sfc areas is significant, especially under stormy conditions. So, even when sfc have a relict origin, they are often subject to sediment reworking by modern shelf processes. *McBride and Moslow* (1991) argue that ebb-tidal deltas provided the initial sand source for the development of many sfc and shelf processes act as modifying agents in the evolution during and after ebb-tidal delta deposition.

Trowbridge (1995) was the first who proposed a process-based model for sfc, using the second hypothesis of morphodynamic self-organization. His model consists of the depth-averaged shallow water equations, ignoring Coriolis and bottom friction terms. The sediment transport due to bedload is linearly related to the mean flow. The model describes the initial

formation of *sfc*r due to the joint action of waves (stirring sand from the bottom) and a long-shore storm-driven flow (causing net sand transport). Trowbridge demonstrated the growth and down-current migration of up-current oriented *sfc*r having similar shape as the observed ridges in the field. The latter is the consequence of a positive coupling between small topographic perturbations superimposed on the mean alongshore uniform equilibrium state and the induced small hydrodynamic perturbations such that sand transport is convergent over *sfc*r.

The model of Trowbridge (1995) was extended by Falqués *et al.* (1999) to include Coriolis terms, bottom shear-stresses and sediment transport due to bottom slopes. The latter was shown to be crucial to obtain a preferred mode of which the spacing agrees with field observations. Restrepo (2001) included the effect of a wave-induced Stokes drift in the model and found that it tempered the growth mechanism. However, the ratio of time scales related to growth and migration of the bedforms is not in accordance with field data and the instability mechanism is very sensitive to the cross-shore profile of the storm-driven current.

Calvete *et al.* (2001a) argued that these artefacts were due to the neglect of suspended load sediment transport and spatial variations in stirring of sediment by waves. The results of their model, which accounts for the processes mentioned above, compare favorably well with field data (both growth and migration of *sfc*r). Moreover, the results are hardly sensitive to the profile of the storm-driven flow. A drawback of the model is that it uses a strongly simplified description of waves in calculating stirring of sediment. The parameterization (derived from a simple wave shoaling model) is such that the near-bed wave orbital velocity decreases with increasing water depths (thus also stirring of sediment by waves). In fact, in the latter model wave properties only depend on the undisturbed reference depth and refraction, shoaling and dissipation due to the presence of bedforms are ignored.

In a recent study by Calvete *et al.* (2005) a sophisticated wave transformation model was used to study the initial formation of sand bars in the surf zone. They showed that explicit modeling of wave-topography interactions is crucial for obtaining good agreement between model results and field observations. Therefore, in the present chapter a morphodynamic model for the inner shelf will be discussed, which includes a process-based wave transformation model. This enables the study of interactions between waves and the bottom topography and the effect on the initial growth of *sfc*r. Important differences with Calvete *et al.* (2005) are a different geometric setting (inner shelf rather than surf zone) and the consideration of obliquely incident waves. The objective is to investigate the effect of the improved wave formulation and in addition the influence of growing bedforms on the wave properties (the latter was not possible before).

The chapter is organized as follows. In section 4.2 a new model will be presented, which extends that of Calvete *et al.* (2001a) with regard to the description of waves and the formulation of sand transport. This is followed in section 4.3 by an outline of the method of analysis. Results will be presented in section 4.4 and are followed by a discussion (section 4.5) on the physical interpretation, agreement with field data and model simplifications. We end with concluding remarks (section 4.6).

4.2 MODEL FORMULATION

The starting point is a reference shelf geometry. Forcing of the water motion on this shelf is due to wind generating both waves and an alongshore current. Waves affect the current through the bed shear-stress. Forcing of currents due to the divergence of wave-induced radiation stresses, the effect of currents on waves through the Doppler shift and wave diffraction are neglected here. This can be justified by assuming that waves hardly break on the inner shelf and that the typical phase speed of the waves is much larger than the current velocity. It is further assumed that the sediment is transported only during stormy weather, which occurs for a specific time fraction (about 5%). In contrast, during fair weather bottom stresses are not sufficiently strong to erode the sediment particles from the bottom. During storms the wave orbital velocity is large compared with the mean storm-induced longshore current. The strong near-bed wave orbital velocity stirs the sediment from the bottom, which is subsequently transported by the mean flow. The long-term bottom evolution is determined by the wave-averaged sediment transport. Divergence of the sediment transport leads to bottom change and this in turn will affect the hydrodynamics. Positive internal feedbacks between the flow field and the erodible bed of the inner shelf will cause growth of bedforms. Below, details about the different parts of the model are given (equations are representative for storms).

4.2.1 SHELF GEOMETRY

The reference geometry consists of an inner shelf with a sloping bed and depth increasing in seaward direction. It is bounded on the landward side ($x = 0$) by the transition from inner shelf to shoreface (depth H_0) and on the seaward side ($x = L_s$) by an outer shelf with constant depth H_s . The bottom profile is longshore uniform. The transition from the shoreface to the inner shelf is assumed to be straight and without interruptions. An orthogonal coordinate system is used such that the x -axis points in the cross-shore (seaward) direction and the y -axis in the alongshore direction (pointing into the paper). The z -axis is directed vertically upward and $z = 0$ represents the still water level. A sketch of the geometry is presented in Figure 4.1.

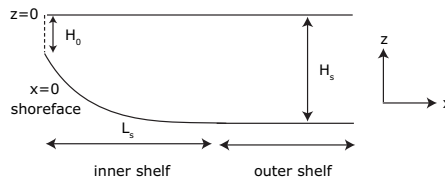


Figure 4.1: Side view of a typical longshore- and time-averaged bottom topography of the continental shelf, representing the inner and outer shelf, in the shore-normal direction. Symbols are explained in the text.

4.2.2 HYDRODYNAMICS

WAVES

The wave transformation model is based on linear wave theory. This is valid if waves have a small steepness and amplitudes, which are much smaller than the water depth. For waves (wind and swell) and water depths (inner shelf region) considered this will generally be the case.

Wind-generated waves usually have randomly varying wave heights, periods and directions. *Longuet-Higgins* (1952) discussed the statistical properties of waves characterized by a narrow band of frequencies and orientations. The narrow spectrum is centered around a peak frequency, wavenumber and wave orientation. Locally, a realization of the free surface elevation ζ (measured with respect to the mean water level $z = z_s$) is described by

$$\zeta = \frac{\mathcal{H}}{2} \cos \Phi, \quad \Phi = \kappa_x x + \kappa_y y - \omega t. \quad (4.1)$$

Here, Φ is the wave phase, whilst the wave height \mathcal{H} is random and described by a Rayleigh distribution. Furthermore, $\kappa_x = -\kappa \cos \theta$ and $\kappa_y = \kappa \sin \theta$ are the x - and y -component of the wavevector $\vec{\kappa}$ and κ is the wavenumber. The peak frequency associated with the random wave field is ω and θ is the angle of wave incidence measured with respect to the shore-normal (clockwise deviation with respect to the shore-normal means positive θ and vice versa, see Figure 4.2). Finally, t is time.

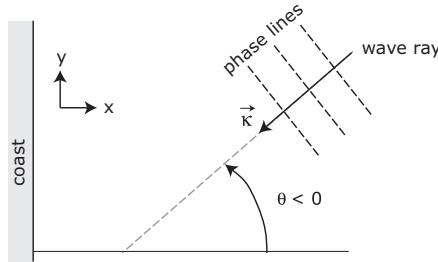


Figure 4.2: Definition of the angle of wave incidence θ . It is measured with respect to the shore-normal. Clockwise (anti-clockwise) deviation with respect to the shore-normal means positive (negative) θ .

The probability density distribution of values \mathcal{H}' attained by the wave height reads

$$P(\mathcal{H}') = \frac{2\mathcal{H}'}{\mathcal{H}_{rms}^2} e^{-(\mathcal{H}'/\mathcal{H}_{rms})^2}, \quad (4.2)$$

with \mathcal{H}_{rms} the root-mean-square wave height. Furthermore, the wave energy density \mathcal{E} (per surface area) of a random wave field is defined as

$$\mathcal{E} = \rho g \langle \zeta^2 \rangle = \frac{1}{8} \rho g \mathcal{H}_{rms}^2. \quad (4.3)$$

Here, ρ is the water density, g is the acceleration due to gravity and the brackets $\langle \rangle$ denote a time average over several wave periods and integration over all possible wave heights.

Below, equations are discussed that govern the behavior of κ , θ , ω and \mathcal{E} , which are allowed to vary slowly in space and time. From the definition for the wave phase Φ in equation (4.1) it can be deduced that locally

$$\vec{\kappa} = (\kappa_x, \kappa_y) = \left(\frac{\partial \Phi}{\partial x}, \frac{\partial \Phi}{\partial y} \right), \quad \omega = -\frac{\partial \Phi}{\partial t}. \quad (4.4)$$

From this follows the law of conservation of wave crests:

$$\frac{\partial \vec{\kappa}}{\partial t} + \vec{\nabla} \omega = 0, \quad (4.5)$$

which shows that the change in the number of wave crests in a certain domain is determined by the difference between incoming and outgoing waves through the boundaries. Here, $\vec{\nabla}$ is the two-dimensional (horizontal) nabla vector with components $\frac{\partial}{\partial x}$ and $\frac{\partial}{\partial y}$ in the x - and y -direction, respectively. The frequency of gravity waves is related to wavenumber κ by the dispersion relation

$$\omega^2 = g\kappa \tanh(\kappa D). \quad (4.6)$$

The wavenumber is the length of the wavevector, $\kappa = (\kappa_x^2 + \kappa_y^2)^{1/2}$, and D is the water depth (averaged over many waves). The angle of wave incidence is governed by the wavenumber identity relation:

$$\frac{\partial}{\partial y} (\kappa \cos \theta) + \frac{\partial}{\partial x} (\kappa \sin \theta) = 0. \quad (4.7)$$

Finally, the wave energy density is controlled by the wave energy balance:

$$\frac{\partial \mathcal{E}}{\partial t} + \vec{\nabla} \cdot (\vec{c}_g \mathcal{E}) = \mathcal{F} - \mathcal{D}. \quad (4.8)$$

The group velocity vector of the waves \vec{c}_g has amplitude c_g and components $c_{gx} = -c_g \cos \theta$ and $c_{gy} = c_g \sin \theta$. Its magnitude c_g is

$$c_g = \frac{\partial \omega}{\partial \kappa} = \frac{\omega}{2\kappa} \left(1 + \frac{2\kappa D}{\sinh(2\kappa D)} \right). \quad (4.9)$$

The two terms on the right-hand side of equation (4.8) are the source of energy provided by wind forcing \mathcal{F} and the energy dissipation \mathcal{D} , respectively. Dissipation can be the consequence of different processes, e.g. bottom friction, whitecapping and wave breaking. In the inner shelf region the dissipation is dominated by bottom friction. The formulation for the dissipation of wave energy used in this study is adopted from *Komen et al.* (1994):

$$\mathcal{D} = \frac{2c_f \kappa u_{rms} \mathcal{E}}{\sinh(2\kappa D)}. \quad (4.10)$$

Here, c_f is the bottom drag coefficient and

$$u_{rms} = \frac{\omega \mathcal{H}_{rms}}{2 \sinh(\kappa D)} \quad (\text{hereafter written as } u_w), \quad (4.11)$$

is the root-mean-square amplitude of the near-bed wave orbital velocity (hereafter called wave orbital velocity). It is assumed that dissipation and generation of wave energy cancel on the outer shelf, hence $\mathcal{F} = \mathcal{D}|_{x=L_s}$. This implies that wave properties do not change on the outer shelf.

As boundary conditions the offshore root-mean-square wave height, wave period ($T = 2\pi/\omega$) and offshore angle of wave incidence are imposed. The transformation of wave properties across the inner shelf domain is determined by equations (4.5)-(4.11).

CURRENTS

It is assumed that the large-scale currents (i.e., that part of the water motion that remains after averaging over a number of waves) are governed by the depth- and wave-averaged (2DH) shallow water equations

$$\frac{\partial \vec{v}}{\partial t} + (\vec{v} \cdot \vec{\nabla}) \vec{v} + f \vec{e}_z \times \vec{v} = -g \vec{\nabla} z_s + \frac{\vec{\tau}_s - \vec{\tau}_b}{\rho D}, \quad (4.12)$$

$$\frac{\partial D}{\partial t} + \vec{\nabla} \cdot (D \vec{v}) = 0. \quad (4.13)$$

Here, \vec{v} is the depth- and wave-averaged current velocity with components u and v in the x - and y -direction, respectively. Furthermore, f is the Coriolis parameter, \vec{e}_z is a unit vector in the vertical direction, $D = z_s - z_b$ is the water depth and $\vec{\tau}_s$ and $\vec{\tau}_b$ represent the wind stress and bed shear-stress, respectively. In the definition for the water depth, z_s and z_b are the free surface elevation and the bottom depth both measured with respect to the undisturbed water level $z = 0$. In the momentum equations (4.12) forcing terms due to wave-induced radiation stresses, horizontal momentum diffusion, density gradients and tides are neglected. It is assumed that the mean storm-driven flow is in the alongshore direction (cross-shore component is neglected), which is driven by a prescribed wind stress τ_{sy} .

During storms the wave orbital velocity is much larger than the magnitude of the storm-induced current. Under wave-dominated conditions the mean bed shear-stress is linearly related to the mean flow. Assuming waves and currents to be near-parallel, it follows

$$\vec{\tau}_b = \rho r u_w \vec{v}, \quad (4.14)$$

where u_w has been defined in the first part of this section. The dimensionless friction coefficient r computed for random waves, is a factor $\sqrt{\pi}/2$ larger compared to the case of monochromatic waves considered in *Calvete et al. (2001a)*. Note that the mean bottom stress is related to the depth-averaged current rather than to the bottom velocity.

The boundary conditions are that the cross-shore flow component u vanishes at $x = 0$ and far offshore. The bed level z_b has a fixed value at these two positions. As a consequence, no net exchange of water occurs between the shoreface and inner shelf.

4.2.3 BOTTOM EVOLUTION AND SEDIMENT TRANSPORT

The evolution of the bottom follows from conservation of sediment mass:

$$(1 - p) \frac{\partial z_b}{\partial t} + \vec{\nabla} \cdot \vec{q}_b + \vec{\nabla} \cdot \vec{q}_s = 0, \quad (4.15)$$

where the porosity of the bed is indicated by p and \vec{q}_b and \vec{q}_s are the wave-averaged volumetric sediment transport per unit width as bedload and suspended load, respectively. Field observations by *Green et al.* (1995) show that during storms large amounts of sand are in suspension and transported as suspended load without having any contact with the bed. In case of bedload transport sediment moves within a thin layer close to the bed by rolling, sliding and hopping and is in frequent contact with the bed. *Calvete et al.* (2001a) argued that both types of transport must be included in the sediment transport formulation to correctly describe the growth and migration of sfcr. Therefore, both bedload and suspended load transport are considered in equation (4.15). Formulations for these transports are given below. As a simplification, the sediment is considered to be noncohesive and of a single grain size.

BEDLOAD

The bedload transport of sediment is described by the formulation of *Bailard* (1981). For storm conditions and waves propagating almost parallel to the storm-driven current, it follows

$$\vec{q}_b = \begin{cases} \frac{3}{2} \nu_b (u_w^2 - u_c^2) (\vec{v} - \lambda_b u_w \vec{\nabla} z_b) & u_w^2 > u_c^2, \\ 0 & u_w^2 \leq u_c^2. \end{cases} \quad (4.16)$$

The coefficient ν_b depends on sediment properties and λ_b is the bed slope parameter, which is related to the angle of repose of the sediment. Coefficient λ_b is a factor $3\sqrt{\pi}/4$ larger compared to the case of monochromatic waves. Furthermore, u_c is the critical wave orbital velocity above which erosion of sediment occurs. The first contribution to \vec{q}_b represents the net sediment transport due to stirring of sediment by waves and the subsequent transport by the net current. The second contribution accounts for gravitational effects on sediment grains in the bedload layer. Hereafter, the first contribution is called the current-induced sediment transport and the second the bed slope-induced sediment transport. Bedload sediment transport only occurs if the shear-stress exerted on the bed exceeds a critical value.

SUSPENDED LOAD

The volumetric suspended load sediment transport per unit width, averaged over a large number of wave cycles, is a modified version of the suspended load transport proposed by *Bailard* (1981) and reads

$$\vec{q}_s = \mathcal{C} \vec{v} - \lambda_s u_w^5 \vec{\nabla} z_b. \quad (4.17)$$

Here, \mathcal{C} is the depth-integrated volume concentration of sediment and λ_s is the bed slope parameter for suspended sediment. The latter is a factor $15\sqrt{\pi}/8$ larger compared to the case of monochromatic waves. A formulation for the depth-integrated volume concentration of sediment is governed by a concentration equation

$$\frac{\partial \mathcal{C}}{\partial t} + \vec{\nabla} \cdot (\mathcal{C} \vec{v}) = w_s (c_a - c_b). \quad (4.18)$$

Here, w_s is the settling velocity of the sediment grains, c_a their reference volume concentration and c_b their actual volume concentration near the bed. The second term on the left-hand side accounts for settling lag effects, i.e., it takes time for sediment to reach the bottom when the decreasing current cannot maintain it in suspension. Thus, settling occurs at some distance from the location where sediment has been entrained. The first term on the right-hand side of equation (4.18) accounts for the entrainment of sediment into suspension, the second term for deposition of sediment. For the reference volume concentration the formulation from *Van Rijn* (1993) is adopted:

$$c_a = \begin{cases} \hat{c}_a \left(\frac{u_w^2 - u_c^2}{u_c^2} \right)^{3/2} & u_w^2 > u_c^2, \\ 0 & u_w^2 \leq u_c^2. \end{cases} \quad (4.19)$$

Here, the coefficient \hat{c}_a is a constant, which is a factor $3\sqrt{\pi}/4$ larger compared to the case of monochromatic waves. The actual near-bed volume concentration c_b can be expressed in terms of the depth-integrated volumetric concentration as follows

$$c_b = \frac{C}{\delta D}. \quad (4.20)$$

Here, δ is the ratio of the thickness of the suspended load sediment layer and the actual water depth. The latter is assumed to be constant in space and time. As in the case of bedload, transport of suspended sediment only occurs if the shear-stress exerted on the bed exceeds a critical value leading to entrainment of sediment particles. The corresponding boundary condition is that the concentration vanishes far from the coast.

4.2.4 ADDITIONAL ASSUMPTIONS

The model formulation can be further simplified. Sfcf evolve on a time scale (decades to centuries), which is long compared to that of hydrodynamic processes (seconds to weeks). This allows use of the quasi-steady approximation: time derivatives in equations (4.5), (4.8), (4.12)-(4.13) and (4.18) are neglected. Physically, this means that the water motion adjusts instantly to a new bed level. Application of the quasi-steady approach to equation (4.5) implies that the wave frequency ω is a constant (given by the boundary condition). Furthermore, the rigid-lid approximation is used, which is justified by the fact that water particles have a small velocity compared to the phase speed of gravity waves (small Froude number). As the free surface elevation is much smaller than the undisturbed water depth in this case, the local depth can be approximated by $D \simeq \tilde{D} = -z_b$ in all equations.

4.3 SOLUTION METHOD

The initial growth of morphodynamic features is investigated by applying a linear stability analysis. The starting point is a longshore uniform basic state, which describes an incoming wave field and a longshore storm-induced current. The inner shelf has a plane slope and sfcf are not yet present. The morphodynamic evolution of small perturbations in the basic state yields information about the growth or decay of features. As the focus is on the initial growth of bed features, the governing equations are linearized, which means that only terms that are

proportional to the amplitude of the perturbations are retained. The linearization procedure is outlined in section 4.3.2. The result is an eigenvalue problem, which is solved numerically using a spectral method. The solution for a fixed bed level gives the perturbed wave and velocity fields, which in turn are used to calculate changes in the bed level. From here on we denote solutions of primary wave variables by $\mathcal{X} = (\kappa, \theta, \mathcal{E})$ and those of other dependent variables by $\Psi = (u, v, z_s, \mathcal{C}, z_b)$.

4.3.1 BASIC STATE

It turns out that in case $H = H(x)$, as stated in section 4.2.1, the model allows for a basic state that is steady and alongshore uniform. Hence, $\mathcal{X} = \mathcal{X}_b(x)$ and $\Psi = \Psi_b(x)$, where we write $\mathcal{X}_b = (K, \Theta, E)$ and $\Psi_b = (U, V, \xi, C, -H)$. Thus, K , Θ and E represent the basic state wavenumber, angle of wave incidence and wave energy, respectively. Likewise, U , V , ξ , C and H represent the basic state cross-shore and longshore velocity component, free surface elevation, depth-integrated volume concentration of sediment and bottom elevation, respectively.

Now substitute $\mathcal{X} = \mathcal{X}_b$ in equations (4.6)-(4.11). It follows, as ω is constant, that equation (4.6) relates the basic state wavenumber $K(x)$ to water depth $H(x)$. This relation is transcendental in K and can be solved using a root-finding procedure. Next, equation (4.7) reduces to $K \sin \Theta = \text{constant}$, which is Snell's law. For a given angle of wave incidence $\Theta = \Theta_s$ on the outer shelf, it follows

$$\sin \Theta = \frac{K_s \sin \Theta_s}{K}. \quad (4.21)$$

Here, K_s is the wavenumber at $x = L_s$, which is known from the dispersion relation. As it is assumed that dissipation and generation of wave energy cancel on the outer shelf, wave properties do not change on the outer shelf and $K_s = K_\infty$. The basic state wave energy $E(x)$ is governed by:

$$\frac{d}{dx} (-E C_g \cos \Theta) = \mathcal{F}_b - \mathcal{D}_b, \quad (4.22)$$

where C_g , \mathcal{F}_b and \mathcal{D}_b (thus U_w) are obtained from equations (4.9)-(4.11) by substitution of basic state variables. As boundary condition the wave energy $E = E_s$ (or equivalently, $H_{rms,s}$) on the outer shelf is prescribed. In fact, E_s is equal to the wave energy far offshore, as wave properties do not change on the outer shelf in the model. The basic state wave orbital velocity $U_w(x)$ is important for calculating the basic state longshore current and sediment transport.

The basic state describes a longshore current with a cross-shore gradient, i.e., $U = 0$ and $\vec{v} = (0, V(x))$. The latter is driven by a constant alongshore wind stress τ_{sy} . The momentum equations for the basic state reduce to the following form:

$$fV = g \frac{d\xi}{dx}, \quad 0 = \frac{\tau_{sy} - \tau_{by}}{\rho H}. \quad (4.23)$$

The first equation determines the cross-shore set-up or set-down of the water level due to Coriolis effects. The second equation and the linear friction law (4.14) determine the basic state alongshore velocity profile:

$$V = \frac{\tau_{sy}}{\rho r U_w}. \quad (4.24)$$

Note that the formulation for the alongshore velocity is only valid under wave-dominated conditions. The corresponding basic state depth-integrated relative volume concentration $C(x)$ follows from substitution of the basic state variables into equations (4.18)-(4.20),

$$C = \begin{cases} \delta H \hat{c}_a \left(\frac{U_w^2 - u_c^2}{u_c^2} \right)^{3/2} & U_w^2 > u_c^2, \\ 0 & U_w^2 \leq u_c^2. \end{cases} \quad (4.25)$$

It follows from equations (4.16)-(4.20) that the total sediment transport in the basic state has a longshore component, which is independent of y , but a nonconstant offshore component (due to the transverse bottom slope). The latter implies that the sediment mass balance is not identically satisfied. However, the change in bed level due to divergence of this transport is much slower ($\sim 10^{-5}$ m yr $^{-1}$) than the change in bed level of sfcf ($\sim 10^{-2}$ m yr $^{-1}$), hence this effect can be neglected. Thus, to a good approximation, the basic state defines a morphodynamic equilibrium. In this case the sediment and mass conservation equations are automatically obeyed.

4.3.2 LINEAR STABILITY ANALYSIS

The stability properties of the basic state are considered by studying the dynamics of small perturbations evolving on this basic state. Hence, $\mathcal{X} = \mathcal{X}_b + \mathcal{X}'$ is substituted in equations (4.6)-(4.11) and together with $\Psi = \Psi_b + \Psi'$ into equations (4.12)-(4.15). Both \mathcal{X}_b and Ψ_b are defined in section 4.3.1. Furthermore, $\mathcal{X}'(x, y, t) = (\kappa', \theta', e')$ and $\Psi'(x, y, t) = (u', v', \eta', c', h')$ denote the perturbed variables, which are assumed to have small values with respect to their basic state values. To close the model, also perturbations in the group velocity, energy dissipation and wave orbital velocity need to be considered: $(c_g, \mathcal{D}, u_w) = (C_g, \mathcal{D}_b, U_w) + (c'_g, \mathcal{D}', u'_w)$. Expressions for c'_g , \mathcal{D}' and u'_w in terms of κ' , θ' , e' and h' readily follow from equations (4.9)-(4.11). As the morphodynamic patterns, which are investigated, are naturally confined to the inner shelf, appropriate offshore boundary conditions are $\mathcal{X}', \Psi' \rightarrow 0$ for $x \rightarrow \infty$. At the shoreface ($x = 0$) the boundary conditions are a vanishing cross-shore flow component ($u' = 0$) and a bottom elevation, which is fixed to its basic state value ($h' = 0$). Linearizing the equations with respect to the small perturbed variables results in a linear system of differential equations. Note that use of the quasi-steady approximation implies that time derivatives of hydrodynamical variables are excluded. The system of perturbed equations sustains solutions, which are periodic in the longshore direction and of which the amplitude can grow (or decay) exponentially in time:

$$(\mathcal{X}', \Psi', c'_g, \mathcal{D}', u'_w) = \Re \left\{ \left(\hat{\chi}(x), \hat{\psi}(x), \hat{c}_g(x), \hat{\mathcal{D}}(x), \hat{u}_w(x) \right) e^{iky + \sigma t} \right\}. \quad (4.26)$$

Here, \Re denotes the real part of the solution, k the longshore wavenumber (which can be assigned any value), the hats denote the as yet unknown cross-shore structure of the solutions

and σ the complex frequency. Substituting expressions (4.26) into the equations for the small perturbations yields

$$\hat{\kappa} = \left(\frac{K^2}{KH + \frac{1}{2} \sinh(2KH)} \right) \hat{h}, \quad (4.27a)$$

$$\frac{d}{dx} \left(K \cos \Theta \hat{\theta} \right) - ikK \sin \Theta \hat{\theta} = -\frac{d}{dx} (\sin \Theta \hat{\kappa}) - ik \cos \Theta \hat{\kappa}, \quad (4.27b)$$

$$\frac{d}{dx} (-C_g \cos \Theta \hat{e}) + ik C_g \sin \Theta \hat{e} = -\frac{d}{dx} (E \hat{c}_{gx}) - ik E \hat{c}_{gy} - \hat{D}. \quad (4.27c)$$

Here, $\hat{c}_{gx} = (-\cos \Theta \hat{c}_g + C_g \sin \Theta \hat{\theta})$ and $\hat{c}_{gy} = (\sin \Theta \hat{c}_g + C_g \cos \Theta \hat{\theta})$ are the x - and y -component of the perturbed group velocity, respectively. The expression for the cross-shore structure of the perturbed wave orbital velocity, which is e.g. used in calculating \hat{D} , follows from equation (4.11):

$$\hat{u}_w = U_w \left(\frac{\hat{e}}{2E} - \frac{H\hat{\kappa} - K\hat{h}}{\tanh(KH)} \right). \quad (4.28)$$

A similar procedure is followed for deriving the perturbed flow, sediment concentration and sediment transport equations, which are given in appendix 4.A. Differences with the equations in chapter 2 are that due to the consideration of perturbations in the wave orbital velocity an extra friction term $-rV u'_w/H$ appears in the alongshore momentum equation, an additional entrainment term $3 \frac{w_s \hat{c}_a}{u_c^3} U_w (U_w^2 - u_c^2)^{1/2} u'_w$ appears in the concentration equation and in the equation for the perturbed bedload transport the term $3\nu_b U_w V u'_w$ is added. Another difference is that no sediment transport occurs unless the wave orbital velocity exceeds a critical value u_c .

The equations above, together with the corresponding boundary conditions which were specified before, define an eigenvalue problem

$$\sigma \mathcal{S} \begin{bmatrix} \hat{\chi} \\ \hat{\psi} \end{bmatrix} = \mathcal{L}_k \begin{bmatrix} \hat{\chi} \\ \hat{\psi} \end{bmatrix}, \quad (4.29)$$

where σ are the complex eigenvalues and $(\hat{\chi}, \hat{\psi})$ are the eigenfunctions. The latter ones give the cross-shore structure of the perturbations. The 8×8 matrix \mathcal{S} contains the temporal information of the perturbations and all its elements are zeros, except for $\mathcal{S}(8, 8) = 1 - p$. Finally, the linear matrix operator \mathcal{L}_k involves spatial derivatives and is therefore dependent on the longshore wavenumber k .

The growth rate and migration speed of the perturbations are given by the complex frequency ($\sigma = \sigma_r + i\sigma_i$). The real part σ_r is the growth rate and the migration speed is given by $V_m = -\sigma_i/k$. If, for specific choices of the model parameters, $\sigma_r < 0$ for all k the basic state is stable. Conversely, if there is a range of wavenumbers k for which $\sigma_r > 0$, there are exponentially growing modes and the basic state is unstable. The mode which has the largest growth rate, is called the fastest growing or most preferred mode. The basic idea of a linear

stability analysis is that, starting from some random perturbation (which contains all Fourier modes), the fastest growing mode will dominate the solution after some time. The inverse of the growth rate σ_r gives a characteristic time scale for the formation in nature (called the e -folding growth time T_g). The eigenvalue problem is solved numerically using a spectral collocation method. Thus, variables are expanded in Chebyshev polynomials and equations are evaluated at N collocation points (see *Boyd, 2001*, for details).

4.4 RESULTS

4.4.1 PARAMETER VALUES: DEFAULT CASE

Results of the model are presented for a specific setting of the reference topography and for values of the parameters, which are representative for the micro-tidal inner shelf of Long Island. It is situated at the Atlantic coast of North America near New York at a latitude of $\sim 40^\circ$ N. Several studies (cf. *Swift and Field, 1981*) have indicated the presence of large-scale bedforms in this area. The reference bottom profile, defined as the longshore- and time-averaged bottom profile of the continental shelf, is modeled as $z = -H(x)$, where

$$H(x) = \begin{cases} H_0 + \beta x & 0 \leq x \leq L_s, \\ H_s & x > L_s. \end{cases} \quad (4.30)$$

Representative values for the geometrical parameters are $H_0 = 14$ m, $H_s = 20$ m and $L_s = 5.5$ km, hence the bottom slope $\beta = (H_s - H_0)/L_s \sim 1.1 \times 10^{-3}$. The Coriolis parameter at this location is $f = 1 \times 10^{-4} \text{ s}^{-1}$.

Observations by *Niedoroda and Swift (1981)* and *Lentz et al. (1999)* indicate the importance of northeastern storms for the wave climate near Long Island. A typical value for the root-mean-square wave height on the outer shelf of Long Island is $H_{rms,s} = 1.5$ m. Note that the significant wave height, which is used in many studies, is a factor $\sqrt{2}$ larger. The waves approach from the northeast and the angle of wave incidence $\Theta_s = -20^\circ$ (counter clockwise, with respect to the shore-normal) when entering the inner shelf. As we assume a stationary wave field, the wave frequency is constant. A typical value for the wave period is $T = 11$ s, so the wave frequency is $\omega \sim 0.6 \text{ s}^{-1}$. A wave friction factor $c_f = 3.5 \times 10^{-3}$ is used for determining dissipation of wave energy. For calculating the bottom shear-stress experienced by the current a friction coefficient $r = 2.0 \times 10^{-3}$ is used.

The wind associated with the northeastern storms exerts a stress on the water surface, which forces an alongshore current. Based on the field data discussed above the alongshore wind stress is chosen as $\tau_{sy} = -0.4 \text{ N m}^{-2}$ (southward). The alongshore current V is established as a balance between the storm-induced wind stress and the bottom stress. Note that the latter depends on the wave orbital velocity according to equation (4.24). It is further assumed that grain size $d_{50} = 0.35$ mm, porosity $p = 0.4$, bedload parameter $\nu_b = 5.6 \times 10^{-5} \text{ s}^2 \text{ m}^{-1}$, suspended load parameter $\hat{c}_a = 1.2 \times 10^{-5}$, critical velocity for erosion $u_c = 0.25 \text{ m s}^{-1}$ and bed slope parameters $\lambda_b = 0.65$ and $\lambda_s = 7.5 \times 10^{-4} \text{ s}^4 \text{ m}^{-3}$. Field data (*Williams et al., 1999*) indicate that $\delta \sim 0.2$ for strong waves superimposed on a mean current.

4.4.2 BASIC STATE AND LINEAR STABILITY ANALYSIS: DEFAULT CASE

In this section results are presented for the default parameter values given in the previous section. The cross-shore profiles for the basic state wavelength, angle of wave incidence, root-mean-square wave height and wave orbital velocity are shown in Figure 4.3. A decrease in water depth towards the shore causes a shortening and refraction of the waves. The wave height increases towards the shore due to a decrease in the group velocity of the waves. As a result, the wave orbital velocity also increases into shallower depths and reaches an amplitude of about 0.54 m s^{-1} at the shoreface.

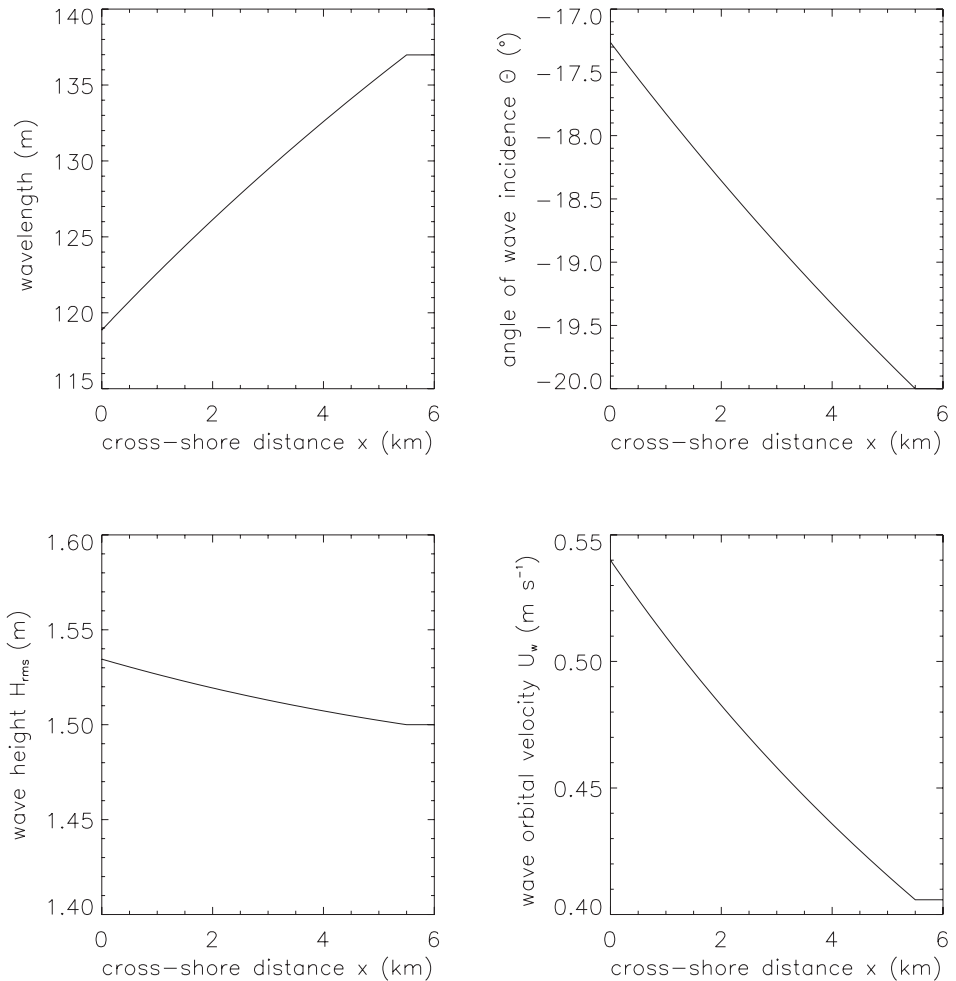


Figure 4.3: Basic state; cross-shore profiles of wavelength, angle of wave incidence, root-mean-square wave height and wave orbital velocity. Default case.

The cross-shore profiles of the basic state longshore current and depth-integrated concentration are shown in Figure 4.4. The magnitude of the longshore current decreases towards the shoreface, reaching a value of 0.36 m s^{-1} . This is a consequence of the larger bottom friction for shallower depths. The depth-integrated concentration of sediment increases towards the shoreface, as the larger wave orbital velocity stirs more sediment into suspension.

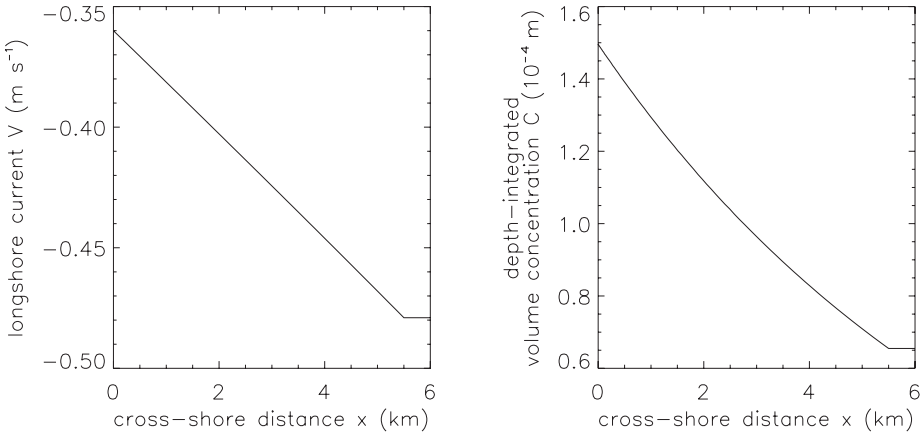


Figure 4.4: Basic state; cross-shore profiles of longshore current and depth-integrated volume concentration. Default case.

The growth rate of small perturbations evolving on the basic state as a function of their longshore wavenumber k is displayed in Figure 4.5a.

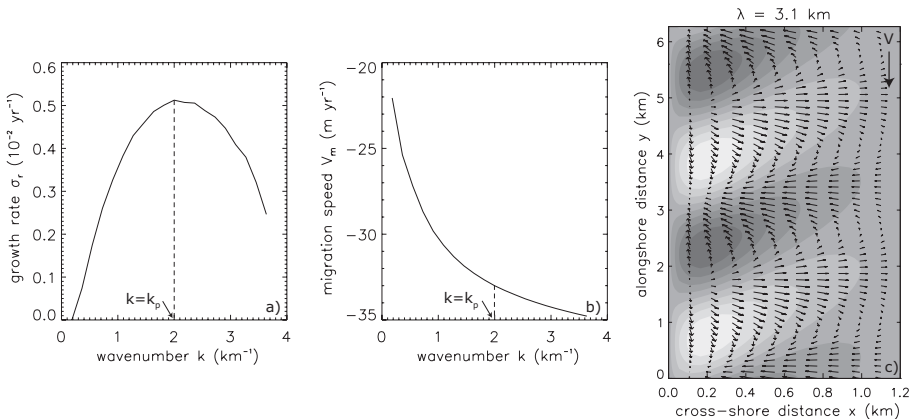


Figure 4.5: Growth rates (a) and migration velocities (b) as a function of the longshore wavenumber. The dashed lines indicate the most preferred mode. (c) Bottom pattern (grayscale; light: crests, dark: troughs) and perturbations (small arrows) in basic longshore velocity field (in the direction of the thick arrow) for the most preferred mode. The aspect ratio has been increased to show the arrows.

It is assumed that growth of the perturbations only takes place during storms, which occur during a time fraction of 5%. Model output is corrected for this. For this default case one growing solution is obtained. The dashed line indicates the wavenumber $k = k_p$ of the most preferred mode, which has the largest growth rate. Here $k_p \sim 2.0 \text{ km}^{-1}$, which corresponds to a longshore wavelength of the bedforms of $\lambda = 2\pi k^{-1} \sim 3.1 \text{ km}$. The preferred mode migrates with approximately 33 m yr^{-1} in the downstream direction (see Figure 4.5b). The bottom pattern of this preferred bedform is shown in Figure 4.5c. The light areas denote the crests and the dark areas the troughs. Clearly, sfcr are found with seaward ends rotated upstream with respect to the shoreface attachments. The angle between crest axis and coastline (from here on denoted as φ) is about 30° . The sfcr extend 1 km in the offshore direction. The thin arrows denote the flow perturbations and show an offshore (onshore) current deflection over the crests (troughs). The e -folding time for the growth of sfcr is $T_g = \sigma_r^{-1} \sim 195 \text{ yr}$.

In Figure 4.6a both the bottom pattern of the preferred mode (grayscale) and perturbations in the wavevector (small arrows) are shown.

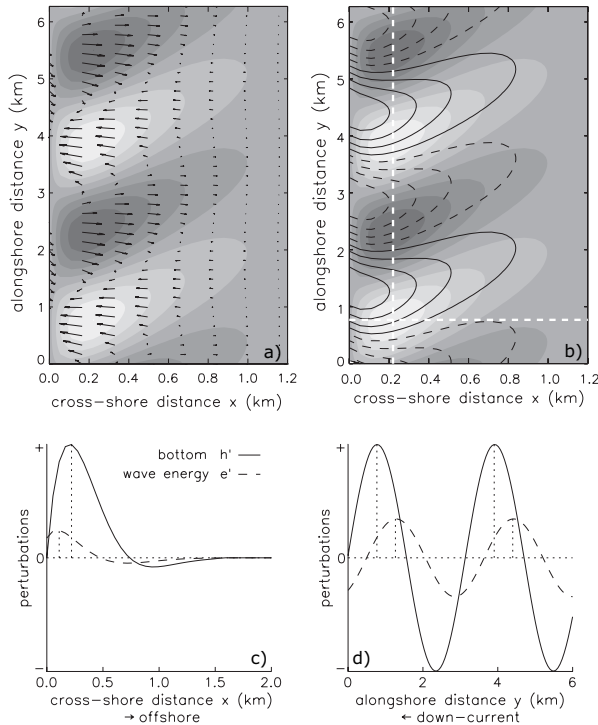


Figure 4.6: (a) Spatial structure of the perturbed bottom (grayscale; light: crests, dark: troughs) and of the perturbed wavevector (small arrows); the fastest growing mode. The aspect ratio has been increased to show the arrows. (b) Spatial pattern of the most preferred bottom mode and of the perturbed wave energy (contours; solid: $e' > 0$, dashed: $e' < 0$). The dashed white lines indicate the position of normal and longshore cross-sections through the sfcr, which are shown in (c) and (d), respectively.

A significant convergence of wave rays is visible on the upstream side of the sfcf, which is due to bedform-induced wave refraction. The focusing of waves in the upstream region causes an increase in wave energy, which is clearly visible in Figure 4.6b. The shore-normal (Figure 4.6c) and longshore (Figure 4.6d) cross-sections at the positions of the dashed white lines show that perturbations in wave energy are located up-current and onshore with respect to the bottom perturbations.

In Figure 4.7a the spatial distribution of the perturbed wave orbital velocity and bottom of the most preferred mode are shown. A small phase shift in the cross-shore direction exists (see Figure 4.7b). The longshore cross-section along the vertical white dashed line (Figure 4.7c) reveals that the pattern of the perturbed wave orbital velocity is shifted up-current with respect to that of the bottom. As will be demonstrated later on, this phase shift between the perturbed wave orbital velocity and the perturbed bottom is crucial to understand the growth of bedforms due to their feedback with the waves.

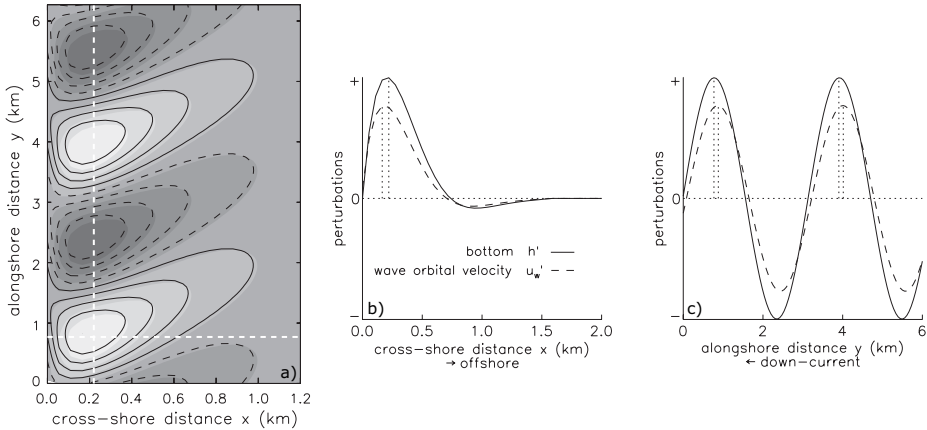


Figure 4.7: (a) Bottom pattern of the most preferred mode (grayscale; light: crests, dark: troughs) and spatial distribution of the perturbed wave orbital velocity (contours; solid: $u_w' > 0$, dashed: $u_w' < 0$). The dashed white lines indicate the position of normal and longshore cross-sections through the sfcf, which are shown in (b) and (c), respectively.

Focusing of wave energy in areas upstream of the ridges causes an enhanced entrainment of sediment in these areas and therefore an increase in depth-integrated sediment concentration (results not shown).

4.4.3 SENSITIVITY TO THE WAVE-BEDFORM FEEDBACK MECHANISM

In this section the effect of wave-topography interactions on growth, migration and spatial characteristics of sfcf is investigated. This is done by excluding perturbations in the wave orbital velocity: $u_w' = 0$, hence $u_w = U_w$. Physically, this means that wave refraction and shoaling and dissipation of wave energy due to the presence of bedforms are neglected together with the friction term related to perturbations in the wave orbital velocity. Note that

the latter was assumed in all previous models for sfcr, although a basic state wave orbital velocity was parametrically described. Default values for the parameters were used.

Results (not shown) reveal that the basic state is stable with respect to perturbations having a wavenumber $k > 2.2 \text{ km}^{-1}$. For smaller wavenumbers two modes are found with positive growth rates. The first mode has a maximum growth rate for a wavelength $\lambda = 6.9 \text{ km}$, whereas the second mode attains its maximum for $\lambda = 4.9 \text{ km}$. The growth rates are positive, but very small: e -folding time scales are $\sim 10^4 \text{ yr}$. Their migration speeds are $\sim 0.7 \text{ m yr}^{-1}$ in the direction of the longshore basic current. The bottom pattern of both modes consists of up-current oriented sfcr, which span the whole width of the inner shelf. The angle between crest axis and coastline is $\varphi \sim 30^\circ$ for the first mode and $\varphi \sim 25^\circ$ for the second mode.

4.4.4 SENSITIVITY TO THE REFERENCE BOTTOM SLOPE

Previous models (cf. *Trowbridge, 1995*) indicated that the growth of sfcr decreases monotonically with decreasing transverse bed slopes and no growth occurs in case that $\beta = 0$. However, these models did not account for perturbations in the wave orbital velocity. Therefore, we investigated the sensitivity of the growth process to the transverse bottom slope with the new model. Experiments were performed using default parameter settings, except for changing the water depth at the outer shelf H_s (and thus the transverse bed slope). The slope was gradually increased from 0 to the default value of 1.1×10^{-3} .

Already in case of a horizontal bottom, growing perturbations are obtained. The fastest growing mode has an e -folding time of $\sim 250 \text{ yr}$ and an alongshore spacing of 2.7 km . The bedforms are closely confined to the shoreface, up-current oriented and they migrate with 35 m yr^{-1} in the downstream direction. They span only about 15% (up to 0.8 km) of the inner shelf width. The obliqueness of the crest axis with respect to the coastline is somewhat larger than 35° . Increasing the transverse bed slope to the default value results in a slightly larger longshore spacing, 25% increase in growth rate and a minor decrease in migration speed. The offshore extent of sfcr increases from 0.8 km ($\beta = 0$) to 1.0 km (default slope).

4.4.5 SENSITIVITY TO OTHER MODEL PARAMETERS

One noticeable new element in the present study is the incorporation of a wave module based on physical principles. Consequently, it is important to investigate the dependence of model results on three new parameters viz., wave height, wave period and angle of wave incidence at the offshore boundary $x = L_s$. Unless mentioned otherwise, default values for the parameters were used. A range of conditions was examined. The offshore wave height $H_{rms,s}$ was varied between 1.0 and 5.0 m , representing a calm to a rough sea. The wave period T was varied such that both wind and swell seas are examined: $4 - 14 \text{ s}$. The offshore angle of wave incidence Θ_s was varied between -2° and -50° (from the northeast), which covers the range of conditions observed. According to *Draper (1991)* wave height and wave period are related, i.e., the higher the wave, the larger the wave period. Therefore, some extra experiments were performed in which wave height and wave period were varied according to *Draper's* formulation. Finally, experiments were carried out to investigate the effect of wave dissipation and a critical velocity for erosion on the results.

VARYING OFFSHORE WAVE HEIGHT

For the different offshore wave heights the basic state is computed and the stability problem is solved. Figure 4.8 shows the cross-shore profile of the basic state wave orbital velocity for different offshore wave heights. Waves with larger offshore wave height have a larger wave orbital velocity on the outer shelf. The higher the waves, the stronger their shoaling towards the coast, which results in a stronger increase of wave orbital velocities. The amplitude of the basic state longshore current is inversely related to the amplitude of the wave orbital velocity. Therefore, in case of a rough sea the longshore current is relatively weak on the outer shelf and it decreases comparatively fast towards the shoreface. For the depth-integrated sediment concentration the opposite holds (but more strongly), as the latter is proportional to U_w^3 .

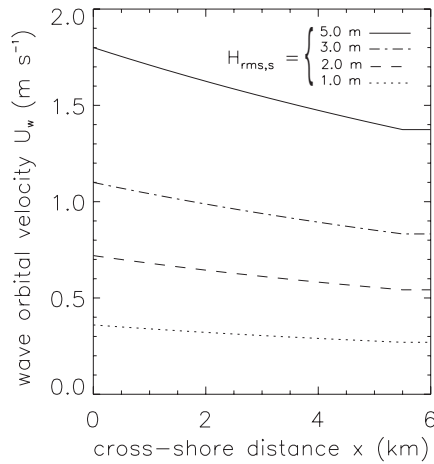


Figure 4.8: Cross-shore profiles of the wave orbital velocity in the basic state for different offshore wave heights.

Performing the linear stability analysis for different offshore wave heights revealed that the system exhibits one growing mode in all cases. Figure 4.9 shows the preferred wavelength, e -folding growth time and migration speed as a function of the offshore wave height. In all cases the waves were assumed to be present during 5% of the time. The alongshore spacing between two successive crests increases from $\lambda = 3.5 \pm 0.3$ km for $H_{rms,s} = 1.0$ m to $\lambda = 11.5 \pm 0.3$ km for $H_{rms,s} = 5.0$ m. The e -folding growth time decreases rapidly with increasing $H_{rms,s}$, which indicates an increase in growth rate with a factor 13. Even more remarkable is the strong increase in migration speed from 10 m yr^{-1} for a wave height of 1.0 m to 300 m yr^{-1} for a wave height of 5.0 m, both directed downstream. Note however that for 5.0 m high waves the assumed time fraction of occurrence should probably be a factor 10 smaller and corresponding values for growth time and migration speed would be 590 yr and 30 m yr^{-1} , respectively. Results of experiments with wave heights and periods related as for the *Draper* (1991) formula (results not shown) indicate that precise knowledge about both wave height and wave period is crucial for obtaining accurate estimates of growth times. Differences between the default and Draper cases are most significant for small wave heights.

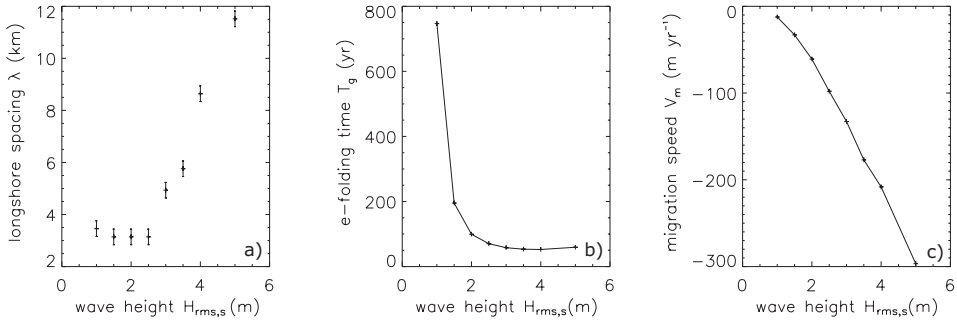


Figure 4.9: The sensitivity of the longshore spacing (a), *e*-folding growth time (b) and migration speed (c) of the fastest growing mode to the wave height at the outer shelf. Other parameters have their default values. The uncertainty in the longshore spacing is indicated with the error bars. Uncertainties in *e*-folding growth time and migration speed are very small, so no error bars are shown.

The increase in alongshore spacing of the bedforms for higher offshore waves is accompanied by an increase in their cross-shore extent. This is clearly visible when Figure 4.10a, which displays the spatial structure of the most preferred mode for a wave height of 5.0 m, is compared with Figure 4.5c.

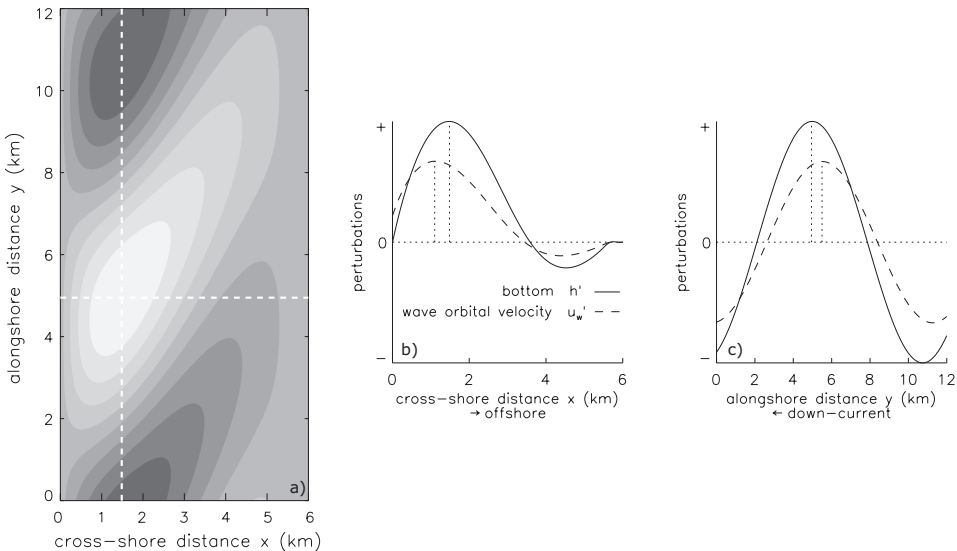


Figure 4.10: (a) Bottom pattern (grayscale; light: crests, dark: troughs) of the most preferred mode for a wave height of 5.0 m. The dashed white lines indicate the position of normal and longshore cross-sections through the sfc, which are shown in (b) and (c), respectively.

For a wave height of 5.0 m the bedforms extend offshore to approximately 100% of the inner shelf width, instead of about 18% for the default case. The obliqueness of the crest axis with respect to the coastline increases from $\varphi \sim 25^\circ$ ($H_{rms,s} = 1.0$ m) to $\varphi \sim 35^\circ$ ($H_{rms,s} = 5.0$ m). Another important feature is visible in Figures 4.10b and 4.10c, which show the perturbations in the wave orbital velocity and the bottom perturbations at a specific normal and alongshore transect through the sfc. For small wave heights the perturbed wave orbital velocity attains its maximum almost at the same offshore position as the ridge crest. However, faced in the longshore direction, the perturbation in the wave orbital velocity is slightly shifted up-current with respect to the position of the crest. When wave heights are increased the up-current phase shift in the alongshore direction between u'_{wv} and h' increases significantly (Figure 4.10c). Furthermore, a clear cross-shore phase shift is formed, where the perturbed wave orbital velocity is shifted onshore with respect to the bottom perturbation (Figure 4.10b).

VARYING WAVE PERIOD

Similarly as before, the basic state is computed for different wave periods. Results (not shown) reveal that the basic state wave orbital velocity is larger for low-frequency waves. This can be understood by realizing that two processes are competing here. The first is covered by the dispersion relation, which shows a more than linear decrease in wavenumber with decreasing wave frequency. The indirect effect is an increase of the wave orbital velocity. The second effect is the direct reduction of the wave orbital velocity for low-frequency waves. The competition is such that the indirect effect wins and wave orbital velocities increase for longer wave periods. As a consequence, the total sediment concentration in the water column will increase, whilst the basic state amplitude of the longshore velocity will decrease for waves with lower frequencies.

The stability analysis which is performed for different wave periods, indicates that one growing solution is obtained as long as the wave period exceeds 6 s. Figure 4.11 shows the preferred wavelength, e -folding growth time and migration speed for this mode as a function of the wave period.

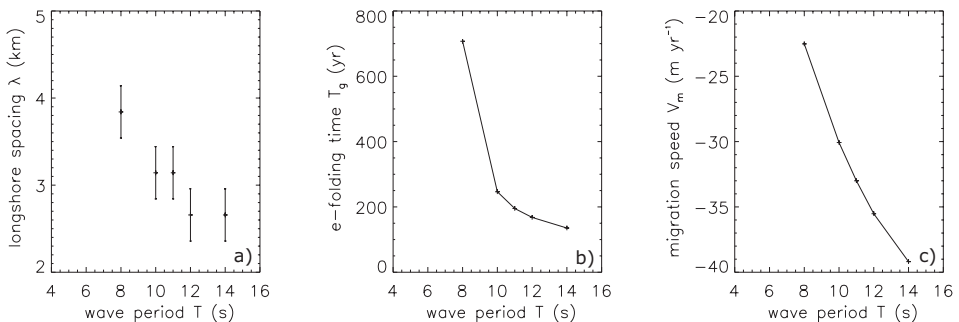


Figure 4.11: As Figure 4.9, but sensitivity to a change in wave period.

The longshore spacing of the bedforms slightly decreases with an increase in wave period, but it saturates at a value of $\lambda = 2.7 \pm 0.3$ km. The e -folding growth time decreases with a factor 5, where the largest decrease takes place at shorter wave periods. The migration speed of the sfcr increases more or less linearly with increasing wave period and in all cases sfcr propagate downstream. The spatial structure of the bedforms is similar to the ones shown in Figure 4.5c. The crests reach up to 1 km offshore in all the experiments. The angle between crest axis and coastline ranges from $\varphi \sim 25^\circ$ to 35° , being the largest for low-frequency waves. Investigation of the phase shift between perturbed wave orbital velocities and bottom perturbations has shown an increase in the longshore phase shift for longer wave periods. For both low- and high-frequency waves the cross-shore maximum in the perturbed wave orbital velocity is exactly on top of the ridge and no phase shift exists.

VARYING OFFSHORE ANGLE OF WAVE INCIDENCE

The basic state is computed while varying the offshore angle of wave incidence. The sensitivity of the magnitude of basic state variables to changes in the offshore angle of wave incidence is small. In case of more oblique incident waves the wave orbital velocity and depth-integrated concentration of sediment become smaller and the current amplitude becomes larger.

The linear stability analysis for distinct offshore angles of wave incidence provided clear mutual differences regarding the preferred wavelength, e -folding growth time and migration speed (see Figure 4.12) of the most preferred mode.

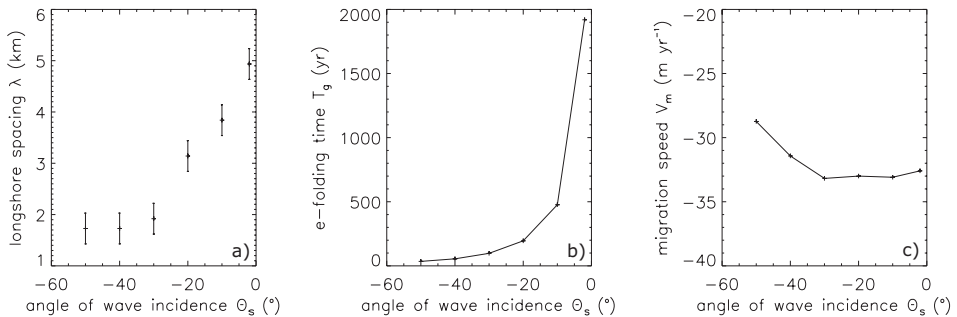


Figure 4.12: As Figure 4.9, but sensitivity to a change in the offshore angle of wave incidence.

For angles of wave incidence $|\Theta_s| > 30^\circ$ no clear maximum in the growth rate curve was found and thus no information is provided concerning the preferred wavelength of the evolving bottom patterns. For these specific experiments, the most preferred wavelength is estimated using the wavenumber at which the growth rate curve starts to saturate. For an angle of wave incidence almost normal to the shore at the outer shelf, the longshore spacing between successive crest is ~ 5 km. Increasing the offshore angle of wave incidence to -50° leads to a reduction in this spacing of at least 3 km. A similar behavior is observed for the offshore distance to which sfcr extend. The latter decreases from ~ 1.5 km (about 30% of the inner shelf width) to ~ 0.5 km (10% of the shelf width). The angle between crest axis and coastline

increases from about 25° to 30° for a change in the offshore angle of wave incidence from -2° to -20° . For $|\Theta_s| > 20^\circ$ the angle between crest axis and coastline is independent of the offshore angle of wave incidence. More oblique incident waves favor a faster development of bottom patterns. The e -folding growth time decreases with about a factor 50 for very oblique incident waves with respect to near-normal incident waves. The sensitivity of the bedform propagation speed to the offshore angle of wave incidence is limited. Enlarging the offshore angle of wave incidence from -2° to -50° results at first in a small increase in the down-current migration speed, but in the end a decrease to about 29 m yr^{-1} . For angles of wave incidence which are sufficiently large, also a secondary and tertiary mode emerge.

ROLE OF OTHER PROCESSES

So far we have presented results for cases in which the influences of both dissipation of wave energy and a threshold velocity for erosion are taken into account. The latter is a new element with respect to former studies, whereas dissipation is new in the sense that wave processes are explicitly described in this study. Experiments reveal that the above-mentioned processes are responsible for a 16% reduction in growth rates and a 13% decrease in propagation speeds. Critical shear-stresses for erosion contribute most significantly to the damping of growth and migration. The longshore spacing of bedforms is not affected by the two processes. Finally, the relative importance of bedload and suspended load transport in the default case is determined. Simulations show that 87% of bedform growth and migration are caused by suspended load transport.

4.5 DISCUSSION

4.5.1 PHYSICAL INTERPRETATION

For the default setting of the model parameters, it has been demonstrated that the basic state is unstable and growing bottom perturbations resemble up-current oriented sfc. In this section the physical processes responsible for the growth, migration and spatial pattern of these sfc are analyzed. A convenient procedure, which was also used by *Trowbridge* (1995) and *Calvete et al.* (2001a), is to derive an equation which combines the continuity equation for water (4.13) and the conservation equation for sediment mass (4.15). Linearizing both equations with respect to small perturbations and combining the results yields the so-called bed evolution equation

$$\begin{aligned}
 & \overbrace{(1-p) \frac{\partial h'}{\partial t}}^{T0} + \overbrace{\frac{3}{2} \nu_b U_w^2 V \frac{\partial h'}{\partial y}}^{T1} - \overbrace{\vec{\nabla} \cdot (\lambda_{bs} \vec{\nabla} h')}^{T2} = \\
 & - \overbrace{\frac{d}{dx} \left(\frac{3}{2} \nu_b \frac{U_w^2}{H} \right) H u'}^{T3} - \overbrace{\delta \frac{dC_a}{dx} H u'}^{T4} - \overbrace{\frac{\partial}{\partial y} (3\nu_b U_w V u'_w)}^{T5} - \overbrace{\frac{\partial}{\partial y} (\delta V H c'_a)}^{T6},
 \end{aligned} \tag{4.31}$$

where $\lambda_{bs} = (3/2)\nu_b \lambda_b U_w^3 + \lambda_s U_w^5$. The formulation is as in section 4.3, before substituting the longshore periodic and exponentially growing solutions. Here, in case of wave orbital velocities exceeding the critical velocity for erosion, the effects of the latter are ignored. Thus, the

basic state reference volume concentration is written as $C_a = \hat{c}_a U_w^3 / u_c^3$ for $U_w^2 > u_c^2$ (derived from equation (4.19) by substitution of basic state variables). By straightforward calculations it follows that the perturbed reference volume concentration is $c'_a = 3 \hat{c}_a U_w^2 u'_w / u_c^3$.

In the bed evolution equation, term T0 represents the growth or decay of bedforms. Bedforms grow (decay) if $\partial h' / \partial t > 0$ ($\partial h' / \partial t < 0$) above the crests. Term T1 describes the alongshore migration of the bed perturbations due to bedload processes. Term T2 is a consequence of the downslope sediment transport and causes diffusion of bedforms. The terms on the right-hand side of the bed evolution equation are possible sources of instabilities. Term T3 represents the *Trowbridge* (1995) mechanism in the specific case of $(3/2)\nu_b U_w^2 \rightarrow K_{stir} = \text{constant}$, in which K_{stir} is called the sediment load. Essential for this mechanism to work is the presence of a transversely sloping reference bottom. Trowbridge demonstrated that in order to have growth, the current should exhibit an offshore deflection over the ridge crest. In other words, there must be a positive correlation between u' and h' . The latter only occurs if sfcr are up-current oriented. In addition, taking into account both term T3 and T4 in equation (4.31) gives the mechanism proposed by *Calvete et al.* (2001a). They found that in order to have growth of up-current oriented sfcr, the cross-shore gradient in the reference volume concentration (dC_a/dx) should be negative above ridge crests. Thus, the basic state wave orbital velocity U_w should increase towards the shoreface. Again, essential is the presence of an inner shelf with transverse bottom slope.

Finally, terms T5 and T6 in the bed evolution equation are a consequence of bedform-induced perturbations in the wave orbital velocity u'_w and reference volume concentration c'_a , respectively. These terms, of which term T6 is the dominant one, describe a new physical mechanism, which is hereafter called the wave-bedform feedback mechanism. The latter is, in contrast with the other two mechanisms, also effective in case of a nonsloping reference bottom. In order to have a positive feedback between waves and bedforms, term T6 (the dominant one) should be negative above a ridge and thus $\partial c'_a / \partial y > 0$ (note that V is negative). As c'_a is linearly related to u'_w , this means that $\partial u'_w / \partial y > 0$ at the crests. More precisely, in order to have growth the spatial correlation $\overline{h'(\partial u'_w / \partial y)}$ should be positive, where the bar denotes averaging over the domain. Assuming $h' = \hat{h}(x) \cos(ky)$ and $u'_w = \hat{u}_w(x) \cos(ky - \phi(x))$, where ϕ denotes an alongshore phase shift between u'_w and h' , it follows

$$h' \frac{\partial u'_w}{\partial y} \sim k \int_0^\infty \sin \phi \hat{h} \hat{u}_w dx. \quad (4.32)$$

From this we see that a positive phase shift ϕ between \hat{u}_w and \hat{h} can initiate growth of bedforms and therefore the maximum in the perturbed wave orbital velocity should be located upstream of the maximum in the bed perturbation. This is only the case for up-current rotated sfcr, which exhibit a clear convergence of perturbed wave energy on their upstream side (see Figure 4.6b-d) with a corresponding increase in the magnitude of the wave orbital velocity (see Figure 4.7). Thus, the enhanced stirring of sediment by waves in the upstream region causes an increase in the sediment concentration, which is subsequently transported by the background current and deposited on the downstream side of sfcr. The wave-bedform feedback mechanism thus leads to enhanced growth and migration of the bedforms.

Similar derivations for the *Trowbridge* (1995) and *Calvete et al.* (2001a) mechanisms show that a phase shift between the cross-shore velocity perturbation (u') and the bed perturbation (h') can also initiate growth. However, the growth according to the wave-bedform feedback mechanism is linearly related to the alongshore wavenumber k (because of the longshore derivative $\partial u'_w / \partial y$), whereas the other two mechanisms are not. Consequently, the wave-bedform feedback mechanism dominates over the two other mechanisms, albeit that the latter are still significant. This is clearly visible in Figure 4.13, which shows, for the default case in Figure 4.5, the relative contributions of the different terms in equation (4.31) to total growth and migration.

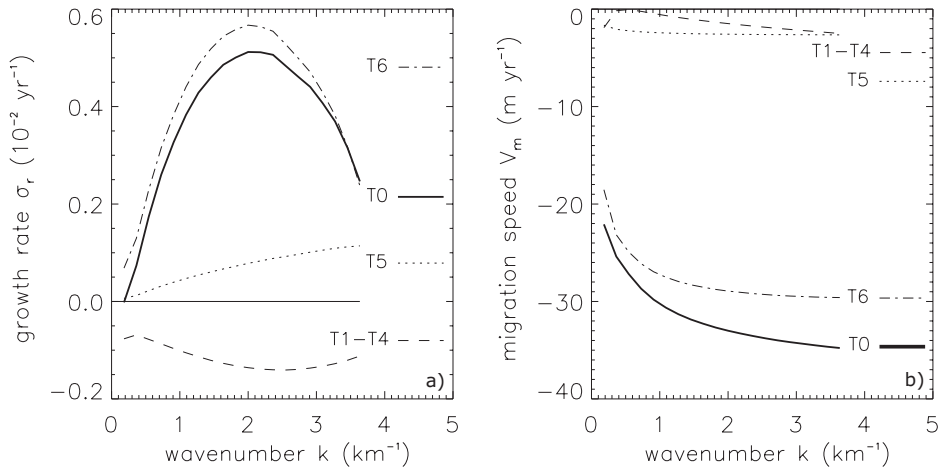


Figure 4.13: Relative contributions of the different terms in equation (4.31) to the growth rate (a) and migration speed (b) of the mode for the default case shown in Figure 4.5. Here, T0 is total and T1-T4 means T1+T2+T3+T4.

Analysis of equations (4.27b) and (4.27c) shows that the phase shift between wave orbital velocity perturbations and the bed topography is mainly a consequence of bedform-induced wave refraction. The latter is controlled by the second term on the left-hand side of the 'generalized Snell's law' (4.27b). The focusing of wave energy due to wave refraction is governed by the first two terms on the right-hand side of equation (4.27c). The latter process is clearly visible in e.g. Figure 4.6a in the convergence of wave rays upstream of the sfc, which leads to an increase of perturbed wave energy in that area.

The sensitivity of model results to variations in the parameters is largely determined by the wave-bedform feedback mechanism. The increase in growth rate and migration speed for higher offshore waves is due to the increase in amplitude of the basic state wave orbital velocity and the increase in phase shift between h' and u'_w . However, also bed slope effects increase strongly, which causes the preferred mode to have a larger wavelength (as the down-slope movement of sediment is most effective for the small length scales). An increase in

wave period leads to similar behavior for the growth rates and migration rates, however the effect is smaller as the magnitude of the basic state wave orbital velocity and increase in phase shift between h' and u'_w are limited. Thus, changes in the longshore spacing are minor. The large increase in growth rate for an increase in the angle of wave incidence at the outer shelf is a consequence of the large increase in phase shift between h' and u'_w . Note that in case of near-normal wave incidence almost no wave refraction is taking place, and thus the wave-bedform feedback mechanism is relatively inefficient compared to the *Trowbridge* (1995) and *Calvete et al.* (2001a) mechanisms.

4.5.2 COMPARISON WITH OBSERVATIONS

The model results have been compared with data of sfc from different inner shelves. Particular attention has been paid to the alongshore spacing between successive crests, the angle between crestlines and coastline, the cross-shelf extent of sfc, their growth time and their migration speed.

For the default parameter setting in section 4.4 (representative for Long Island inner shelf) the most preferred mode is characterized by an alongshore spacing $\lambda \sim 3.1$ km. This is slightly smaller than the observed spacing at this shelf (*Niedoroda and Swift*, 1981; *Schwab et al.*, 2000). Generally, observed spacings of sfc range from 2–6 km. Note that Figure 4.9a indicates that the spacing predicted by the model increases when larger values of the wave height at the outer shelf are taken. In case that $H_{rms,s} = 3$ m the model predicts $\lambda \sim 4.9$ km.

The angle between the coastline and the crest axis obtained with the model in case of the default parameter setting is $\varphi \sim 30^\circ$. Positive values of φ indicate that sfc are upstream oriented, i.e., their offshore ends are shifted upstream with respect to their attachments at the shoreface. The value of this angle for sfc that occur at Long Island inner shelf is $\varphi \sim 30 - 40^\circ$ (*Schwab et al.*, 2000). Thus, the model predicts the correct orientation of the crests. For experiments with different wave periods, offshore wave heights or offshore angles of wave incidence we obtain $\varphi = 30^\circ \pm 5^\circ$. *Duane et al.* (1972) analyzed data of sfc at different shelves and concluded that most sfc have angles φ between 10° and 50° . Almost all sfc have positive angles, so they are upstream oriented. This is also predicted by the model.

A noticeable difference between sfc obtained with the present model and those found with earlier models (*Trowbridge*, 1995; *Calvete et al.*, 2001a) is that they are more trapped to the coast. In the default case the offshore extent of sfc is 1 km, i.e., about 20% of the width of the inner shelf, whereas the previous models yield sfc that fully cover the shelf. The observed sfc at Long Island shelf extend about 2.5 km over the shelf, i.e., a coverage of about 50%. Inspection of patterns of sfc at other shelves, as presented in *Swift et al.* (1978) and *Van de Meene and Van Rijn* (2000), reveals that most sfc occupy about half of the width of the inner shelf. Such values of the cross-shore extent of sfc are predicted with our model in case that $H_{rms,s}$ is about 3.5 m. We stress that previous models always predict sfc that cover the entire shelf.

Finally, we consider the growth time scale T_g and migration speed V_m of sfc. The present model yields a growth time scale $T_g \sim 195$ yr and a migration speed $V_m \sim 33$ m yr⁻¹ (downstream migration) for the default case. There are no direct field data of the e -folding growth time T_g , but considering the lifetime of sfc (several thousands of years) the model result is satisfactory. With regard to the migration speed, observed values range from 1 – 50 m yr⁻¹, depending on the measuring period (e.g. *Duane et al.*, 1972; *Van de Meene and Van Rijn*, 2000). All sfc migrate in the downstream direction, as is also predicted by the model. In all observational studies it is stressed that storms are highly episodic events and that during a single, severe storm sfc can migrate over longer distances than in an entire year without such a storm. Also, an important thing to note is that the modeled values are subject to high uncertainties. They scale linearly with the time fraction during which storms prevail (here a time fraction of 5% is assumed), the reference concentration near the bed (which is controlled by parameter \hat{c}_a) and the thickness of the suspended load layer (controlled by parameter δ). In our model the formulation of \hat{c}_a is that proposed by *Van Rijn* (1993), for which \hat{c}_a is inversely proportional to the reference height z_a above the bed where the reference concentration is defined. In the model simulations the value of z_a is based on the assumption that there are no dunes and sandwaves present on the sea bottom. However, in reality such relatively small-scale bedforms (compared to sfc) are definitely observed. As a consequence, the value of z_a becomes larger and that of \hat{c}_a becomes smaller. A factor of order 5 – 10 seems quite plausible.

4.5.3 MODEL SIMPLIFICATIONS

The observed patterns of sfc are actually rather complex and the model only describes the gross characteristics. The model used in this study is largely simplified with respect to reality, there might be other processes that affect the growth of sfc in nature. First, in the model radiation stresses exerted by the waves and wave-induced Stokes drift are ignored. Second, the linear stability analysis employed yields no information about the finite amplitude of sfc. By using a depth-averaged model, the role of the vertical structure of the currents is neglected. However, field data (e.g. *Niedoroda et al.*, 1984) have revealed the presence of vertical circulation cells perpendicular to the coast. This suggests that taking into account 3D processes in the current model is important. Another simplification is the use of one single grain size in the experiments, whereas data clearly show variations in grain size over sfc.

In the present study we consider the micro-tidal American shelf, for which it is justifiable to consider only storm-driven currents and neglect the relatively weak tidal flows. However, near e.g. the Dutch and German coasts strong tidal currents occur and bottom stresses are sufficiently strong to erode and transport sediment even during fair weather conditions. *Calvete et al.* (2001b) demonstrated that dependent on the actual tidal conditions, intensity of the storm-driven flow and fraction of time during which storms prevail a variety of large-scale bedforms, including tidal sand banks and sfc, are formed. According to *Walgreen et al.* (2002) overtides can have a large effect on migration speeds of sfc, but not on their growth rates. It would be interesting to investigate the effect of tidal flow in the context of the present model.

4.6 CONCLUSIONS

In this chapter a new model has been discussed that describes the initial formation of sfc on micro-tidal inner shelves due to the interaction between waves, a storm-driven current along the coast and the sandy bottom. The most distinct differences between the present model and those of *Trowbridge* (1995) and *Calvete et al.* (2001a) is that here the behavior of waves is described by equations, which are derived from physical principles, rather than by a parameterization, and that interactions between waves and bedforms are accounted for. Moreover, erosion of sediment now only occurs if the wave orbital velocity exceeds a critical value.

For a model setting that resembles the situation at Long Island inner shelf, it has been found that the fastest growing modes resemble sfc of which the offshore ends are shifted upstream with respect to their attachments to the shoreface. Typical alongshore distances between successive crests are several kilometers and sfc migrate several tens of meters per year. Compared to results obtained with previous models the sfc are more trapped to the coast, only for large wave heights at the outer shelf (> 3.5 m) the bedforms extend over the entire shelf. Including a critical velocity for erosion has a tempering effect on the growth.

A physical analysis has revealed that in this model sfc grow due to three different mechanisms. The first is the one described by *Trowbridge* (1995), which involves the offshore deflection of the current over sfc over a transversely sloping bottom. The second is described by *Calvete et al.* (2001a) and involves the joint action of cross-shore gradients in the depth-averaged sediment concentration of the reference state (i.e., the state in which bedforms are absent) and the offshore deflection of currents over the ridges. The third is new and is referred to as the wave-bedform feedback mechanism. It significantly contributes to further growth of upstream oriented sfc, because the latter cause wave rays to converge (diverge) on the upstream (downstream) sides of the crests. Consequently, focusing (defocusing) of wave energy in these areas occurs, which subsequently results in enhanced (reduced) stirring of sediment by waves, hence also of sediment load, which is subsequently transported as suspended load by the storm-driven flow. This mechanism is in general more effective than the first two mechanisms. The consequence is that both growth and migration of sfc are now controlled by suspended load transport of sediment; bedload transport only plays a minor role. Furthermore, the formation of sfc does not require the presence of a transversely sloping bottom, albeit that model results are in better agreement with field data in case that the modeled shelf geometry has such a slope. We conclude that comparison of model results with field data at different shelves is satisfactory, given the large uncertainties in the magnitude of the suspended load sediment transport and in the time fraction during which storms prevail and sfc evolve.

APPENDIX

4.A PERTURBED FLOW AND SEDIMENT TRANSPORT

The perturbed cross-shore and longshore velocity component, free surface elevation, depth-integrated volume concentration of suspended sediment, wave orbital velocity and bottom elevation are denoted by u' , v' , η' , c' , u'_w and h' , respectively. After linearization of equations (4.12)-(4.14) and equations (4.18)-(4.20) with respect to these small perturbations, the following system is obtained:

$$\begin{pmatrix} \mathcal{L}_{11} & \mathcal{L}_{12} & \mathcal{L}_{13} & \mathcal{L}_{14} \\ \mathcal{L}_{21} & \mathcal{L}_{22} & \mathcal{L}_{23} & \mathcal{L}_{24} \\ \mathcal{L}_{31} & \mathcal{L}_{32} & \mathcal{L}_{33} & \mathcal{L}_{34} \\ \mathcal{L}_{41} & \mathcal{L}_{42} & \mathcal{L}_{43} & \mathcal{L}_{44} \end{pmatrix} \begin{pmatrix} u' \\ v' \\ \eta' \\ c' \end{pmatrix} = \begin{pmatrix} 0 \\ \mathcal{W}_2 \\ 0 \\ \mathcal{W}_4 \end{pmatrix} u'_w + \begin{pmatrix} 0 \\ 0 \\ -\mathcal{L}_{35} \\ -\mathcal{L}_{45} \end{pmatrix} h'.$$

In this expression, $\mathcal{L}_{..}$ refers to the corresponding elements of operator \mathcal{L} in appendix 2.B, where $\gamma \rightarrow w_s/\delta$ with w_s the settling velocity and δ the ratio of the thickness of the suspended load layer over the total water depth. Due to the fact that perturbations in the wave orbital velocity are included, the vector operator \mathcal{W} appears, which has nonzero elements that are given by

$$\mathcal{W}_2 = -\frac{rV}{H}, \quad \mathcal{W}_4 = 3\frac{w_s\hat{c}_a}{u_c^2}U_w(U_w^2 - u_c^2)^{1/2}.$$

The friction coefficient r , the basic state current V , the basic state bottom elevation H , the basic state wave orbital velocity U_w , the coefficient \hat{c}_a and the critical wave orbital velocity u_c are defined in the main text.

The final step is to derive the linearized version of the evolution equation (4.15) for the bed elevation h' . Hereto, perturbations \bar{q}_b' and \bar{q}_s' are added to the bedload and suspended load sediment transport in the basic state, respectively. The x - and y -component of the perturbed sediment transport due to bedload are

$$\bar{q}_{bx}' = \frac{3}{2}\nu_b(U_w^2 - u_c^2)u' - \frac{3}{2}\nu_b\lambda_b U_w(U_w^2 - u_c^2)\frac{\partial h'}{\partial x}, \quad (4.A-1)$$

$$\bar{q}_{by}' = 3\nu_b U_w V u'_w + \frac{3}{2}\nu_b(U_w^2 - u_c^2)v' - \frac{3}{2}\nu_b\lambda_b U_w(U_w^2 - u_c^2)\frac{\partial h'}{\partial y}. \quad (4.A-2)$$

Here, ν_b is a coefficient and λ_b is the bed slope parameter for bedload sediment transport. The x - and y -component of the perturbed sediment transport due to suspended load are

$$\bar{q}_{sx}' = C u' - \lambda_s U_w^5 \frac{\partial h'}{\partial x}, \quad (4.A-3)$$

$$\bar{q}_{sy}' = C v' + V c' - \lambda_s U_w^5 \frac{\partial h'}{\partial y}. \quad (4.A-4)$$

Here, C is the depth-integrated volumetric concentration of suspended sediment in the basic state and λ_s is the bed slope coefficient for suspended load transport.

CHAPTER 5

EFFECT OF WAVE-BEDFORM FEEDBACKS ON THE FORMATION OF AND GRAIN SORTING OVER SHOREFACE-CONNECTED RIDGES

ABSTRACT

The influence of wave-bedform feedbacks on both the initial formation of shoreface-connected sand ridges (hereafter abbreviated as sfc_r) and on grain size sorting over sfc_r on micro-tidal inner shelves is studied, as well as the effect of sediment sorting on growth and migration of these ridges. This is done by applying a linear stability analysis to an idealized process-based morphodynamic model, which simulates the growth of sfc_r due to the positive coupling between waves, currents and a sandy bed. Work considering uniform sediment (see chapter 4) has shown that wave-topography interactions are important in the evolution process of sfc_r. Whether they are also crucial for the development of a spatial variation between the mean grain size and the bottom topography, as is observed in the field, is investigated in this chapter with a model for a bimodal sediment mixture. Additional new elements with respect to earlier studies are cross-shore dependent sediment properties, a roughness-dependent entrainment of suspended sediment and settling lag effects. The results of the model indicate that sediment sorting causes a reduction of the growth rate and migration speed of sfc_r, whereas the wavelength is only slightly affected. In case that the entrainment of suspended sediment depends on bottom roughness the coarsest sediment is found in the troughs, otherwise the finest sediment occurs in the troughs. Compared to previous work, modeled maximum variations in the mean grain size over the topography are in better agreement with field observations. Settling lag effects are crucial for the damping of high wavenumber mode instabilities such that a preferred wavelength of the bedforms is obtained.

5.1 INTRODUCTION

Sfcr are rhythmic bottom patterns that are found on sandy, storm-dominated inner shelves in water depths of 5 – 30 m. During storms the water motion is characterized by high waves (wave heights of 2 – 4 m) and a mean storm-driven alongshore flow of up to 0.5 m s^{-1} . Field observations (Swift *et al.*, 1978; Antia, 1996a; Van de Meene and Van Rijn, 2000; Schwab *et al.*, 2000, and references herein) reveal that crests of individual sfcr have a length between 10 and 25 km, a height of 1 – 6 m and a mutual spacing in the order of 2 – 6 km. Sfcr are attached to the shoreface and extend seaward in a direction that is obliquely oriented with respect to the shoreline. The orientation is such that the seaward ends of the crests are shifted in the dominant direction of the storm-driven flow. Sfcr evolve on a time scale that is in the order of decades to centuries and they migrate in the direction of the storm-driven flow with $1 – 50 \text{ m yr}^{-1}$, depending on the measuring period. Furthermore, field data indicate a persistent pattern of grain sorting over sfcr. In most cases the sediment at the seabed is coarsest on the landward flanks and finest on the seaward flanks. This phase shift between the mean grain size and topography variations is documented for sfcr on the Mid Atlantic shelf (e.g. Swift *et al.*, 1972; Schwab *et al.*, 2000), the shelf of the German Bight (Antia, 1996a), as well as on the inner shelf of Argentina (Parker *et al.*, 1982).

Both observations (Swift and Field, 1981) and former studies (Trowbridge, 1995; Calvete *et al.*, 2001a) have indicated that sfcr can grow, because of a positive feedback between the water motion and the erodible sandy bed. During stormy weather, bottom stresses exerted by the waves are strong enough to entrain the sediment, which is subsequently transported by the storm-driven flow. The growth and migration of sfcr was investigated by defining a basic state and investigating the dynamics of small perturbations on this basic state. Calvete *et al.* (2001a) demonstrated that the fastest growing bottom perturbations have spatial patterns, growth times and migration speeds that agree quite well with those of observed sfcr. Moreover, the growth and orientation of sfcr were explained in terms of physical mechanisms.

One limitation of these studies is that they consider sediment with a uniform grain size, which is not in accordance with field data. Walgreen *et al.* (2003) analyzed a model that considers the effect of sediment sorting on the formation of sfcr. Results of this model indicate that the phase shift between bed topography and mean grain size is due to the selective transport via suspended load of grains with different sizes. Furthermore, sediment sorting has a net stabilizing effect on the growth of sfcr, whereas their migration speed becomes larger and their wavelength is only slightly affected. A physical explanation of the results was also given. Similar studies are performed by Murray and Thielert (2004) and Coco *et al.* (2007a,b) to clarify observed grain sorting for sorted bedforms. Roos *et al.* (2008) and Van Oyen and Blondeaux (2008) investigated the effect of grain sorting on tidal sand waves.

The models on sfcr discussed so far suffer from the fact that they employ a strongly simplified description of waves in calculating stirring of sediment. In two recent studies by Lane and Restrepo (2007) and Vis-Star *et al.* (2007) a more sophisticated description of waves is applied, based on linear wave theory, which enables to include explicit feedbacks between waves and sfcr. The latter results in additional transport (by the storm-driven flow) of sedi-

ment being entrained by the wave orbital motion, which is generated by the bedforms. In the latter study it is demonstrated that the spatial variations in this sediment transport are such that both the growth and downstream migration of sfcf are enhanced. *Lane and Restrepo (2007)* on the other hand report that they do not obtain growth of bedforms if they include wave-bedform interactions. This seems to be a consequence of their assumption that sediment transport is proportional to the mass transport velocity (which accounts for currents and wave-induced Stokes drift), rather than being proportional to the near-bed current.

In this chapter the model of *Vis-Star et al. (2007)*, see also chapter 4, is extended such that it enables the exploration of wave-bedform feedbacks in a model for bimodal sediment mixtures. This is done by adopting and extending the sediment sorting module for a bimodal sediment mixture of *Walgreen et al. (2003)*. The first aim of this work is to investigate whether wave-bedform interactions play an important role in the initial growth of sfcf, as well as in the initial onset of grain sorting over sfcf. Secondly, the influence of sediment sorting on the characteristics of sfcf is explored. Several new aspects are included in the sediment module. First, the longshore-averaged value of the mean grain size is allowed to vary linearly in the cross-shore direction. As a consequence, also its standard deviation and the fraction of grains in a size class vary in the cross-shore direction. Second, motivated by work of *Murray and Thieler (2004)*, *Coco et al. (2007a,b)* and *Huntley et al. (2008)* on sorted bedforms on the inner shelf, settling lag and roughness-induced turbulence effects are included in the suspended load sediment transport.

In section 5.2 a detailed discussion of the process-based model is given, followed by a description of the solution method in section 5.3. Section 5.4 presents the results, which are discussed in section 5.5. Finally, the conclusions are drawn (section 5.6).

5.2 MODEL FORMULATION

5.2.1 SHELF GEOMETRY

The basic state geometry is shown in Figure 5.1 and represents a semi-infinite domain, bounded on the landward side by the transition from shoreface to inner shelf. In the seaward direction the water depth increases up to the transition to the outer shelf, where the latter is characterized by a flat bottom. The shelf geometry is assumed to be longshore uni-

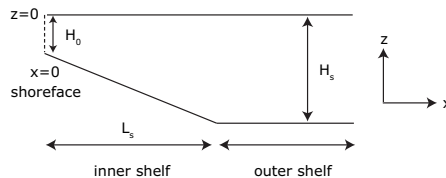


Figure 5.1: Side view of a typical longshore- and time-averaged bottom topography of the continental shelf, representing the inner and outer shelf, in the shore-normal direction. Symbols are explained in the text.

form and bedforms are absent. The x -, y - and z -axis of the orthogonal coordinate system that is used point in the cross-shore, alongshore and vertical direction, respectively. The water depth on the landward side of the inner shelf ($x = 0$) is H_0 , L_s is the inner shelf width and the depth of the outer shelf is indicated by H_s .

5.2.2 HYDRODYNAMICS

WAVES

Linear wave theory is used to describe the properties of offshore waves approaching the shoreface. For the waves and water depths considered here (the inner shelf region) this approximation is reasonable. The equations used are similar as in the study by *Vis-Star et al.* (2007). Rayleigh distributed random waves are considered, characterized by a narrow band of frequencies and orientations. The narrow spectrum is centered around a peak frequency, wavenumber and wave orientation. Stationary wave conditions are assumed, which is justified by the fact that the time scale of the waves (order of 10 s) is very small compared to the morphodynamic time scale (order of 100 yr). Under this assumption the law of conservation of wave crests implies that the radian wave frequency ω is constant. Subsequently, the dispersion relation, wavenumber identity relation and wave energy balance determine the wavenumber κ , the angle of wave incidence θ and the wave energy density \mathcal{E} (per surface area) for a certain bottom profile with water depth D . The rigid-lid approximation is used, i.e., the effects of the free surface on the local water depth are neglected, thus $D = z_s - z_b$ is approximated by $\tilde{D} = -z_b$. Here, z_s and z_b are the free surface elevation and the bottom depth both measured with respect to the undisturbed water level $z = 0$. Refraction of waves by currents is not taken into account. The root-mean-square amplitude of the near-bed wave orbital velocity (hereafter called wave orbital velocity) is calculated as

$$u_w = \frac{\omega \mathcal{H}_{rms}}{2 \sinh(\kappa \tilde{D})}. \quad (5.1)$$

Here, \mathcal{H}_{rms} is the root-mean-square wave height, which follows from the definition for the wave energy: $\mathcal{E} = \rho g \mathcal{H}_{rms}^2 / 8$. In the latter expression, ρ is the water density and g the acceleration due to gravity. The wave orbital velocity is an important variable in both the current part and the sediment transport part of the model. Offshore wave properties (height, period and angle of incidence) are imposed.

CURRENTS

The water motion is described by the depth- and wave-averaged (2DH) shallow water equations

$$(\vec{v} \cdot \vec{\nabla})\vec{v} + f \vec{e}_z \times \vec{v} = -g \vec{\nabla} z_s + \frac{\vec{\tau}_s - \vec{\tau}_b}{\rho \tilde{D}}, \quad (5.2)$$

$$\vec{\nabla} \cdot (\tilde{D} \vec{v}) = 0. \quad (5.3)$$

Here, $\vec{v} = (u, v)$ is the depth- and wave-averaged velocity, f the Coriolis parameter, \vec{e}_z a unit vector in the vertical direction and g the gravitational acceleration. Furthermore, $\vec{\tau}_s$ represents the wind stress, $\vec{\tau}_b$ the bed shear-stress and $\vec{\nabla}$ is the two-dimensional (horizontal)

nabla vector. In the momentum equations (5.2) forcing terms due to wave-induced radiation stresses, horizontal momentum diffusion, density gradients and tides are not considered. It is assumed that the mean storm-driven flow is in the alongshore direction (cross-shore component is neglected), due to a given wind stress τ_{sy} .

This model only represents stormy weather conditions, during which the wave orbital velocity is much larger than the magnitude of the storm-driven current. It is assumed that during fair weather conditions the water motion is not strong enough to erode the sediment from the bottom. In case of storms the bed shear-stress is linearly related to the mean flow:

$$\vec{\tau}_b = \rho r u_w \vec{v}, \quad (5.4)$$

with r a dimensionless friction coefficient computed for random waves and u_w given in equation (5.1). Boundary conditions are that the cross-shore flow component u vanishes at $x = 0$ and far offshore and periodic conditions in the longshore direction are assumed.

5.2.3 SEDIMENT CHARACTERISTICS

The sediment considered in the present study is a mixture of grains of two different sizes, with d_1 and d_2 the grain diameters of the fine and coarse material, respectively. As the distribution of grain sizes in a mixture appears to be close to log-normal, it is convenient to use a logarithmic scale for the grain diameter, the phi-scale:

$$d_i = 2^{-\phi_i} \quad \text{or} \quad \phi_i = -\log_2 d_i \quad (i = 1, 2), \quad (5.5)$$

where d_i is measured in units of mm (Dyer, 1986). Note that the larger the phi-value the smaller the grain size. The weight percentages of the fine and coarse grain size class are given by \mathcal{F}_1 and \mathcal{F}_2 , respectively, and

$$\sum_{i=1}^2 \mathcal{F}_i = 1. \quad (5.6)$$

The probabilities are used to calculate two statistical properties of the sediment mixture, the mean grain size ϕ_m and the standard deviation v_s . The latter two are defined as

$$\phi_m = \sum_{i=1}^2 \phi_i \mathcal{F}_i, \quad v_s^2 = \sum_{i=1}^2 (\phi_i - \phi_m)^2 \mathcal{F}_i. \quad (5.7)$$

The standard deviation of the distribution gives a measure of the sorting of the sediment mixture. A poorly sorted mixture of sediment has large values of v_s , whereas a well-sorted, almost uniform sample corresponds to small v_s values. The mean grain diameter follows from $d_m = 2^{-\phi_m}$.

5.2.4 SEDIMENT DYNAMICS

The bottom evolution is determined by divergence of the sediment transport. The latter depends on the sediment composition. In the case of a sediment mixture the grain size distribution itself will also change. A simple model is used (Seminara, 1995, and references herein)

to describe the bottom sediment as consisting of a well-mixed active layer (\mathcal{F}_i is independent of depth) and underneath a substrate of which the mean grain size and sorting do not vary in time. A sketch is given in Figure 5.2, where $z_b = -H + h'$ denotes the bottom location, H denotes the undisturbed water depth and h' is the bed elevation with respect to this reference level. The thickness of the active layer L_a is in the order of 2 – 3 mm.

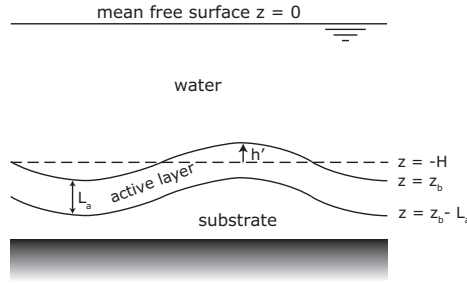


Figure 5.2: Definition of the sediment layer as used in the model. The thickness of the active layer is denoted by L_a and h' is the elevation of the bottom with respect to the reference level $z = -H$.

It is assumed that during the initial growth stage of bedforms, rearrangement occurs of material in the active layer, whereas negligible interaction between substrate and active layer takes place. This implies that mass conservation for each size class is given by

$$(1 - p) \left(\mathcal{F}_i \frac{\partial z_b}{\partial t} + L_a \frac{\partial \mathcal{F}_i}{\partial t} \right) = -\vec{\nabla} \cdot \vec{q}_i. \quad (5.8)$$

Here, p is the bed porosity, t is time and \vec{q}_i is the wave-averaged total volumetric transport of sediment per unit width of grains with size d_i . Summation of equation (5.8) for the two size fractions and using the constraint (5.6) results in an evolution equation for the bed level. Back-substitution of this result into equation (5.8) for $i = 1$ yields an equation for the grain size distribution of the fine fraction. The results are

$$(1 - p) \frac{\partial z_b}{\partial t} = -\vec{\nabla} \cdot \vec{q}_1 - \vec{\nabla} \cdot \vec{q}_2, \quad (5.9a)$$

$$0 = \mathcal{F}_1 \vec{\nabla} \cdot \vec{q}_2 - \mathcal{F}_2 \vec{\nabla} \cdot \vec{q}_1. \quad (5.9b)$$

Strictly speaking, the left-hand side of equation (5.9b) is $L_a \frac{\partial \mathcal{F}_1}{\partial t}$, but the magnitude of this term is only a very small factor of that of the contributions related to the divergence of the sediment fluxes and can therefore be excluded.

Sediment in each grain size class is transported both as bedload (\vec{q}_{bi}) and suspended load (\vec{q}_{si}), thus

$$\vec{q}_i = \vec{q}_{bi} + \vec{q}_{si}. \quad (5.10)$$

Expressions for \vec{q}_{bi} and \vec{q}_{si} are derived from expressions for a single grain size. Corrections for the availability of sediment in a size class and for dynamic hiding effects (fine grains hide

between the coarser grains and hence experience a smaller fluid drag) are needed to calculate the sediment transport of grains of a specific size. Static hiding effects due to the presence of a critical shear-stress for erosion are neglected.

The bedload sediment transport is calculated as

$$\vec{q}_{bi} = \mathcal{F}_i \mathcal{G}_{bi} \vec{q}_b, \quad \vec{q}_b = \frac{3}{2} \nu_b u_w^2 \left(\vec{v} - \lambda_b u_w \vec{\nabla} z_b \right), \quad \mathcal{G}_{bi} = \left(\frac{d_i}{d_m} \right)^{c_b}. \quad (5.11)$$

Here, the strength of hiding is indicated by exponent c_b in the transport capacity function \mathcal{G}_{bi} for bedload. The formulation is as discussed by *Seminara* (1995), *Ribberink* (1987) and references herein. Note that in absence of hiding $c_b = 0$, whereas for typical sand mixtures $c_b \sim 0.75$. Thus, the bedload transport for grains with a diameter $d_i > d_m$ ($d_i < d_m$) is enhanced (reduced) compared to the bedload transport for grains with a diameter d_m due to dynamic hiding. The expression for \vec{q}_b originates from *Bailard* (1981), where the first contribution represents the net sediment transport due to stirring of sediment by waves and the subsequent transport by the net current. Coefficient ν_b depends on sediment properties (but not on d_i , which is already included in \mathcal{G}_{bi}). The second contribution to \vec{q}_b accounts for the effect of bottom slopes, with λ_b the bed slope parameter, which is assumed to be constant.

Suspended load transport plays a significant role during storms (*Green et al.*, 1995) and is formulated as

$$\vec{q}_{si} = \mathcal{C}_i \left(\vec{v} - \hat{\lambda}_s u_w^2 \vec{\nabla} z_b \right). \quad (5.12)$$

Here, all grain size dependence is included in \mathcal{C}_i , which is the depth-integrated volumetric concentration of available grains in class i . Furthermore, $\hat{\lambda}_s$ is the bed slope coefficient for suspended load transport, which is different from the λ_s in previous chapters, as the concentration \mathcal{C}_i is outside the parentheses. The depth-integrated volumetric concentration of available sediment is governed by a concentration equation for grains in class i

$$\vec{\nabla} \cdot (\vec{v} \mathcal{C}_i) = w_{si} (\mathcal{F}_i E_i - c_{bi}). \quad (5.13)$$

The term on the left-hand side accounts for settling lag effects, i.e., it takes time for sediment to reach the bottom when the decreasing current cannot maintain it in suspension. Thus, settling occurs at some distance from the location where sediment has been entrained. The first term on the right-hand side accounts for the entrainment of sediment into suspension, the second term for deposition of sediment. Furthermore, w_{si} is the settling velocity of grains of diameter d_i , E_i is the dimensionless entrainment of these grains and c_{bi} their actual volume concentration near the bed. The entrainment of a size fraction is multiplied by the probability \mathcal{F}_i that sediment of this grain size is actually present. In previous chapters of this thesis the entrainment formulation according to *Van Rijn* (1993) was used, which is derived for uniform sediment. In this chapter the entrainment formulation of *Garcia and Parker* (1991) is used, because it is based on laboratory experiments with sediment mixtures, thereby accounting for possible hiding effects. They propose

$$E_i = A \lambda_E^5 Z_i^5 u_w^5, \quad Z_i = \frac{\sqrt{c_{fi}}}{w_{si}} R_{pi}^{0.6} \left(\frac{d_i}{d_m} \right)^{e_h}, \quad (5.14)$$

with $A = 1.3 \times 10^{-7}$ a constant. Furthermore, $\lambda_E = 1 - 0.288 v_s$ is a sorting-dependent straining parameter, c_{fi} is a drag coefficient of grains in size class i and $R_{pi} = \sqrt{g' d_i^3} / \nu$ is the particle Reynolds number of these grains with g' the reduced acceleration due to gravity and $\nu \sim 1.36 \times 10^{-6} \text{ m}^2 \text{ s}^{-1}$ the kinematic viscosity coefficient of water. Hiding effects are described by the last factor in the expression for Z_i and involves the exponent e_h . The actual near-bed volume concentration c_{bi} in equation (5.13) can be expressed in terms of the depth-integrated volumetric concentration as follows

$$c_{bi} = \frac{\mathcal{C}_i}{\delta_i \tilde{D}}. \quad (5.15)$$

Here, δ_i is the ratio of the thickness of the suspended load layer for grains of diameter d_i over the total water depth \tilde{D} . This ratio is assumed to be constant in space and time.

Strictly speaking, equation (5.13) has to be solved for $i = 1$ and $i = 2$. In this chapter it is assumed that

$$\mathcal{C}_i = \mathcal{F}_i \mathcal{G}_{si} \mathcal{C}_m, \quad (5.16)$$

where \mathcal{C}_m is the depth-integrated volumetric concentration corresponding to grain size d_m , which obeys

$$\vec{\nabla} \cdot (\vec{v} \mathcal{C}_m) = w_{sm} \left(E_m - \frac{\mathcal{C}_m}{\delta_m \tilde{D}} \right), \quad E_m = AZ_m^5 u_w^5. \quad (5.17)$$

Here, E_m is the entrainment of grains of diameter d_m such that Z_m corresponds to the value of Z_i for $d_i = d_m$. Furthermore, δ_m is the ratio of the thickness of the suspended load layer for grains with size d_m over the total water depth \tilde{D} . It is straightforward to show, using equations (5.14)-(5.15), that equation (5.16) is a solution of equation (5.13) if settling lag effects are ignored and the transport capacity function for suspended load \mathcal{G}_{si} is given by

$$\mathcal{G}_{si} = \frac{E_i}{E_m} \frac{\delta_i}{\delta_m} = \lambda_E^5 \frac{\delta_i}{\delta_m} \left(\frac{c_{fi}}{c_{fm}} \right)^{5/2} \left(\frac{w_{sm}}{w_{si}} \right)^5 \left(\frac{R_{pi}}{R_{pm}} \right)^3 \left(\frac{d_i}{d_m} \right)^{5e_h}. \quad (5.18)$$

Here, the drag coefficient, settling velocity and particle Reynolds number for grains of size d_m are denoted as c_{fm} , w_{sm} and R_{pm} , respectively. In appendix 5.A it is shown that this approach is not strictly correct in the sense that it slightly overestimates (underestimates) the settling lag experienced by the coarse (fine) sediment.

Expression (5.18) can be rewritten by assuming

$$\frac{c_{fi}}{c_{fm}} = \left(\frac{d_i}{d_m} \right)^{e_f}, \quad \frac{w_{sm}}{w_{si}} = \left(\frac{d_i}{d_m} \right)^{-e_w}, \quad (5.19)$$

and using the definition for R_{pi} and δ_i , which yield

$$\frac{R_{pi}}{R_{pm}} = \left(\frac{d_i}{d_m} \right)^{3/2}, \quad \frac{\delta_i}{\delta_m} = \frac{w_{sm}}{w_{si}}. \quad (5.20)$$

Substitution of equations (5.19)-(5.20) in equation (5.18) yields

$$\mathcal{G}_{si} = \lambda_E^5 \left(\frac{d_i}{d_m} \right)^{c_s}, \quad (5.21)$$

where $c_s = c_{s1} + c_{s2} + c_{s3}$, with $c_{s1} = 5e_h$, $c_{s2} = 4.5 - 6e_w$ and $c_{s3} = 2.5e_f$. The suspended load transport capacity function \mathcal{G}_{si} for grains with size d_i accounts for four different effects. The factor λ_E^5 combined with the c_{s1} dependence in the definition of \mathcal{G}_{si} incorporates hiding effects. Thus, it accounts (1) for the fact that the entrainment of fine grains is tempered with respect to that of coarse grains and (2) a reduced entrainment of grains from both size classes for a poorly sorted sediment mixture compared to grains in uniform sediment due to a more efficient packing of the bottom sediment. Typically $e_h = 0.2$, according to *Garcia and Parker* (1991). The coefficient c_{s2} specifies the dependence of the entrainment function on the particle Reynolds number and the settling velocity. The decrease of settling velocity with grain size, favors the entrainment of fine sediment over coarser sediment (which is opposite to the hiding effect). The formulation of Hallermeier (see *Soulsby*, 1997) for fine to coarse sand yields $e_w = 1.1$. The coefficient c_{s3} , which has not been considered in the context of sfcf, represents the dependence of the drag coefficient on the grain size. Following work on sorted bedforms by *Murray and Thieler* (2004), *Coco et al.* (2007a) and *Huntley et al.* (2008), it accounts for more vigorous turbulent motions and related increase of entrainment of sediment, above a rough (coarse) surface compared to a fine sediment surface. According to *Murray and Thieler* (2004) e_f should be in the order of 1. Note that in absence of hiding $c_s \neq 0$. The exponent c_s is typically negative if $e_f = 0$, which physically means that the depth-integrated concentration for grains of sizes smaller than the mean is larger than for grains of sizes larger than the mean grain size. In case that $e_f \neq 0$, typically $c_s > 0$.

The boundary conditions for equations (5.9) and (5.17) are that the bed level is fixed at $x = 0$ and far offshore and \mathcal{C}_m is bounded far offshore.

5.3 SOLUTION METHOD

The initial growth of morphodynamic features is investigated by applying a linear stability analysis. It is a similar analysis as that employed in the early study by *Trowbridge* (1995) and it is based on the hypothesis that sfcf form as free morphodynamic instabilities of a basic state. As the initial growth is considered, equations are linearized. The basic state is discussed in section 5.3.1 and the linearization procedure is outlined in section 5.3.2.

5.3.1 BASIC STATE

For a longshore uniform bottom profile $z_b = -H(x)$ without bedforms (see section 5.2.1) the model allows for a basic state, which is steady and alongshore uniform. The dispersion relation for the basic state follows from substitution of basic state variables into equation (4.6) in chapter 4 and reads

$$\omega^2 = gK \tanh(KH). \quad (5.22)$$

As ω is constant, the latter relates the basic state wavenumber K to water depth H . Expressions for the angle of wave incidence Θ and wave energy E in the basic state are given in equations (4.21) and (4.22) in chapter 4. For the basic state wave orbital velocity, which is important for calculating the basic state flow and sediment transport, it follows

$$U_w = \frac{\omega H_{rms}}{2 \sinh(KH)}, \quad H_{rms}^2 = \frac{8E}{\rho g}. \quad (5.23)$$

The latter is obtained by substituting basic state variables into equation (5.1) and H_{rms} is the root-mean-square wave height in the basic state (which is related to the wave energy).

The basic state cross-shore and alongshore momentum balance are given in equation (4.23) in chapter 4. It describes a longshore current with a cross-shore gradient ($U = 0$, $V = V(x)$), which is driven by an alongshore wind stress τ_{sy} and inversely related to the wave orbital velocity due to frictional effects (see chapter 4, equation (4.24)). The basic state depth-integrated volumetric suspended sediment concentration corresponding to the mean grain size follows from equation (5.17) by substitution of basic state variables and reads

$$C_m = A\delta_m Z_m^5 H U_w^5. \quad (5.24)$$

Furthermore, the probabilities F_i , mean grain size Φ_m and standard deviation of the sediment mixture Υ_s in the basic state need to be considered. The constraint (5.6) in the basic state yields

$$F_1 = 1 - F_2. \quad (5.25)$$

Note that F_1 and F_2 can have any cross-shore profile. In the basic state, the expressions for the mean grain size and the standard deviation as defined in section 5.2.3, read

$$\Phi_m = \phi_1 F_1 + \phi_2 F_2, \quad \Upsilon_s^2 = F_1 F_2 (\phi_1 - \phi_2)^2. \quad (5.26)$$

From this, expressions for ϕ_1 and ϕ_2 are derived in terms of the basic state mean grain size and standard deviation:

$$\phi_1 = \Phi_m + \Upsilon_s \sqrt{\frac{F_2}{F_1}}, \quad \phi_2 = \Phi_m - \Upsilon_s \sqrt{\frac{F_1}{F_2}}. \quad (5.27)$$

It follows from equations (5.11) and (5.12) that the total sediment transport in the basic state $\vec{Q}_i = \vec{Q}_{bi} + \vec{Q}_{si}$ has a longshore component, which is independent of y , but a nonconstant offshore-directed cross-shore component (due to the transverse bed slope):

$$\vec{Q}_{bi} = F_i G_{bi} \vec{Q}_b \simeq F_i G_{bi} \frac{3}{2} \nu_b U_w^2 V \vec{e}_y, \quad \vec{Q}_{si} \simeq C_i V \vec{e}_y, \quad (5.28)$$

where \vec{e}_y is a unit vector in the y -direction. Here, the bed slope-induced sediment transport is neglected, as the change in bed level due to divergence of this transport is much slower ($\sim 10^{-5}$ m yr $^{-1}$) than the change in bed level of sfcf ($\sim 10^{-2}$ m yr $^{-1}$). Thus, to a good approximation, the basic state defines a morphodynamic equilibrium. In equation (5.28), G_{bi}

is the transport capacity function for bedload and follows from equation (5.11) by substitution of basic state variables and using definition (5.5):

$$G_{bi} = 2^{c_b(\Phi_m - \phi_i)}. \quad (5.29)$$

Furthermore, $C_i = F_i G_{si} C_m$ in equation (5.28), where G_{si} is the transport capacity function for suspended load, which is derived from equation (5.21):

$$G_{si} = \Lambda_E^5 2^{c_s(\Phi_m - \phi_i)}, \quad \Lambda_E = 1 - 0.288\Upsilon_s, \quad (5.30)$$

where Λ_E is the basic state straining parameter (see section 5.2.4).

5.3.2 LINEAR STABILITY ANALYSIS

The dynamics of small perturbations on the basic state is investigated in order to gain knowledge about the stability of these features. Hereafter, perturbed variables are denoted by primes and are assumed to be small compared to their basic state values. As the focus is on the initial growth of bedforms, the equations are linearized with respect to the small perturbations.

The perturbed wavenumber κ' , angle of wave incidence θ' and wave energy e' are functions of the bottom perturbation h' (see equations (4.27a)-(4.27c), where expressions are given after substitution of longshore periodic and exponentially growing solutions). Using equation (4.28), the perturbed wave orbital velocity u'_w is expressed in terms of the bottom perturbation h' .

The linearized versions of equations for the perturbed flow and volumetric suspended sediment concentration corresponding to the mean grain size are given in appendix 5.B. Here, it suffices to state that the equations are almost identical to those in appendix 2.B in chapter 2, except that C is replaced by C_m and $\gamma \rightarrow w_{sm}/\delta_m$. Furthermore, due to the consideration of perturbations in the wave orbital velocity an extra friction term $-rV u'_w/H$ appears in the longshore momentum equation and an additional entrainment term $5w_{sm}AZ_m^5 U_w^4 u'_w$ appears in the concentration equation corresponding to the mean grain size. The equations for u' , v' , η' and c'_m are solved for a given bottom perturbation h' . Note that the flow variables also depend on u'_w , but the latter is known in terms of h' . The perturbed free surface elevation η' is eliminated by cross-differentiating the linearized momentum equations. From the linearized continuity equation an expression is obtained, which relates v' to h' and u' . In this way, only the equations for u' and c'_m have to be solved, where u' and c'_m (thus also v' and u'_w) are functions of h' .

Considering the sediment characteristics, perturbations are added to the probabilities $\mathcal{F}_i = F_i + f'_i$, the mean grain size $\phi_m = \Phi_m + \phi'_m$ and standard deviation $v_s = \Upsilon_s + v'_s$. The constraint on the probabilities (5.6), in its linearized form, reads

$$f'_1 = -f'_2. \quad (5.31)$$

The perturbations in the mean grain size and standard deviation are expressed in f'_1 by using expressions (5.7), (5.27) and (5.31):

$$\phi'_m = \frac{\Upsilon_s}{\sqrt{F_2 F_1}} f'_1, \quad v'_s = \frac{\Upsilon_s (F_2 - F_1)}{2F_2 F_1} f'_1. \quad (5.32)$$

Finally, the linearized versions of the evolution equation (5.9a) for the bottom perturbation h' and the evolution equation (5.9b) for the perturbed probabilities f'_i are needed to solve the problem. They read

$$(1 - p) \frac{\partial h'}{\partial t} = -\vec{\nabla} \cdot \vec{q}'_1 - \vec{\nabla} \cdot \vec{q}'_2, \quad (5.33a)$$

$$0 = F_1 \vec{\nabla} \cdot \vec{q}'_2 - F_2 \vec{\nabla} \cdot \vec{q}'_1. \quad (5.33b)$$

Expressions for \vec{q}'_1 and \vec{q}'_2 , in terms of h' , f'_1 and f'_2 , are given in appendix 5.B. Due to the consideration of perturbations in the wave orbital velocity an extra bedload transport term $3\nu_b U_w V u'_w$ appears in equation (5.B-3) of this appendix. Equation (5.31) is used to eliminate f'_2 from the expressions for \vec{q}'_1 and \vec{q}'_2 , whereas u' , v' , c'_m , u'_w are already expressed in h' , as explained above. The boundary conditions are u' , $h' \rightarrow 0$ for $x \rightarrow \infty$ and $u' = 0$, $h' = 0$ at $x = 0$.

Equations (5.33a) and (5.33b) allow for longshore traveling wave solutions of which the amplitude can grow (or decay) in time:

$$(h', f'_1) = \Re \left\{ \left(\hat{h}(x), \hat{f}_1(x) \right) e^{iky + \sigma t} \right\}. \quad (5.34)$$

Here, \Re denotes the real part of the solution, k the longshore wavenumber (which can be assigned any value), the hats denote the as yet unknown cross-shore structure of the solutions and σ the complex frequency. Substituting expressions (5.34) into equations (5.33a) and (5.33b) results in an eigenvalue problem for \hat{h} , whilst \hat{f}_1 is an algebraic function of \hat{h} . The physical meaning of the latter is that the fractions of fine and coarse grains adapt instantaneously to bottom changes.

The growth rate and migration speed of the perturbations are given by the complex frequency ($\sigma = \sigma_r + i\sigma_i$). The real part σ_r is the growth rate and the migration speed is given by $V_m = -\sigma_i/k$. If, for specific choices of the model parameters, $\sigma_r < 0$ for all k the basic state is stable. The basic state is unstable if there is a range of wavenumbers k for which $\sigma_r > 0$. The mode which has the largest growth rate, is called the fastest growing or most preferred mode. The inverse of the growth rate σ_r gives a characteristic time scale for the formation in nature (called the e -folding growth time T_g). The solutions were obtained numerically using a spectral collocation method. Thus, variables are expanded in Chebyshev polynomials and equations are evaluated at N collocation points (see *Boyd*, 2001, for details).

5.4 RESULTS

5.4.1 PARAMETER VALUES: DEFAULT CASE

Parameter values are representative for the Long Island inner shelf and are partly taken from *Figueiredo et al. (1982)* and *Schwab et al. (2000)*. Long Island is located along the Atlantic coast of North America at a latitude of $\sim 40^\circ$ N, for which the Coriolis parameter is $f = 1 \times 10^{-4} \text{ s}^{-1}$. Going seaward, the depth of the inner shelf increases from $H_0 = 14 \text{ m}$, to $H_s = 20 \text{ m}$ and the inner shelf width is $L_s = 5.5 \text{ km}$. Therefore, the transverse bottom slope is $\beta = (H_s - H_0)/L_s \sim 1.1 \times 10^{-3}$. Typical values for the offshore root-mean-square wave height, offshore angle of wave incidence, wave period and alongshore wind stress are $H_{rms,s} = 1.5 \text{ m}$, $\Theta_s = -20^\circ$, $T = 11 \text{ s}$ and $\tau_{sy} = -0.4 \text{ N m}^{-2}$ (southward), respectively. In the default experiment a uniform fraction of fine and coarse sand is used: $F_1 = 0.7$ and $F_2 = 0.3$. Furthermore, a mean grain size $d_m = 0.35 \text{ mm}$ ($\Phi_m = 1.5$) is adopted with a sorting parameter $\Upsilon_s = 0.5$. For the exponent in the transport capacity function for bedload $c_b = 0.75$ is used. In equations (5.18)-(5.19), $e_h = 0.2$, $e_w = 1.1$ and $e_f = 0$ are chosen, such that the exponent in the transport capacity function for suspended load $c_s = -1.1$. Note that roughness-induced turbulence effects are neglected for the moment. Values of the other parameters are: $r = 2.0 \times 10^{-3}$, $\nu_b = 5.6 \times 10^{-5} \text{ s}^2 \text{ m}^{-1}$, $\lambda_b = 0.65$, $\hat{\lambda}_s = 0.30 \text{ s m}^{-1}$, $w_{sm} = 0.04 \text{ m s}^{-1}$, $E_m = 1.3 \times 10^{-4}$, $\delta_m = 0.20$ and $p = 0.4$.

5.4.2 BASIC STATE AND LINEAR STABILITY ANALYSIS: DEFAULT CASE

In this section solutions of the morphodynamic (eigenvalue) problem are presented for the parameter values specified in the previous section. The cross-shore profiles for the wave orbital velocity and net longshore current in the basic state are given in Figure 5.3.

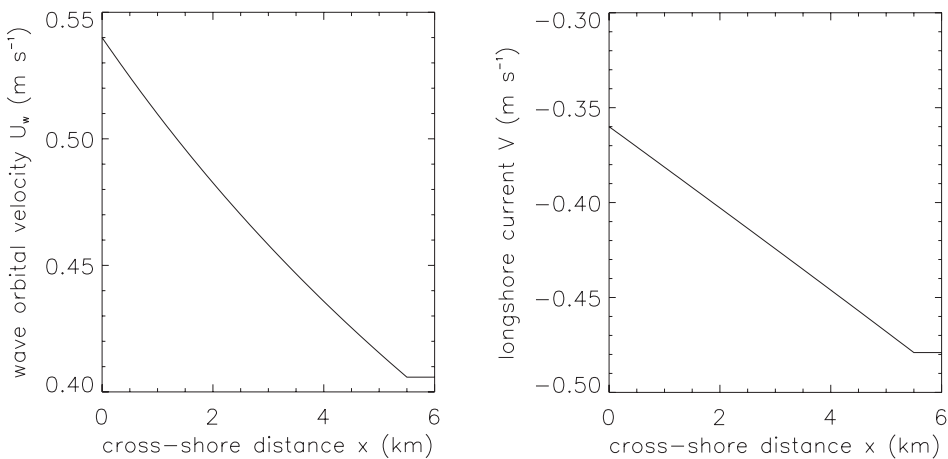


Figure 5.3: Basic state; cross-shore profiles of the wave orbital velocity and longshore current. Default case.

The wave orbital velocity increases into shallower depths and reaches an amplitude at the shoreface of 0.54 m s^{-1} . The magnitude of the longshore current decreases towards the shoreface, reaching a value of 0.36 m s^{-1} (minus sign indicates southward direction). This is a consequence of the larger bottom friction for shallower depths.

The growth rates and migration velocities for the default case as a function of the longshore wavenumber are shown in Figure 5.4a and Figure 5.4b, respectively. Sfcr for which a maximum growth rate is attained, have wavelengths $\lambda_p = 2\pi k_p^{-1} \sim 2.7 \text{ km}$. The corresponding e -folding time scale for the initial growth is about 180 yr. The sfcr migrate with a speed of 48 m yr^{-1} in the downstream direction.

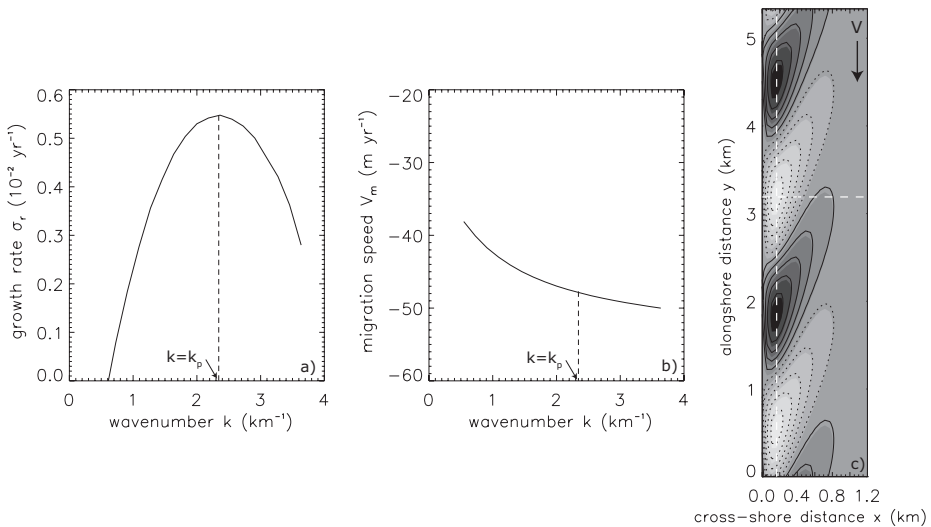


Figure 5.4: Growth rates (a) and migration velocities (b) as a function of the longshore wavenumber, default case. The most preferred mode (with wavenumber $k = k_p$) is indicated by the dashed black lines. (c) Bottom pattern (grayscale; light: crests, dark: troughs) and perturbations in the distribution of the mean grain size (contours; solid lines: finer; dashed lines: coarser) for the most preferred mode. The dashed white lines indicate the position of normal and longshore cross-sections through the sfcr, which are shown in Figure 5.5. The arrow indicates the direction of the basic state longshore velocity.

In Figure 5.4c the bottom pattern belonging to the initially fastest growing mode is shown. In this figure the basic state velocity is directed from top to bottom and thus sfcr are characterized by an up-current orientation. The sfcr extend approximately 1 km offshore. Furthermore, the contour lines indicate the distribution of the fine and coarse sediment over the sfcr. It is visible that the grain size distribution is approximately 180° out of phase with the ridge topography: the finest sediment is found slightly upstream of the troughs. The latter is confirmed by the normal and longshore cross-sections through the sfcr (see Figure 5.5), which show the bottom topography and perturbed fraction of fine grains along the dashed white lines in Figure 5.4c.

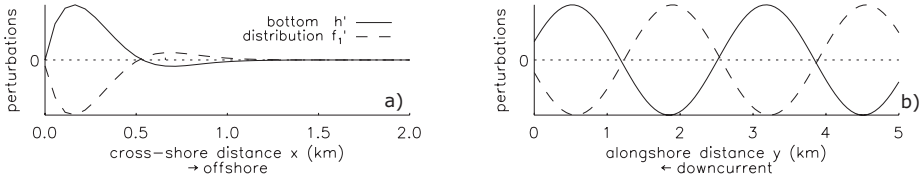


Figure 5.5: Normal (a) and longshore (b) cross-section through the sfcz in Figure 5.4 at the location of the dashed white lines. Shown are perturbations in bottom h' and in the fraction of fine grains f'_1 (or similar, in mean grain size ϕ'_m). Quantities are scaled by their maximum values.

The ratio of the maximum variation in the perturbed fraction of fine grains and the maximum variation in the bottom topography is $[f'_1]/[h'] \sim 0.56/H_0$. Thus, in case of a ridge of 1 m in height, the variation in the fraction of fine grains will be 0.04. For a diameter of the fine and coarse grains of 0.28 mm and 0.59 mm, respectively (as in the default case), this corresponds to a total variation in the mean grain size of approximately 0.02 mm.

As long as $F_1 \neq F_2$, equation (5.32) indicates that $v'_s \neq 0$ and thus changes in the standard deviation of the sediment mixture occur. Shore-normal and alongshore cross-sections of the bottom topography and perturbed standard deviation are shown in Figure 5.6.

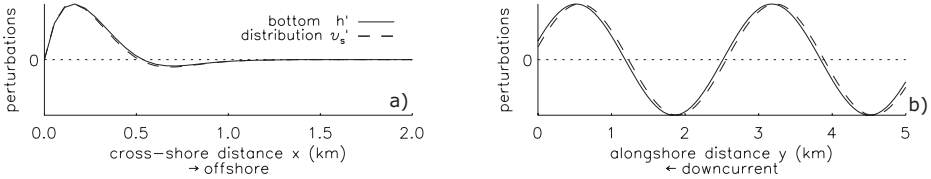


Figure 5.6: Normal (a) and longshore (b) cross-section through the sfcz in Figure 5.4 at the location of the dashed white lines. Shown are perturbations in bottom h' and in the standard deviation v'_s . Quantities are scaled by their maximum values.

Clearly, the (finer) sediment, which is located in the troughs, is better sorted ($v'_s < 0$) than the (coarser) sediment on the crests. The ratio of the maximum variation in the perturbed sediment sorting and the maximum variation in the bottom topography is $[v'_s]/[h'] \sim 0.26/H_0$. Thus, in case of a ridge of 1 m in height, the variation in sediment sorting will be 0.02, which is approximately a 4% change with respect to the basic state sediment sorting of 0.5.

5.4.3 SENSITIVITY TO SEDIMENT CHARACTERISTICS

Experiments were conducted to explore the sensitivity of model results to different values of the standard deviation of the sediment mixture. For a fixed fraction of the fine and coarse sediment in the mixture and for a fixed mean grain size (default values) the standard deviation of the mixture was varied between zero and one. Thus, in case of $\Upsilon_s = 0.0$ sediment is uniform with a grain size $d_1 = d_2 = 0.35$ mm, whereas for e.g. $\Upsilon_s = 1.0$ sediment is nonuniform with $d_1 = 0.22$ mm and $d_2 = 1.0$ mm.

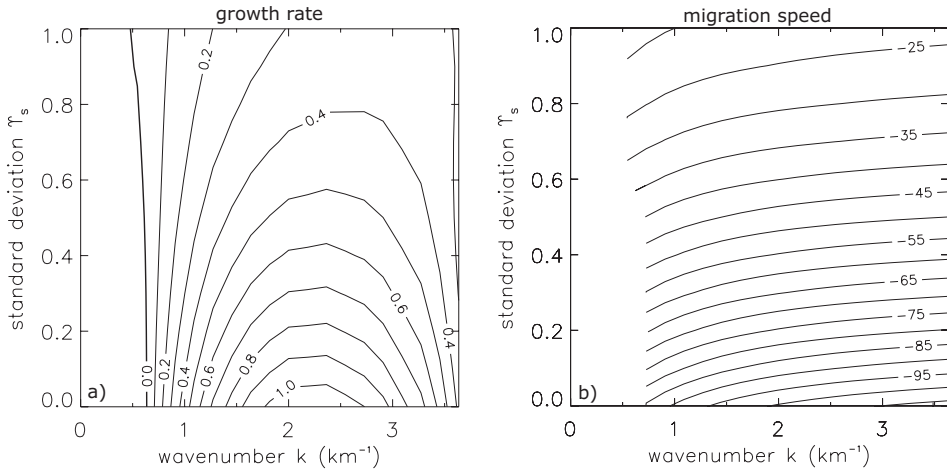


Figure 5.7: Contour plots of equal (a) growth rate (10^{-2} yr^{-1}) and (b) migration speed (m yr^{-1}) of the initially most preferred mode in the $k - \Upsilon_s$ plane. All other parameter values, except of d_1 and d_2 , are as in the default case.

Results (shown in Figure 5.7) indicate that a poorly sorted sediment mixture (large Υ_s) causes sfcr to grow slower compared to sfcr composed of a well-sorted mixture. With an increase in standard deviation, the total transport of the two grain sizes in a mixture is reduced. The latter can be interpreted as the result of a more efficient packing of the bottom material when grains of different sizes are present. Also a decrease in the migration speed of the most preferred mode is found when Υ_s is increased. An interpretation of the results will be given in section 5.5.

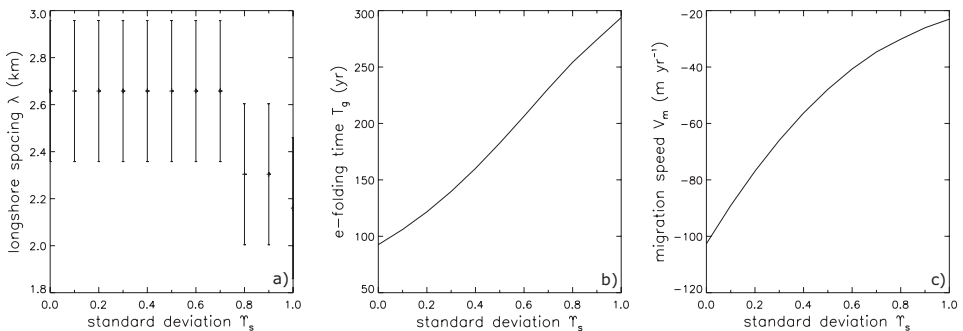


Figure 5.8: Longshore spacing (a), e -folding growth time (b) and migration speed (c) of the initially fastest growing mode as a function of the standard deviation Υ_s of the sediment mixture. All other parameter values, except of d_1 and d_2 , are as in the default case. The uncertainty in longshore spacing is indicated with the error bars. Uncertainties in the e -folding time and migration speed are very small, so no error bars are shown.

Figure 5.8 shows that the longshore spacing of the most preferred mode does not change significantly if the value of Υ_s is varied. The change in e -folding growth time (thus in growth rate) is about a factor 3.5 and in migration speed about a factor 4 over the complete range of standard deviation Υ_s . The bottom pattern of the most preferred mode remains unaltered if the standard deviation of the mixture is varied and is similar as in Figure 5.4c. The same holds for the locations of the maxima and minima in the mean grain size: a persistent 180° phase shift between the perturbed topography and the perturbed mean grain size is found.

The influence of the relative weight percentage of the grains in the coarse and fine size class on the characteristics of sfcw was investigated. For a fixed mean grain size and standard deviation of the mixture (default values) the fraction of fine grains was varied such that $0.1 \leq F_1 \leq 0.9$ (if F_1 equals zero or one, sediment is uniform). In case of $F_1 = 0.1$ this means considering a sediment mixture with $d_1 = 0.12$ mm and $d_2 = 0.39$ mm, whereas for e.g. $F_1 = 0.9$ the fine particles have a diameter $d_1 = 0.31$ mm and the coarse particles a diameter $d_2 = 0.99$ mm. Results (shown in Figure 5.9) indicate that a larger fraction of fine grains has a stabilizing effect on growth rates and migration speeds.

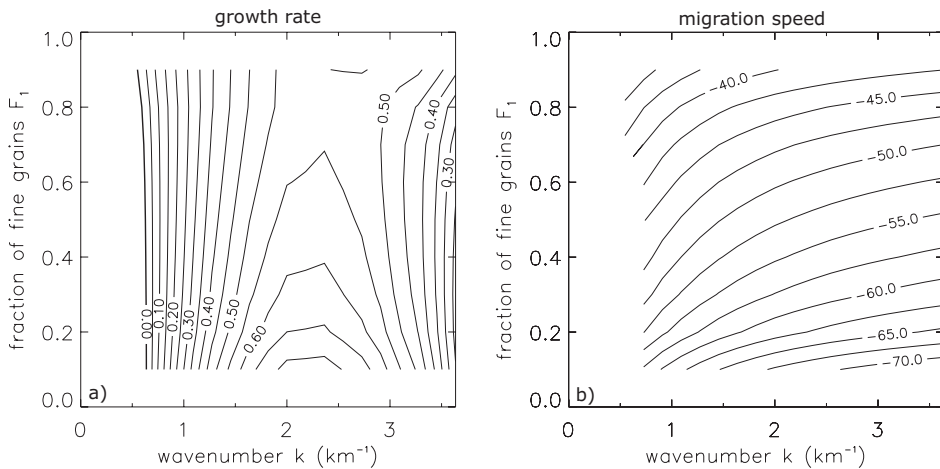


Figure 5.9: Contour plots of equal (a) growth rate (10^{-2} yr^{-1}) and (b) migration speed (m yr^{-1}) of the initially most preferred mode in the $k - F_1$ plane. All other parameter values, except of d_1 and d_2 , are as in the default case.

The plots in Figure 5.10 reveal that no significant change in the preferred distance between successive bedforms occurs for a change in parameter F_1 . The change in e -folding growth time and migration speed is about a factor 1.5 over the entire range of probability F_1 . The cross-shore extent of the bottom patterns slightly decreases with an increase in F_1 . The distribution of the mean grain size is not affected by changing the value of probability F_1 . However, the sorting pattern is affected (results not shown): for $F_1 > 0.5$ the sediment is best sorted in the troughs, whereas for $F_1 < 0.5$ the best sorted sediment is found on the crests. In case that $F_1 = F_2 = 0.5$ the sediment sorting is equal to that of the basic state in the whole domain.

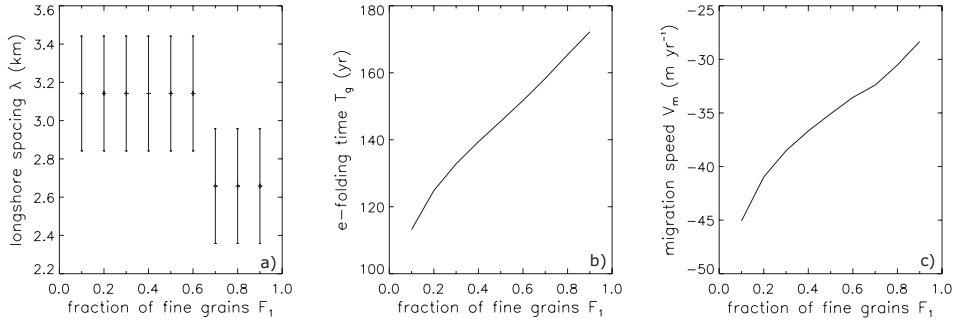


Figure 5.10: Longshore spacing (a), e -folding growth time (b) and migration speed (c) of the initially fastest growing mode as a function of the fraction of fine grains F_1 of the sediment mixture. The uncertainty in longshore spacing is indicated with the error bars. Uncertainties in the e -folding time and migration speed are very small, so no error bars are shown.

Also the mean grain size d_m was varied. Keeping all the other parameters at their default values a mean grain size of $d_m = 0.20$ mm implies that $d_1 = 0.16$ mm and $d_2 = 0.34$ mm. A mixture with a mean grain size of $d_m = 0.60$ mm consists of small grains with a diameter $d_1 = 0.48$ mm and coarse grains of diameter $d_2 = 1.02$ mm. Results are summarized in Table 5.1.

Table 5.1: Bedform characteristics (longshore spacing, cross-shore extent, growth rate, e -folding growth time, migration speed, $H_0 [f'_1]/[h']$ and $H_0 [v'_s]/[h']$) of the initially fastest growing mode as a function of the mean grain diameter d_m of the sediment mixture.

d_m (mm)	0.20	0.30	0.40	0.50	0.60
λ_p (km)	-	3.5	2.1	1.6	1.2
cross-shore extent (km)	-	1.2	0.7	0.5	0.4
σ_r (0.01 yr^{-1})	-	0.45	0.61	0.63	0.63
T_g (yr)	-	223	164	159	159
V_m (m yr^{-1})	-	-62	-38	-27	-20
$H_0 [f'_1]/[h']$	-	0.58	0.52	0.44	0.35
$H_0 [v'_s]/[h']$	-	0.28	0.24	0.21	0.17

A sediment mixture should be characterized by a mean grain size $d_m > 0.20$ mm to result in the evolution of sfc. Once this threshold is exceeded, an increase in the mean grain size results in an increase in growth rate and a decrease in migration speed. Furthermore, a reduction in alongshore spacing between successive crests and a decrease in the cross-shore extent of sfc is obtained for an increase in d_m . Neither the phase shift between sfc and perturbations in the mean grain size nor the sorting pattern are affected by the mean grain size of the mixture.

In the previous experiments it was assumed that the basic state properties of the sediment mixture (grain size distribution function, mean grain size and standard deviation) have a fixed value in space. However, observations indicate that often sediment becomes finer going offshore. To investigate the effect of an x -dependent sediment distribution, a run was performed for a grain size fraction, which is linear dependent on x : $F_1 = 0.5$ at the shoreface to $F_1 = 0.8$ at the transition to the outer shelf. The grain size of both the coarse and fine fraction are the same as in the default experiment. Thus, the mean grain size and the sorting parameter are also dependent on the cross-shore position. Results (not shown) indicate that bedform characteristics are hardly affected by including x -dependent sediment properties. The sorting pattern will change as soon as $F_1 < F_2$ in that part of the domain where sfcf are situated: the sediment is finer and more poorly sorted in the troughs and coarser, better sorted on the crests.

5.4.4 SENSITIVITY TO HIDING AND ROUGHNESS-INDUCED TURBULENCE

In this section the effect of including a grain size dependent drag coefficient in the sediment transport is investigated. As explained at the end of section 5.2.4, this corresponds to a change in the exponent c_s from $c_s = -1.1$ to $c_s = 1.4$ in the transport capacity function for suspended load. Figure 5.11 shows the growth rates and migration velocities as a function of the longshore wavenumber.

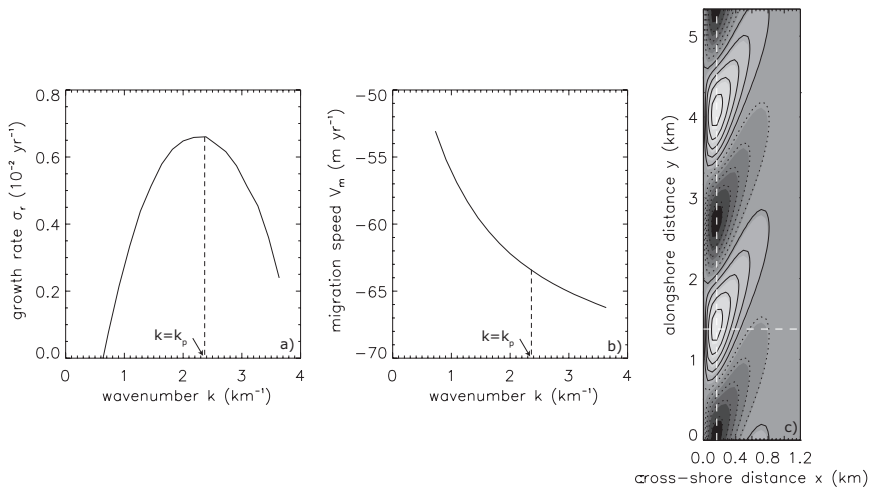


Figure 5.11: Growth rates (a) and migration velocities (b) as a function of the longshore wavenumber. The initially most preferred mode (with wavenumber $k = k_p$) is indicated by the dashed black lines. (c) Bottom pattern (grayscale; light: crests, dark: troughs) and perturbations in the distribution of the mean grain size (contours; solid lines: finer; dashed lines: coarser) for the most preferred mode. The dashed white lines indicate the position of normal and longshore cross-sections through the sfcf, which are shown in Figure 5.12. Here, entrainment of sediment depends on bottom roughness such that $c_s = 1.4$.

A maximum growth rate of about $0.66 \times 10^{-2} \text{ yr}^{-1}$ is found for $k = k_p \sim 2.4 \text{ km}^{-1}$, which corresponds to a longshore wavelength of the bedforms of $\sim 2.7 \text{ km}$. This initially most preferred mode migrates with a speed of $\sim 65 \text{ m yr}^{-1}$ in the downstream (southward) direction. Taking into account roughness-induced turbulence effects thus lead to an increase in growth rates and a slight increase in migration speeds. The bottom pattern of the most preferred mode is shown in Figure 5.11c and shows up-current oriented sfcr that extend approximately 1 km offshore. The contour lines in this figure indicate the perturbations in the distribution of the mean grain size. Clearly, including roughness-induced turbulence effects leads to a change in the phase difference between the ridge topography and grain size distribution: the finest sediment is found slightly up-current of the crests instead of the troughs. The normal and longshore cross-sections through the ridges along the dashed white lines in Figure 5.11c confirm this (see Figure 5.12). The ratio of the maximum variation in f'_1 and the maximum variation in h' increases to become $[f'_1]/[h'] \sim 0.84/H_0$.

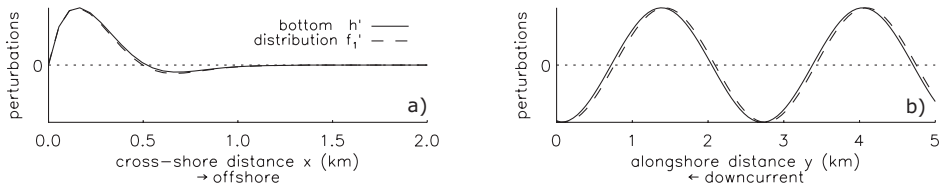


Figure 5.12: Normal (a) and longshore (b) cross-section through the sfcr in Figure 5.11 at the location of the dashed white lines. Shown are perturbations in bottom h' and in the fraction of fine grains f'_1 (or similar, in mean grain size ϕ'_m). Quantities are scaled by their maximum values. Here, entrainment of sediment depends on bottom roughness such that $c_s = 1.4$.

Cross-sections of the bottom perturbations and perturbations in the standard deviation of the sediment mixture are given in Figure 5.13. Clearly, the (finer) sediment, which is located on the crests, is better sorted ($v'_s < 0$) than the (coarser) sediment in the troughs. The ratio of the maximum variation in the perturbed sediment sorting and the maximum variation in the bottom topography $[v'_s]/[h'] \sim 0.41/H_0$ and is larger compared to the case where roughness-induced turbulence effects were neglected.

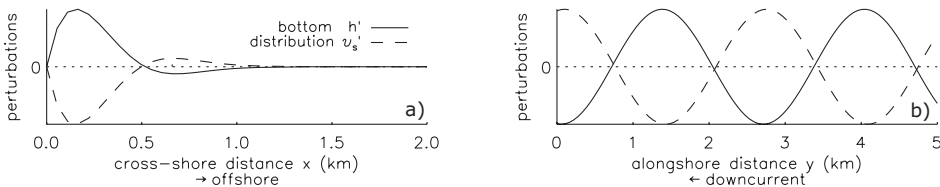


Figure 5.13: Normal (a) and longshore (b) cross-section through the sfcr in Figure 5.11 at the location of the dashed white lines. Shown are perturbations in bottom h' and in the standard deviation v'_s . Quantities are scaled by their maximum values. Here, entrainment of sediment depends on bottom roughness such that $c_s = 1.4$.

5.4.5 SENSITIVITY TO SETTLING LAG EFFECTS

In order to investigate the sensitivity of results to settling lag effects in the concentration equation, the parameter δ_m is varied. The importance of settling lag effects is among other things dependent on the grain size of the sand that is considered: the smaller the grain size, the stronger settling lag effects. Results are shown in Figure 5.14 for a case in which settling lag effects are not taken into account, a case in which δ_m has its default value and a case in which δ_m has a value, which is twice the default one.

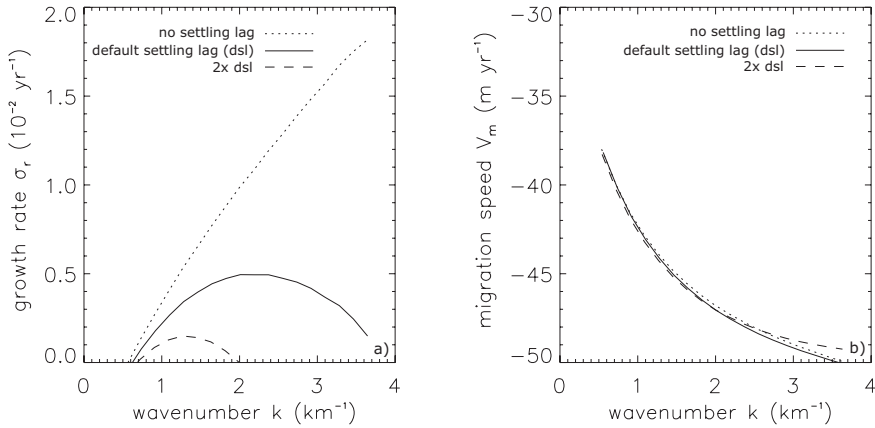


Figure 5.14: Growth rates (a) and migration velocities (b) as a function of the longshore wavenumber to show sensitivity of model results to settling lag effects. The dotted curve is the result in case that settling lag effects are neglected, the straight curve represents the default experiment and the dashed curve is the result in case of a δ_m that is twice as large as in the default experiment.

Experiments reveal that settling lag effects are crucial for the damping of high wavenumber perturbations. Furthermore, growth rates become considerably smaller when settling effects are included, whereas migration speeds are hardly affected. The mean grain size and sorting pattern is not affected by settling lag effects. On the other hand, the ratio of the maximum variation in the perturbed mean grain size/sediment sorting and the maximum variation in the bottom topography slightly decreases when settling lag effects become more important.

5.4.6 SENSITIVITY TO OTHER MODEL PARAMETERS

The dependence of results on wave height, wave period and angle of wave incidence at the offshore boundary was investigated. Changes in the growth rate, migration speed and shape of bedforms do not differ from results obtained by *Vis-Star et al.* (2007). The phase shift between maxima in f'_1 and h' is very robust (180°) under changes in offshore wave properties.

Also experiments were performed changing the water depth at the outer shelf H_s and thus the transverse bottom slope. As this model accounts for perturbations in the wave orbital velocity, already in case of a horizontal bottom growing perturbations are obtained. Sensitivity is in accordance with results presented in *Vis-Star et al.* (2007).

5.5 DISCUSSION

5.5.1 PHYSICAL INTERPRETATION

A physical interpretation of the results presented so far will be given in this section. The growth of sfcR in the present model is due to three different mechanisms. The first mechanism was already described by *Trowbridge (1995)*, in which the offshore deflection of the storm-driven flow over sfcR for a transversely sloping bottom of the inner shelf is essential. The second is the one described by *Calvete et al. (2001a)*, which involves both the offshore deflection of the current over sfcR and cross-shore gradients in the depth-averaged volumetric suspended sediment concentration in the basic state. The third mechanism was found most recently and described by *Vis-Star et al. (2007)* as the wave-bedform feedback mechanism. The up-current oriented sfcR affect the wave field in such a way that wave rays converge on the upstream sides of sfcR. As a result, the perturbed wave energy in these areas increases and stirring of sediment by waves is enhanced. Subsequently, the storm-driven flow transports the additional sediment as suspended load downstream. The third mechanism is more effective than the first two in the case of obliquely incident waves and even active in the absence of a transversely sloping bed. Both growth and migration of sfcR are controlled by suspended load transport of sediment in case of the wave-bedform feedback mechanism. Below an explanation is given of (1) the stabilizing effect of an increase in standard deviation of the sediment mixture, (2) the distribution of the mean grain size and standard deviation over sfcR and (3) the damping of high wavenumber perturbations due to settling lag effects.

STABILIZING EFFECT OF AN INCREASE IN STANDARD DEVIATION OF THE MIXTURE

For a bimodal sediment mixture compared to uniform sediment, both the growth rate and migration speed of sfcR decrease if the standard deviation is increased (see Figure 5.7). The latter is caused by a reduction of the entrainment of both fine and coarse sediment due to a better packing of the sediment for a more poorly sorted sediment mixture (which is represented by the straining factor λ_E in the transport capacity function for suspended load). In case that wave-bedform feedbacks are important, both growth and migration are controlled by suspended load transport and thus reduce with an increase in the standard deviation of the sediment mixture. Note that the decrease in migration speed with increase in standard deviation of the mixture is in contrast with previous results (*Walgreen et al., 2003*), which is due to the fact that in their case the migration speed was determined by bedload transport due to the neglect of wave-bedform interactions.

DISTRIBUTION OF THE MEAN GRAIN SIZE AND STANDARD DEVIATION OVER SFCR

To understand the distribution of the mean grain size and sorting of sediment over the bedforms, the evolution equation for the perturbed fraction of fine sand (5.33b) is analyzed. In case that only suspended load transport is considered (it dominates over bedload transport), bed slope effects are neglected and F_1 and F_2 are constants, it reduces to

$$-M_1 \vec{\nabla} \cdot \vec{q}_{sm}' = VC_m (M_2 + M_1 M_3) \frac{\partial f_1'}{\partial y}, \quad (5.35)$$

where

$$\begin{aligned} M_1 &= F_1 F_2 (G_{s1} - G_{s2}), \\ M_2 &= F_2 G_{s1} + F_1 G_{s2}, \\ M_3 &= \Upsilon_s \left(\frac{c_s \ln 2}{\sqrt{F_1 F_2}} - 5 \frac{0.288(F_2 - F_1)}{2\Lambda_E F_1 F_2} \right). \end{aligned}$$

Furthermore, $\vec{q}_{sm}' = (C_m u', C_m v' + V c_m')$ is the perturbed suspended load transport corresponding to the mean grain size. Using the linearized continuity equation to relate v' to u' and h' , the divergence of \vec{q}_{sm}' becomes

$$\vec{\nabla} \cdot \vec{q}_{sm}' = H \frac{d}{dx} \left(\frac{C_m}{H} \right) u' + \frac{C_m V}{H} \frac{\partial h'}{\partial y} + V \frac{\partial c_m'}{\partial y}. \quad (5.36)$$

Equation (5.35) relates alongshore changes in the fraction of fine grains to the divergence of the suspended load transport corresponding to the mean grain size $\vec{\nabla} \cdot \vec{q}_{sm}'$. If settling lag effects are ignored, the concentration equation (i.e., the fourth equation of the system at the top of appendix 5.B) boils down to an exact balance between erosion and deposition of sediment, from which it follows that

$$c_m' = 5 \frac{C_m}{U_w} u_w' - \frac{C_m}{H} h'. \quad (5.37)$$

Substitution of equation (5.36) into equation (5.35) for c_m' as given in (5.37), yields

$$-M_1 \left(H \frac{d}{dx} \left(\frac{C_m}{H} \right) u' + 5 \frac{V C_m}{U_w} \frac{\partial u_w'}{\partial y} \right) = V C_m (M_2 + M_1 M_3) \frac{\partial f_1'}{\partial y}. \quad (5.38)$$

In this expression, $V < 0$ (southward) and the cross-shore gradient in the depth-averaged volumetric suspended sediment concentration $d/dx (C_m/H) < 0$ (sediment entrainment decreases with depth). For $c_s < 0$ (as in the default case) and all other parameters having their default values the suspended load transport for grains of size smaller than the mean is larger than for grains of size larger than the mean ($G_{s1} > G_{s2}$), which implies that M_1 is positive. Furthermore, $(M_2 + M_1 M_3)$ is positive for default parameter values.

The distribution of the mean grain size over the bedforms is dependent on the relative magnitude of the two terms on the left-hand side of equation (5.38). In previous work only the term related to u' was present, as interactions between bedforms and waves were ignored. In that case the distribution of the fraction of fine grains is related to the perturbed cross-shore velocity. *Trowbridge* (1995) already showed that $u' > 0$ if $h' > 0$. Hence, $\partial f_1'/\partial y \propto -u' \propto -h'$. As a consequence, the distribution of the mean grain size for suspended load is 90° out of phase with the topography such that the finer sand is found on the seaward (down-current) flank of sfc. In this chapter wave-bedform interactions are included and appear to play a dominant role in both the evolution of the bottom and the mean grain size. Thus, the term proportional to $\partial u_w'/\partial y$ dominates over the term proportional to u' in equation (5.38). It follows immediately that $f_1' \propto -u_w'$. The study by *Vis-Star et al.* (2007) revealed that the pattern of the perturbed wave orbital velocity is slightly shifted up-current with respect to that of the bottom. Thus, an approximate 180° phase shift exists between the pattern of the mean

grain size for suspended load and the topography. According to equation (5.32), $v'_s \propto -f'_1$ for $F_1 > F_2$ and thus the perturbed sorting of sediment is in phase with the topography. This explains the results in section 5.4.2, where the finer and better sorted sediment is found in the troughs and the coarser and more poorly sorted sediment on the crests.

As was shown in section 5.4.4, including roughness-induced turbulence effects leads to a change in the phase difference between the perturbed mean grain size and the bedforms. Roughness-induced turbulence effects cause c_s to become positive, which implies that $G_{s1} < G_{s2}$ (suspended load transport for grains of size smaller than the mean is smaller than for grains of size larger than the mean) and thus $M_1 < 0$. On the other hand, the sign of $(M_2 + M_1 M_3)$ does not change and is still positive. Therefore, the balance in equation (5.38) becomes $f'_1 \propto u'_w \propto h'$ due to the wave-bedform feedback mechanism. This explains the 0° phase shift between the bottom and mean grain size pattern, as obtained in section 5.4.4. The finer (coarser) sediment, which is now located on the crests (in the troughs), is still better (more poorly) sorted, as $v'_s \propto -f'_1$ still holds.

DAMPING OF HIGH WAVENUMBER PERTURBATIONS DUE TO SETTLING LAG EFFECTS

For small-scale (high wavenumber) perturbations, the terms in the concentration equation involving y -derivatives constitute the major balance, thus

$$c'_m \simeq -\frac{C_m}{H} h'. \quad (5.39)$$

Substitution of expression (5.39) into equation (5.36) yields

$$\vec{\nabla} \cdot \vec{q}'_{sm} = 5 \frac{w_{sm} C_m}{\delta_m H U_w} u'_w, \quad (5.40)$$

where u'_w is slightly shifted up-current with respect to h' (*Vis-Star et al.*, 2007) and thus approximately $u'_w \propto h'$. As a consequence, at the crests ($h' > 0$) the transport \vec{q}'_{sm} is divergent, which explains that high wavenumber perturbations are more effectively damped when settling lag effects are included.

This result is consistent with results obtained by *Schramkowski et al.* (2002) for local bedforms in tidal embayments. They argue that for long-wave perturbations the sediment dynamics can be approximated by a balance between erosion and deposition. However, in case of short-wave perturbations the advective contributions to the sediment concentration cannot be neglected and have a stabilizing effect. Similar conclusions were reached by *Federici and Seminara* (2006) and *Garotta et al.* (2006) for sand bars in rivers.

5.5.2 COMPARISON WITH OBSERVATIONS

Most field data on sfc, including sfc on the Long Island shelf, reveal a phase difference of approximately 90° between the mean grain size and the topography: the coarsest sand appears on the landward (up-current) flank and the finest sediment on the seaward (down-current) flank. However, the modeled phase shift between the pattern of the mean grain size and the bottom topography for the default case is 180° : troughs (crests) consist of the finest

(coarsest) sediment. The latter is attributed to the importance of wave-bedform interactions. The 180° phase difference between f'_1 and h' is quite robust. It only changes when the hiding coefficient for suspended load transport c_s becomes positive, which is the case when the grain size dependency of the drag coefficient is taken into account. In that case the mean grain size and topography are approximately in phase, with the finest sediment on the crests and coarsest sediment in the troughs. Notice that for some of the sfcf a phase shift between the mean grain size and topography is observed that is different from 90° . According to *Hoogendoorn and Dalrymple* (1986) the finest sediment is observed at the base of the downstream flanks of the Canadian sfcf, which seems to indicate a phase shift close to 180° . *Figueiredo* (1980) reports for the ridges on the inner shelf of southern Brazil that the coarse sediment is found in the troughs and the medium to fine sand appears on the ridge crests, thus implying a 0° phase shift. Grain size variations are also observed over other type of bedforms. *Miselis and McNinch* (2006) report for nearshore oblique bars of North Carolina that the coarser sediment almost always appears in the troughs. Both a 0° and 180° degree phase shift between mean grain size and topography are observed for tidal sand waves in the southern North Sea (*Roos et al.*, 2008).

A considerable improvement with respect to *Walgreen et al.* (2003) is that the modeled maximum variation in the fraction of fine and coarse sediment over sfcf has increased. The latter is contributed to the fact that interactions between waves and the topography are included. According to model results in case $c_s < 0$, variations in the mean grain size d_m are $\sim 0.02 [h']$ mm. For heights of sfcf $h' \sim 1 - 6$ m (observed values) the mean grain size would vary between 0.02 mm and 0.12 mm. These values become slightly higher for simulations with $c_s > 0$: grain size variations are 0.03–0.18 mm. Observations (e.g. *Schwab et al.*, 2000, for the Long Island shelf) suggest that the variation in the mean grain size is in the order of 0.25 – 0.40 mm. Inspection of grain size variations on other shelves, as presented in *Swift et al.* (1978) and *Stubblefield and Swift* (1981), reveals grain size variations in the range of 0.05 – 0.65 mm. Thus, modeled grain size variations are slightly smaller than observed, but seem to be the right order of magnitude.

In literature mostly qualitative information is given about variations in the standard deviation over sfcf. For sfcf in general, including the sfcf on the Long Island shelf, sediment is best sorted on the crest and most poorly sorted in the troughs (*Swift et al.*, 1972, 1978; *Schwab et al.*, 2000). Data from sfcf in the German Bight (*Antia*, 1993) indicate a better degree of sorting on the downstream flank. In the model $F_1 > F_2$, which implies that $v'_s \propto -f'_1$ (see equation (5.32)). Thus, the finer sediment ($f'_1 > 0$) is better sorted ($v'_s < 0$). Therefore, model results for which the drag coefficient is grain size dependent ($c_s > 0$) are in best agreement with the data for Long Island.

5.5.3 MODEL SIMPLIFICATIONS

The model used in this chapter is based on several simplifying assumptions. First, a linear stability analysis is employed, which only yields information about the initial growth of and grain sorting over sfcf. If wave-bedform feedbacks are taken into account, both growth and migration of sfcf are controlled by suspended load transport. Thus, the principal mechanism

of grain sorting is not expected to change on the long term. Second, the model overestimates the effects of settling lag for the coarse grains and underestimates them for the fine grains. It is interesting to investigate whether solving the concentration equation for both the coarse and fine sediment will affect the model results. A third simplification is that the bottom sediment is represented by one well-mixed active layer, which does not interact with the substrate beneath. Furthermore, the mean grain size and sorting of the substrate are assumed not to vary in time. As a first step, a more realistic representation of the bottom layer would be to introduce an exchange layer to the one-layer model such that vertical sorting is accounted for (Ribberink, 1987). A mathematical analysis of the equations leads to the expectation that sorting characteristics will not change for a two-layer representation of the bottom sediment. A more sophisticated way to represent the bottom sediment is by a continuous vertical distribution (cf. Van Ledden *et al.*, 2004).

In recent years studies by Murray and Thieler (2004), Coco *et al.* (2007a,b) and Huntley *et al.* (2008) have focussed on investigating so-called 'sorted bedforms', which are particularly found on sediment-starved shoreface and inner shelf environments. The sorted bedforms are found in very poorly sorted sediment mixtures and a robust phase shift of 90° between f'_1 and h' is observed. Inspired by their work the effect of including the term $L_{a0} \frac{\partial f'_1}{\partial t}$, which was excluded on the left-hand side of equation (5.33b), was investigated. This term defines the adjustment time scale of the grain size distribution to bottom changes, which in general will be very small for sfcf. For the default model setting, the thickness of the active layer in the basic state is $L_{a0} = d_m 2^{T_s} \sim 5 \times 10^{-4}$ m. In additional simulations, the latter was increased to a value of ~ 3 m, which is the value used for sorted bedforms. The distribution of the mean grain size and standard deviation over sfcf was not affected. Only increasing L_{a0} up to about 10 m would change the phase shift between h' and f'_1 from 180° to 0° . But this is certainly not realistic for sfcf.

5.6 CONCLUSIONS

The main objective of the present study was to obtain a better understanding of the initial formation of sfcf and the corresponding grain size distribution. For this, a model was developed and analyzed, which consists of the depth-averaged shallow water equations, a sediment transport formulation and mass balance of sediment. A new aspect in the hydrodynamic module (with respect to previous studies on sfcf) is that the behavior of waves is described by equations, which follow from physical principles, rather than by parameterizations. Important are the inclusion of feedbacks between the growing bedforms and the waves. The sediment is represented by two grain size classes. The important new aspects in the sediment transport module are that the entrainment of suspended sediment depends on bottom roughness and settling lag effects are included in the sediment concentration equation.

Default model experiments for a setting which resembles the Long Island micro-tidal inner shelf, show that the growth and migration of sfcf stabilizes for a bimodal sediment mixture compared to uniform sediment. Furthermore, results reveal the presence of the finer sand approximately in the troughs and the coarser sand slightly up-current of the crests. In case

that roughness-induced turbulence effects are taken into account in the suspended sediment transport, the trend is opposite: the coarser sand is located in the troughs and the finer sand on the crests. Both results are not in agreement with field data for the Long Island sfcf in which the coarsest sand is found on the landward flank and the finest sand on the seaward flank. However, field data on e.g. Canadian and Brazilian sfcf and also on some other type of bedforms reveal that often coarse sediment is observed in the troughs. An interesting model result is that the modeled maximum variation in the probabilities of fine and coarse sediment over the sfcf has the right order of magnitude (10^{-1} mm). Crucial here is the inclusion of wave-bedform interactions.

A physical analysis has revealed that the phase shift between the mean grain size and the bottom topography obtained by the model is due to the wave-bedform feedback mechanism. It causes convergence of wave rays at the upstream sides of sfcf and thus results in enhanced stirring of sediment by waves at these locations. In case that roughness-induced turbulence effects are neglected, the additional entrainment of grains is more effective for grains of size smaller than the mean compared to grains of size larger than the mean. Thus, more fine than coarse sand is eroded from the crests and therefore the crests become coarser. On the other hand, more fine than coarse sand is deposited in the troughs where wave energy is reduced, which results in troughs consisting of finer sand. In case that the drag coefficient is dependent on the physical roughness of the seabed, results are fundamentally different. Due to a change in grain size and ripple size from the coarse to fine domains, the physical roughness of the seabed is larger (smaller) in areas where the sediment is relatively coarse (fine). Including this effect, the entrainment of grains of size larger than the mean is enhanced compared to the entrainment of grains of size smaller than the mean: troughs become coarser and crests become finer. Furthermore, the effects of settling lag are crucial to cause damping of small-scale perturbations.

APPENDICES

5.A SETTLING LAG IN THE CONCENTRATION EQUATION

The depth-integrated volumetric concentration of available grains in class i is governed by the sediment concentration equation (5.13). In case that settling lag effects are ignored (the term on the left-hand side vanishes) a balance between sediment erosion and deposition near the bed exists and expression (5.16) is an exact solution. Including settling lag effects and assuming that expression (5.16) still holds, an equation for the depth-integrated volumetric concentration corresponding to the mean grain size C_m can be derived:

$$\mu_c \vec{\nabla} \cdot (\vec{v} C_m) = w_{sm} (E_m - \frac{C_m}{\delta_m \tilde{D}}). \quad (5.A-1)$$

Here, \vec{v} is the depth- and wave-averaged flow velocity and δ_m the ratio of the thickness of the suspended load layer of grains of diameter d_m over the total water depth $\tilde{D} = -z_b$. Furthermore, w_{sm} is the settling velocity of sediment with the mean grain size and E_m the entrainment of these grains. Considering fine sediment ($i = 1$),

$$\mu_c = \frac{w_{sm}}{w_{s1}} \frac{\delta_1}{\delta_m} > 1, \quad (5.A-2)$$

where w_{s1} is the settling velocity of grains of diameter d_1 and δ_1 is the ratio of the thickness of the suspended load layer of grains of size d_1 over the total water depth. However, equation (5.A-1) is solved for $\mu_c = 1$, which implies that settling lag effects are slightly underestimated for the fine sediment. Considering coarse sediment ($i = 2$),

$$\mu_c = \frac{w_{sm}}{w_{s2}} \frac{\delta_2}{\delta_m} < 1, \quad (5.A-3)$$

where w_{s2} is the settling velocity of grains of diameter d_2 and δ_2 is the ratio of the thickness of the suspended load layer of grains of size d_2 over the total water depth. As equation (5.A-1) is solved for $\mu_c = 1$, settling lag effects are slightly overestimated for the coarse grains.

5.B PERTURBED FLOW AND SEDIMENT TRANSPORT

The perturbed cross-shore and longshore velocity component, free surface elevation, depth-integrated volume concentration of suspended sediment corresponding to the mean grain size, wave orbital velocity and bottom elevation are denoted by u' , v' , η' , c'_m , u'_w and h' , respectively. After linearization of equations (5.2)-(5.4) and equation (5.17) with respect to these small perturbations, the following system is obtained:

$$\begin{pmatrix} \mathcal{L}_{11} & \mathcal{L}_{12} & \mathcal{L}_{13} & \mathcal{L}_{14} \\ \mathcal{L}_{21} & \mathcal{L}_{22} & \mathcal{L}_{23} & \mathcal{L}_{24} \\ \mathcal{L}_{31} & \mathcal{L}_{32} & \mathcal{L}_{33} & \mathcal{L}_{34} \\ \mathcal{M}_{41} & \mathcal{M}_{42} & 0 & \mathcal{M}_{44} \end{pmatrix} \begin{pmatrix} u' \\ v' \\ \eta' \\ c'_m \end{pmatrix} = \begin{pmatrix} 0 \\ \mathcal{U}_2 \\ 0 \\ \mathcal{U}_4 \end{pmatrix} u'_w + \begin{pmatrix} 0 \\ 0 \\ \mathcal{H}_3 \\ \mathcal{H}_4 \end{pmatrix} h'.$$

In this expression, $\mathcal{L}_{..}$ refers to the corresponding elements of operator \mathcal{L} in appendix 2.B. Furthermore, the elements $\mathcal{M}_{..}$ are

$$\mathcal{M}_{41} = \frac{dC_m}{dx} + C_m \frac{\partial}{\partial x}, \quad \mathcal{M}_{42} = C_m \frac{\partial}{\partial y}, \quad \mathcal{M}_{44} = V \frac{\partial}{\partial y} + \frac{w_{sm}}{\delta_m H}.$$

Here, C_m is the basic state volumetric suspended sediment concentration corresponding to the mean grain size. The basic state current and bottom elevation are denoted by V and H , respectively. Furthermore, w_{sm} is the settling velocity for grains with size d_m and δ_m is the ratio of the thickness of the suspended load layer for these grains over the total water depth. Expressions and values for the latter variables are given in the main text of this chapter. Due to the fact that perturbations in the wave orbital velocity are included, the vector operator \mathcal{U} appears, which has nonzero elements that are given by

$$\mathcal{U}_2 = -\frac{rV}{H}, \quad \mathcal{U}_4 = 5w_{sm}AZ_m^5U_w^4.$$

The friction coefficient r , the basic state wave orbital velocity U_w , A and Z_m are defined in the main text. Finally, elements of the vector operator \mathcal{H} , which operates on h' , need to be considered and read

$$\mathcal{H}_3 = V\frac{\partial}{\partial y}, \quad \mathcal{H}_4 = -\frac{w_{sm}C_m}{\delta_m H^2}.$$

The final step is to derive the linearized evolution equations for the bed elevation h' (equation (5.9a)) and the distribution function f'_i (equation (5.9b)). Hereto, perturbations $\vec{q}_i' = \vec{q}_{bi}' + \vec{q}_{si}'$ are added to the total volumetric sediment transport in the basic state \vec{Q}_i . The contribution to the perturbed sediment transport due to bedload \vec{q}_{bi}' is

$$\vec{q}_{bi}' = G_{bi}\vec{Q}_b f'_i + F_i\vec{Q}_b g'_{bi} + F_i G_{bi}\vec{q}_b', \quad (i = 1, 2), \quad (5.B-1)$$

where G_{bi} , F_i and \vec{Q}_b are the basic state transport capacity function for bedload, the distribution function for grains in class i and the bedload sediment transport in case of a uniform sediment sample, respectively (see section 5.3.1). Linearizing the most right expression in equation (5.11) with respect to the perturbation in the mean grain size ϕ'_m results in the perturbed transport capacity function for bedload transport:

$$g'_{bi} = c_b \ln 2 G_{bi} \phi'_m, \quad (5.B-2)$$

where c_b is a coefficient, which indicates the strength of hiding. Note that g'_{bi} is a function of f'_1 , which follows from equation (5.32). The linearized form of equation (5.11) for \vec{q}_b is

$$\vec{q}_b' = \frac{3}{2}\nu_b \left(U_w^2 u' - \lambda_b U_w^3 \frac{\partial h'}{\partial x}, 2U_w V u'_w + U_w^2 v' - \lambda_b U_w^3 \frac{\partial h'}{\partial y} \right). \quad (5.B-3)$$

The contribution to the perturbed sediment transport due to suspended load \vec{q}_{si}' is

$$\vec{q}_{si}' = \left(C_i u' - C_i \hat{\lambda}_s U_w^2 \frac{\partial h'}{\partial x}, C_i v' + V c'_i - C_i \hat{\lambda}_s U_w^2 \frac{\partial h'}{\partial y} \right), \quad (5.B-4)$$

where C_i is the depth-integrated volumetric concentration of available grains in class i and $\hat{\lambda}_s$ is the bed slope coefficient for suspended load transport. Furthermore, the perturbation added to C_i , denoted as c'_i , is a function of c'_m and follows from equation (5.16):

$$c'_i = G_{si} C_m f'_i + F_i C_m g'_{si} + F_i G_{si} c'_m. \quad (5.B-5)$$

The expression for the basic state transport capacity function for suspended load transport G_{si} is given in equation (5.30). Linearizing expression (5.21) with respect to ϕ'_m and the perturbed straining factor λ'_E results in an expression for the perturbed transport capacity function for suspended load transport:

$$g'_{si} = G_{si} \left(c_s \ln 2 \phi'_m + 5 \frac{\lambda'_E}{\Lambda_E} \right), \quad \lambda'_E = -0.288 v'_s. \quad (5.B-6)$$

Here, c_s is a coefficient, which has several components, including hiding. Furthermore, Λ_E is the basic state straining factor defined in section 5.3.1 and v'_s is the perturbed standard deviation of the sediment mixture. Note that g'_{si} is a function of f'_1 , as is obvious from equation (5.32).

CHAPTER 6

GENERAL DISCUSSION AND CONCLUSIONS

The focus of this thesis is on the morphodynamics of shoreface-connected sand ridges (hereafter abbreviated as sfc_r). Sfc_r are large-scale bedforms observed on the inner shelf of coastal seas where storms occur frequently and water depths are between 5 and 30 m. As was mentioned in chapter 1, the main aim of this study was to explore which physical processes are of importance for the formation, subsequent long-term evolution and main characteristics of these ridges. The four research questions on page 13 set the starting point of the research. In order to find answers to these questions, existing idealized morphodynamic models were used and extended with potentially important physical processes. The main idea behind these models is that bedforms can evolve due to interactions between the water motion and the erodible seabed. The detailed model results are described in chapters 2 to 5. Here, an overall discussion and conclusions of the findings are presented, where each of the following sections covers one of the four research questions (see page 13). At the end, in section 6.5, suggestions for future research are given.

6.1 FORMATION OF SFC_R: IMPROVED FORMULATION FOR STIRRING OF SEDIMENT BY WAVES

In the past several studies have demonstrated that sfc_r can grow due to feedbacks between waves (which stir sediment from the bottom), the storm-driven current (which transports the sediment) and the sandy bottom. However, a serious drawback of these studies is that they all use a strongly simplified, parametric description of waves in calculating stirring of sediment. Sediment stirring is (1) not explicitly determined by wave properties and (2) only dependent on the undisturbed reference depth without bedforms. In this section and section 6.2.1 the first drawback is considered, whereas the second drawback is discussed in section 6.3 and section 6.4.

In chapter 2 a morphodynamic model was presented in which wave variables are calculated with a shoaling-refraction model instead of using a parameterization. Stirring of sediment by waves is explicitly determined by the wave orbital velocity. The model was meant to investigate the initial evolution of sfcf. The shoaling-refraction model allows for sensitivity studies with respect to the period, height and direction of the waves. The model setting resembles the Long Island inner shelf, which is a micro-tidal storm-dominated shelf. The bottom patterns that were obtained after application of a linear stability analysis resemble sfcf of which the offshore ends are shifted up-current with respect to their attachments to the shoreface. The typical time scale on which bottom perturbations grow is in the order of centuries. The perturbations migrate with a typical speed of several meters per year in the down-current direction. Successive crests are typically spaced several kilometers apart.

The two mechanisms that cause the growth of sfcf in chapter 2 were already described by *Trowbridge* (1995) and *Calvete et al.* (2001a). The first involves the offshore deflection of the current over the crests of sfcf in case that the inner shelf has a transverse bottom slope. The second involves the net convergence of sediment caused by the joint action of cross-shore gradients in the depth-averaged sediment concentration in the basic state and the offshore deflection of the current over sfcf. A necessary condition for growth of sfcf is that the transverse bottom slope of the inner shelf exceeds a critical value. This critical bottom slope is larger for larger offshore angles of wave incidence, for higher waves and for waves with longer periods. Exceeding the critical bottom slope results in the evolution of sfcf. Varying the offshore boundary conditions for the wave properties (offshore angle of wave incidence between 0° and -50° , offshore wave height between 1.2 m and 2.0 m, wave period between 8 s and 14 s) revealed preferred wavelengths for sfcf between 7 and 10 km, growth rates up to $1 \times 10^{-4} \text{ yr}^{-1}$ and down-current migration speeds between 21 and 26 m yr^{-1} . The growth rates and migration speeds are computed for continuous storm conditions, whereas in reality storms only occur during a certain time fraction. For a typical 5% time fraction of storms, the growth rates and migration speeds would be a factor 20 smaller. The model predicts an increase in the preferred wavelength of the bedforms if the offshore angle of wave incidence, offshore wave height or wave period become larger. The growth rate is smallest for high-angle, high-amplitude and low-frequency waves. The migration speed is hardly dependent on the offshore angle of wave incidence, but it shows a maximum for an offshore wave height of 1.8 m and is largest for low-frequency waves. The variation in growth rate, migration speed and longshore spacing for a change in offshore wave characteristics is the consequence of a different wave transformation across the inner shelf.

6.2 LONG-TERM EVOLUTION OF SFCF

6.2.1 IMPROVED FORMULATION FOR STIRRING OF SEDIMENT

The improved formulation for the wave variables and thus for the sediment stirring was also added to a fully nonlinear version of the morphodynamic model in chapter 3, which is meant to study the long-term evolution of sfcf. A nonlinear stability analysis was performed in which a truncated series of eigenmodes of the linear stability analysis were used to compute the temporal evolution of modal amplitudes. Model simulations again reveal that growth of

sfcr is possible if the transverse bottom slope of the inner shelf exceeds a critical value. In that case, the height of sfcr initially grows exponentially, followed by saturation towards a constant maximum height due to nonlinear interactions between individual eigenmodes. In time, the shape of the ridges becomes asymmetrical (steeper seaward flanks) and the migration speed decreases. Furthermore, the initially most preferred mode is also the dominant one in the saturated state. Varying offshore wave characteristics results in the smallest finite maximum height and largest saturation time for high-angle, high-amplitude or low-frequency waves. Analysis of the potential energy balance of sfcr reveals that bed slope-induced sediment transports are crucial for the saturation process.

A limitation of the nonlinear stability analysis is that it exhibits explosive behavior for values of the inner shelf slope that are larger than 60% of observed values. Instability behavior occurs when the smallest length scale included in the nonlinear analysis grows rapidly. Sometimes model performance improves when more eigenmodes are included in the nonlinear stability analysis, although it is not always clear which modes should be added. Additional experiments were performed in chapter 3 by adding subharmonic modes (i.e., eigenmodes with wavelengths being larger than that of the most preferred mode) to the nonlinear analysis. The sensitivity of the characteristics of finite-amplitude sfcr to changes in the number of modeled subharmonics was also explored.

6.2.2 ADDING SUBHARMONIC MODES

In case that subharmonic modes are included, it appears that the initially most preferred mode no longer yields a significant contribution to the solution in the saturated state. The alongshore distance between successive sfcr increases by about 20%. An important result is that the overall characteristics like the instantaneous global growth rate, instantaneous global migration speed, finite bedform height and alongshore spacing are not sensitive to the number of subharmonics. However, the evolution of the individual modal amplitudes of the sfcr is strongly dependent on the number of subharmonics considered and thus is only predictable for a finite amount of time. An interesting result is that for simulations including subharmonic modes sfcr form patches in the transient stage. The patchiness of ridges, which was never obtained with previous models, disappears in the saturated state. Results indicate that it takes a very long time before saturation of the individual modal amplitudes takes place. This suggests that observed ridges are still in their transient stage and have not yet reached saturation. The latter is confirmed by the fact that observed sfcr occur in patches of 4 – 8 ridges, whereas according to model results this would only occur for sfcr in the transient stage.

6.3 WAVE-BEDFORM INTERACTIONS

In chapter 4 the wave formulation (and thus the formulation for sediment stirring) is further improved by also accounting for refraction and shoaling and dissipation of wave energy due to the presence of bedforms on the seabed, also called wave-bedform interactions. Model simulations show that including wave-bedform interactions results in a new and third physical mechanism through which sfcr can grow and migrate. This new mechanism is related to the convergence of wave energy slightly upstream of the crests, which induces an enhanced

entrainment of sediment at that location. This sediment is subsequently transported by the storm-driven longshore current. A transverse bottom slope is no longer necessary to obtain growth of ridges. The wave-bedform feedback mechanism dominates over the mechanisms described by *Trowbridge* (1995) and *Calvete et al.* (2001a) for obliquely incident waves. In case of the wave-bedform feedback mechanism both growth and migration are controlled by suspended load transport and are enhanced. The successive distance between individual crests becomes shorter and sfcf become more trapped to the coast. *Lane and Restrepo* (2007) report that they do not obtain growth of bedforms if they include wave-bedform interactions, which seems to be a consequence of their assumption that sediment transport is proportional to the mass transport velocity (which accounts for currents and wave-induced Stokes drift), rather than proportional to the near-bed current.

6.4 WAVE-BEDFORM FEEDBACKS AND GRAIN SORTING

Instead of considering uniform sand, the influence of wave-bedform feedbacks on the initial formation of sfcf in case of a bimodal sediment mixture was investigated in chapter 5. Model experiments indicate that the sensitivity of the wavelength to sorting is small, whereas sediment sorting leads to a stabilization of the growth rate and migration speed of sfcf. The latter can be interpreted as the result of a more efficient packing of the bottom material when grains of different sizes are present. In case that the entrainment of suspended sediment is dependent on bottom roughness the coarsest sediment is found in the troughs, whereas in all other cases the troughs are covered with the finest sediment. Results are not in agreement with observations for sfcf on the Long Island shelf, which reveal the finest (coarsest) sand on the down-current (up-current) flank. However, some sfcf on other inner shelves exhibit grain size patterns, which are in agreement with those obtained by the model. The finest sediment is best sorted in case of $F_1 > F_2$, which is consistent with field data. The modeled maximum variation in the mean grain size over the topography is in the order of 0.02 – 0.18 mm, which is the right order of magnitude considering field data. It is crucial to take into account settling lag effects in the concentration equation such that high wavenumber instabilities are damped and a preferred wavelength of the bedforms is obtained.

6.5 SUGGESTIONS FOR FUTURE RESEARCH

Several subjects require further attention in the research into the formation and long-term evolution of sfcf. For nonlinear experiments including wave-bedform feedbacks, sfcf continue to grow on the long term and numerical instabilities arise before they saturate. An explanation for the latter is that stirring of sediment by waves increases with increasing ridge height. This tendency will be counteracted by e.g. wave breaking, a process, which is not yet implemented in the model. Another interesting addition in this respect is the forcing of currents due to the divergence of wave-induced radiation stresses. *Caballeria et al.* (2002) and *Garnier et al.* (2006) were able to obtain results with a nonlinear model for bars in the nearshore zone including wave-topography feedbacks, but they only account partially for wave refraction. The important new mechanism obtained in case that stirring of sediment by waves is affected by bedforms indicates that a nonlinear study including this effect will be very valuable.

Results presented in this thesis do not account for three-dimensional characteristics of the water motion and the entrained sediment concentration; depth-averaged variables are used. *Pu-
trevu and Svendsen* (1999) developed a method to account for 3D effects in a 2-dimensional model framework, in which it is essential to have knowledge about the vertical structure of the short-wave-averaged velocity and concentration. As a first step, a simplified version of their approach has been used by multiplying the depth-averaged variables with a form function representing their vertical structure. In that case neither the spatial pattern of the bedforms nor the pattern of the mean grain size seem to change, whereas the growth rate will increase and the migration speed decrease. Much more complicated is the full analysis of a 3-dimensional flow interacting with bedforms on the seabed, but it is probably of importance for the distribution of the mean grain size over the bedforms.

Another process, which might influence the evolution of sfcf and the mean grain size pattern, is current refraction due to waves. In a recent study by *Van Leeuwen et al.* (2006) this process was incorporated in a model to study the initial formation of nearshore bed patterns. They showed that current refraction due to waves weakens the growth of transverse bars, whereas crescentic bar formation is not affected. It would be interesting to investigate whether the formation and long-term evolution of sfcf is influenced by current refraction due to waves.

In all chapters the formation and evolution of sfcf is investigated for storm conditions. In reality however fair weather and storms will alternate and storms will involve different wind forcings. Simulations in which different weather types alternate would give valuable insight into the time scales involved in and the irregularity of the evolution of sfcf.

BIBLIOGRAPHY

- Amos, C. L., M. Z. Li, and K. S. Choung (1996), Storm-generated, hummocky stratification on the outer-Scotian shelf, *Geo-Marine Lett.*, *16*, 85–94.
- Anthony, D., and J. O. Leth (2002), Large-scale bedforms, sediment distribution and sand mobility in the eastern North Sea off the Danish west coast, *Mar. Geol.*, *182*, 247–263.
- Antia, E. E. (1993), Sedimentology, morphodynamics and facies association of a mesotidal barrier island shoreface (Spiekeroog, southern North Sea), Ph.D. thesis, Univ. Bremen, Germany.
- Antia, E. E. (1996a), Shoreface-connected ridges in German and US Mid-Atlantic bights: similarities and contrasts, *J. Coastal Res.*, *12*, 141–146.
- Ashton, A. D., and A. B. Murray (2006), High-angle wave instability and emergent shoreline shapes: 1. modeling of sand waves, flying spits, and capes, *J. Geophys. Res.*, *111*, F04011, doi:10.1029/2005JF000422.
- Bagnold, R. A. (1963), Mechanics of marine sedimentation, *The Sea*, *3*, 507–528.
- Bailard, J. A. (1981), An energetics total load sediment transport model for a plane sloping beach, *J. Geophys. Res.*, *86*(C11), 10,938–10,954.
- Besio, G., P. Blondeaux, and G. Vittori (2006), On the formation of sand waves and sand banks, *J. Fluid Mech.*, *557*, 1–27.
- Blondeaux, P., E. Foti, and G. Vittori (2000), Migrating sea ripples, *Eur. J. Mech. B/Fluids*, *19*(2), 285–301.
- Boyd, J. P. (2001), *Chebyshev and Fourier spectral methods*, Dover, New York.
- Bruun, P. (1954), *Coast erosion and the development of beach profiles. Technical Memorandum*, vol. 44, Beach Erosion Board, Corps of Engineers.
- Bruun, P. (1962), Sea-level rise as a cause of shore erosion, *J. Waterways and Harbors Div. ASCE*, *88*, 117–130.
- Caballeria, M., G. Coco, A. Falqués, and D. A. Huntley (2002), Self-organization mechanisms for the formation of nearshore crescentic and transverse sand bars, *J. Fluid Mech.*, *465*, 379–410.
- Cacchione, D. A., W. D. Grant, and G. B. Tate (1984), Rippled scour depressions on the inner continental shelf off central California, *J. Sed. Petr.*, *54*, 1280–1291.
- Calvete, D. (1999), Morphological stability models: shoreface-connected sand ridges, Ph.D. thesis, Univ. Politècnica de Catalunya, Spain.
- Calvete, D., and H. E. De Swart (2003), A nonlinear model study on the long-term behavior of shore face-connected sand ridges, *J. Geophys. Res.*, *108*(C5), doi:10.1029/2001JC001091.
- Calvete, D., A. Falqués, H. E. de Swart, and M. Walgreen (2001a), Modelling the formation of shoreface-connected sand ridges on storm-dominated inner shelves, *J. Fluid Mech.*, *441*, 169–193.

- Calvete, D., M. Walgreen, H. E. de Swart, and A. Falqués (2001b), A model for sand ridges on the shelf: effect of tidal and steady currents, *J. Geophys. Res.*, *106*(C5), 9311–9325.
- Calvete, D., H. E. de Swart, and A. Falqués (2002), Effect of depth-dependent wave stirring on the final amplitude of shoreface-connected sand ridges, *Cont. Shelf Res.*, *22*, 2763–2776.
- Calvete, D., N. Dodd, A. Falqués, and S. M. van Leeuwen (2005), Morphological development of rip channel systems: normal and near-normal wave incidence, *J. Geophys. Res.*, *110*(C10).
- Canuto, C., M. Y. Hussaini, A. Quarteroni, and T. A. Zang (1988), *Spectral methods in fluid dynamics*, Springer-Verlag, New York.
- Coco, G., T. K. Burnet, B. T. Werner, and S. Elgar (2004), The role of tides in beach cusp development, *J. Geophys. Res.*, *109*, C04011, doi:10.1029/2003JC002154.
- Coco, G., A. B. Murray, and M. O. Green (2007a), Sorted bed forms as self-organized patterns: 1. model development, *J. Geophys. Res.*, *112*, F03015, doi:10.1029/2006JF000665.
- Coco, G., A. B. Murray, M. O. Green, E. R. Thieler, and T. M. Hume (2007b), Sorted bed forms as self-organized patterns: 2. complex forcing scenarios, *J. Geophys. Res.*, *112*, F03016, doi:10.1029/2006JF000666.
- Cooper, J. A. G., and O. H. Pilkey (2004), Sea-level rise and shoreline retreat: time to abandon the Bruun Rule, *Glob. and Plan. Change*, *43*, 157–171.
- Crapper, G. D. (1984), *Introduction to water waves*, Ellis Horwood, New York.
- De Swart, H. E., and D. Calvete (2003), Non-linear response of shoreface-connected sand ridges to interventions, *Ocean Dynamics*, *53*, 270–277, doi:10.1007/s10236-003-0044-9.
- Draper, L. (1991), Wave climate atlas of the British isles, *Tech. Rep. OTH 89 303*, Dept. of Energy, HMSO, London.
- Duane, D. B., M. E. Field, E. P. Miesberger, D. J. P. Swift, and S. J. Williams (1972), Linear shoals on the Atlantic continental shelf, Florida to Long Island, in *Shelf Sediment Transport: Process and Pattern*, edited by D. J. P. Swift, D. B. Duane, and O. H. Pilkey, pp. 447–498, Dowden, Hutchinson and Ross, Stroudsburg.
- Dyer, K. R. (1986), *Coastal and estuarine sediment dynamics*, John Wiley and Sons, London.
- Dyer, K. R., and D. A. Huntley (1999), The origin, classification and modelling of sand banks and ridges, *Cont. Shelf Res.*, *19*, 1285–1330.
- Edwards, J. H., S. E. Harrison, S. D. Locker, A. C. Hine, and D. C. Twichell (2003), Stratigraphic framework of sediment-starved sand ridges on a mixed siliciclastic/carbonate inner shelf; west-central Florida, *Mar. Geol.*, *200*, 195–217.
- Falqués, A., A. Montoto, and V. Iranzo (1996), Bed-flow instability of the longshore current, *Cont. Shelf Res.*, *16*, 1927–1964.
- Falqués, A., D. Calvete, and H. E. de Swart (1999), Morphodynamics of shoreface-connected ridges, in *Proc. of the 26th ICCE*, edited by B. L. Edge, pp. 2851–2864, ASCE, Reston (VI).
- Falqués, A., G. Coco, and D. A. Huntley (2000), A mechanism for the generation of wave-driven rhythmic patterns in the surf zone, *J. Geophys. Res.*, *105*(C10), 24,071–24,087.
- Federici, B., and G. Seminara (2006), Effect of suspended load on sandbar instability, *Water Resour. Res.*, *42*, doi:10.1029/2005WR004399.
- Figueiredo, A. G. (1980), Response of water column to strong wind forcing, southern Brazilian inner shelf: implications for sand ridge formation, *Mar. Geol.*, *35*, 367–376.
- Figueiredo, A. G., J. E. Sanders, and D. J. P. Swift (1982), Storm-graded layers on inner continental shelves: examples from southern Brazil and the Atlantic coast of the central United States, *Sed. Geol.*, *31*, 171–190.

- Fredsøe, J., and R. Deigaard (1992), *Mechanics of coastal sediment transport*, World scientific, Singapore.
- Garcia, M., and G. Parker (1991), Entrainment of bed sediment into suspension, *J. Hydr. Eng.*, 117(4), 414–435.
- Garnier, R., D. Calvete, A. Falqués, and M. Caballeria (2006), Generation and nonlinear evolution of shore-oblique/transverse sand bars, *J. Fluid Mech.*, 567, 327–360.
- Garotta, V., M. B. Pittaluga, and G. Seminara (2006), On the migration of tidal free bars, *Phys. Fluids*, 18, doi:10.1063/1.2221346.
- Gerkema, T. (2000), A linear stability analysis of tidally generated sand waves, *J. Fluid Mech.*, 417, 303–322.
- Grant, W. D., and O. S. Madsen (1979), Combined wave and current interaction with a rough bottom, *J. Geophys. Res.*, 84(C4), 1797–1808.
- Green, M., C. E. Vincent, I. N. McCave, R. R. Dickson, J. M. Rees, and N. Pearson (1995), Storm sediment transport: observations from the British North Sea shelf, *Cont. Shelf Res.*, 15(8), 889–912.
- Gyr, A., and K. Hoyer (2006), *Sediment transport: a geophysical phenomenon*, Springer-Verlag, Dordrecht.
- Harrison, S. E., S. D. Locker, A. C. Hine, J. H. Edwards, D. F. Naar, and D. C. Twichell (2003), Sediment-starved sand ridges on a mixed carbonate/siliciclastic inner shelf off west-central Florida, *Mar. Geol.*, 200, 171–194.
- Hommes, S., S. J. M. H. Hulscher, and A. Stolk (2007), Parallel modeling approach to assess morphological impacts of offshore sand extraction, *J. Coastal Res.*, 23(6), 1565–1579.
- Hoogendoorn, E. L., and R. W. Dalrymple (1986), Morphology, lateral migration and internal structures of shoreface-connected ridges, Sable Island Bank, Nova Scotia, Canada, *Geology*, 14, 400–403.
- Huntley, D. A., G. Coco, K. R. Bryan, and A. B. Murray (2008), Influence of "defects" on sorted bedform dynamics, *Geophys. Res. Lett.*, 35, L02601, doi:10.1029/2007GL030512.
- Huthnance, J. M. (1982), On one mechanism forming linear sand banks, *Est., Coastal and Shelf Sci.*, 14, 79–99.
- Karniadakis, G. E., M. Israeli, and S. A. Orszag (1991), High-order splitting methods for the incompressible Navier-Stokes equations, *J. Comput. Phys.*, 97, 414–443.
- Komen, G. J., L. Cavaleri, M. Donelan, K. Hasselmann, S. Hasselmann, and P. A. E. M. Janssen (1994), *Dynamics and modelling of ocean waves*, Univ. Press, Cambridge.
- Lane, E. M., and J. M. Restrepo (2007), Shoreface-connected ridges under the action of waves and currents, *J. Fluid. Mech.*, 582, 23–52, doi:10.1017/S0022112007005794.
- Lentz, S., R. T. Guza, S. Elgar, F. Feddersen, and T. H. C. Herbers (1999), Momentum balances on the North Carolina inner shelf, *J. Geophys. Res.*, 104(C8), 18,205–18,226.
- Liu, Z. X., D. X. Xia, S. Berne, K. Y. Wang, T. Marsset, Y. X. Tang, and J. F. Bourillet (1998), Tidal deposition systems of China's continental shelf, with special reference to the eastern Bohia Sea, *Mar. Geol.*, 145(3-4), 225–253.
- Longuet-Higgins, M. S. (1952), On the statistical distribution of the heights of sea waves, *J. Mar. Res.*, 11, 245–266.
- Masetti, R., S. Fagherazzi, and A. Montanari (2008), Application of a barrier island translation model to the millennial-scale evolution of Sand Key, Florida, *Cont. Shelf Res.*, 28, 1116–1126.
- McBride, R. A., and T. F. Moslow (1991), Origin, evolution, and distribution of shoreface sand ridges, Atlantic inner shelf, U.S.A., *Mar. Geol.*, 97, 57–85.

- McCledden, C. E., and R. L. McMaster (1971), Probable holocene transgressive effects on the geomorphic features of the continental shelf off New Jersey, United States, *Marit. Sed.*, 7, 69–72.
- Mei, C. C. (1989), *The applied dynamics of ocean surface waves*, World Scientific, Singapore.
- Miselis, J. L., and J. E. McNinch (2006), Calculating shoreline erosion potential using nearshore stratigraphy and sediment volume: Outer Banks, North Carolina, *J. Geophys. Res.*, 111, F02019, doi: 10.1029/2005JF000389.
- Murray, A. B., and E. R. Thieler (2004), A new hypothesis and exploratory model for the formation of large-scale inner-shelf sediment sorting and "rippled scour depressions", *Cont. Shelf Res.*, 24, 295–315.
- Niedoroda, A. W., and D. J. P. Swift (1981), Maintenance of the shoreface by wave orbital currents and mean flow: observations from the Long Island coast, *Geophys. Res. Lett.*, 8, 337–340.
- Niedoroda, A. W., D. J. P. Swift, T. S. Hopkins, and C. H. Ma (1984), Shoreface morphodynamics on wave-dominated coasts, *Mar. Geol.*, 60, 331–354.
- Open University (2001), *Waves, tides and shallow-water processes*, Butterworth-Heinemann, Singapore.
- Parker, G., N. W. Lanfredi, and D. J. P. Swift (1982), Seafloor response to flow in a southern hemisphere sand-ridge field: Argentina inner shelf, *Sed. Geol.*, 33, 195–216.
- Pattiaratchi, C., and M. Collins (1987), Mechanisms for linear sandbank formation and maintenance in relation to dynamical oceanographic observations, *Prog. Oceanogr.*, 19, 117–156.
- Putrevu, U., and I. Svendsen (1999), Three-dimensional dispersion of momentum in wave-induced nearshore currents, *Eur. J. Mech. B/Fluids*, pp. 409–427.
- Restrepo, J. M. (2001), Wave-current interactions in shallow waters and shore-connected ridges, *Cont. Shelf Res.*, 21, 1331–1360.
- Ribas, F., A. Falqués, and A. Montoto (2003), Nearshore oblique sand bars, *J. Geophys. Res.*, 108(C4), 1–17.
- Ribberink, J. S. (1987), Mathematical modelling of one-dimensional morphological changes in rivers with non-uniform sediment, Ph.D. thesis, Tech. Univ. Delft, the Netherlands.
- Roos, P. C., S. J. M. H. Hulscher, M. A. F. Knaapen, and R. M. J. V. Damme (2004), The cross-sectional shape of tidal sandbanks: modeling and observations, *J. Geophys. Res.*, 109, F02003, doi: 10.1029/2003JF000070.
- Roos, P. C., S. J. M. H. Hulscher, F. V. der Meer, T. A. G. P. V. Dijk, I. G. M. Wientjes, and J. V. der Berg (2008), Grain sorting over offshore sandwaves: observations and modelling, in *Proc. of the 5th IAHR symposium*, vol. 1, edited by Dohmen-Janssen and Hulscher, pp. 649–656, Taylor & Francis.
- Schielen, R., A. Doelman, and H. E. de Swart (1993), On the nonlinear dynamics of free bars in straight channels, *J. Fluid Mech.*, 252, 325–356.
- Schramkowski, G. P., H. M. Schuttelaars, and H. E. de Swart (2002), The effect of geometry and bottom friction on local bed forms in a tidal embayment, *Cont. Shelf Res.*, 22, 1821–1833.
- Schwab, W. C., E. R. Thieler, J. R. Allen, D. S. Foster, B. A. Swift, and J. F. Denny (2000), Influence of inner-continental shelf geologic framework on the evolution and behavior of the barrier-island system between Fire Island Inlet and Shinnecock Inlet, Long Island, New York, *J. Coastal Res.*, 16(2), 408–422.
- Seminara, G. (1995), Effect of grain sorting on the formation of bedforms, *Appl. Mech. Rev.*, 48(9), 549–563.
- Short, A. D. (1999), *Handbook of beach and shoreface morphodynamics*, Wiley, West Sussex.
- Soulsby, R. L. (1997), *Dynamics of marine sands*, Thomas Telford, London.

- Stubblefield, W. L., and D. J. P. Swift (1981), Grain size variation across sand ridges, New Jersey continental shelf, *Geo-Marine Lett.*, *1*(1), 45–48, doi:10.1007/BF02463301.
- Swift, D. J. P., and M. E. Field (1981), Evolution of a classic sand ridge field: Maryland sector, North American inner shelf, *Sedimentology*, *28*, 461–482.
- Swift, D. J. P., B. Holliday, N. Avignone, and G. Shideler (1972), Anatomy of a shoreface ridge system, False Cape, Virginia, *Mar. Geol.*, *12*, 59–84.
- Swift, D. J. P., G. Parker, N. W. Lanfredi, G. Perillo, and K. Figge (1978), Shoreface-connected sand ridges on American and European shelves: a comparison, *Est. and Coastal Mar. Sci.*, *7*, 257–273.
- Trowbridge, J. H. (1995), A mechanism for the formation and maintenance of the shore oblique sand ridges on storm-dominated shelves, *J. Geophys. Res.*, *100*(C8), 16,071–16,086.
- Twitchell, D., G. Brooks, G. Gelfenbaum, V. Paskevich, and B. Donahue (2003), Sand ridges off Sarasota, Florida: a complex facies boundary on a low-energy inner shelf environment, *Mar. Geol.*, *200*, 243–262.
- Van de Meene, J. W. H. (1994), The shoreface-connected ridges along the central Dutch coast, Ph.D. thesis, Nederlandse geografische studies, the Netherlands.
- Van de Meene, J. W. H., and L. C. Van Rijn (2000), The shoreface-connected ridges along the central Dutch coast. part 1: field observations, *Cont. Shelf Res.*, *20*(17), 2295–2323.
- Van de Meene, J. W. H., J. R. Boersma, and J. H. J. Terwindt (1996), Sediment structures of combined flow deposits from shoreface-connected ridges along the central Dutch coast, *Mar. Geol.*, *131*, 151–175.
- Van der Vegt, M., H. M. Schuttelaars, and H. E. de Swart (2007), Modeling the formation of undulations of the coastline: the role of tides, *Cont. Shelf Res.*, *27*, 2014–2031, doi:10.1016/j.scr.2007.04.006.
- Van Ledden, M., W. G. M. van Kesteren, and J. C. Winterwerp (2004), A conceptual framework for the erosion behaviour of sandmud mixtures, *Cont. Shelf Res.*, *24*, 1–11.
- Van Leeuwen, S. M., N. Dodd, D. Calvete, and A. Falqués (2006), Physics of nearshore bed pattern formation under regular or random waves, *J. Geophys. Res.*, *111*, F01023, doi:10.1029/2005JF000360.
- Van Oyen, T., and P. Blondeaux (2008), Grain sorting effects on the formation of tidal sand waves, *Submitted to J. Fluid Mech.*
- Van Rijn, L. C. (1993), *Principles of sediment transport in rivers, estuaries and coastal seas*, Aqua Publ., Amsterdam.
- Vis-Star, N. C., H. E. de Swart, and D. Calvete (2007), Effect of wave-topography interactions on the formation of sand ridges on the shelf, *J. Geophys. Res.*, *112*, C06012, doi:10.1029/2006JC003844.
- Vittori, G., and P. Blondeaux (1992), Sand ripples under sea waves. part 3. Brick-pattern ripple formation, *J. Fluid Mech.*, *239*, 23–45.
- Vittori, G., H. E. de Swart, and P. Blondeaux (1999), Crescentic bedforms in the nearshore region, *J. Fluid Mech.*, *381*, 271–303.
- Walgreen, M., D. Calvete, and H. E. de Swart (2002), Growth of large-scale bed forms due to storm-driven and tidal currents: a model approach, *Cont. Shelf Res.*, *22*(18–19), 2777–2793.
- Walgreen, M., H. E. de Swart, and D. Calvete (2003), Effect of grain size sorting on the formation of shoreface-connected sand ridges, *J. Geophys. Res.*, *108*(C3), 3063.
- Williams, J. J., C. P. Rose, P. D. Thorne, B. A. O'Connor, J. D. Humphery, P. J. Hardcastle, S. P. Moores, J. A. Cooke, and D. J. Wilson (1999), Field observations and predictions of bed shear stresses and vertical suspended sediment concentration profiles in wave-current conditions, *Cont. Shelf Res.*, *19*, 507–536.
- Wright, L. D., and A. D. Short (1984), Morphodynamic variability of surf zones and beaches: a synthesis, *Mar. Geol.*, *56*, 93–118.

SAMENVATTING

KUSTAANGEHECHTE ZANDBANKEN

De context van het onderzoek dat wordt besproken in dit proefschrift betreft kustzeeën, die met een zekere regelmaat zwaar weer te verduren krijgen. Onder die omstandigheden zorgt een combinatie van hoge golven en sterke stromingen ervoor dat zand op de bodem wordt opgewoeld en meegevoerd. Hierdoor wordt, deels verborgen voor het menselijk oog, een rijke variëteit aan bodempatronen gevormd. Eén type van dergelijke bodempatronen staat centraal in dit proefschrift: de kustaangehechte zandbanken of sfc (shoreface-connected sand ridges).

Kustaangehechte zandbanken komen op verschillende plekken in de wereld voor, echter alleen in kustzeeën met dieptes tussen de 5 en 30 m, waar zand op de bodem ligt en waar regelmatig stormen overheen trekken. Langs grote gedeeltes van de Oost-Amerikaanse kust, langs de kust van Brazilië en Argentinië en ook langs de Canadese kust is dit het geval. Verder wordt de aanwezigheid van kustaangehechte zandbanken gerapporteerd in zowel het Nederlandse als het Belgische, Duitse en Deense gedeelte van de Noordzee. De sterkte van het getij varieert aanzienlijk over de genoemde regio's. Figuur 1.2a op bladzijde 4 laat de kustaangehechte zandbanken zien in het zuidoostelijke gedeelte van de Noordzee, langs het Duitse waddeneiland Spiekeroog. Kustaangehechte zandbanken worden veelal waargenomen in groepen van 4 – 8 banken, die diagonaal georiënteerd zijn met een hoek van 10° – 50° ten opzichte van de kustlijn. De oriëntatie is gerelateerd aan de dominante richting van de stormgedreven stroming, zodanig dat het zeewaartse uiteinde van de banken stroomopwaarts verschoven is ten opzichte van het landwaartse uiteinde. Individuele banken zijn tientallen kilometers lang, enkele meters hoog en hebben een breedte van enkele kilometers. De banken bewegen in de richting van de stormgedreven stroming met een snelheid van enkele meters per jaar. De Argentijnse en Noord-Amerikaanse kustaangehechte zandbanken vertonen een duidelijke asymmetrie: de stroomafwaartse kant is steiler dan de stroomopwaartse kant. Verder wordt een variatie in de korrelgrootte van het zand waargenomen over de zandbanken (ook wel korrelgrootte sortering genoemd). Op veel zandbanken bevindt het grove zand zich op de landwaartse flank en het fijne zand zich op de zeewaartse flank (zie Figuur 1.2b).

Het is om verschillende redenen belangrijk meer inzicht te krijgen in de fysische processen die de morfodynamica van kustaangehechte zandbanken bepalen. Kennis over verplaatsingen en vormveranderingen van zandbanken is cruciaal voor zowel de stabiliteit van buizen, kabels en boorplatformen in de zeebodem, alsook voor de veiligheid van scheepsroutes en anker-

plaatsen. De grote hoeveelheden zand waaruit zandbanken bestaan, zijn interessant voor de bouw en zand is al gewonnen uit bijvoorbeeld de Nederlandse Zeeland ruggen. Menselijke activiteiten, zoals zandwinning en het uitbaggeren van belangrijke vaargeulen, kunnen grote consequenties hebben voor de stabiliteit van de kust. Daarom is diepgaand onderzoek vereist om het herstelvermogen van de zandbanken in kaart te brengen.

Kustaangetichte zandbanken worden gevormd gedurende een tijdsbestek van enkele decennia tot eeuwen. Waarnemingen zijn echter alleen beschikbaar voor kortere tijdsperiodes en geven vaak informatie over òf morfologische veranderingen òf de waterbeweging en niet over allebei. In dit proefschrift wordt daarom gebruik gemaakt van morfodynamische modellen, die de golven, de stroming en de bodemveranderingen beschrijven door middel van fysische wetten. De gebruikte modellen zijn gebaseerd op de theorie dat zandbanken ontstaan en groeien door middel van morfodynamische zelforganisatie.

MORFODYNAMISCHE ZELFORGANISATIE

Morfodynamische zelforganisatie is het proces waarbij de golven, de stroming en de bodem elkaar voortdurend beïnvloeden door middel van het transport van zand. Wanneer er sprake is van een positieve terugkoppeling gaan kleine verstoringen in de bodem groeien en worden bodempatronen gevormd. De waterbeweging is verantwoordelijk voor het transport van zand: golven woelen bijvoorbeeld zand op en de stroming voert zand mee. Kleine oneffenheden in de bodem leiden tot kleine verstoringen in de waterbeweging, waardoor er lokaal meer (minder) zand weggevoerd dan aangevoerd wordt, met erosie (depositie) van zand als gevolg. Wanneer erosie van zand plaatsvindt op een locatie waar initieel een klein putje in de bodem aanwezig is, wordt dit putje verder uitgediept en is er sprake van een positieve terugkoppeling. In het geval van een negatieve terugkoppeling wordt een putje opgevuld door depositie van zand op die plaats. Wanneer er noch een positieve, noch een negatieve terugkoppeling optreedt, dan is het systeem in morfodynamisch evenwicht. Bedenk ook dat bodempatronen zich zullen verplaatsen wanneer de depositie van zand niet exact op de kam plaatsvindt. Het morfodynamische zelforganisatie mechanisme is geïllustreerd in Figuur 1.3 op bladzijde 6.

De gebruikte modellen, gebaseerd op het zelforganisatie mechanisme, zijn sterk geïdealiseerd in vergelijking met de werkelijkheid en hebben als doel essentiële processen voor ontstaan en groei van de zandbanken te identificeren. De modellen maken gebruik van een stabiliteitsanalyse: de stabiliteit van een morfodynamisch evenwicht wordt bepaald door het op willekeurige plaatsen aanbrengen van kleine bodemverstoringen. De waterbeweging, en daarmee het zandtransport, reageren op deze bodemverstoringen met als gevolg een af- of toename van de hoogte van de verstoringen. In het laatste geval zullen bodempatronen ontstaan met een bepaalde ruimtelijke structuur. Om de beginfase van het ontstaan van kustaangetichte zandbanken te begrijpen is een lineaire stabiliteitsanalyse toereikend: de bodemverstoringen zijn nog klein en beïnvloeden elkaars groei niet. De kustlangse golfenlengte van de verstoring die het hardste groeit, is het meest doeltreffend en zal de lengteschaal van de kustaangetichte zandbanken bepalen. Ook andere belangrijke kenmerken, zoals patroon, oriëntatie, groeisnelheid en migratiesnelheid van de zandbanken, worden door het model berekend. Op de lange termijn zullen de zandbanken in hoogte toenemen en met elkaar

gaan wisselwerken door middel van niet-lineaire processen. Een volledig niet-lineair morfodynamisch model beschrijft de tijdsontwikkeling van hoogtes van bekende oplossingen (die kustaangehechte zandbanken representeren) van het lineaire model. Het niet-lineaire model geeft inzicht in de evenwichtshoogte van de banken, hun migratiesnelheid, hun ruimtelijke patroon en de tijd die nodig is om de evenwichtshoogte te bereiken.

BELANGRIJKSTE NIEUWE ASPECTEN TEN OPZICHTE VAN EERDER ONDERZOEK

In dit proefschrift (alle hoofdstukken) worden golfkarakteristieken berekend met een op fysica gebaseerd golfmodel, in plaats van de tot nog toe gebruikte parametrische beschrijving. Hierdoor is het mogelijk de gevoeligheid van modelresultaten voor de periode, hoogte en richting van de golven te onderzoeken. Bovendien worden in de hoofdstukken 4 en 5 wisselwerkingen tussen golven en kustaangehechte zandbanken meegenomen en niet langer verwaarloosd. Nieuw in hoofdstuk 3 is de analyse van de potentiële energiebalans van de kustaangehechte zandbanken, die tot interessante inzichten heeft geleid. Een belangrijk nieuw element voor de korrelgrootte sortering over de zandbanken (hoofdstuk 5) is het verdisconteren van bodemruwheidseffecten in de opwerveling van (grof en fijn) sediment.

RESULTATEN

In hoofdstuk 2 is onderzocht welke processen van belang zijn voor de vorming van kustaangehechte zandbanken. Nieuw is dat golfkarakteristieken worden berekend met een op fysica gebaseerd golfmodel. Modelsimulaties laten zien dat een noodzakelijke conditie voor de groei van de zandbanken is dat de bodemhelling een kritische waarde overschrijdt. Deze kritische bodemhelling is groter naarmate golven onder een grotere hoek op de kust invallen, golven hoger zijn of laag-frequent. Als de helling van de bodem voldoende steil is, ontstaan bodempatronen waarvan de karakteristieke kustlangse lengteschaal, groeitijd en migratiesnelheid afhangen van de golfcondities op zee. De kustlangse afstand tussen de banken neemt toe in het geval dat de golfhoek, golfhoogte of golfperiode toeneemt. De groeisnelheid van de zandbanken is het kleinst voor schuin invallende golven of hoge golven, dan wel voor golven met een lage frequentie. De migratiesnelheid wordt nauwelijks beïnvloed door de hoek van inval van de golven. Echter, banken verplaatsen zich het snelst voor laag-frequente golven en golven met een hoogte van circa 1.8 m. De resultaten worden verklaard door middel van het identificeren en analyseren van fysische mechanismen.

In hoofdstuk 3 is de evolutie van kustaangehechte zandbanken op de lange termijn onderzocht met een model, waarin de volledige niet-lineaire vergelijkingen worden opgelost. Dit model beschrijft de tijdsontwikkeling van de hoogte van bekende oplossingen van het lineaire systeem (hoofdstuk 2), die lijken op waargenomen kustaangehechte zandbanken. De resultaten laten zien dat bodempatronen met eindige hoogte ontstaan wanneer de bodemhelling een kritische waarde β_{c1} overschrijdt. Wanneer de bodemhelling te hoog wordt ($\beta > \beta_{c2}$), vertoont het model explosief gedrag. Zowel β_{c1} als β_{c2} zijn functies van de modelparameters. De eindige hoogte van de banken neemt af en de tijd waarin deze hoogte wordt bereikt neemt toe naarmate golven schuiner invallen op de kust. Een zelfde gedrag wordt waargenomen voor een toename in de golfhoogte en golfperiode. Uit een analyse van de potentiële energiebalans van de zandbanken blijkt, dat deze niet eindeloos doorgroeien, omdat de hellingen te

steil worden. Hoe hoger een zandbank is, des te lastiger is het om het zand omhoog te transporteren en meer zand zal terugrollen ten gevolge van de helling van de bank. Een constante evenwichtshoogte wordt bereikt wanneer de aan- en afvoer van nieuw zand gelijk is.

In hoofdstuk 3 is verder de gevoeligheid van de resultaten onderzocht voor een verandering in het aantal ($N - 1$) gemodelleerde subharmonischen, d.w.z. oplossingen van het gelineariseerde systeem met een kustlangse golflengte die groter is dan die van de initieel snelst groeiende oplossing. De ontwikkeling van de hoogte van kustaangehechte zandbanken blijkt onafhankelijk van het aantal subharmonischen te zijn. De saturatietijdschaal is enkele duizenden jaren en suggereert dat waargenomen kustaangehechte zandbanken nog niet in evenwicht zijn. Gedurende de periode van groei komen de gemodelleerde zandbanken voor in groepen, maar in de loop van de tijd wordt het gehele domein bedekt met zandbanken. De migratiesnelheid van de banken neemt iets af in de tijd en de gemiddelde kustlangse afstand tussen individuele banken in de evenwichtstoestand is zo'n 20% groter dan in de beginfase van groei van de banken. De saturatietijdschaal, evenwichtshoogte, gemiddelde kustlangse onderlinge afstand en migratiesnelheid van de zandbanken variëren nauwelijks met N . Echter, individuele tijdreeksen van de hoogtes van afzonderlijke lineaire oplossingen en van de berekende bodempatronen zijn sterk afhankelijk van de keuze voor N . Aangezien de waarde van de laatste parameter niet goed bekend is, suggereert dit resultaat dat de gedetailleerde evolutie van kustaangehechte zandbanken slechts over een beperkt tijdsinterval kan worden voorspeld.

In hoofdstuk 4 is de rol van wisselwerkingen tussen golven en zandbanken op de initiële vorming van kustaangehechte zandbanken onderzocht. Modelexperimenten tonen aan dat golf-zandbank wisselwerkingen ervoor zorgen dat de zandbanken meer tegen de kust aangedrukt komen te liggen. Zowel de groei als de migratie van de zandbanken wordt beheerst door transport van zand in de waterkolom, niet door zandtransport dichtbij de bodem. Het model laat zien dat alleen die zandbanken groeien waarvan de stroomopwaartse kant naar de kust toegebogen ligt. Dit komt omdat de golven extra sterk refracteren wanneer ze de kam van een zandbank passeren en minder sterk wanneer ze een geul passeren, want refractie is afhankelijk van de waterdiepte. Dit heeft tot gevolg dat stroomopwaarts van de kam golfbanen bij elkaar komen, de golfhoogte op die plaats toeneemt en extra zand wordt opgewoeld. De stroming voert dit mee en laat het materiaal vervolgens iets stroomafwaarts van de kammen achter, omdat daar de golfhoogte lager is. Er komt meer zand bij dan dat er erodeert en het resultaat is extra groei en migratie. Dit nieuwe mechanisme is ook werkzaam wanneer de zeebodem vlak is. De oriëntatie, onderlinge kustlangse afstand en vorm van de kustaangehechte zandbanken komen goed overeen met die van waargenomen banken in verschillende kustzeeën.

Tot slot is in hoofdstuk 5 de invloed van golf-zandbank wisselwerkingen onderzocht op zowel de initiële vorming van kustaangehechte zandbanken, alsook op de korrelgrootte sortering over de banken en het effect van sorteringsprocessen op groei en migratie van de banken. Modelresultaten duiden aan dat sortering van zand een afname in de groei en migratie van de zandbanken veroorzaakt, terwijl de golflengte nauwelijks wordt beïnvloed. De afname in groei en migratie is een gevolg van een verminderde porositeit van het bodemmateriaal wanneer het uit verschillende korrelgroottes bestaat. Erosie van bodemmateriaal is hierdoor

lastiger. In het geval dat de opwerveling van zand afhankelijk is van de bodemruwheid wordt het grove zand nabij de troggen gevonden, in alle andere gevallen vlakbij de kammen. Een fysische analyse heeft uitgewezen dat de faseverschuiving, die het model berekent tussen de gemiddelde korrelgrootte van het zand en de zandbanken, een direct gevolg is van de golf-zandbank wisselwerkingen. Iets stroomopwaarts van de kammen wordt het meeste zand opgewerveld. Dit zand bestaat uit fijn en grof materiaal. Wanneer bodemruwheidseffecten worden verwaarloosd, is de opwerveling van fijn materiaal effectiever dan dat van grof materiaal (omdat grof materiaal makkelijker neerdwarrelt). Het grove zand blijft achter enigszins stroomopwaarts van de kammen, het fijne zand komt terecht nabij de troggen. Het meenemen van bodemruwheidseffecten leidt tot fundamenteel andere resultaten. De ruwheid van de bodem is groter in gebieden met grotere korrels, mede omdat bodemribbels in die gebieden groter zijn. Door de grotere bodemruwheid is de erosie van grof materiaal effectiever dan dat van fijn materiaal: het fijne zand blijft achter nabij de kammen, het grove zand komt terecht in de buurt van de troggen. Vergeleken met voorgaande studies is de gemodelleerde maximum variatie in de gemiddelde korrelgrootte over de zandbanken beter in overeenstemming met de waarnemingen.

DANKWOORD

IK WIL JE IETS ZEGGEN, MAAR IK DENK DAT IK HET BETER KAN SCHRIJVEN.
DAAROM SCHRIJF IK JE.
MAAR MISSCHIEN KAN IK HET JE TOCH BETER ZEGGEN.*

Huib, ik wil je bedanken voor je betrokkenheid, creativiteit, inzet en enthousiasme van de afgelopen jaren. Wat ik erg heb gewaardeerd is dat je meteen in de startblokken ging staan als ik maar even mijn hoofd om je deur stak en zachtjes zei: "Zeg Huib, ...". Je ziet alle obstakels, vragen en schijnbare onmogelijkheden als uitdagingen die hoe dan ook opgelost zullen worden; iets wat ik door de nodige tegenvallers heen ook enigszins heb geleerd (denk ik). Mieke en Rinse, ik vond het leuk jullie ook te leren kennen.

A great pleasure was the collaboration with 'the Catalan guys from Barcelona'. First of all, I want to thank Daniel Calvete for the inspiring discussions about morfo-number-such-and-such, for surprisingly quick extensions of the code and for providing useful comments on all kinds of things. I enjoyed the visits to Esther, Victor and Neil; shame on my poor Catalan vocabulary, cause the boys had to read books for me instead of me reading for them. Albert Falqués and Cesca Ribas, I am grateful for your support during my master project and concerning my PhD project, I am still happy I was not the only one encountering 'messy modes'. Also thanks to Yolanda Ciriano and Roland Garnier for the pleasant stays in Barcelona.

Voor hun bijdrage in de 'messy modes'-discussie wil ik ook Maarten van der Vegt, Henk Schuttelaars en Joost Rommes bedanken. I was very happy to meet Giovanni Coco and Brad Murray and enjoyed the collaboration on sortodynamics. I want to thank Nick Dodd for the interest in my research project. Leerzaam was de zomerschool in Denemarken, georganiseerd door Aart Kroon; ik kijk daar met veel plezier op terug. Tomas van Oyen wil ik bedanken voor de plezierige afstudeerbegeleidingsfase. Voor nu sterkte met je eigen promotieonderzoek!

Sjef, de colleges dynamische oceanografie hebben ons heel wat uurtjes doen samenwerken. Jouw idee om het einde van de collegeperiode te vieren met een heerlijke pannenkoek is al die jaren geweldig gebleken. De Krommerijn pannenkoek bleef onverdeeld favoriet. De wandelingen door Amelisweerd waren net zo waardevol en zorgden ervoor dat we van elkaars wel en wee op de hoogte bleven. Ook Sidonie bedankt voor het warme onthaal in Bergen aan Zee.

*Bron: Toon Tellegen - Bijna iedereen kon omvallen - 1993

Ik wil alle IMAU (oud)-collega's bedanken voor de prettige werkatmosfeer. Karin Huijts, ik had me geen betere kamergenootte kunnen bedenken! Bedankt voor al die gezellige jaren, de leuke gesprekken over sporten, werken, fietsen, trouwen, kamerplanten, Limburg en noem maar op. Ik wens je voor de komende tijd heel veel sterkte toe, samen met Rudo. Carlijn van Tuyll, succes met de laatste loodjes en Jeroen Hazewinkel, reizende rakker, laat die interne golven maar komen. Yvonne Wouda, ik heb al die jaren jouw sporen mogen volgen die ingesleten zijn in het fietspad tussen Vianen en de Uithof, wetende dat jij me zowel 's ochtends als 's middags al voorgegaan was; dank je! Hans Coops, ook een speciaal woord van dank voor je interesse en de leuke gesprekken. Frank Witte en Diederik Kruijssen, ik heb genoten van de relatieveer ... eh ... relativiteits-uurtjes.

Ik ben blij met alle vrienden die ik om me heen heb staan. Mattanja, ik heb vele jaren je huisgenoot mogen zijn, erg leuk! En dat die squashrackets heel bleven als jij ermee aan de haal ging; de zwaartekracht deed er niets tegen. De sportieve uurtjes waren erg waardevol, bedankt! Verder wil ik graag noemen, Hielke, al jaar en dag een zeer gewaardeerde vriend, alle andere mensen van de after-Ichthus kring, Dirk-Jan en Hanneke, Gerrit, huiskring-genoten en gemeenteleden van de Rehobothkerk.

Lieve Christiaan, ik ben je innig dankbaar voor je liefde, steun en vertrouwen! Het voortdurende gebrom van mijn laptop is binnenkort toch echt verleden tijd; ja, zelfs jij had een computer nog nooit zo versleten gezien als die van mij. Bedankt voor je relativiseringsvermogen en het heerlijke plekje thuis. 't Is maar goed dat je één grote hobby hebt, modelbouwen en modelvliegen, waarin bijna net zoveel tijd gaat zitten als in een promotie. Dat mijn vliegtuig nog steeds heel is, mag geen wonder heten. Een zonnestraal in ons leven is de kleine Benjamin. Lieve Benjamin, als je eens wist hoeveel jouw geschater, opgewekte gebrabbel en trotse, eerste stapjes hebben bijgedragen aan een vlotte pen in de eindfase ... ik hou van je! Papa en mama, ik wil jullie bedanken voor jullie eeuwige liefde, betrokkenheid en steun! Ook mijn schoonouders, bedankt, voor de mooie plek waar we jaren mochten wonen en de nauwe betrokkenheid bij elkaar. Sigrid en Gertwin, vele zaterdagen tuften jullie onze kant op; bedankt voor de gezelligheid! Rianne, je pannenkoeken waren onovertroffen, je betrokkenheid hartverwarmend. Maaïke, lieve zus, jij ook bedankt! Opa en oma Vis, hartelijk dank voor uw bijdrage aan mijn proefschrift. En opa, de Latijnse bul mag u als eerste lezen. Alle andere familie, hier niet bij name genoemd, evenzoveel hartelijk bedankt!

Kinderen - spelenderwijs voltrekken ze het wonder. Zeggen met bloemen waar geen woorden voor zijn. Zeggen met woorden waar geen bloemen voor zijn. Spelenderwijs voltrekken zij de hemel op aarde.[†]

*Als de Here het huis niet bouwt,
tevergeefs zwoegen de bouwlieden daaraan.[‡]*

[†]Bron: Hans Bouma - Droom die mens werd, 101 gedichten bij een geboorte - 2005

[‡]Bron: Bijbel - Psalm 127:1a - NBG-vertaling 1951

CURRICULUM VITAE

Ik ben geboren op 26 oktober 1979 in Rotterdam en getogen in Krimpen aan den IJssel, alwaar het eerste Deltawerk werd gerealiseerd met de bouw van de stormvloedkering in de Hollandsche IJssel (1958). In 1997 heb ik mijn VWO diploma behaald aan de Gereformeerde Scholengemeenschap Randstad (GSR) in Rotterdam. Daarna werd de keuze: Natuurwetenschappen en Bedrijf & Bestuur (NWBB) aan de Universiteit Utrecht (1997-2001). De interdisciplinaire aanpak heeft me in deze studie erg aangesproken. In mijn afstudeeronderzoek bij TNO in Apeldoorn heb ik gekeken of een geïntegreerde aanpak van twee verschillende milieuproblemen (het broeikas effect en verzuring) kan leiden tot kostenvoordelen. In 2001 behaalde ik het doctoraal diploma NWBB, met een specialisatie in economie en recht. In de tussentijd was ik begonnen met het volgen van vakken bij de faculteit Natuur- en Sterrenkunde in Utrecht en besloot deze studie te voltooien. Geboeid door het klimaatsysteem koos ik voor een specialisatie in de Meteorologie en Fysische Oceanografie (MFO). Op sociaal en bestuurlijk vlak was ik in deze tijd actief bij christelijke studentenvereniging Ichthus Utrecht. Het slotakkoord van heel wat jaren studeren werd gevormd door een studie, waarin het modelleren van golven en stromingen en het effect daarvan op schuingelegde banken dichtbij de kust centraal stond. In 2003 heb ik hiervoor (een zeer plezierige) drie maanden doorgebracht met de Grup de Morfodinàmica Costanera aan de Universitat Politècnica de Catalunya in Barcelona. Na het behalen van mijn doctoraal diploma Natuur- en Sterrenkunde in januari 2004, begon ik in februari 2004 een promotieonderzoek naar kustaangehechte zandbanken onder begeleiding van Huib de Swart aan het Instituut voor Marien en Atmosferisch onderzoek Utrecht (IMAU) en in dienst van de Stichting voor Fundamenteel Onderzoek der Materie (FOM). De inhoud van dit onderzoek, te vinden in dit proefschrift, zal ik op 26 november 2008 verdedigen.

